Modification of Titania with Gold-Copper Bimetallic Nanoparticles and Preparation of Copper-Based Photocatalysts : Application in Water Treatment

Hai Zibin



UNIVERSITÉ PARIS SUD

Ecole Doctorale de Chimie – ED 470
Laboratoire de Chimie-Physique (LCP)

THESE

PRESENTEE POUR OBTENIR LE GRADE DE
DOCTEUR EN SCIENCES DE L'UNIVERSITE PARIS-SUD

Spécialité Chimie-Physique
Soutenue le 02/07/2013

Par: **Zibin HAI**

Modification of Titania with Gold-Copper Bimetallic Nanoparticles and Preparation of Copper-Based Photocatalysts: Application in Water Treatment

Commission d'examen:

Pr. Jiafu Chen, *Directeur de thèse*
DR. Hynd Remita, *Co-directrice de thèse*
Pr. Yupeng Tian, Président du Jury
Pr. Guozhong Wu, *Rapporteur*
Dr. Nancy Brodie-Linder, *Rapporteur*
Pr. Shu-hong Yu, *Examinateur*
Pr. Hewen Liu, *Examinateur*
Pr. Isabelle Lampre, *Examinatrice*

ACKNOWLEDGMENTS

First of all, I would like to thank my supervisor, Prof. Jiafu Chen for his supports and guidance during my Ph. D study at University of Science and Technology of China. His critical idea and thoughtful advice was a guiding light for my research from the beginning and to the end. Throughout my study and research project, he has constantly given me advice with good insight.

I also express my sincere gratitude and appreciation to my co-supervisor Prof. Hynd Remita, for providing me with this unique research opportunity at LCP of University Paris-sud. I appreciate the selfless help she gave to me in my study and life when I was in Paris. This thesis is accomplished under her expert guidance. I am deeply impressed by her profound knowledge in science and dedicated attitude to research. I shall benefit from this experience in my future work and life.

Special thanks also given to my thesis committee: Prof. Guozhong Wu and Dr. Nancy Brodie-Linder for their precious time spent on reading this thesis and for giving advice and suggestions.

I also express my thanks to Sébastien Sorgues and Christophe Colbeau-Justin (LCP, Université Paris-Sud, France) for the TRMC measurements and helpful discussions. I also would like to thank Laurent Delannoy (LRS, UPMC, Paris, France) for the thermal treatment of the samples. I also thank Patricia Beaunier (LRS, Université Paris-VI, France) for the TEM characterization. Thanks to Daniel Bahena Uribe and Prof. Miguel José-Yacamann (Department of Physics & Astronomy, UTSA, USA) for the STEM-EDS characterizations. I also thank Shengquan Fu and Jianliu Huang (USTC, China) for the SEM characterizations.

I also would like to thank my colleagues Chunhua Zhu and Guanglai Shen in USTC. They helped me with my experiments and life. I greatly acknowledge my colleagues in

Paris-Sud, Priyanka Ray, Nadia El Kolli, Anais Lehoux, Abdel Karim El Omar, Mohamed El Mehdi Zekri, and Michele who gave me a lot of help and made my life meaningful in Paris-Sud. I also address my thanks to Professor Jun Lü and her students Tong Sheng, from Hefei University of Technology, who offered me the photocatalytic apparatus to fulfill my experiments.

At last, I must thank my family, who has given me the inspiration and courage to undertake the PhD study. I own special thanks to my father Gang Hai and my mother Xia Zhang, who painstakingly raised me and cultivated me to be a useful man. Especially, I give my thanks to my wife Xiangyun Jin, who gave me love and encouragement. During the year I studied in France, she was waiting for me. She arranged all the home affairs so I could throw myself into my thesis.

Zibin HAI

May 2nd, 2013

CONTENTS

ABBREVIATIONS

AOPs:	Advanced Oxidation Processes
BET:	Brunauer, Emmett and Teller
CB:	Conduction Band
DP:	Deposition Precipitation
DPU:	Deposition Precipitation with Urea
DRS:	Diffuse Reflectance Spectroscopy
EDS:	Energy-Dispersive Spectroscopy (or EDX: Energy-Dispersive X-ray)
HAADF:	High Angle Annular Dark Field
MO:	Methyl Orange
NHE:	Normal Hydrogen Electrode
NPs:	Nanoparticles
NTs:	Nanotubes
P25:	A mixture of anatase (80%) and rutile (20%)
PAA:	Polyacrylic Acid
PP:	PAA and PVA
PVA:	Polyvinyl Alcohol
PZC:	Point of zero charge
RhB:	Rhodamine B
SAED:	Selected-Area Electron Diffraction
SDS:	Sodium Dodecyl Sulfate
SEM:	Scanning Electron Microscopy
SPR:	Surface plasmon resonance
TEM:	Scanning Transmission Electron Microscopy
TER:	Triethylrhodamine
THPC:	Tetrakis Hydroxymethyl Phosphonium Chloride
TRMC:	Time Resolved Microwave Conductivity
UV:	Ultra Violet
VB:	Valence Band
XPS:	X-ray Photoelectron Spectroscopy
XRD:	X-Ray Diffraction

LIST OF TABLES

LIST OF FIGURES

GENERAL INTRODUCTION

General Introduction

Photocatalysis with semiconductors has recently emerged as a promising method for environmental decontamination in water and air treatment. Titanium dioxide (TiO_2) has proven to be the most promising semiconductor photocatalyst not only because of its excellent photoactivity, but also because of its non-toxicity, chemical stability and low cost. However, the fast charge-carrier recombinations and the wide band-gap of TiO_2 limit its application under solar light. Hence, many efforts have been devoted to solve these problems, such as modification with metal nanoparticles or other semiconductors, doping with transition metals or nitrogen and sulfur… In this thesis work, we modified TiO_2 with gold and/or copper to enhance its photocatalytic activity.

Semiconductors with intrinsic band-gap suitable for visible light photocatalysis havealso attracted considerable attention in the past decades. Radiolytic synthesis of copper oxides and copper sulfides with special morphologies and their photocatalytic activity were also investigated in this work.

This manuscript contains four chapters:

The first chapter lays the foundation for this thesis, it will outline several themes. We will make a brief review of various conventional advanced oxidation processes used for wastewater treatment. Basic principles of the photocatalysis processes are described. We will review significant effects on photocatalytic activity of semiconductors. We also will summarize ways to improve the photocatalytic activity. The main deposition methods for semiconductor surface modification will be introduced. The principles of radiolytic synthesis of metal nanoparticles will be presented. We also will describe the research front of non-TiO_2 visible light photocatalysis, and particularly radiolytic synthesis of copper oxides and copper sulfides.

In the second chapter, we describe the experimental conditions, including materials, synthetic protocols for the modification of TiO_2 and preparation of copper compounds, the characterization techniques and the equipments used for the photocatalytic reactions of different model pollutants.

Chapter 3 presents the results obtained for modification of TiO_2 with Au, Cu monometallic nanoparticles or Au-Cu bimetallic nanoparticles by various deposition methods, including colloid deposition by radiolysis, colloid deposition by chemical method, deposition-precipitation method with urea. The photocatalytic properties of the modified TiO_2 were studied for degradation of rhodamine B, phenol and methyl orange under UV and visible light. Time resolved microwave conductivity (TRMC) technique was used to follow the kinetics of excited electrons induced after laser excitation of TiO_2. The results of the photocatalytic activities of TiO_2 under UV excitation related to lifetime of the photogenerated charge-carriers are presented.

In chapter 4, the radiolytic synthesis of copper oxides and copper sulfides of different morphologies and their photocatalytic activity are presented.

Finally, we present the conclusion of this work with some perspectives.

CHAPTER I

FOUNDATION IN PHOTOCATALYSIS

Chapter 1 Foundation in Photocatalysis

1.1 Water Pollution

In recent years, global environmental pollution has become a serious problem that needs to be solved urgently. The on-going industrialization has been bringing about serious pollution to air and water. Water is essential to our existence. The pollution from both the atmosphere and soil will eventually enter water by deposition and dissolution. Thus, water remediation has emerged as a high national and international priority over the past decades.

Hazardous wastes caused a big threat to water. Both advanced industrialized nations and developing countries encounter tremendous environmental problems related to the remediation of hazardous wastes. The hazardous wastes exist in military installations and civilian effluents. For military installations, problems with hazardous wastes are related to the disposal of hazardous chemicals in lagoons, underground storage tanks, and dump sites. Consequently, the surrounding soil or underlying groundwater aquifers were contaminated with various kinds of hazardous wastes. In the civilian sector, the elimination of toxic and hazardous chemical wastes such as halogenated hydrocarbons from waste effluents and previously contaminated sites has become a major concern.[1] Commonly, general classes of compounds of concern include: volatile organics, chlorinated aromatics, dibenzofuran, dioxins, chlorophenols, chlorinated aliphatic and olefinic compounds, nitrogenous compounds, hydrocarbons, carboxylic acids, alcohols, halocarbons, heteroatom compounds…[2] Besides, aqueous soluble dyes and other aromatic molecules, such as rhodamine B, methyl orange, and phenol etc. are widely used in textile and other industries. These compounds are considerably stable in the environment under natural light.

Conventional methods for elimination of these pollutants are aeration, extraction, high-temperature incineration, filtration, distillation, reverse osmosis, ion exchange, absorption, biological treatment, ozonation, and etc. However, most of the organic compounds are resistant to conventional chemical and biological treatments. The so-called advanced oxidation processes (AOPs) have been reported to be effective for the near ambient

degradation of soluble organic contaminants from waters and soils, because they can contribute to an almost total degradation.[3-4] Of these, advanced oxidation processes (AOPs) will probably constitute the best option in the near future.[5]

1.2 Advanced Oxidation Processes (AOPs)

As defined broadly, AOPs are mainly considered to be the aqueous phase oxidation processes which are based primarily on the oxidizing hydroxyl radical in the mechanism resulting in the destruction of the model pollutants or xenobiotic or contaminant compounds.[5-6]

Highly reactive hydroxyl radicals ($HO^{\bullet}$) [$E^0(HO^{\bullet}/H_2O = +\ 2.8\ V_{NHE}$)] are traditionally known to be the active species responsible for the decomposition of organic pollutants.[7-8] Owing to their high standard reduction potential of 2.8 V vs NHE (Normal standard hydrogen electrode) in acidic media,[9] these radicals are able to oxidize almost all organic compounds to carbon dioxide (CO_2) and water.[10]

AOPs show considerable similarities because of the participation of hydroxyl radicals in most of the mechanisms that are operative during the reaction. Hydroxyl radicals are extremely unstable because of their high reactivity. Considering that the hydroxyl radicals are unstable and reactive, they must be produced continuously *in-situ* through chemical or photochemical reactions.

Generally, AOPs use photolysis (UV), ozone (O_3), hydrogen peroxide (H_2O_2), ozone in combination with UV (O_3/UV), hydrogen peroxide and UV light (H_2O_2/UV), ozone plus hydrogen peroxide (O_3/H_2O_2), Fenton's reagent (see page 11) and photocatalysis (which is based on interaction of light with semiconductors).[5, 11-12] Compared to the AOPs based on O_3/UV, H_2O_2/UV, or on photo-Fenton processes (techniques which have been practically employed to carry out the mineralization of organic compounds), semiconductor-based photocatalysis has also shown a promising potential in organic pollutant degradation in recent years. The various AOPs are described in detail in the following paragraph.

1.2.1 Photolysis (UV)

This process is based on excitation of organic molecules by UV irradiation.[5, 13] Direct photolysis involves the interaction of light with molecules—in addition to water—to bring about their dissociation into fragments. It is reported that photolysis can be more effective when UV irradiation is combined with ozone, hydrogen peroxide, homogeneous, heterogeneous catalysis or photocatalysis.[11, 14]

1.2.2 O_3

In the O_3 AOP, two possible ways of oxidizing action may be taken into account: the direct way owing to the direct reaction between O_3 and the dissolved molecules,[15] and the radical way (indirect way) because of the reaction triggered by the radicals generated in the ozone decomposition (hydroxyl radicals).[5] Compared to other oxidizing reagents, O_3 is more efficient in organic pollutant degradation. In addition, it is not harmful for most of the organisms. To our knowledge, ozonation has been widely used for drinking water disinfection.[16] However, the limitation of its application in water treatment is due to its high energy consumption.[11]

1.2.3 O_3/UV

Photolytic ozonation (O_3/UV process) is an effective means for the oxidation and destruction of organic pollutants in aqueous solution.[17-19] It has a crucial potential for wastewater treatment. In principle, aqueous systems saturated with O_3 are irradiated with UV light at 253.7 nm. In this case, the extinction coefficient of O_3 at 253.7 nm is 3300 M^{-1} cm^{-1}, which is much higher than that of hydrogen peroxide.[11] O_3/UV process generates HO• radicals by the light-induced homolysis O_3 and the subsequent by the interaction of O (^1D) with water.[20-21] The global reaction is shown in equation 1.1:

$$O_3 + H_2O \xrightarrow{h\nu<310\,nm} 2HO^{\bullet} + O_2 \qquad (1.1)$$

O_3/UV is more effective for the decomposition of some organic compounds than either UV or O_3 alone.[11] In this O_3/UV process, it is worth noting a high synergetic effect between O_3 and UV photolysis.

1.2.4 H_2O_2/UV

This method is based on the formation of HO· radicals by the photolysis of hydrogen peroxide and the subsequent propagation reactions:

$$H_2O_2 + hv \rightarrow 2HO^{\bullet} \quad (1.2)$$

Irradiation with a wavelength shorter than 400 nm is able to photolyze the H_2O_2 molecule. The accepted mechanism is the cleavage of the molecule H_2O_2 into two hydroxyl radicals. Under UV irradiation (250 nm < λ), the yield of photolysis of aqueous hydrogen peroxide is around 50 times lower than O_3. This process needs a relatively large amount of H_2O_2 or a much longer UV-exposure time than, for instance, AOP of UV/O_3.[11]

Hydroxyl radical can react with H_2O_2 to generate the hydroperoxyl radical (HOO·), which is also an oxidative species (equation 1.3). Hydrogen peroxide is also known to decompose to hydroxyl radical by a dismutation reaction with a maximum rate at the pH equal to its pKa value of 11.6 (equation 1.4)

$$HO^{\bullet} + H_2O_2 \rightarrow H_2O + HOO^{\bullet} \quad (1.3)$$

$$H_2O_2 + HO_2^{\bullet} \rightarrow H_2O + O_2 + HO^{\bullet} \quad (1.4)$$

The generated hydroxyl radical can react with organic pollutants by hydrogen abstraction, electrophilic addition and electron transfer mechanisms. However, the disadvantage of this AOP is the absorption coefficient of H_2O_2 and quantum efficiency of HO· is very low at wavelength longer than 250 nm.

1.2.5 O_3/H_2O_2

In this process, hydroxyl radicals are generated by a radical-chain mechanism by interaction between O_3 and the H_2O_2.[5, 22-23] Equation 1.5 shows the global reaction:

$$2O_3 + H_2O_2 \rightarrow 2HO^{\bullet} + 3O_2 \quad (1.5)$$

1.2.6 O_3/H_2O_2/UV

This AOP is based on the O_3/H_2O_2 process. The efficiency of this process is tremendously improved by association with UV irradiation. It is considered to be the most effective process for extremely polluted effluents.[24] However, the process is not an economic method.

1.2.7 Fenton's reagent

In this process, hydroxyl radicals are generated by means of the reaction between H_2O_2 and iron (II). The overall reaction for the hydroxyl radical generation in acidic solution is shown in equation 1.6:

$$H_2O_2 + Fe^{2+} \rightarrow Fe^{3+} + HO^{\bullet} + OH^{-} \qquad (1.6)$$

The mechanism for the ferric ion in decomposition of H_2O_2 in acidic solution to release hydroxyl radicals has been intensively discussed in former studies.[25]

1.2.8 Photocatalysis

Photocatalysis has proven to be a promising technology for degrading aromatic compounds.[26-29] Compared to the other conventional AOPs discussed above, photocatalysis may be more effective and more economicas the involved semiconductor can continuously catalyze the decomposition of organic pollutants under irradiation. The energy is transformed directly from solar to chemical without consumption of oxidizing reagents. Electron-hole pairs are produced in the semiconductors under irradiation (in most cases UV light). These charged carriers can recombine or migrate to the surface (when they escape from recombination) of the semiconductor creating radicals. Under O_2, these radicals can oxidize most of the organic molecules. The general equation taking place in semiconductors under irradiation is shown as following:

$$\text{Semiconductor} \xrightarrow[\geq E_g]{h\nu} \text{Semiconductor} + (e_{CB}^{-} + h_{VB}^{+}) \qquad (1.7)$$

(h_{VB}^{+} represents the positive holes, E_g refers to band-gap)

However, this promising technique is still in a developmental stage.[30]

1.3 Photocatalysis for decomposition of organic dyes

Studies on photocatalysis by TiO_2 have been reported since the start of 20th century. In 1938, Doodeve and Kitchener reported that photodegradation of dyes by TiO_2 occurred both in vacuum and under oxygen. But at that time, this phenomenon was identified as a mechanism of photo-bleaching.[31] It was also found that TiO_2 itself did not change through the photo-bleaching reaction. However the terminology of "photocatalyst" was not used for TiO_2 but it was called a photosensitizer.

After the report of photocatalytic water splitting by Fujishima,[32] there were some studies on other applications of the photocatalytic activity of TiO_2 in decomposition of organic pollutants such as organic dyes . Frank and Bard reported for the first time the decomposition of cyanide in the presence of aqueous TiO_2 suspension.[33] A mechanism was given for this photodecomposition process based on the known procedure on TiO_2 electrodes. The electrons in the conduction band reduce oxygen while the holes in the valence band cause the oxidation of CN^-:

$$CN^- + 2OH^- + 2h_{VB}^+ \rightarrow CNO^- + H_2O \qquad (1.8)$$

And the further oxidation of CNO^- is possible. Although the quantum efficiencies here were lower than those found for a single crystal TiO_2 electrode coupled to a platinum cathode in a photoelectrochemical cell, their are still respectable.

In a photodecomposition system which includes the photocatalyst and the organic molecules, photo-induced molecular transformations or decompositions occur at the surface of the catalyst. Depending on where the initial excitation takes place, photocatalysis can be generally divided into two classes of processes:

1) Catalyzed photoreaction. The initial photoexcitation occurs in an adsorbate molecule which then interacts with the ground state catalyst substrate.

2) Sensitized photoreaction. The initial photoexcitation takes places in the catalyst substrate and the photo-excited catalyst then transfer an electron or energy into a ground state molecule, the process is called a sensitized photoreaction.

The initial photoexcitation of the system is followed by subsequent electron transfer and (or) energy transfer. In consequence, chemical reactions in the photocatalysis processes are attributed to the de-excitation processes by electron transfer or energy transfer.

1.4 Rising of Photocatalysis

Fujishima and Honda discovered the photocatalysis in water splitting on TiO_2 electrodes for the first time in 1972, marking the beginning of a new era in photocatalysis.[32] Before, the photocatalytic investigation of TiO_2 might have just attracted partially scientists' attention in the field of either catalysis or photochemistry. Then, this report on water splitting by TiO_2 attracted the attention not only of electrochemists but also of many scientists in a broad area, and study of photocatalysis by TiO_2 is now developing widely in both academic and industrial society.[34] The application of photocatalysis in the fields of polluted water treatment, solar-to chemical energy conversion via water splitting (hydrogen generation) and CO_2 reduction into light hydrocarbons are attracting much attention.[35]

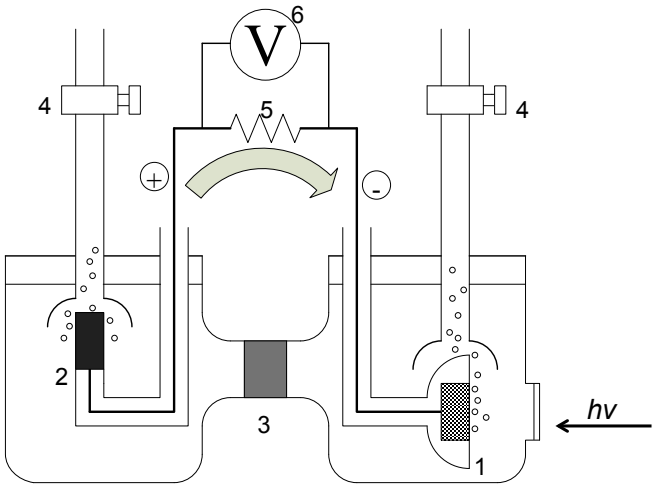

Figure 1.1 Schematic diagram of photoelectrochemical cell. (1) n-type TiO_2 electrode; (2) platinum black counter electrode; (3) ionically conducting separator; (4) gas buret; (5) load resistance; and (6) voltmeter. From ref. [32]

Figure 1.1 gives the schematic diagram of a photoelectrochemical cell designed by Fujishima for water splitting. A single crystal wafer of n-type TiO_2 (rutile) was employed as anode while the platinum black as the cathode. Both of the electrodes were submerged in an aqueous electrolyte of pH 4.7. The TiO_2 anode was connected to a platinum black electrode

with copper lead wire through an external load resistance. An ionically conducting separator was placed between the two basins to segregate the electrolytes. When the surface of the TiO_2 electrode was irradiated with light consisting of wavelengths shorter than 415 nm, that is 3.0 eV, which corresponds to the band gap of TiO_2, a photocurrent flowing from the platinum positive electrode to the TiO_2 negative electrode was detected by the voltmeter. The direction of the current gave the evidence that the oxidation half reaction (oxygen evolution) occurs at the TiO_2 electrode and the reduction half reaction (hydrogen evolution) takes place at the platinum black electrode.

To show more details, the two half reactions at the anode and the cathode were featured on one particle-based TiO_2 molecule combined with platinum particles. It can be seen from **Figure 1.2** that an electron is transferred from valence band into conduction band, excited by the energetic UV photons. In the meanwhile, a positive hole which has a high oxidation potential was produced in the valence band and it is able to drive the oxidation of H_2O to O_2 and H^+. The excited electron moved to the platinum particle because the Fermi energy level of platinum is lower than that of conduction band of TiO_2. Finally, hydrogen was generated from the H^+ reduction by the excited electrons on the surface of the platinum electrode.

It must be figured out that there are two indispensable requirements for the thermodynamically favorable water-splitting reaction; the first one is that the conduction band should have higher energy than the hydrogen-evolution potential and the second one is that the valence band should be lower than the oxygen-evolution potential.

By UV irradiation of TiO_2, it is then possible to decompose water without employing any external voltage, according to the following equations:

$$\mathrm{TiO_2} + 2\,h\nu \rightarrow 2\,e^- + 2\,h^+ \tag{1.9}$$

$$2\,h^+ + \mathrm{H_2O} \rightarrow \frac{1}{2}\,\mathrm{O_2} + 2\,\mathrm{H^+} \tag{1.10}$$

$$2\,e^- + 2\,\mathrm{H^+} \rightarrow \mathrm{H_2} \tag{1.11}$$

(h^+ refers to the hole)

So, the overall reaction is:

$$H_2O + 2\,h\nu \rightarrow \frac{1}{2}O_2 + H_2 \qquad (1.12)$$

When semiconductor photocatalysts are used in organic pollutant degradation, the redox potential of the generated holes should be sufficiently positive to produce hydroxyl radicals. Furthermore, the redox potential of the electrons must be negative to be able to reduce adsorbed O_2 to superoxide ($O^{2-\cdot}$).[36-37] The hydroxyl radical can be generated by the reaction of oxidative holes with surface adsorbed water (H_2O) or hydroxyl anions. It has such a strong oxidizing activity that it breaks down the aromatic structure of organic pollutants into a variety of intermediate products and finally to inorganic molecules like H_2O, CO_2 etc.

According to the discussion above, these two half reactions in photocatalysis could be used to solve not only the problem of energy shortage, but also to treat the serious environmental pollution.

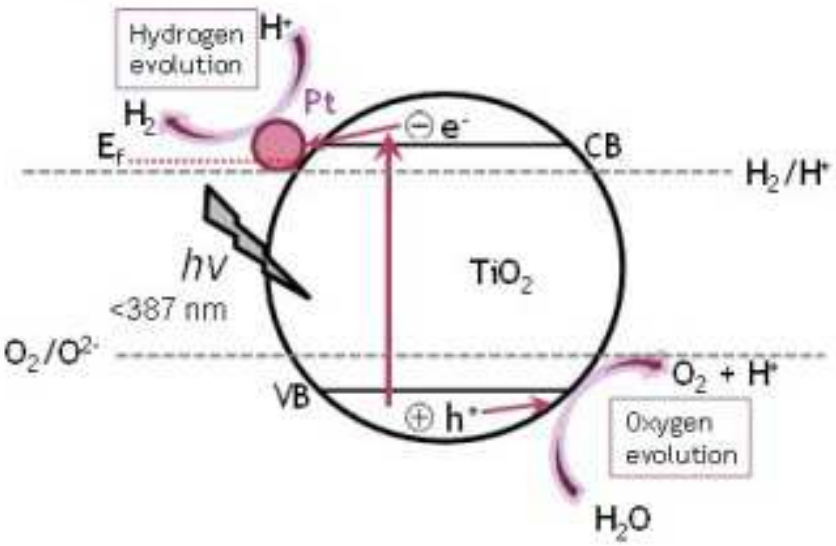

Figure 1.2 Scheme of water splitting process in a particle-based semiconductor catalyst linked with a platinum particle.

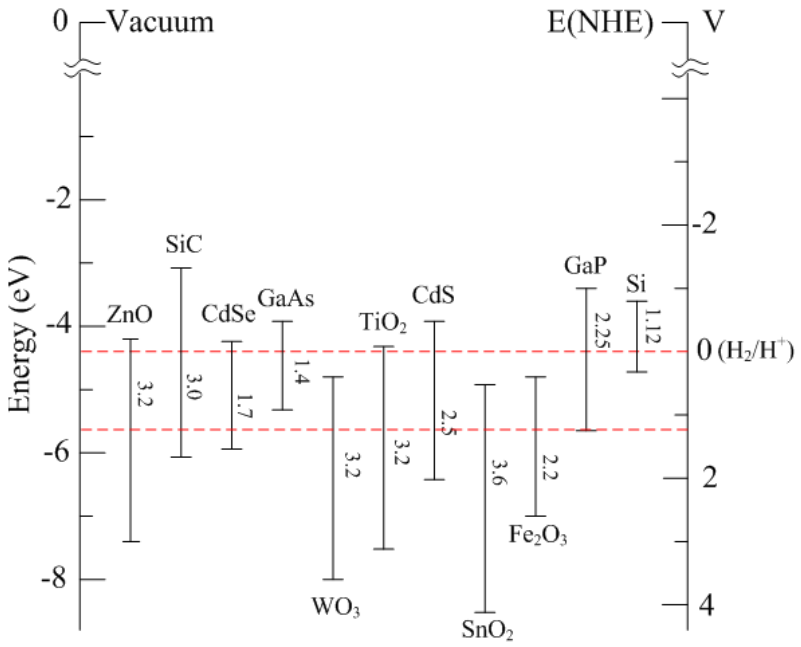

Figure 1.3 CB and VB positions for various semiconductors in aqueous electrolytes at pH = 1.

1.4.1 Band-gap Positions

The VB and CB positions of a range of semiconductors including oxides, non-oxides and elemental Si are presented in **Figure 1.3**. A potential scale (V) versus the normal hydrogen electrode (NHE) is presented on the right side and the internal energy scale is given on the left for comparison to the vacuum level. Redox potentials for the water-splitting half-reactions versus the NHE are also indicated with dashed red lines. From the scheme, we can see that for the water-splitting reaction to take place without external potential application, the band-gap should straddle these redox potentials, that means that the CB should have higher energy (more negative potential) than the hydrogen evolution potential while the VB should be lower than the oxygen evolution potential.

Although the band-gap energy is a significant property for photocatalysis. the ability of a photocatalyst to absorb visible and/or UV light is the crucial factor, but other properties have also to be considered such as: the photocatalyst should be also i) chemically and biologically inert and photostabe, ii) nontoxic, and iii) inexpensive. The semiconductors TiO_2, ZnO, CeO_2, $SrTiO_3$, WO_3, Fe_2O_3, Bi_2S_3, GaN, CdS and ZnS can all act as photoactive materials for redox/charge-transfer processes owing to their electronic structures which are characterized

by a filled valence band and an empty conduction band. Among these semiconductors, TiO_2 is the most widely used photocatalytic material because it fulfills all of the above requirements as well as exhibiting adequate conversion values.[36, 38] TiO_2 has many advantages such as it has high photon harvesting performance in UV light region; it widely exists on the earth and exhibits an extremely chemical stability; it is biologically inert and non-toxic; moreover, it is cheap and easy to synthesize. In this thesis, one part of the work is surface modification of TiO_2 to enhance its photocatalytic activity under UV and visible illumination.

1.5 Basic Principles in the Photocatalysis Process

1.5.1 Semiconductor Photoexcitation

Originally, when a semiconductor is irradiated with light with sufficient energy (larger than the band gap), photochemical processes occur in the semiconductor (Figure 1.4). As shown in the insert, an electron is excited from the valence band to the conduction band, forming a positive hole in the valence band. Just after that, recombination of the generated electron-hole pairs takes place in the core of semiconductor (trace **a**). Some electron-holes can escape from recombination and migrate to the surface of the semiconductor, and finally can recombine with each other (trace **b**) or react with the species at the surface. Besides, recombination also occurs on the surface between the electron-holes *in-situ* generated on the surface. The electron-holes on the surface can either react with electron acceptor (trace **d**) or electron donor (trace **c**). These two paths are examples of direct reactions between the semiconductor and the adsorbate (electron donor or acceptor). While the recombination in trace **a** and **b** results in luminescence. These pathways illustrate the fundamental processes of photocatalysis in a semiconductor.

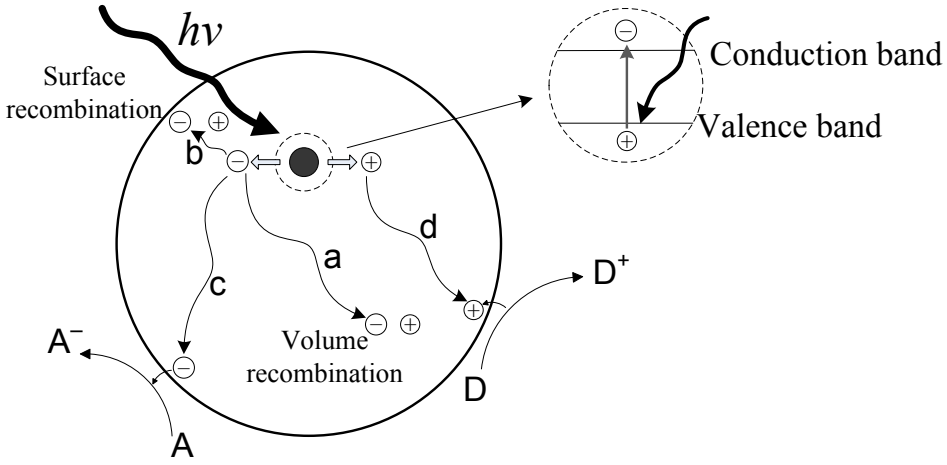

Figure 1.4 Photochemical processes in a semiconductor followed by deexcitation events. Where A is electron acceptor and D is electron donor. From ref. [39]

1.5.2 Characteristic Times

The general mechanism for the heterogeneous photocatalysis on TiO_2 on the basis of laser flash photolysis measurements has been proposed by Hoffman *et al.*[1] A succession of photochemical processes takes place in the volume and on the surface of the solid. **Figure 1.5** shows the scheme of characteristic times in the photocatalysis processes, where the photoreactions are initiated from the charge-carrier generation. The absorption of a photon occurs very rapidly, on the order of 10^{-15} s.[39]

Then, the charge-carrier trapping occurs, including electrons trapping and holes trapping. The >TiOH in the equations represents the primary hydrated surface functionality of TiO_2.[1, 40] $\{>Ti^{4+}OH^{\cdot}\}$ is the surface-trapped VB hole (hydroxyl radical), and $\{>Ti^{3+}OH\}$ is the surface-trapped CB electron. The eq. 1.15 represents a dynamic equilibrium indicating a reversible trapping of CB electrons in a shallow trap below the CB edge. So, there is a finite probability that e^{-} could transfer back into the CB at room temperature.

From this characteristic times scheme, we could clearly conclude that the two routes to enhance the photocatalytic activity are: i) increasing of charge-carrier yields, ii) trapping the charge-carrier to postpone their recombination.

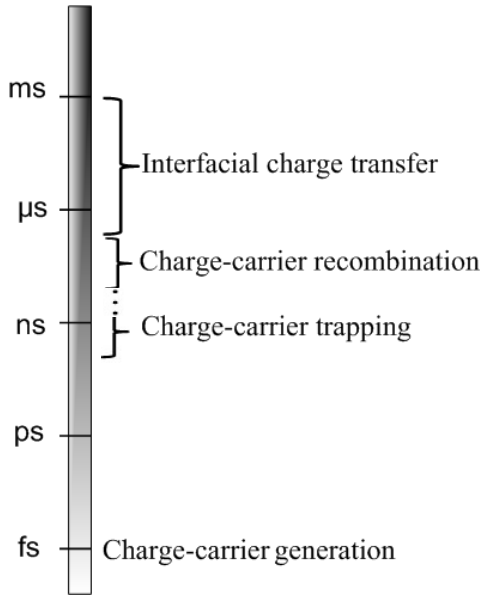

Figure 1.5 Scheme of characteristic times in the photocatalysis process.

a) Charge-carrier generation:

$$TiO_2 \xrightarrow{h\nu} h_{VB}^{+} + e_{CB}^{-} \qquad \text{fs} \qquad (1.13)$$

b) Charge-carrier trapping.

$$\text{Fast trap} \qquad h_{VB}^{+} + > Ti^{4+}OH \rightarrow \left\{ > Ti^{4+}OH^{\bullet} \right\}^{+} \quad 10 \text{ ns} \qquad (1.14)$$

$$\text{Shallow trap} \qquad e_{CB}^{-} + > Ti^{4+}OH \leftrightarrow \left\{ > Ti^{3+}OH \right\} \quad 100 \text{ ps} \qquad (1.15)$$

$$\text{Deep trap} \qquad e_{CB}^{-} + Ti^{4+} \rightarrow Ti^{3+} \quad 10 \text{ ns} \qquad (1.16)$$

c) Charge-carrier recombination

$$\text{slow recombination} \quad e_{CB}^{-} + \left\{ > Ti^{4+}OH^{\bullet} \right\}^{+} \rightarrow > Ti^{4+}OH \quad 100 \text{ ns} \qquad (1.17)$$

$$\text{fast recombination} \quad h_{VB}^{+} + \left\{ > Ti^{3+}OH \right\} \rightarrow > Ti^{4+}OH \quad 10 \text{ ns} \qquad (1.18)$$

d) Interfacial charge transfer.

$$\text{slow} \quad \left\{ > Ti^{4+}OH^{\bullet} \right\}^{+} + D \rightarrow > Ti^{4+}OH + D^{\bullet+} \quad 100 \text{ ns} \qquad (1.19)$$

$$\text{very slow} \quad e^{-} + A \rightarrow > Ti^{4+}OH + A^{\bullet-} \quad \text{ms} \qquad (1.20)$$

1.5.3 Quantum Efficiency (QE)

The efficiency of the photocatalytic process is measured by a quantum yield which is defined as the number of events occurring per absorbed photon. In the case of a photodecomposition reaction, the quantum yield (Φ) is defined as the ratio of the amount of molecules decomposed over that of photons absorbed. It is very difficult to measure the actual absorbed light in heterogeneous systems because of the scattering of light by the semiconductor surfaces. However, it is generally assumed that all the light is absorbed and the efficiency is quoted as an apparent quantum yield. Sometimes the QE is measured as the yield of a particular product in spite of several products produced in the photocatalytic reactions. The QE for an ideal system follows the simple relationship below:

$$\Phi = \frac{k_{CT}}{k_{CT} + k_R} \qquad \text{(eq. 1.21)}$$

In this equation 1.21, k_{CT} represents the rate of charge transfer, and k_R refers to the rate of the electron-hole recombination.

1.5.4 Recombination Effects

Apparently, a semiconductor with a lower band-gap is able to absorb more photons in the visible region, which would lead to a better photocatalytic activity under sunlight. In fact, there are many semiconductors with low band-gap energy in the visible region, such as GaAs (E_g is around 1.4 eV) shown in **Figure 1.3**. However these semiconductors are not efficient in photocatalysis. One of the main reasons for their poor photocatalytic performance is the high recombination rate of their generated electron-hole pairs. The recombination effect could scavenge the electron-hole pairs and thus lower the possibility of electron-hole transfers from the semiconductor to the adsorbed molecules. This effect dominates in many of the semiconductors with small band-gap energies over electron-hole transfer making these semiconductors inefficient.

Obviously, electron-hole recombination is detrimental to the efficiency of a semiconductor photocatalyst. Therefore, modifications of semiconductor surface such as

deposition of metal, doping, or combinations with other semiconductors can be beneficial in decreasing the electron-hole recombination rate and thereby increasing the quantum efficiency of the photocatalysts.

1.6 Ways to enhance the photocatalytic activity

1.6.1 Quantum size effects

The size of the semiconductor particles can have an effect on the band-edge positions; these are known as quantum size effects. Quantum size effects occur for semiconductor particles on the order of 10-100 Å in size. The anomalies arise when the size of the semiconductor particles become comparable to the de Broglie wavelength of the charge-carriers in the semiconductor. These effects could increase the band-gap of the semiconductors as the nanoparticle size gets smaller and smaller. **Figure 1.6** illustrates the increases in band gap for CdS and CdSe when the particle size decreases. For CdS, the band-gap dramatically increases from its characteristic value for the bulk CdS of ~2.6 eV to 3.0 eV for the particles in the order of 26 Å in size. In the case of CdSe, the band-gap increases by 0.32 eV as the particle size decreased from 4.2 nm to 2.8 nm. The more positive valence band implies an increased oxidizing capability of the holes. As well, the more negative conduction band means an enhancement on reducing capability of the generated electrons.

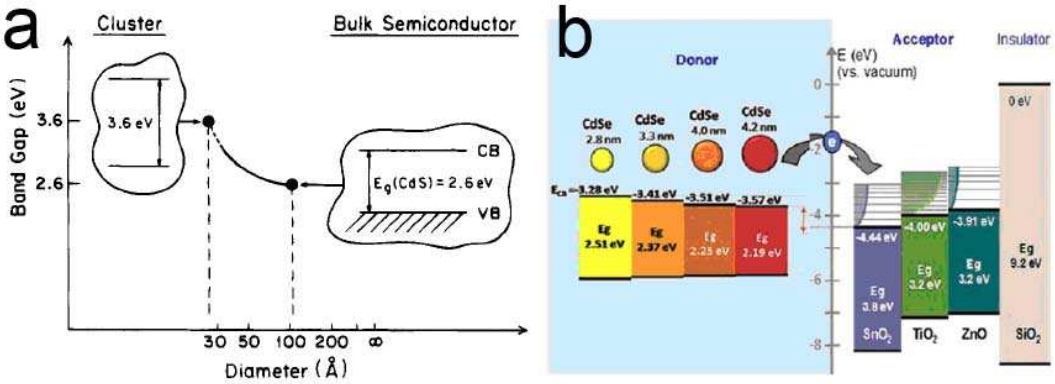

Figure 1.6 Quantum size effect on semiconductor band-gap of (a) CdS, and (b) CdSe and metal oxides. [39, 41]

The reason for the increased band-gap with decreasing size can be ascribed to the

confinement of electron and hole in a potential well of small geometrical dimensions. The confinement produces a quantization of discrete electronic states and thus increases the effective band gap of the semiconductor.[39, 42-43]

These changes on the band-edge positions of the valence band and the conduction band influence the photocatalytic properties of the semiconductor, providing an interesting yet challenging aspect to the design of novel photocatalysts.

1.6.2 Metal Semiconductor Modification

Semiconductors can be modified by deposition of metal particles on their surface. The metal that modifies TiO_2 does not form part of the crystalline framework, but exists in a separate phase in interfacial contact with TiO_2 particles. In order to obtain stable and durable materials, the metal used in this approach should be chemically inert. Based on this, noble metals are most suitable for this purpose.

In the past decades, various metals such as Au, Ag, Pt, Pd, Rh, Ni, Co, Ir, and Cu were used to modify the surface of TiO_2 or other substrates.[44-54] The modification with metal nanoparticles (NPs) can result in an enhancement in photocatalytic activity under UV illumination. The approved interpretation is that the metal NPs act as electron traps, which can decrease the electron-hole pair recombination rate, consequently prompt the holes to diffuse to the semiconductor surface where oxidation of organic species can occur. The scheme of the electron trapping by deposited metal NPs is illustrated in **Figure 1.7**. This mechanism was confirmed by time resolved microwave conductivity (TRMC) measurements, where a reduction in the photoconductance was observed for the semiconductor excited with UV laser.[50] Takai et al. used methylene blue (MB) as an indicator to prove the electrons were stored in the TiO_2 supported Ag NPs.[55] Moreover, modification with bimetallic NPs can result in better catalytic activity compared to the monometallic ones, ie. Ag-Au[35, 56-57], Au-Cu,[58-61] and Pt-Au [48] modified titania. We have shown in this work that the bimetallic Au-Cu alloyed nanostructures were more efficient in electron scavenging than the monometallic Au and Cu ones.[62]

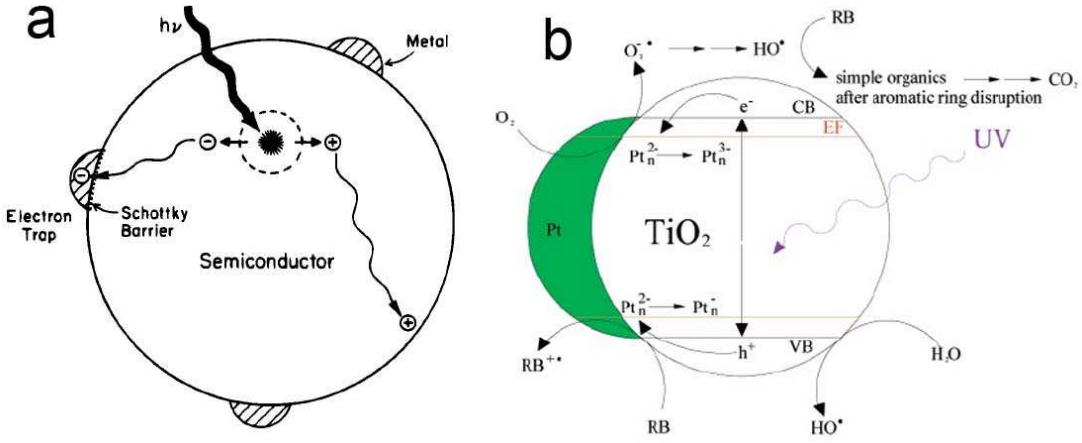

Figure 1.7 Schematic illustrations of **(a)** photo-excited metal-modified semiconductor particle, and **(b)** RhB degradation under UV irradiation on Pt cluster modified TiO_2. [39, 50]

There are different mechanisms proposed to explain the enhancement caused by modification with plasmonic metal NPs under visible illumination. Plasmonic metal nanostructures are characterized by their strong interaction with resonant photons through an excitation of surface plasmon resonance (SPR). SPR can be described as the resonant photo-induced collective oscillation of surface electrons, established when the frequency of photons match the intrinsic frequency of surface electrons oscillating against the restoring force of positive nuclei.[63] The first view, most commonly, is that incident photons are absorbed by metal NPs injecting electrons into the conduction band of TiO_2.[64-69] The metallic plasmonic NPs (mainly Au, Ag, Cu which have a plasmon resonance in the visible range) essentially act like a dye sensitizer, absorbing resonant photons and transferring the excited electron to the nearby semiconductor particle (**Figure 1.8**). Besides, the electron transfer implies that plasmon activation of metal particles on semiconductor particles by visible light generates positive charges on the metal particles and conduction-band electrons on the semiconductor particles. The oxidation and reduction reactions occur simultaneously as with conventional photocatalysts activated by UV-light.[39, 70] Because of the excellent mobility of charge-carriers and high absorption cross-sections, which is up to 10^5 larger than the cross-section of typical dye sensitizer molecules, plasmonic nanostructure of noble metals represent very promising sensitizers.[71] Another advantage for the noble metal NPs is that they are very stable under light compared to dye sensitizers.

Tsukamoto *et al.* put forward a new idea on the charge transfer mechanism.[70] It is that the joint active site consisting of Au/anatase/rutile phases facilitates smooth e^- transfer from the photoactivated Au NPs to TiO_2 (**Figure 1.9**). In a system of anatase/rutile modified with Au NPs, a) plasmon activation of gold NPs transfers e^- to the tightly bound rutile; b) e^- then move to well-conjugated anatase; and c) O_2 is reduced there by e^-. Usually, e^- transfer from rutile to anatase is thermodynamically unfavorable because the conduction band potential (E_{CB}) of rutile (-0.05 V vs NHE) is less negative than the E_{CB} of anatase (-0.25 V).[72] However, the e^- injection from Au NPs to rutile accumulates e^- in its conduction band and contributes to the negative shift of E_{CB} (**Figure 1.9b**).[73-75] As a result, the consecutive e^- transfer from Au particles to rutile and then to anatase leads to a photoactivity under visible irradiation.

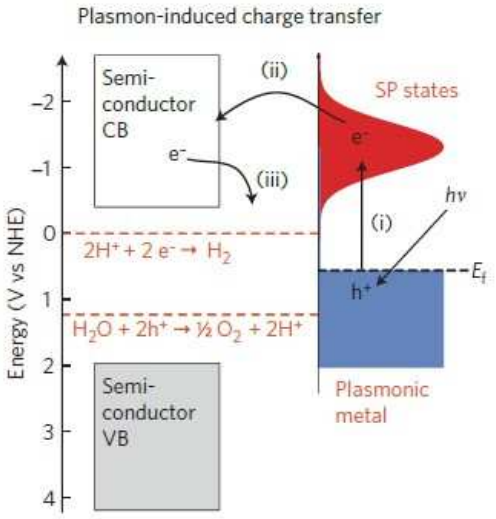

Figure 1.8 Mechanism of SPR-induced charge transfer. (i) electrons near the metal Fermi level, Ef are excited to surface plasmon states; (ii) the electrons transfer to a nearby semiconductor particle; (iii) this activates electron-driven processes such as the hydrogen-evolution half-reaction.[63]

Besides the charge injection mechanism, near-field electromagnetic mechanism was also proposed to interpret SPR-induced enhancements in the photocatalytic activity of semiconductors on systems where the semiconductor and the plasmonic metal were separated from each other by thin, non-conductive spacers preventing any direct charge exchange between the two building blocks.[76-78] This mechanism is based on the interaction of the

semiconductor with the strong SPR-induced electric fields localized nearby at the metallic nanostructure. The electric fields close to plasmonic nanostructures (a few nanometers) are orders of magnitude higher than the field of incident photons. Photo-excited plasmonic nanostructures essentially play a role of concentrators that can amplify the local light intensity. As the rate of electron-hole formation in a semiconductor is proportional to the local intensity of the electric field (more specifically $|E|^2$),[79-80] the electron-hole generation in some regions of the semiconductor increases by a few orders of magnitude (even grow out of nothing when the light energy is not sufficient to excite the semiconductor).

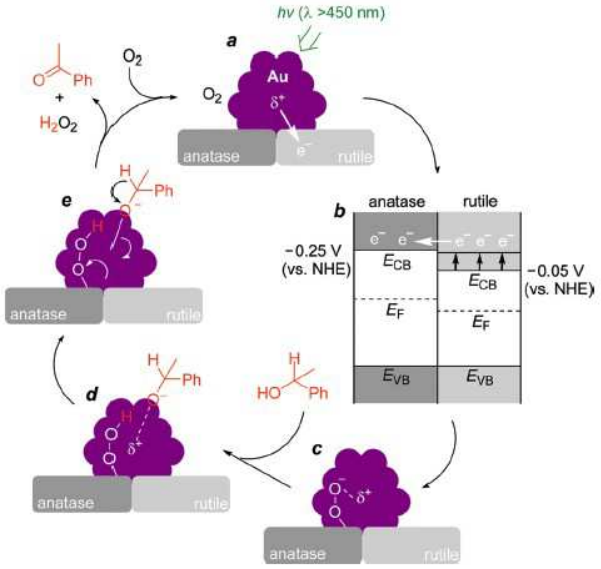

Figure 1.9 Proposed mechanism for Aerobi oxidation of Alcohol on the Au/P25 catalyst under visible light illumination.[70] (P25 is a commercial TiO_2 that is a mix of anatase and rutile)

1.6.3 Composite Semiconductors (Semiconductor Modification)

Coupled semiconductor photocatalysts provide an available way to increase the photocatalytic efficiency by extending the light absorption range, or by increasing the charge-carriers separation. Serpone et al. reported for the first time that coupling of the semiconductors CdS and TiO_2 led to significant enhancement in efficiency of the photocatalytic process.[81-82] Figure 1.10 illustrates the photoexcitation process for the composite semiconductors CdS-TiO_2. A photo-excited electron can be injected from the valence band of CdS into the conduction band of TiO_2 while the holes remain in the VB of CdS. The difference in the energy levels of these two semiconductors plays a significant role

in achieving such a charge-carrier separation. The separated electrons and holes are then free to undergo electron transfer to the adsorbates on the surface of semiconductors. The charge injection process in a composite semiconductor system has been further demonstrated by carrying out methyl viologen (MV^{2+}) reduction by TiO_2 particles, but with excitation of CdS in the CdS/TiO_2 system.[83-84] The reduction of MV^{2+} in the presence of TiO_2 indicates an efficient charge injection process with a quantum efficiency of 100%. This result shows that the coupling of semiconductors with the appropriate energy levels can improve the photocatalytic activity by better charge separation. Several combinations of semiconductor couples have since been investigated extensively.[83, 85-87]

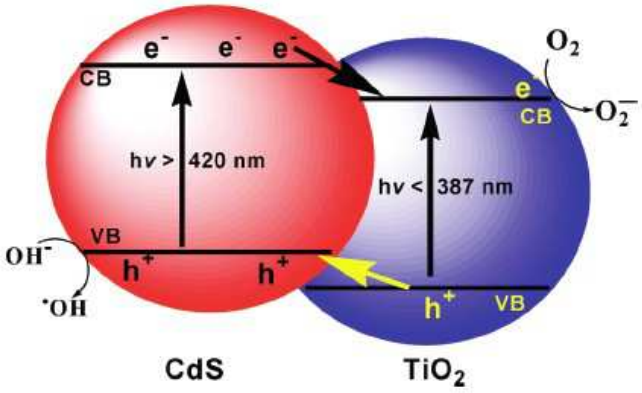

Figure 1.10 Schematic diagram representing inter-particle electron transfer process from the conduction band (CB) of photoexcited CdS to the CB of TiO_2.[88]

Most recently, TiO_2-graphene composite was found to be a promising photocatalyst under visible illumination. Some publications are related to this novel titania composite.[89-93] Such composite possesses a great adsorptivity of dyes, extended photo-responding range (by the formation of a chemical Ti-O-C bond), and enhanced charge separation and transportation properties simultaneously. The enhancement in photocatalytic activity was ascribed to the giant two-dimensional planar structure of graphene, which served as a better platform for adsorption of dyes and charge transportation and separation. This provides a new possibility in addressing various environmental issues and energy crisis.

1.6.4 Doping

1.6.4.1 Metal doping

Although the photocatalytic activity of TiO_2 is among the highest for all the semiconductors, it requires high energy light of wavelength shorter than 387 nm. This great shortcoming of TiO_2 tremendously limits the practical use because the natural solar light predominantly consists of visible light and also because the use of UV light is costly and needs eye and skin protection for any personnel exposed to the radiation. Thus, strategies were developed in the past two decades to push the absorption onset of pristine TiO_2 towards longer wavelengths by doping with transition metal or non-metal elements.

Doping with transition a metal benefits the improved trapping of electrons inhibiting electron-hole recombination. Choi *et al.* systematically studied the effects of 21 different metal ion dopants on the photocatalytic activity of quantum-sized pristine TiO_2. Enhanced photoactivity was observed for Fe^{III}, Mo^{V}, Ru^{III}, Os^{III}, Re^{V}, V^{IV}, Cu^{II}, and Rh^{III} substitution for Ti^{IV} at the 0.5 atom % content in the TiO_2 matrix.[94] Fe^{III} doped TiO_2 was found to have the maximum enhancement in quantum efficiency for $CHCl_3$ oxidation.[1, 95-96] The concentration of the beneficial transition metal dopants is very small and large concentrations are detrimental.[39] In general, metal dopants undergo corrosion causing a gradual decay in photocatalytic reactions.[69]

1.6.4.2 Non-metal doping

Asahi *et al.* reported visible light active N-doped TiO_2 that triggered the nascent TiO_2 materials to be photoactive over the visible light region.[97] Whether visible-light photoactivity could be introduced in TiO_2 by doping, it depends on three requirements: (i) the doping should produce states in the band-gap of TiO_2 that absorb visible light; (ii) the conduction band minimum, including subsequent impurity states, should be as high as that of TiO_2 or higher than the H_2/H_2O level to ensure its photoreduction activity; (iii) the states in the gap should overlap sufficiently with the band states of TiO_2 to transfer photoexcited carriers to reactive sites at the photocatalysts surface within their lifetime. Condition ii and iii require the use of anionic species for the doping rather than cationic metals, which often offer quite localized *d* states deeply in the band gap of TiO_2 and contribute to recombination centers of charge-carriers. The doped TiO_2 was yellowish owing to the noticeable absorption in the

region of visible light (< 500 nm) (**Figure 1.11a**). The doped photocatalysts showed activity under visible illumination for degradation of acetaldehyde and decoloration of methylene blue solution (**Figure 1.11**c). Nitrogen atoms were believed to substitute for lattice oxygen atoms, evidenced by the peak at 396 eV in the N 1s XPS spectra (**Figure 1.11**b).[97]

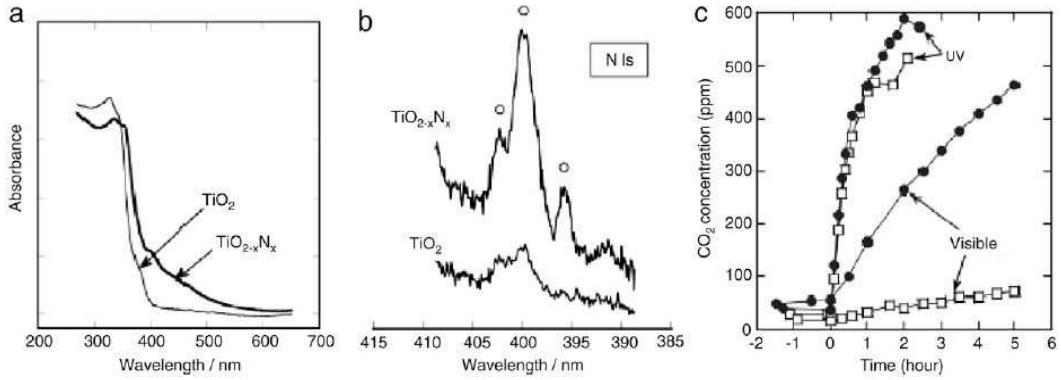

Figure 1.11 (a) Optical absorption spectra of $TiO_{2-x}N_x$ and pristine TiO_2 films. **(b)** N 1s XPS spectra of $TiO_{2-x}N_x$ and TiO_2 films. **(c)** CO_2 evolution as a function of irradiation time during the photodegradation of acetaldehyde gas in the presence of $TiO_{2-x}N_x$ (solid circles) and pristine TiO_2 (open squares) under UV illumination and visible irradiation. [97-98]

After the breakthrough in visible photocatalysis by N-doped TiO_2, researchers started to attempt the doping of TiO_2 with non-metal atoms such as N[99-102], C[103-105], S[106-107], B[108], P[109], F[110], and Cl[111], where the shift of the absorption threshold of TiO_2 into the visible range and the photocatalytic activity under visible illumination were reported.

The mechanism of photoactivity under visible light for the non-metal doped semiconductors is still in debate.[112-113] One school proposed that corresponding increases in photoactivity of TiO_2 were owing to a narrowing of the intrinsic band-gap, while others contended that the band gap of TiO_2 was not narrowed but rather that the ensuing oxygen vacancies formed upon doping. However, doping with non-metal elements normally requires harsh preparation conditions and the degree of doping is difficult to determine with chemical analyses.

1.6.5 Surface Sensitization

Surface sensitization of a wide band-gap semiconductor can be achieved by

chemisorbing or physisorbing photosensitive dyes. The photo-sensitization process can also expand the wavelength range of excitation for the semiconductor. Electrons are excited from the sensitizer and then transferred to the semiconductor.[39, 114] Grätzel showed that TiO_2 could be photo-sensitized with a dye in the presence of a redox couple to produce electrical power; this has since become known as the Grätzel solar cell.[115-117] Some common photosensitive dyes are used as sensitizers including erythrosine B, thionine, and analogs of $Ru(bpy)_3^{2+}$.[118-119] **Figure 1.12a** presents the mechanism of the photosensitized degradation on a TiO_2 particle, compared to other kinds of photoexcitation processes. If the oxidative energy level of the excited state of the dye molecule with respect to the conduction band edge of the semiconductor is favorable (more negative, **Figure 1.12b**), the excited dye molecule can then transfer electrons to the conduction band of the semiconductor. The electrons can be captured by adsorbed species on the surface, such as hydroxyl anions or O_2 groups. Owing to the high surface area of nanosized semiconductor systems and the adequate spectrum characteristic of common dyes, the joined systems might absorb a high proportion of the incident solar energy flow (even high as 46%), despite that obtained efficiencies, in solar simulation under AM 1.5 conditions, are still low (around 7-11%).[120-122]

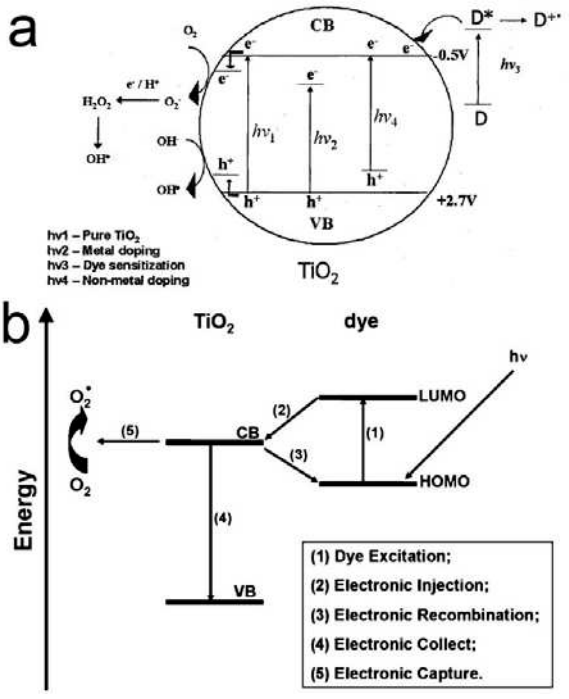

Figure 1.12 (a) Various electron excitations in TiO_2 photocatalysis,[123] and **(b)** electronic transitions in the dye sensitizing photodegradation process.[120]

Meanwhile, the electron in the CB of the semiconductor can go back to the organic dye (electronic recombination, **Figure 1.12b**, pathway 3) or also undergo de-excitation to the semiconductor VB (**Figure 1.12**b, pathway 4). This fact is drawback to the photocatalysis process and must be avoided to improve the photocatalytic activity. This can be achieved by modifying the surface of semiconductor, which can lead to significant improvements in adsorbing kinetics of dyes or preventing electronic recombination by forming a high energy barrier on the return route of electron to the dye.[124]

1.7 Deposition methods

The parameters such as particle size, dispersion and loading play an important role on the photocatalytic activity of the modified semiconductor photocatalysts. All these parameters are strongly dependent on the preparation procedure. In general, there are three deposition methods: colloid deposition, photo-deposition, and deposition precipitation method. The details, advantages and disadvantages of these procedures are demonstrated in the following paragraphs.

1.7.1 Colloid Deposition

Colloid deposition method is the simplest method, consisting in preparation of metal colloidal solution followed by adsorption of the metal NPs on the substrate surface. For this deposition procedure, there are different methods to prepare metal colloidal solution in water or other solvents. For instance, the most popular methods are reduction of $AuCl_4^-$ with citrate in aqueous phase (the Turkevich method)[125] or the two-phase protocol consisting of reduction of $AuCl_4^-$ by $NaBH_4$ in water and extraction into toluene of the Au NPs by means of a phase transfer agent (the Brust method).[126] Gold NPs of 5 nm with narrow size distribution can be obtained. Besides, an alternative is reduction of Au^{III} ions by tetrakis (hydroxymethyl) phosphonium chloride (THPC), giving a hydrosol of gold NPs with average diameter 1~2 nm.[127] THPC acts simultaneously as reducing and stabilizing agent. Moreover, a characteristic method induced by radiolytic reduction was used to synthesize metal colloidal suspensions in the presence of surfactants or polymer stabilizing

agents.[128-129] Some strong reducing species such as aqueous electrons, hydrogen radicals generated in the radiolysis process are able to reduce metal ions to lower valences and finally to metal atoms. The radiolytic synthesis will be discussed in detail in the following section. These prepared metal colloids can be consequently used as precursors for adsorption on a solid surface. However, it has been often observed that in the adsorption stage the prepared metal colloidal particles undergo coalescence and agglomeration forming metal islands of particle size above 50 nm. This would result in inactivation of the photocatalyst due to the weak interaction with the substrate or the small surface/volume ratio of metal NPs.[69]

1.7.2 Photo-Deposition

Besides deposition of prepared metal colloids, photo-deposition has been widely used to prepare titania supported metal NPs. The method of photo-deposition is valid when the support is a semiconductor such as titania. Electrons and holes are able to be generated when the semiconductor is irradiated with light of sufficient energy. The photo-generated electrons are so reductive that they can reduce metal ions into metal NPs that will be simultaneously deposited on the semiconductor surface. Normally, hole scavengers such as an alcohol have to be added to remove the oxidative radicals. This scheme based on generation of Au NPs on the TiO_2 surface by UV irradiation is illustrated in **Figure 1.13**.

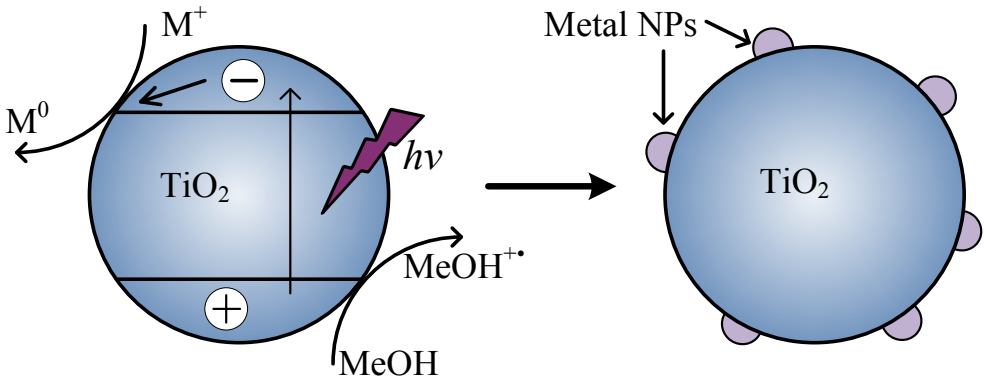

Figure 1.13 Mechanism of the photo-deposition method.

Parameters such as preparation pH, light intensity and deposition time have a significant influence on the nanoparticles size and the final properties of metal deposits. Scaiano *et al.* have shown that the average Au particle size decreased as the intensity of the light increased

in the case of photo-deposition of gold on TiO_2.[130] In contrast, Hidalgo *et al.* reported photo-deposition using irradiation at high light intensity appeared as an ineffective method to obtain Au-TiO_2 catalysts for photocatalytic applications because their conditions lead to very large and heterogeneously distributed gold deposits.[131] This investigation has an identical conclusion to earlier results that deposited gold NPs in smaller size and homogeneous distribution result in an improved photocatalytic activity under UV-vis irradiation.

1.7.3 Deposition-Precipitation (DP)

The most widely used method for preparing Au-TiO_2 catalysts is deposition-precipitation method.[131-132] For many catalytic reactions, supported gold catalysts are more active when metal gold particles are smaller than 5 nm.[133] The gold catalysts method of deposition precipitation with NaOH is developed by Haruta *et al*.[134-136] The DP NaOH method was selected for the production of reference gold catalysts (World Gold Council, www.gold.org). In the DP method, the metal precursors are mixed with the supports forming an aqueous suspension, subsequently precipitated as a hydroxide by increasing the pH value. The key point of the DP method is the prevention of precipitation away from the surface of the supports. The DP method is very simple and convenient and leads to homogeneous samples with reproducible properties and very small metal nanoparticle size (less than 5 nm). **Figure 1.14** illustrates the steps of the deposition-precipitation method.

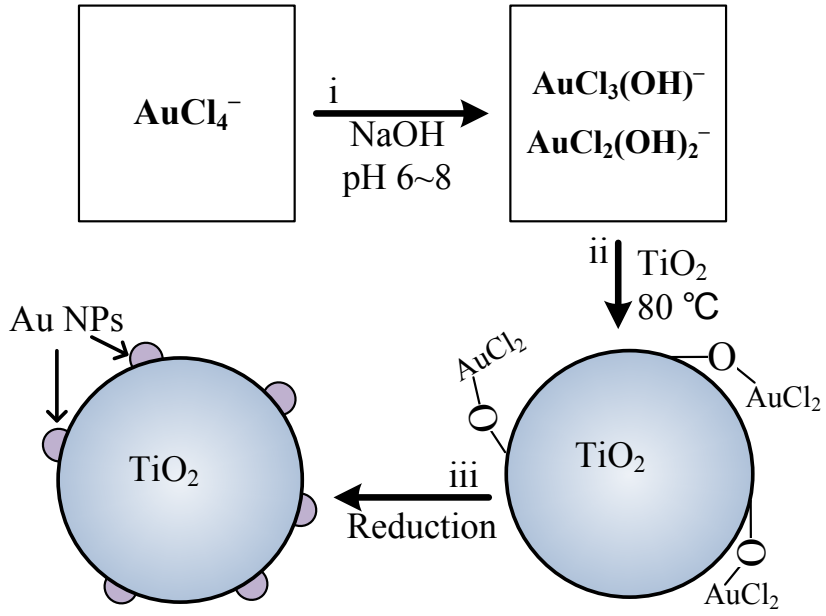

Figure 1.14 The scheme of deposition-precipitation with NaOH method.

TiO_2 is an amphoteric oxide. The surface of TiO_2 is negatively charged in basic solution, owing to the main surface species O^-. The charge of TiO_2 surface becomes less negatively charged when the pH value decreases. TiO_2 carries no net charge at a certain pH value, which is called point of zero charge (PZC, ~ 6 for TiO_2). When the pH value is lower than PZC_{TiO2}, the TiO_2 surface is positively charged because of the surface species OH_2^+.[137] In the first step, $AuCl_4^-$ exchanged chloride ions with hydroxyl to form gold hydroxy chloride complexes; the main species in solution is $AuCl_3(OH)^-$ at room temperature and remains the same up to 150 °C.[138-139] When the DP time increases and therefore the pH value reaches PZC_{TiO2} or much higher (7 or 8 instead of 2), the gold speciation in solution is different, probably $AuCl_2(OH)^-$ at 80 °C. The mechanism of adsorption of gold hydroxy chlorides is not an electrostatic interaction but the formation of a surface complex by reaction with surface OH on TiO_2.[140] As in eq. 1.22, the gold complexes can form Ti-O-$AuCl_2$:

$$TiOH + AuCl_2(OH)_2^- \leftrightarrow TiOAuCl_2 + H_2O + OH^- \qquad (1.22)$$

This adsorption mechanism can interpret the DP NaOH results: (i) the amount of deposited gold reaches a maximum at pH 6, when the surface charge is neutral; (ii) Au is bound to oxygen atoms of the TiO_2 surface (Au-O-Ti) (no gold hydroxide are formed).[135]

After the deposition takes place, the samples are reduced to obtain gold NPs on the TiO_2 surface. Various routes are used for the reduction, such as thermal treatment under hydrogen gas and radiolytic reduction in aqueous suspension.

There are some disadvantages of DP with NaOH, such as the maximum metal loading is low (≤3 wt.%) when pH is in the range 7-10, deposition yield is less than 100% and inapplicability of some supports with a point of zero charge below 5 [137, 140]. For this reason, Geus *et al.* improved the method of DP with urea ($CO(NH_2)_2$), acting as the precipitating base.[141-142] Urea can gradually and homogeneously release hydroxyl ions throughout the whole solution, as the following equation:[137]

$$CO(NH_2)_2 + 3H_2O \rightarrow 2NH_4^+ + CO_2 + 2OH^- \quad (1.23)$$

This gradual addition of hydroxyl ions avoids local increase in pH and precipitating of metal hydroxide in solution. Compared to DP NaOH procedure, DP urea method can result in a complete deposition of Au on the TiO_2 substrate. The depositon-precipitation mechanism could first involve an initial electrostatic interaction between anionic gold species $AuCl_4^-$ or $AuCl_3(OH)^-$ and the positively charged TiO_2 surface at acidic pH, then the growth of the particles of gold precipitate on these sites, which act as nuclei. When the pH increases in the DP urea procedure, the surface charge intensity of the gold precipitate clusters is modified, leading to a fragmentation, and then to a decrease in the gold particle size with increasing deposition time.[137] We can conclude that the DP urea method, as well as the DP NaOH, is a suitable method for the preparation of gold catalysts on various oxide substrates with point of zero charge in the range of 6-8 (TiO_2, Al_2O_3, CeO_2) but not for silica (PZC ~2).

1.8 Radiolytic Synthesis

Various physical and chemical routes have been used to prepare metal clusters or nanoparticles. In an aqueous phase, the method of preparation of metal NPs involves in general reduction of metal precursor salt by a suitable reducing agent (such as sodium borohydride, ascorbic acid, formaldehyde and hydrazine). Besides, the reduction of metal precursor salt may also be carried out using UV-irradiation, microwave radiation and ionizing

radiations like γ, X-rays or electron (or ion) beams. Among these methods, radiolytic synthesis in solution exhibits the advantage of simple physicochemical conditions (such as room temperature, atmospheric pressure, absence of contaminants) and leads to homogeneous reduction and nucleation in solutions and heterogeneous media.[143]

When aqueous solutions are irradiated by high energy radiation (γ-rays, electron beams, X-rays) excitation and ionization of water takes place as following:[144]

$$H_2O \xrightarrow{\gamma-ray} e_{aq}^{-}, H_3O^+, H^\bullet, OH^\bullet, H_2, H_2O_2 \quad (1.24)$$

During the irradiation of deoxygenated water, many active intermediates are produced, including strong reductive hydrated electrons (e_{aq}^-) and hydrogen atoms ($H^\bullet$), which are strong reducing species with the respective redox potentials: $E^0(H_2O/e_{aq}^-)$ = -2.8 V_{NHE} and $E^0(H^+/H^\bullet)$ = -2.3 V_{NHE} at pH 7.[145-146] At pH 7, the radiolytic yields (quantity of radicals formed per Joule of deposited energy) of the radicals are: $G(e_{aq}^-)$ = 0.26, $G(H^\bullet)$ = 0.06 μmol J^{-1}.[145-146] These radicals can reduce dissolved metal ions to the zero valence state. In the case of a free or complexed monovalent metal ion M^+, the reduction proceeds through:

$$M^+ + e_{aq}^- \rightarrow M^0 \quad (1.25)$$

$$M^+ + H^\bullet \rightarrow M^0 + H^+ \quad (1.26)$$

For the multi-valent metal ions, they are firstly reduced to lower valences and finally to zero-valent state according to a multi-step reaction mechanism involving intermediate valencies (by disproportionation for example). These redox reactions in the case of Au^{III} are demonstrated in detail in chapter 3.3.

In the meantime, strong oxidative hydroxyl radicals $^\bullet OH$ [$E^0(^\bullet OH/H_2O)$ = + 1.9 V_{NHE} at pH 7, $G(^\bullet OH)$ = 0.27μmol J^{-1}] are also generated during the irradiation of deoxygenated water.[145] In this case, hydroxyl scavengers are added to the aqueous solutions to remove oxidative species, and thus obtain a reductive environment (eq. 1.27). Primary and secondary alcohols (such as 2-propanol) or formate are chosen as scavengers, which also react with hydrogen atoms to form reducing radicals (eq. 1.28). [144, 147]:

$$CH_3CHOHCH_3 + OH^{\bullet} \rightarrow CH_3C^{\bullet}OHCH_3 + H_2O \quad k_2 = 1.9 \times 10^9 \text{ L mol}^{-1} \text{ s}^{-1} \quad (1.27)$$

$$CH_3CHOHCH_3 + H^{\bullet} \rightarrow CH_3C^{\bullet}OHCH_3 + H_2 \quad k_3 = 7.4 \times 10^7 \text{ L mol}^{-1} \text{ s}^{-1} \quad (1.28)$$

$$HCOO^- + HO^{\bullet}(\text{or } H^{\bullet}) \rightarrow COO^{\bullet -} + H_2O \,(\text{or } H_2) \quad (1.29)$$

Due to their redox potentials [E^0 ($(CH_3)_2CO/(CH_3)_2C^{\bullet}OH$) = –1.8 V_{NHE} at pH 7, and $E^0(CO_2/COO^{\bullet -})$ = -1.9 V_{NHE}], the radicals formed by reactions (1.28) and (1.29) are almost as powerful reducing agents as H• atoms (–2.3 V_{NHE}). Therefore, these secondary radicals are able to directly reduce metal ions into lower valencies for the multi-valent metal ions and even into a zero valence state for the monovalent metal cations. The reactions leading to the monovalent cations are the following:

$$M^+ + (CH_3)_2C^{\bullet}OH \rightarrow M^0 + (CH_3)_2CO + H^+ \quad (1.30)$$

$$M^+ + COO^{\bullet -} \rightarrow M^0 + CO_2 \quad (1.31)$$

Owing to the quasi-uniform energy distribution in the irradiated medium, the metal ions are homogeneously reduced leading to a homogeneous nucleation throughout the solution. Considering the binding energy between two metal atoms is stronger than the atom-solvent or atom-ligand bond energy, the atoms dimerize when they encounter. Then, by a cascade of coalescence processes, M_2 progressively coalesce to growing clusters (**Figure 1.15**):

$$M^0 + M^0 \rightarrow M_2 \quad (1.32)$$

$$M_m + M_p \rightarrow M_n \quad (1.33)$$

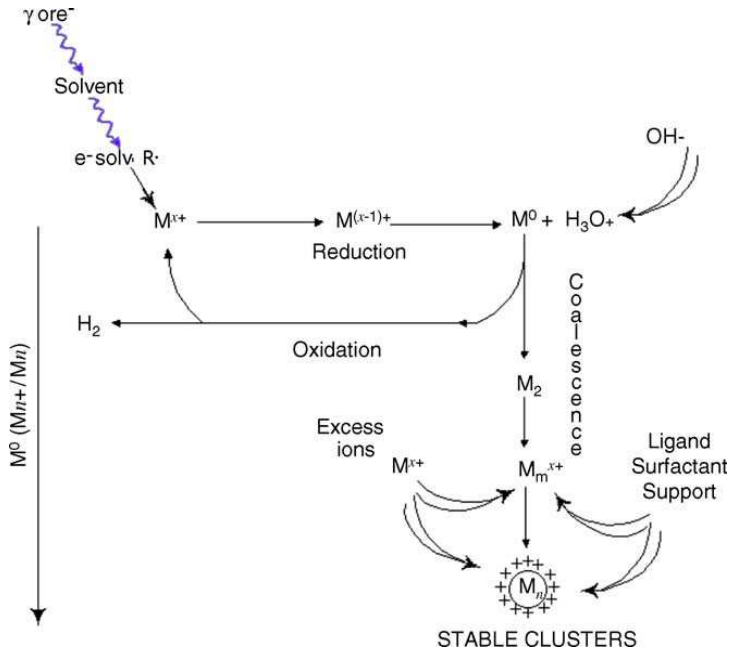

Figure 1.15 Scheme of metal ion reduction in solution by ionizing radiation in the presence of alcohol for scavenging oxidizing species. The isolated atoms formed M^0 coalesce into clusters. They associate excess ions. They are stabilized by ligands, polymers or supports. The redox potential $E^0(M^{n+}/M^n)$ increases with the nuclearity. The smallest oligomers may undergo corrosion.[144]

The atoms or clusters also associate with unreduced ions and these association processes are fast. Finally, according to a multi-step coalescence process, metal clusters are formed with a remarkable monodispersity:

$$M^0 + M^+ \rightarrow M^{2+} \quad (1.34)$$

$$M^{2+} + M^{2+} \rightarrow M_4^{2+} \quad (1.35)$$

$$M_m + M^+ \rightarrow M_{m+1}^{+} \quad (1.36)$$

$$M_{m+x}^{x+} + M_{p+y}^{y+} \rightarrow M_{n+z}^{z+} \quad (1.37)$$

$$M_{n+1}^{+} + e_{aq}^{-} \rightarrow M_{n+1} \quad (1.38)$$

where *m*, *n* and *p* represent the cluster nuclearities (number of reduced atoms), and *x*, *y* and *z* refer to the number of associated ions.[144-145, 148]

1.8.1 Determination of Radiolytic Yield of Metal Species Reduction

In the experiments, we have to calculate the dose (D) required to totally reduce metallic

salts with a certain concentration C_0. Thus, for a solution containing low metal salt concentrations, the maximum reduction yield for an aqueous solution containing oxidant radical scavengers like 2-propanol is:

$$G_{red}(\max) = G_{e_{aq}^-} + G_{H^\bullet} + G_{OH^\bullet} \approx 0.6\ \mu\text{mol J}^{-1} \tag{1.39}$$

Therefore, in the case of a metallic salt solution with a concentration (C_0) and oxidation state (Z), the minimum dose (D_{min}) for the complete reduction can be presented as follow:

$$D_{min} = \frac{Z \cdot C_0 (\text{mol L}^{-1})}{G_{red}(\max)\ (\text{mol L}^{-1})} \tag{1.40}$$

The absorbance of plasmonic metals increases with the dose of irradiation. According to Beer-Lambert law: A = ε*lc*, the concentration (C) of ions reduced by a dose of irradiation (D) can be deduced from the absorbance (*A*).

The plateau (A_{max}) towards which the curve bends at high dose is due to the total reduction of the metal ions to atoms (**Figure 1.16**). Supposing that the final concentration of the metal atoms is equal to the initial concentration (C_0) of the metal ions, the molar extinction coefficient can be deduced from the A_{max}:

$$\varepsilon = \frac{A_{max}}{C_0 \cdot l} \tag{1.41}$$

where *l* is the optical path length.

Assuming the molar extinction coefficient (ε in L mol^{-1} cm^{-1}) of the metal at a certain wavelength is a constant whatever the aggregation state and the size (what is in fact not really exact), we can deduce the radiolytic reduction yield (linear part of the curve A = f(*D*), **Figure 1.16**):

$$G = \frac{Z}{\varepsilon \cdot l} \times \frac{\Delta(A)}{\Delta(D)} \tag{1.42}$$

The curve, C = f(*D*) can be deduced from the absorbance spectra (if ε does not change with the size of the aggregates) recorded at different doses.

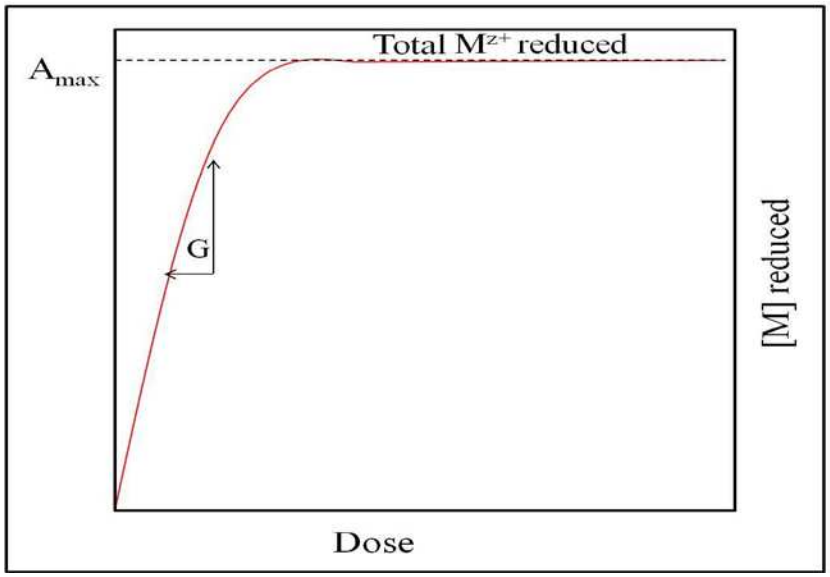

Figure 1.16 Evaluation of the advancement of radiolytic reduction as a function of the dose absorbed by the sample.

Radiolysis has been used successfully to synthesize various noble (such as silver, gold and platinum) and non-noble (nickel, copper and iron) metal nanoparticles in aqueous solution (and in other solvents such as alcohols) and in heterogeneous media (on supports, in polymeric membranes, in mesophases…).[147-150] The nanosized metal clusters or particles are readily oxidized due to their relatively low redox potential compared to that of the bulk counterparts. For this reason, the deoxygenation (by purging with an inert gas) of the solutions prior to irradiation must be performed to prevent the possible oxidation. Moreover, since water radiolysis leads to the formation of protons in addition to that of hydrated electrons, radio-induced acidification of the solution may lead to non-noble metal cluster corrosion. Therefore, preparing a slight basic solution of a non-noble metal salt is able to avoid the back oxidation by protons.

1.8.2 Effect of dose rate

The dose rate effect on the mean size of the radiolytic synthesized nanoparticles has been widely studied.[148, 151-154] Increasing the dose rate (the deposited energy into the irradiated medium, expressed in Grays (1 Gy = 1 J kg^{-1}) leads to more reduced metal ions in the same time and then to more seeds. As a consequence, the metal particles become smaller and less dispersed in size at a high dose rate. In contrast, in the steady irradiation regime (at

lower dose rates), the association of M^+ ions with reduced atoms and the subsequent coalescence processes are faster than the generation rate of the reducing species. Therefore, the reduction of M^+ ions occurs probably *in-situ* on the charged clusters M_{n+1}^+ already formed. As a result, because of the continuous growth of the seed (development) larger particles are obtained by radiolysis at low dose rate.

For the bimetallic (or multi-metallic) systems, the dose rate can have an effect on the structure of the multi-component metal particles. Different bimetallic systems were studied, such as Ag-Au, Ag-Pd, Au-Pd, Au-Pt nanoparticles. Alloyed or core-shell nanoparticles can be obtained depending on the dose rate. For example in case of the Au/Ag system, different structures can be obtained depending on the dose rate and on the metal precursors.[155] When an aqueous solution containing Au^{III} ($AuCl_4^-$) and Ag^+ is γ-irradiated at a low dose rate of 3.8 kGy h^{-1}, the evolution of the optical absorption spectra with increasing γ- irradiation doses exhibits a maximum which is shifting from 520 nm to 430 nm with increasing the initial ratio $[Ag^+]/[Au^{III}]$. These two maxima correspond to the plasmon resonance absorption bands of gold and silver respectively. Meanwhile, the colloidal solution turns from pink to yellow. This evidences that gold NPs are obtained at the beginning with a lower dose, whereas Au_{core}-Ag_{shell} NPs are formed at higher dose. The structure of the nanoparticles has been confirmed by EDS. In the case of low dose rate, the reduction process is controlled by the redox potential of each metal complex. The reduction of gold ions is thus more efficient than that of silver. Silver ions are initially reduced however the silver atoms will transfer electrons to gold ions as long as gold ions are present in solution. Thus, the silver reduction occurs only when gold ions are completely reduced. In particular, the silver ions are adsorbed at the surface of gold clusters, leading to Au_{core}-Ag_{shell} nanoparticles.

In the case of irradiation of the same gold and silver precursor solution at a higher dose rate of 35 kGy h^{-1}, the absorption spectra display a constant maximum at 480 nm, which is an intermediate value between the plasmon bands of gold and silver. Furthermore, the absorption peak does not shift with the dose while its intensity progressively increases showing that the composition and structure of the NPs is identical from the beginning to the end of irradiation. EDS analysis of the nanoparticles at different irradiation times has confirmed that they were

formed by silver and gold, and that the composition is the same along the diameter. At such a higher dose rate, the radio-induced reduction of metal ions is faster than the inter-metallic electron transfer leading to alloyed Au-Ag nanoparticles.

The structure of multi-metallic NPs can also be affected by the constitution of mixed metal salts. For example, alloyed Cu_3Pd, CuPd, NiPt, CuAu and AgPt clusters or particles could be obtained even at low dose rate (γ-irradiation with moderate dose rate, less than 30 kGy h^{-1}).[156] By contrast, alloying may require a higher dose rate (35 kGy h^{-1}) for Ag-Au and Ag-Pd bimetallic systems.[155]

1.8.3 Effect of stabilizing agent

In order to limit the size of the nanoparticles and to avoid cluster coalescence into large particles, stabilizing agents are added to the solutions prior to irradiation. Polymers [poly(vinyl)alcohol PVA, poly acrylic acid PAA, polyacrylate PA, poly(acrylamide) PAM, poly(vinyl)pyrolydone PVA etc.] or surfactants (sodium dodecylsulphate SDS, cetyl-trimethylammonium bromide CTAB etc.) were often used. Functional groups with high affinity for the metal ensure the anchoring of the molecule at the cluster surface while the polymeric chain protects the cluster from coalescence. Moreover, the stabilizing agents should not chemically reduce the ions adsorbed on the clusters so as to prevent their growth. In these conditions, small metal clusters or particles were successfully stabilized.[157-159]

Radiolysis has been proven to exhibit significant advantages compared to chemical or electrochemical methods:

The radiation is distributed homogeneously at all points in the solvent and thus induces an initial dispersion of the reducing agents.

Radiolytic syntheses take place at room temperature and atmospheric pressure.

This process does not require the addition of a chemical reducing agent, as it is the solvent which provides the reductants.

e^-_{sol} is a very strong reducing species. Therefore, metals such as Fe, Ni or cobalt which are difficult to reduce by chemical methods can be reduced easily by radiolysis.

The great penetration power of the ionising radiation allows reductions in solution, in

heterogeneous media and in porous matices. The reduction kinetics can be monitored by controlling the dose rate. Therefore the size or shape of nanoparticles, and the composition and structure of bimetallic nanoparticles can be easily controlled by changing the dose rate.

1.9 Non-TiO_2 Visible Light Photocatalysis

Bismuth tungstate (Bi_2WO_6) is one of promising semiconductor materials in terms of visible photocatalysis. Recently, Bi_2WO_6 with various nanostructures such as nanoparticles, nanorods, nanoplates, nanooctahedra, spherelike superstructures, flowerlike nanostructures, nanocages and hierarchical hollow spheres have been prepared by a variety of methods to improve its photoactivity.[160]

Copper compounds, such as copper oxide and copper sulfide have also been intensively studied in a form of single-phase material or composite photocatalyst. Owing to their low band-gap energy compared to TiO_2, they can be excited by visible illumination. The morphology of copper oxide or copper sulfide significantly affects the photocatalytic properties of the catalysts. Li *et al.* reported that a spindly CuO exhibited a high photocatalytic activity in the degradation of dye pollutants, including rhodamine B, methyl orange and methylene blue in the presence of H_2O_2 under halogen tungsten lamp irradiation.[161] Kuo *et al.* reported octahedral CuO exhibited higher photocatalytic activity under visible illumination than cubic ones, suggesting the (111) faces of Cu_2O nanostructures are more photoactive than the (100) faces.[162] Similar results were also reported by Xu *et al.* where octahedral Cu_2O particles were found to be more photoactive than cubic Cu_2O.[163] Hara *et al.* reported that Cu_2O had stable photocatalytic activity in splitting of water under visible light irradiation.[164] Ding *et al.* prepared CuS nanoflowers by a polyol route and they showed their photocatalytic activity under visible illumination.[165]

CuO/ZnO nanocomposites were prepared by Saravanan *et al.* and were used for degradation of real textile waste water under visible light illumination.[166] Since the coupling of CuO/ZnO reduces the band gap of ZnO, extending the wavelength range to visible light region. The presence of CuO also improves the charge-carrier separation. The maximum photocatalytic efficiency is observed for 5% CuO loaded on ZnO. Zhang *et al.*

have reported that CuS/ZnS composite was prepared by surface modification of ZnS porous nanosheets with CuS. The synthesized CuS/ZnS porous nanosheets reach a high H_2-production rate under visible light illumination. The high visible light photocatalytic H_2-production activity is owing to the interfacial charge transfer (IFCT) from the valence band of ZnS to CuS. It is also pointed out that the reduction of partial CuS to Cu_2S enhances H_2-production activity. This shows a possibility for replacing noble metal catalysts by economical CuS in the photocatalysis and also exhibits a facile method for enhancing photocatalytic activity by photo-induced IFCT.[167]

To our best knowledge, very little work on the radiolytic synthesis of copper oxides and copper sulfides have been reported. Liu *et al.* synthesized Cu_2O crystals with various shapes, such as eight-pod cubes, six-armed starlike and octahedra etc. by γ radiolysis, however the photocatalytic properties of these Cu_2O productions were not addressed.[168] Qiao *et al.* prepared spindle-like nanocrystalline CuS by γ-irradiation in an ethanol system. They did not report the photocatalytic properties of the synthesized CuS.[169] Therefore, more research is needed in this area.

1.10 Summary

In this chapter, a brief introduction is given on potential applications of photocatalysis in water treatment, the fundamental photocatalytic mechanism and routes of photoactivity improvement. Various deposition methods and the principle of radiolytic synthesis of metal nanoparticles are also discussed. In addition, non-TiO_2 visible light photocatalysis (in particular with copper oxides and sulfides) is described and the potential application of the semiconductor in photocatalysis under visible light is discussed.

1.11 Aim of this research and its significance

The aim of this thesis work is to improve the photocatalytic efficiency of TiO_2 by various modification methods and to synthesize non-TiO_2 based visible photocatalysts (copper oxide and sulfide nanostructures). For the TiO_2 based photocatalysts, charge-carrier recombination

rate is significant for their photocatalytic activity. The size and distribution of the deposited metal NPs on the substrate TiO_2 are crucial for the electron trapping. Colloid deposition and deposition precipitation methods are employed to modify TiO_2 with Au-Cu bimetallic NPs. Noble metal Au associated with non-noble metal Cu can be a good option for achieving better photocatalytic activities at low cost.

Additionally, the use of solar energy for photocatalysis in the hydrogen generation or environmental purification is the future goal in scientific and industrial fields. Visible photoactive Cu_2O and CuS with special structures synthesized by radiolysis open up possibilities for the development of solar-induced photocatalysts. These nanostructures may also have applications in other fields such as catalysis, water splitting, and solar cells.

References

[1] Hoffmann, M. R.; Martin, S. T.; Choi, W. and Bahnemann, D. W., *Chem. Rew.* **1995**, *95*, 69-96.

[2] Wang, L. K.; Hung, Y. T.; Lo, H. H. and Yapijakis, C., *Handbook of Industrial and Hazzardous Wastes Treatment-Second Edition*, Marcel Dekker, Inc., **2004**, p.

[3] Andreozzi, R.; Caprio, V.; Insola, A. and Martota, R., *Catal. Today* **1999**, *53*, 51-59.

[4] Benitez, F. J.; Beltran-Herdia, J.; Acero, J. L. and Pinilla, M. L., *Ind. Eng. Chem. Res.* **1997**, *36*, 638-644.

[5] Esplugas, S.; Gimenez, J.; Contreras, S.; Pascual, E. and Rodriguez, M., *Water Res.* **2002**, *36*, 1034-1042.

[6] Ollis, D. in *Comparative aspects of advanced oxidation processes. Emerging Technologies in Waste Management II*, *Vol.* Washington, DC, **1993**, pp. 18-34.

[7] Peyton, G. R.; Huang, F. Y.; Burleson, J. L. and Glaze, W. H., *Environ. Sci. Technol.* **1982**, *16*, 449-453.

[8] Haag, W. R. and Yao, C. C. D., *Environ. Sci. Technol.* **1992**, *26*, 1005-1013.

[9] Weichgrebe, D., *Chem. Ing. Technol.* **1992**, *64*, 438-440.

[10] Bigda, R. J., *Cehm. Eng. Prog.* **1995**, *91*, 62-66.

[11] Pera-Titus, M.; Garcia-Molina, V.; Banos, M. A.; Gimenez, J. and Esplugas, S., *Appl. Catal. B* **2004**, *47*, 219-256.

[12] Kamat, P. V. and Vinodgopal, L. K., *Molecular and Supramolecular Photochemistry: Organic and Inorganic Chemistry, ed. V*, Marcel Dekker, New York, **1998**, p.

[13] Legrini, O.; Oliveros, E. and Braun, A., *Chem. Rev.* **1983**, *93*, 671-698.

[14] Lipczynska-Kochany, E., *Chemosphere* **1992**, *24*, 1369-1380.

[15] Straehelin, S. and Hoigne, J., *Environ. Sci. Technol.* **1982**, *16*, 676-681.

[16] Abe, K. I. and Tanaka, K., *Toxicol. Environ. Chem.* **1996**, *54*, 187-193.

[17] Beltran, F. J.; Gonzalez, J. F. and Alvarez, P., *Ing. Quim.* **1997**, *331*, 161-168.

[18] Davis, R. A.; Rinker, R. G. and Sandall, O. C., *J. Hazard. Mater.* **1995**, *41*, 65-72.

[19] Esplugas, S.; Yue, P. L. and Pervez, M. I., *Water Res.* **1994**, *28*, 1323-1328.

[20] Glaze, W. H.; Kang, J. W. and Chapin, D. H., *Ozone Sci. Eng.* **1987**, *9*, 335-342.

[21] Peyton, G. R. and Glaze, W. H., *Environ. Sci. Technol.* **1988**, *22*, 761.

[22] Glaze, W. H. and Kang, J. W., *Ind. Eng. Chem. Res.* **1989**, *28*, 1573-1580.

[23] Adam, C. D.; Scanlan, P. A. and Secrist, N. S., *Environ. Sci. Technol.* **1994**, *28*.

[24] Mokrini, A.; Oussi, D. and Esplugas, S., *Water Sci. Technol.* **1997**, *35*, 95-102.

[25] Wanlling, C. and Goosen, A., *J. Am. Chem. Soc.* **1973**, *95*, 2987-2991.

[26] Chu, W., *Environ. Sci. Technol.* **1999**, *33*, 421-425.

[27] Davis, A. P. and Green, D. L., *Environ. Sci. Technol.* **1999**, *33*, 609-617.

[28] Calza, P. C.; Minero, C. and Pelizzeti, E., *Environ. Sci. Technol.* **1997**, *31*, 2198-2203.

[29] Xie, Y. B. and Li, X. Z., *J. Hazard. Mater.* **2006**, *138*, 526-533.

[30] Dionysiou, D. D.; Khodadoust, A.; Kern, A. M.; Suidan, M. T.; Baudin, I. and Laine, J. M., *Appl. Catal. B* **2000**, *24*, 139-155.

[31] Doodeve, C. F. and Kitchener, J. A., *Trans. Faraday Soc.* **1938**, *34*, 570-579.

[32] Fujishima, A. and Honda, K., *Nature* **1972**, *238*, 37-38.

[33] Frank, S. N. and Bard, A. J., *J. Am. Chem. Soc.* **1977**, *99*, 303-304.

[34] Hashimoto, K.; Irie, H. and Fujishima, A., *Jpn. J. Appl. Phys.* **2005**, *44*, 8269-8285.
[35] Zielinska-Jurek, A.; Kowalska, E.; Sobczak, J. W.; Lisowski, W.; Ohtani, B. and Zaleska, A., *Appl. Catal. B* **2011**, *101*, 504-514.
[36] Fox, M. A. and Dulay, M. T., *Chem. Rev.* **1993**, *93*, 341.
[37] Mills, A.; Davies, R. H. and Worsley, D., *Chem.Soc. Rev.* **1993**, *22*, 417.
[38] Kubacka, A.; Fernandez-Garcia, M. and Colon, G., *Chem. Rev.* **2012**, *112*, 1555-1614.
[39] Linsebigler, A. L.; Lu, G. and John T. Yates, J., *Chem. Rew.* **1995**, *95*, 735-758.
[40] Stumm, W., *Chemistry of the Solid-Water Interface*, Wiley-Intersciences, New York, **1992**, p. 428.
[41] Kamat, P. V., *J. Phys. Chem. Lett.* **2012**, *3*, 663-672.
[42] Atkins, P., *Physical Chemistry*, Oxford University Press, **1998**, p.
[43] Mcquarrie, D. A. and Simon, J. D., *Physical Chemistry A Molecular Approach*, University Science Books, **1997**, p.
[44] Alaoui, O. T.; Herissan, A.; Quoc, C. L.; Zekri, M. M.; Sorgues, S.; Remita, H. and Colbeau-Justin, C., *J. Photochem. Photobiol. A* **2012**, *242*, 34-43.
[45] Kisch, H.; Zang, L.; Lange, C.; Maier, W. F.; Antonius, C. and Meissner, D., *Angew. Chem., Int. Ed.* **1998**, *37*, 3034-3036.
[46] Subramanian, V.; Wolf, E. E. and Kamat, P. V., *J. Phys. Chem. B* **2001**, *105*, 11439-11446.
[47] Subramanian, V.; Wolf, E. E. and Kamat, P. V., *J. Am. Chem. Soc.* **2004**, *126*, 4943-4950.
[48] Doherty, R. P.; Krafft, J.-M.; Methivier, C.; Casale, S.; Remita, H.; Louis, C. and Thomas, C., *J. Catal.* **2012**, *287*, 102-113.
[49] Grabowska, E.; Zaleska, A.; Sorgues, S.; Kunst, M.; Etcheberry, A.; Colbeau-Justin, C. and Remita, H., *J. Phys. Chem. C* **2013**, *117*, 1955-1962.
[50] Kowalska, E.; Remita, H.; Colbeau-Justin, C.; Hupka, J. and Belloni, J., *J. Phys. Chem. C* **2008**, *112*, 1124-1131.
[51] Wang, H.; Faria, J. L.; Dong, S. and Chang, Y., *Mater. Sci. Eng., B* **2012**, *177*, 913-919.
[52] Xu, S.; Ng, J.; Zhang, X.; Bai, H. and Sun, D. D., *Int. J. Hydrogen Energy* **2010**, *35*, 5254-5261.
[53] Tada, H.; Kiyonaga, T. and Naya, S.-I., *Chem. Soc. Rev.* **2009**, *38*, 1849-1858.
[54] Subramanian, V.; Wolf, E. E. and Kamat, P. V., *J. Am. Chem. Soc.* **2004**, *126*, 4943-4950.
[55] Takai, A. and Kamat, P. V., *ACS Nano* **2011**, *5*, 7369-7376.
[56] Veres, A.; Rica, T.; Janovak, L.; Domok, M.; Buzas, N.; Zollmer, V.; Seemann, T.; Richardt, A. and Dekany, I., *Catal. Today* **2012**, *181*, 156-162.
[57] Wongwisate, P.; Chavadej, S.; Gulari, E.; Sreethawong, T. and Rangsunvigit, P., *Desalination* **2011**, *272*, 154-163.
[58] Ou, T.-C.; Chang, F.-W. and Roselin, L. S., *J. Mol. Catal. A: Chem.* **2008**, *293*, 8-16.
[59] Llorca, J.; Dominguez, M.; Ledesma, C.; Chimentao, R. J.; Medina, F.; Sueiras, J.; Angurell, I.; Seco, M. and Rossell, O., *J. Catal.* **2008**, *258*, 187-198.
[60] Chimentao, R. J.; Medina, F.; Fierro, J. L. G.; Llorca, J.; Sueiras, J. E.; Cesteros, Y. and Salagre, P., *J. Mol. Catal. A: Chem.* **2007**, *274*, 159-168.
[61] Pasini, T.; Piccinini, M.; Blosi, M.; Bonelli, R.; Albonetti, S.; Dimitratos, N.; Lopez-Sanchez, J. A.; Sankar, M.; He, Q.; Kiely, C. J.; Hutchings, G. J. and Cavani, F., *Green Chem.* **2011**, *13*, 2091-2099.
[62] Hai, Z. B.; El-Kolli, N.; Uribe, D. B.; Beaunier, P.; Jose-Yacaman, M.; Etcheberry, A.; Sorgues, S.; Colbeau-Justin, C.; Chen, J. F. and Remita, H. in *Modification of TiO2 by Bimetallic Au-Cu Nanoparticles for Wastewater Treatment Vol.*

[63] Linic, S.; Christopher, P. and Ingram, D. B., *Nature Mater.* **2011**, *10*, 911-921.
[64] Tian, Y. and Tatsuma, T., *J. Am. Chem. Soc.* **2005**, *127*, 7632-7637.
[65] Silva, C. G.; Juarez, R.; Marino, T.; Molinari, R. and Garcia, H., *J. Am. Chem. Soc.* **2011**, *133*, 595-602.
[66] Kowalska, E.; Abe, R. and Ohtani, B., *Chem. Comm.* **2009**, 241-243.
[67] Kowalska, E.; Mahaney, O. O. P.; Abe, R. and Ohtani, B., *Phys. Chem. Chem. Phys.* **2010**, *12*, 2344-2355.
[68] Primo, A.; Marino, T.; Corma, A.; Molinari, R. and Garcia, H., *J. Am. Chem. Soc.* **2011**, *133*, 6930-6933.
[69] Primo, A.; Corma, A. and Garcia, H., *Phys. Chem. Chem. Phys.* **2011**, *13*, 886-910.
[70] Tsukamoto, D.; Shiraishi, Y.; Sugano, Y.; Ichikawa, S.; Tanaka, S. and Hirai, T., *J. Am. Chem. Soc.* **2012**, *134*, 6309-6315.
[71] Jain, P. K.; Lee, K. S.; El-Sayed, I. H. and El-Sayed, M. A., *J. Phys. Chem. B* **2006**, *110*, 7238-7248.
[72] Maruska, H. P. and Ghosh, A. K., *Sol. Energy* **1978**, *20*, 443-458.
[73] Ohno, T.; Tokieda, K.; Higashida, S. and Matsumura, M., *Appl. Catal., A* **2003**, *244*, 383-391.
[74] Fujii, M.; Kawai, T. and Kawai, S., *Chem. Phys. Lett.* **1984**, *106*, 517-522.
[75] Dunn, W. W.; Aikawa, Y. and Bard, A. J., *J. Am. Chem. Soc.* **1981**, *103*, 3456-3459.
[76] Awazu, K., *J. Am. Chem. Soc.* **2008**, *130*, 1676-1680.
[77] Christopher, P.; Ingram, D. B. and Linic, S., *J. Phys. Chem. C* **2010**, *19*, 9173-9177.
[78] Ingram, D. B. and Linic, S., *J. Am. Chem. Soc.* **2011**, *133*, 5202-5205.
[79] Anger, P.; Baharadway, P. and Novotny, L., *Phys. Rev. Lett.* **2006**, *96*, 113002-113001-113004.
[80] Lee, J., *Angew. Chem. Int. Ed.* **2006**, *45*, 4819-4823.
[81] Serpone, N.; Borgarello, E. and Graetzel, M., *J. Chem. Soc. Chem. Commun.* **1984**, 342-344.
[82] Serpone, N.; Borgarello, E. and Pelizzeti, E., *J. Electrochem. Soc.* **1988**, *135*, 2760-2766.
[83] Gopidas, K. R.; Bohorquez, M. and Kamat, P. V., *J. Phys. Chem.* **1990**, *94*, 6435.
[84] Spanhel, L.; Weller, H. and Henglein, A., *J. Am. Chem. Soc.* **1987**, *109*, 6632.
[85] Gerischer, H. and Lubke, M., *J. Electronanal. Chem.* **1986**, *204*, 225.
[86] Vogel, R.; Pohl, K. and Weller, H., *Chem. Phys. Lett.* **1990**, *174*, 241.
[87] Zhang, Y.; Li, J. and Xu, H., *Appl. Catal. B* **2012**, *123-124*, 18-26.
[88] Serpone, N. and Emeline, A. V., *J. Phys. Chem. Lett.* **2012**, *3*, 673-677.
[89] Wang, W. S.; Wang, D. H.; Qu, W. G.; Lu, L. Q. and Xu, A. W., *J. Phys. Chem. C* **2012**, *116*, 19893-19901.
[90] Li, Q.; Guo, B. D.; Yu, J. G.; Ran, J. R.; Zhang, B. H.; Yan, H. J. and Gong, J. R., *J. Am. Chem. Soc.* **2011**, *133*, 10878-10884.
[91] Zhang, X. Y.; Li, H. P.; Cui, X. L. and Lin, Y. H., *J. Mater. Chem.* **2010**, *20*, 2801-2806.
[92] Khalid, N. R.; Ahmed, E.; Hong, Z. L.; Sana, L. and Ahmed, M., *Current Applied Physics* **2013**, *13*, 659-663.
[93] Zhang, H.; Lv, X. J.; Li, Y. M.; Wang, Y. and Li, J. H., *ACS Nano* **2010**, *4*, 380-386.
[94] Butler, E. C. and Davis, A. P., *J. Photochem. Photobiol., A: Chem.* **1993**, *70*, 273.
[95] Choi, W. Y.; Termin, A. and Hoffmann, M. R., *Angew. Chem. Int. Ed.* **1994**, *33*, 1091.
[96] Choi, W. Y.; Termin, A. and Hoffmann, M. R., *J. Phys. Chem.* **1994**, *98*, 13669-13679.
[97] Asahi, R.; Morikawa, T.; Ohwaki, T.; Aoki, K. and Taga, Y., *Science* **2001**, *293*, 269-271.
[98] Fujishima, A.; Zhang, X. T. and Tryk, D. A., *Surf. Sci. Rep.* **2008**, *63*, 515-582.
[99] Sakthivel, S.; Janczarek, M. and Kisch, H., *J. Phys. Chem. B* **2004**, *108*, 19384-19387.

[100] Kuznetsov, V. N. and Serpone, N., *J. Phys. Chem. B* **2006**, *110*, 25203-25209.
[101] Emeline, A. V.; Zhang, X. T.; Jin, M.; Murakami, T. and Fujishima, A., *J. Phys. Chem. B* **2006**, *110*, 7409-7413.
[102] Mrowetz, M.; Balcerski, W.; Colussi, A. J. and Hoffmann, M. R., *J. Phys. Chem. B* **2004**, *108*, 5995-6003.
[103] Khan, S. U. M.; Al-Shahry, M. and Ingler, W. B., *Science* **2002**, *297*, 2243-2245.
[104] Fujishima, A., *Science* **2003**, *301*, 1673a.
[105] Hagglund, C.; Gratzel, M. and Kasemo, B., *Science* **2003**, *301*, 1673b.
[106] Umebayashi, T.; Yamaki, T.; Itoh, H. and Asai, K., *Appl. Phys. Lett.* **2002**, *81*, 454-456.
[107] Tachikawa, T.; Tojo, S.; Kawai, K.; Endo, M.; Fujistsuka, M.; Ohon, T.; Nishijima, K.; Miyamoto, Z. and Majima, T., *J. Phys. Chem. B* **2004**, *108*, 19299-19306.
[108] Zhao, W.; Ma, W.; Chen, C.; Zhao, J. and Shuai, Z., *J. Am. Chem. Soc.* **2004**, *126*, 4782-4783.
[109] Lin, L.; Lin, W.; Zhu, Y.; Zhao, B. and Xie, Y., *Chem. Lett.* **2005**, *34*, 284-285.
[110] Yu, J. C.; Yu, J. G.; Ho, W. K.; Jiang, Z. T. and Zhang, L. Z., *Chem. Mater.* **2002**, *14*, 3808-3816.
[111] Sun, H.; Wang, S.; Ang, H. M.; Tade, M. O. and Li, Q., *Chem. Eng. J.* **2010**, *162*, 437-447.
[112] Livraghi, S.; Paganini, M. C.; Giamello, E.; Selloni, A.; Valentin, C. D. and Pacchioni, G., *J. Am. Chem. Soc.* **2006**, *128*, 15666-15671.
[113] Serpone, N., *J. Phys. Chem. B* **2006**, *110*, 24287-24293.
[114] Gerischer, H. and Willig, F., *Top. Curr. Chem.* **1976**, *61*, 31.
[115] Hagfeldt, A. and Graetzel, M., *Chem. Rev.* **1995**, *95*, 49-68.
[116] Bach, U.; Tachibana, Y.; Moser, J.-E.; Haque, S. A.; Durrant, J. R.; Graetzel, M. and Klug, D. R., *J. Am. Chem. Soc.* **1999**, *121*, 7445-7446.
[117] Bonhote, P.; Moser, J.-E.; Humphry-Baker, R.; Vlachopoulos, N.; Zakeeruddin, S. M.; Walder, L. and Graetzel, M., *J. Am. Chem. Soc.* **1999**, *121*, 1324-1336.
[118] Patrick, B. and Kamat, P. V., *J. Phys. Chem.* **1992**, *96*, 1423.
[119] Kamat, P. V.; Tvrdy, K.; Baker, D. R. and Radich, J. G., *Solar Cells. Chem. Rev.* **2010**, *110*, 6664-6688.
[120] Libanori, R.; Giraldi, T. R.; Longo, E.; Leite, E. R. and Ribeiro, C., *J. Sol-Gel Sci. Technol.* **2009**, *49*, 95-100.
[121] Wang, Q.; Zhang, Z.; Zakeeruddin, S. M. and Gratzel, M., *J. Phys. Chem. C* **2008**, *112*, 7085.
[122] Nazeeruddin, N. K.; De Angelis, F.; Fantacci, S.; Selloni, A.; Viscardi, G.; Liska, P.; Ito, S.; Bessho, T. and Gratzel, M., *J. Am. Chem. Soc.* **2005**, *127*, 16835.
[123] Li, G. S. **Preparation and Characterization of Porous Visible Light Photocatalysts**, The Chinese University of Hong Kong, Department of Chemistry, 2008.
[124] Kay, A. and Gratzel, M., *Chem. Mater.* **2002**, *14*, 2930.
[125] Kimling, J.; Maier, M.; Okenve, B.; Kotaidis, V.; Ballot, H. and Plech, A., *J. Phys. Chem. B* **2006**, *110*, 15700-15707.
[126] Xu, Z. C.; Shen, C. M.; Yang, T. Z.; Zhang, H. R.; Li, H. L.; Li, J. Q. and Gao, H. J., *Chem. Phys. Lett.* **2005**, *415*, 342-345.
[127] Duff, D. G.; Baiker, A. and Edwards, P. P., *J. Chem. Soc., Chem. Commun.* **1993**, 96-98.
[128] Duff, D. G. and Baiker, A., *Langmuir* **1993**, *9*, 2301-2309.
[129] Duff, D. G. and Baiker, A., *Langmuir* **1993**, *9*, 2310-2317.
[130] Mcgilvray, K. L.; Decan, M. R.; Wang, D. and Scaiano, J. C., *J. Am. Chem. Soc.* **2006**, *128*, 15980-15981.

[131] Hidalgo, M. C.; Murcia, J. J.; Navio, J. A. and Colon, G., *Applied catalysis A: General* **2011**, *397*, 112-120.
[132] Bamwenda, G. R.; Tsubota, S.; Nakamura, T. and Haruta, M., *Catal. Lett.* **1997**, *44*, 83-87.
[133] Bond, G. C.; Louis, C. and Thompson, D. in *Catalysis by Gold*, *Vol. 6* Imperial College Press, London, **2006**.
[134] Haruta, M., *Catal. Surv. Jpn.* **1997**, *61*.
[135] Tsubota, S.; Cunningham, D. a. H.; Bando, Y. and Haruta, M., *Stud. Surf. Sci. Catal.* **1995**, *91*, 227.
[136] Tsubota, S.; Haruta, M.; Kobayashi, T.; Ueda, A. and Nakahara, Y., *Stud. Surf. Sci. Catal.* **1991**, *63*, 695.
[137] Zanella, R.; Delannoy, L. and Louis, C., *Appl. Catal., A* **2005**, *291*, 62-72.
[138] Murphy, P. J. and Lagrange, M. S., *Geochim. Cosmochim. Acta* **1998**, *62*, 3515.
[139] Murphy, P. J.; Stevens, G. and Lagrange, M. S., *Geochim. Cosmochim. Acta* **2000**, *64*, 479.
[140] Zanella, R.; Giorgio, S.; Henry, C. R. and Louis, C., *J. Phys. Chem. B* **2002**, *106*, 7634-7642.
[141] Hermans, L. a. M. and Geus, J. W., *Stud. Surf. Sci. Catal.* **1979**, *4*, 113.
[142] Van Dillen, J. A.; Geus, J. W.; Hermans, L. A. and Van Der Meijden, J., *Proceedings of the 6th International Congress on Catalysis* (London) **1976**, p. 667.
[143] Wishart, J. F. and Rao, B. S. M., *Recent Trends in Radiation Chemistry*, World Scientific, Singapore, **2010**, p.
[144] Belloni, J., *Catal. Today* **2006**, *113*, 141-156.
[145] Abidi, W. and Remita, H., *Recent Pat. Eng.* **2010**, *4*, 170-188.
[146] Buxton, G. V.; Greenstock, C. L.; Helman, W. P. and Ross, A. B., *J. Phys. Chem. Ref. Data* **1988**, *17*, 513-886.
[147] Belloni, J.; Mostafavi, M.; Remita, H.; Marignier, J. L. and Delcourt, M. O., *New J. Chem.* **1998**, 1239-1255.
[148] Gachard, E.; Remita, H.; Khatouri, J.; Belloni, J.; Keita, B. and Nadjo, L., *New J. Chem.* **1998**, *22*, 1257-1265.
[149] Dey, G. R.; Remita, H. and Mostafavi, M., *Chem. Phys. Lett.* **2006**, *83*, 431.
[150] Mirdamadi-Esfahani, M.; Mostafavi, M.; Keita, B.; Nadjo, L.; Kooyman, P. and Remita, H., *Gold Bull.* **2010**, *43*, 49-56.
[151] Surendran, G.; Ksar, F.; Ramos, L.; Keita, B.; Nadjo, L.; Prouzet, E.; Beaunier, P.; Dieudonne, P.; Audonnet, F. and Remita, H., *J. Phys. Chem. C.* **2008**, *112*, 10740-10744.
[152] Redjala, T.; Apostolescu, G.; Beaunier, P.; Mostafavi, M.; Etcheberry, A.; Uzio, D.; Thomazeau, C. and Remita, H., *New J. Chem.* **2008**, *32*, 1403-1408.
[153] Souici, A. H.; Keghouche, N.; Delaire, J. A.; Remita, H.; Etcheberry, A. and Mostafavi, M., *J. Phys. Chem. C* **2009**, *113*, 8050-8057.
[154] Mostafavi, M.; Liu, Y. P.; Pernot, P. and Belloni, J., *Radiat. Phys. Chem.* **2000**, *59*, 49-59.
[155] Treguer, M.; De Cointet, C.; Remita, H.; Khatrouri, M.; Mostafavi, M.; Amblard, J.; Belloni, J. and De Keyzer, R., *J. Phys. Chem. B* **1998**, *102*, 4310.
[156] Marignier, J. L.; Belloni, J.; Delcourt, M. O. and Chevalier, J. P., *Nature* **1985**, *317*, 344.
[157] Keita, B.; Nadjo, L.; De Cointet, C.; Amblard, J. and Belloni, J., *Chem. Phys. Lett.* **1994**, *115*, 218.
[158] Keita, B.; Nadjo, L.; Gachard, E.; Remita, H.; Khatouri, J. and Belloni, J., *New J. Chem.* **1997**, *21*, 851.
[159] Remita, S.; Orts, J. M.; Feliu, J. M.; Mostafavi, M. and Delcourt, M. O., *Chem. Phys. Lett.* **1994**,

218, 115.
[160] Dai, X. J.; Luo, Y. S.; Zhang, W. D. and Fu, S. Y., *Dalton Trans.* **2010**, *39*, 3426-3432.
[161] Li, J. P.; Sun, F. Q.; Gu, K. Y.; Wu, T. X.; Zhai, W.; Li, W. S. and Huang, S. F., *Appl. Catal., A* **2011**, *406*, 51-58.
[162] Kuo, C.-H. and Huang, M. H., *J. Phys. Chem. C* **2008**, *112*, 18355-18360.
[163] Xu, H. L.; Wang, W. Z. and Zhu, W., *J. Phys. Chem. B* **2006**, *110*, 13829-13834.
[164] Hara, M.; Kondo, T.; Komoda, M.; Ikeda, S.; Shinohara, K.; Tanaka, A.; Kondo, J. N. and Domen, K., *Chem. Commun.* **1998**, 357-358.
[165] Ding, T. Y.; Wang, M. S.; Guo, S. P.; Guo, G. C. and Huang, J. S., *Mater. Lett.* **2008**, *62*, 4529-4531.
[166] Saravanan, R.; Karthikeyan, S.; Gupta, V. K.; Sekaran, G.; Narayanan, V. and Stephen, A., *Materials Science and Engineering C* **2013**, *33*, 91-98.
[167] Zhang, J.; Yu, J. G.; Zhang, Y. M.; Li, Q. and Gong, J. R., *Nano Lett.* **2011**, *11*, 4774-4779.
[168] Liu, H. R.; Miao, W. F.; Yang, S. and Zhang, Z. M., *Cryst. Growth Des.* **2009**, *9*, 1733-1740.
[169] Qiao, Z. P.; Xie, Y.; Xu, J. G.; Zhu, Y. J. and Qian, Y. T., *J. Colloid Interface Sci.* **1999**, *214*, 459-461.

CHAPTER II

EXPERIMENTAL

Chapter 2 Experimental

This chapter firstly presents the materials used in the syntheses.Then, the protocols for syntheses are introduced. We used radiolysis and chemical reduction (reduction with THPC) to synthesize metal nanoparticles (NPs) (Au, Au and Au-Cu) in solution. Deposition precipitation method with urea was also employed to deposit metal ions on TiO_2, followed by radiolytic reduction. In chapter 3, we will compare the various preparation methods and then we will present the catalytic activity of modified TiO_2. Radiolytic synthesis of copper sulfides and copper oxides is also decribed. Characterization techniques associated with this research are presented in the third section of this chapter, and the principles of the equipment used are illustrated in the appendix. Finally, the photocatalytic tests of different model pollutants (rhodamine B, phenol and methyl orange) are described, and the photocatalytic reactors or apparatus are shown in detail in appendix.

2.1 Materials

In the experiments of colloid deposition method by radiolytic or chemical route, all the reagents were used as received without further purification unless otherwise indicated. *Titanium dioxide* (TiO_2, Evonik P25, , 50 m^2g^{-1}, 80% of Anatase, 20% of Rutile) was purchased from Evonik, Germany. *Chloroauric Acid* ($HAuCl_4 \bullet 3H_2O$) (used as gold precursor) and *Copper Chloride* ($CuCl_2$) (used as copper precursor) were respectively purchased from Acros Chemicals and Rectapur. *Rhodamine B* ($C_{28}H_{31}ClN_2O_3$) and *phenol* (C_6H_5OH) were purchased from Fluka. *Poly acrylic acid* (PAA, 60% in water), *polyvinyl alcohol* (PVA, analytical pure), *tetrakis (hydroxymethyl) phosphonium chloride* (THPC, 80% in water) were purchased from Aldrich-Sigma. High purity (impurities less than 1 ppm) nitrogen gas from Air Liquid was used to degas the samples prior to gamma irradiation. The suspensions were bubbled with oxygen from Air Liquid during the photocatalytic reactions. Deionized water (Milli Q with 18.6 MΩ•cm) was used all through our experiments.

In the experiments of deposition precipitation with urea, *chloroauric acid* ($HAuCl_4 \bullet 3H_2O$), *copper chloride dihydrate* ($CuCl_2 \bullet 2H_2O$), and *methyl orange*

($C_{14}H_{14}N_3SO_3Na$), were purchased from *Sinopharm* Chemical Reagent Co., Ltd. Deionized water (Milli Q with 18.6 MΩ•cm) was used for all the synthesis and precipitation methods and for the photocatalytic experiments.

In the preparations and photocatalytic reactions of copper oxides and copper sulfides, *copper chloride dihydrate* ($CuCl_2$•$2H_2O$), *sodium hydroxide* (NaOH), *sodium thiosulfate* ($Na_2S_2O_3$·$5H_2O$), *sodium dodecyl sulfate* (SDS), *methyl orange* ($C_{14}H_{14}N_3SO_3Na$), and *isopropyl alcohol* (2-propanol, C3H8O) were purchased from *Sinopharm* Chemical Reagent Co., Ltd.

2.2 Syntheses of metal nanoparticles and copper sulfides and oxides

2.2.1 Preparation of Au-Cu Colloids by Radiolysis and Deposition on P25

Typically, for the preparation of Au-Cu1:1 (1:1 corresponds to the atomic ratio Au/Cu) bimetallic colloid, 2.5 mL of $HAuCl_4$ solution (10^{-2} M) and 2.5 mL $CuCl_2$ solution (10^{-2} M) were added into a 25 mL flask. 5 mL of PAA (0.5 M) and 191 µL of 2-propanol were added consequently to get a concentration of 0.1 M after filling up to constant volume. Then, the mixed solution was transferred to jars and sealed with rubber caps and followed by purging with N_2 for 15 minutes. The mixed solutions were covered with aluminium foils because Au^{III} is sensitive to light. After that, the degassed jars were placed in a γ-irradiation source at a dose rate of 1.4 kGy/h.

The γ-irradiation source is a panoramic Cobalt (^{60}Co) gamma facility (LCP, University of Paris-Sud, to see **Appendix I**). The initial activity of the source in 1995 was 7000 Curies during installation. The maximum dose rate in October 2011 was about 1.4 kGy•h^{-1} .[1]

After γ-irradiation, colloids with a purple or violet color were obtained. They were deposited in a second step on TiO_2. In the preparation of Au-Cu colloids with another stabilizer, such as PVA, the concentration of each stabilizer was kept the same (0.1 M).

After the Au-Cu bimetallic colloids were prepared, the deposition on TiO_2 was performed. The adequate volume of the prepared colloid was put in contact with TiO_2. The

required mass of TiO_2 depends on the metal NPs loading. Here we assumed that the Au ions were reduced completely into Au atoms. In the case of Au-Cu-P25 1%, (the percentages indicated in the thesis manuscript are the mass ratio: metal NPs/TiO_2) the weight of P25 was 100 times higher than that of Au NPs in the solution. After that, P25 was added to the Au-Cu colloids. The purple color of the mixed slurry varied to a certain extent depending on the total mass of Au-Cu bimetallic NPs. The mixtures were stirred (magnetic stirring) for 24 hour in the dark to ensure complete deposition. And then, the slurry was centrifuged to remove the supernatant at a speed of 4000 rpm. The supernatant was analized by UV-visible spectroscopy to check the efficiency of the deposition. After that, the purple precipitate was dried in an oven at 60 °C.

2.2.2 Colloid-Deposition Method by Radiolysis

The preparation of Au-Cu bimetallic NPs modified P25 was done in two steps (see **Figure 2.1**). The first step is the synthesis mono- Au or bi-metallic Au-Cu NPs by radiolysis in the presence of PAA. The procedure is similar to what was described in Section 2.2.1. However, one significant difference is that the total nominal metal content was kept at 0.5% in weight for all the modified P25 samples. In the case of monometallic Au supported on P25, the nominal metal content of Au is 0.5 % in weight. While for the preparation of bimetallic Au-Cu modified P25 with an Au/Cu molar ratio of 1:1, the nominal Au and Cu percentages are 0.38 % and 0.12 %, respectively. The preparation procedure is described below. 1.90 mL of $HAuCl_4$ (10^{-2} M) and 1.90 mL of $CuCl_2$ (10^{-2} M) were added into a flask of 25 mL, followed by adding 5 mL of PAA (0.5 M), 192 µL of 2-propanol and completed with water. The solution was kept in the dark to prevent possible photochemical reduction of Au^{III}. After that, the solution was purged with N_2 to remove O_2 prior to irradiation. Radiolysis of the solution was carried out using a ^{60}Co panoramic gamma source with a radiation dose rate of 1.4 kGy h^{-1}.[2] The exposure time was 5 hours (dose = 7 kGy). The second step was deposition of the synthesized metal NPs by a colloid-deposition route. Deposition was attempted by stirring 1.00 g of P25 into the Au-Cu colloid followed by adding 5 mL of PVA (0.5 M). After 24 hours, the surface modified P25 was separated by centrifugation and

washed repeatedly with water to remove the excess of polymer. The resulting Au-Cu/P25 composite was dried at 60 °C for 24 hours.

Except when specifically mentioned, the Au and Au-Cu samples were calcinated under air, and then reduced again under H_2 at 500 °C (~100 mg of catalyst under 100 mL.min^{-1}, first, under air with a heating rate of 5 °C.min^{-1} then a 15 min plateau. After, a second 15 min plateau under H_2 at 500 °C). After reduction, the samples were cooled down to room temperature under N_2 flow, and transferred in air before characterization.

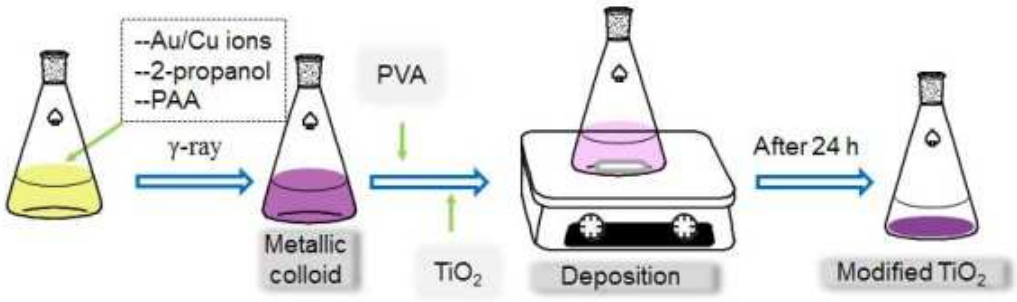

Figure 2.1 Procedure for the colloid deposition method by radiolysis.

2.2.3 Deposition-Precipitation with Urea

A typical synthesis of bimetallic Au-Cu NPs modified P25 at a total metal content of 0.5 wt. % is described as below. 0.478 mL of $HAuCl_4$ solution (10^{-2} M) was added to a jar of 25 mL of distilled water. After that, 250 mg of P25 and 37.5 mg of urea were added in the jar to form a white suspension. Then, the jar was heated up to 90 °C in a water bath with stirring. The temperature of water bath was kept at 90 °C for 2 hours. At this point, the well dispersed suspension turned into a well formed precipitate. After that 0.478 mL of $CuCl_2$ (10^{-2} M) was added into the jar. The temperature decreased naturally to room temperature with keeping magnetic stirring. 0.192 mL of 2-propanol was added to scavenge the oxidative $OH^{\bullet}$ radicals generated during γ-irradiation. The jar was sealed with a rubber cap, followed by purging with nitrogen for 10 minutes. Consequently, the jar was put in a ^{60}Co gamma ray source located in USTC, Hefei (See **Appendix I**). The dose rate was around 170 Gy/min, and the irradiation time was 180 min. A self-made magnetic agitator was used for stirring during the irradiation. After irradiation, the fine white suspension had turned to violet, indicating the formation of

Au-Cu nanoparticles. The slurry was centrifuged, washed several times and then dried in air at 50 °C. A violet powder was obtained.

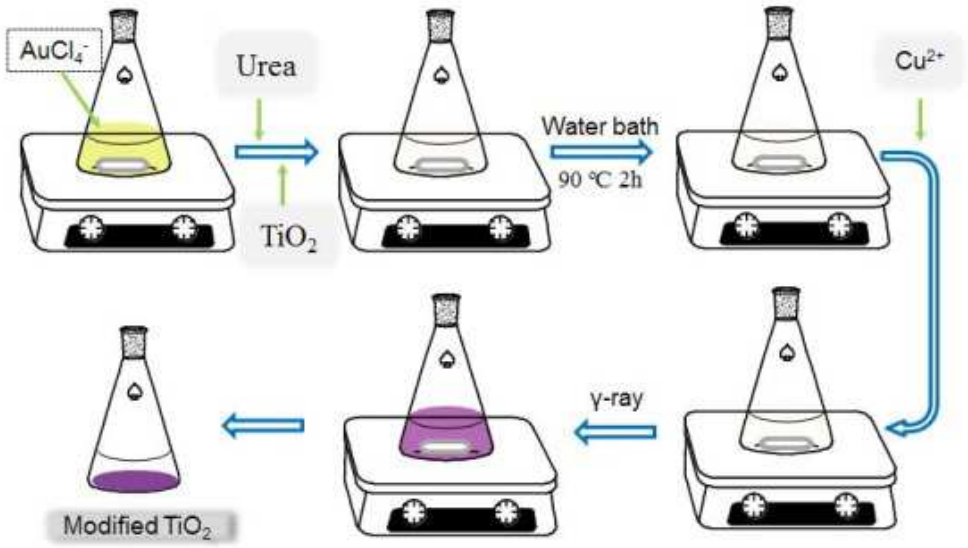

Figure 2.2 Procedure for the deposition-precipitation method with urea.

This above method was named as DPU because it was deposition-precipitation method with urea. In order to compare the deposition efficiency, another deposition method, where the Au and Cu ions were introduced simultaneously, was carried out. Hence, such samples prepared by this method were named ending with DPU-s.

2.2.4 Modification of P25 by THPC Method

The monometallic gold catalysts (0.5 wt.% of Au) were prepared according to Duff and Baiker method.[3-5] This preparation was based on the preparation of a gold sol, which was then deposited onto a support. In a beaker, 1.5 mL of NaOH solution (0.2 M, freshly prepared) was added to 45 mL of deionized water under vigorous stirring. After 5 minutes, 1 mL of tetrakis (hydroxymethy1) phosphonium chloride (THPC, 0.05 M) was added to the mixture followed by 2.5 mL of $HAuCl_4$ solution (10^{-2} M). THPC was used as reducing and stabilizing agent. The color change from transparent to brown was immediately observed indicating the reduction of Au^{III} into Au^0 and the formation of Au NPs. 1 g of P25 support was then added to the mixed solution, which was maintained under vigorous stirring at room temperature during two hours. The solid was separated by centrifugation, washed with deionised water (the

procedure was repeated three times). The samples were then dried at 50 °C for 48 hours.

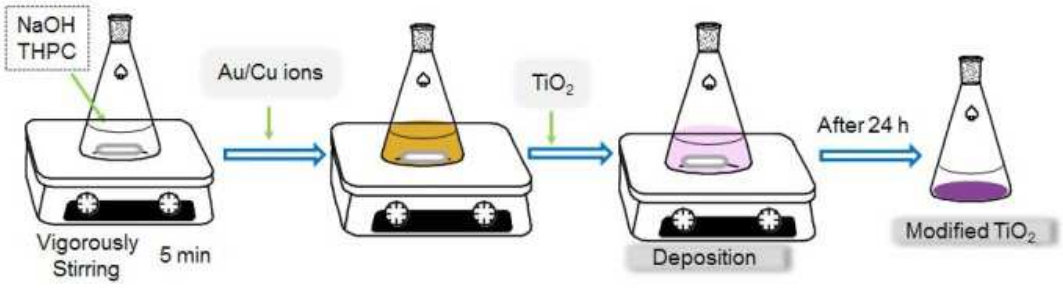

Figure 2.3 Procedure for the colloid deposition method by THPC method.

For the bimetallic Au-Cu catalysts, the unique difference with the protocols of synthesis of monometallic Au catalysts was that gold and copper were simultaneously introduced. The total metal mass percentage was kept at 0.5 wt. % for the monometallic and bimetallic photocatalysts. The compositions of the synthesized photocatalysts are listed in **Table 3.8**.

After drying, all the samples were stored in the dark. Except when specifically mentioned, the Au and Au-Cu modified samples were thermally treated according to the procedure which was described in Section 2.2.2.

2.2.5 Preparation of Copper Oxides

In a typical procedure for synthesizing CuO nanowires, 0.270 g of $CuCl_2 \cdot 2H_2O$ was dissolved in 30 mL of distilled water. 10 mL of aqueous solution 0.375 M NaOH and 1.000 g of SDS were added in sequence. The ratios of $CuCl_2$ to NaOH for the preparation of Cu_2O cubes and octahedra were slightly different. The amount of NaOH decreased to 0.3 M, while the concentrations of the other reactants were the same. In addition, isopropyl alcohol was added as a scavenger of oxidative radicals produced during irradiation. Then, the mixed solution was slowly stirred for 15 min to form a uniform blue suspension. Finally, the blue mixed solution was poured into a wide-mouth bottle and sealed. Then, the bottle was submitted to irradiation with a 2.22×10^{15} Bq ^{60}Co γ-ray source at a dose rate of 30 Gy min^{-1} for 72 h (total dose = 130 kGy) (**Appendix I**). At the end of irradiation, the precipitates were collected. The products were washed with a distilled water and ethanol solution several times and then dried in an oven at 50 °C. **Table 4.1** shows the detailed synthesis conditions of the

copper oxide nanostructures.

2.2.6 Preparation of Copper Sulfide

In a typical procedure to prepare CuS nanotubes, 1.7 mmol of cupric chloride ($CuCl_2 \cdot 2H_2O$) was dissolved in 25 mL water and a green-blue solution then formed. 3.5 mmol of sodium thiosulfate ($Na_2S_2O_3 \cdot 5H_2O$) was added into the solution with gentle stirring until all the reagents dissolved. After that, the color of the solution turned to green. In addition, 8 mL of 2-propanol was added as a scavenger of hydroxyl radicals produced during irradiation. Then, the mixed solution was poured into wide-mouth bottles and sealed. The bottle was exposed to a 2.22×10^{15} Bq ^{60}Co γ-ray source (**Appendix I**). The dose rate was 16 Gy/min and the total irradiation dose was 64 kGy. The obtained black precipitate was washed several times with water. The precipitate was then dried in the air at 60 °C for 48 hours.

Table 2.1 The overall descriptions of the preapared samples in this thesis.

Samples	Preparations	Details	Descriptions
AuCu13PAA	Section 2.2.1	see **Table 3.1**	These are the Au-Cu colloidal solutions prepared by radiolysis in the presence of various polymer stabilizers. The related results are shown in section 3.2.2.
AuCu11PAA			
AuCu31PAA			
AuCu13PVA			
AuCu13PP			
AuCu11PP			
AuCu31PP			
AuPAA@P25(1)	Section 2.2.1	see **Table 3.2**	These are the modified P25 with Au or Au-Cu colloidal NPs of Table 3.1. The samples are without thermal treatment unless otherwise indicated. The related results are shown in section 3.2.3.
AuCu31PAA@P25(1)			
AuCu11PAA@P25(1)			
AuCu13PAA@P25(1)			
AuPVA@P25(1)			
AuCu13PP@P25(1)			

Samples	Preparations	Details	Descriptions
AuCu13PAA@P25(0.5)			
AuCu11PAA@P25(0.5)			
AuCu31PAA@P25(0.5)			
Au/P25	Section 2.2.2	**Table 3.4**	These are the modified P25 with Au or Au-Cu NPs. PVA was added to facilitate the deposition. All the samples are with thermal treatment. The results are shown in section 3.3.1.
AuCu31/P25			
AuCu11/P25			
AuCu13/P25			
Au/P25DPU	Section 2.2.3	**Table 3.5**	These are the modified P25 by deposition precipitation method with urea. The results are shown in section 3.4.2.
AuCu1:1/P25DPU			
AuCu1:3/P25DPU			
Cu/P25DPU			
Au/P25DUP-s	The preparation procedure is similar to that in section 2.2.3.	**Table 3.7**	These are the control samples compared to those by DPU method. DPU-s refers to Au and Cu ions are introduced simultaneously before the water bath. DP means deposition precipitation without urea. The results are shown in section 3.4.4.
AuCu1:3/P25DPU-s			
Cu/P25DPU-s			
Au/P25DP			
AuCu1:3/P25DP			
Cu/P25DP			
Au/P25-T	Section 2.2.4	**Table 3.8**	These are the modified P25 by THPC method. The results are shown in section 3.5.
AuCu11/P25-T			
AuCu13/P25-T			
Cu/P25-T			
1	Section 2.2.5	**Table 4-1**	These are copper oxides prepared by radiolysis. The results are shown in section 4.1.2.
2			
3			
4			
5			

2.3 Characterization Techniques

X-ray diffraction (XRD). The compositions of copper oxides and sulfides were determined by powder XRD, which was performed on a Rigaku TTR-III X-ray diffractometer with Cu Kα radiation (λ=1.541 78 Å).

Scanning electronic microscopy (SEM). The morphology of the as-synthesized products was observed using field-emission scanning electron microscopy (SEM; FEI Sirion 200).

Transmission electron microscopy (TEM). The surface morphology of modified TiO_2 was studied by Transmission Electron Microscopy (TEM, JOEL JEM 100CX II) operating at 100 kV in collaboration with Patricia Beaunier (LRS, UPMC, Paris 6). The irradiated suspensions were first sonicated for a few minutes then a few drops of the suspension were deposited on copper coated carbon grids for TEM observations. Particles size measurements were performed manually using Nano Measurement software on digitized graphs. We measured at least the size of 80 metal nanoparticles. The average size was calculated using the formula followed: $d = \sum n_i d_i / \sum n_i$, where n_i is the number of particles of diameter d_i.[2] High-Resolution TEM and EDX were performed using a JEOL 2010 microscope, equipped with a LaB_6 filament and operating at 200 kV. The images were collected with a 4008 X 2672 pixels CCD camera (Gatan Orius SC1000).

Scanning Transmission Electron Microscopy (STEM). High Angle Annular Dark Field-Scanning Transmission Electronic Microscopy (JOEL JEM-ARM200F: 200 kV FEGSTEM/TEM equipped with a CEOS Cs corrector on the illumination system) was also employed to characterize the morphology of modified TiO_2; STEM-Electron dispersive X-ray spectroscopy (EDS) was used to analyze the compositions of the deposited Au-Cu NPs. The probe current used for acquiring the High-angle annular dark field (HAADF)- and the bright field (BF)-STEM images was 9C (23.2 pA); the condenser lens aperture size was 40 μm. HAADF-STEM images were acquired with a camera length of 8 cm/6 cm and the collection angle of 68–280 mrad/90–270 mrad. The BF-STEM images were obtained using a 3 mm/1mm aperture and a collection angle of 17 mrad/5.6 mrad (camera length in this case was 8 cm). The HAADF as well as the BF images were acquired using a digiscan camera. EDS

measurements for line scan profiles as well chemical maps for the various elements were obtained with a solid state detector and software for two dimensional mapping from EDAX. These experiments were done in collaboration with Miguel José Yacaman (University of Texas at Austin, USA)

UV-vis spectroscopy. The UV-vis absorption spectra of the solutions were recorded using a HP Agilent diode array 8453 UV-Visible spectrophotometer and also using a Shimadzu UV-1800 UV-Visible spectrophotometer.

Diffuse reflectance spectrophotometry (DRS). The diffuse reflectance spectra of the modified TiO_2 samples were obtained using a Cary 5E spectrophotometer equipped with Cary 4/5 diffuse reflection sphere. The baseline was recorded using a poly(tetrafluoroethylene) reference. Besides, a Shimadzu DUV-3700 spectrophotometer was also used to record the UV−vis diffuse reflectance spectra of the samples in the region of 250 to 800 nm.

Thermal gravimetric analysis (TGA). DSC-TGA was performed on a SDT Q600 instrument. Samples were heated in air (the flow rate is 100.0 mL min^{-1}) at 500 °C (with a heating rate of 3 °C min^{-1}).

Nitrogen adsorption-desorption. N_2 adsorption isotherms were performed by BET measurements using a Tristar II 3020M surface area analyser. Brunauer–Emmett–Teller (BET) surface area was determined by a multipoint BET method in the relative pressure (P/P_0) rang of 0.07-0.2. The pore diameter distribution and the BET surface area were calculated using the Barrett–Joiner–Halenda (BJH) and BET method based on the adsorption isotherm.

X-ray photoelectron spectroscopy **(**XPS). XPS analysis was performed on In foils. These experiments were performed in collaboration with Arnaud Etcheberry (ILV, Université Versailles Saint Quentin en Yvelines). Sample drops were deposited on the foils and dried under N_2 flow. The XPS analyzer was a Thermo Electron ESCALAB 220i-XL. Either a non-monochromatic or a monochromatic X-ray Al Kα line was used for excitation. The photoelectrons were detected perpendicularly to the support. A constant analyzer energy mode was used with pass energy of 20 eV. Element atomic percentage determinations were performed using peak area corrected by sensitivity factors using the Thermo Avantage data

base. Fitting procedures were also performed using the Thermo Avantage Program. Besides, for the characterization of the modified TiO_2 (with Au, Cu an Au-Cu) with the deposition precipitation method with urea, XPS analysis was performed in USTC at a Perkin-Elmer RBD upgraded PHI-5000C ESCA system.

Time Resolved Microwave Conductivity (TRMC). The charge-carrier lifetimes in TiO_2 after UV laser excitation were determined by microwave absorption experiments using the TRMC method. The principle of TRMC and the experimental set-up have been widely described in a previous paper.[6] It is also described in detail in **Appendix V**.

2.4 Photocatalytic Reactions

In order to investigate the application of the synthesized photocatalysts for water treatment, we chosed three model pollutants: rhodamine B (RhB) , phenol and methyl orange (MO). All of these compounds are widely used in chemical industries and are not sensitive to the irradiation with natural light. Therefore, it is reasonable to carry out photocatalytic reactions of these model pollutants under UV and visible light. The photocatalytic experiments are described in the following sections.

2.4.1 Photodegradation of Rhodamine B

For the RhB photocatalytic degradation under both of UV-visible and visible light, the photocatalytic reaction system for these tests is described in detail in **Appendix III**. The optical path (in quartz) included water filter and glass filter (GG) to cut off infrared and ultraviolet illumination. An optical filter (GG450) was used to cut off wavelength shorter than 450 nm. The optical path of the cuvette is 10 mm and the volume is about 4 mL. The photocatalyst powders were dispersed in aqueous RhB solution with the initial concentration of 10^{-4} M, keeping the same numerical ratio between the mass of the photocatalysts and the volume of RhB solution as 1.0 g/L. Then, the suspension was put in the ultrasound basin for 30 seconds to disperse the powders into tiny particles. After that, the cuvette was kept stirring on a magnetic stirrer in dark for 15 minutes to reach the equilibrium between adsorption and desorption of RhB on the surface of the photocatalysts. After that, the suspension was

irradiated for 10 min (under UV-visible light) or 100 min (under visible light > 450 nm) under a fixed flow of oxygen and magnetic stirring. An aliquot of 500 µL suspension was taken from the cuvette at fixed time intervals. The aliquots were transferred into glass jars for further centrifugation to remove the photocatalyst nanoparticles. After that, the degraded RhB solutions were analized with the UV-Vis spectrophotometer in a 2 mm quartz cell. The kinetics of the photodegradation was achieved by monitoring the main absorption peak at 554 nm.

2.4.2 Photodegradation of Phenol

Phenol photodegradation under UV-visible light. **Appendix II** shows in detail the photocatalytic reaction system for these tests. The initial phenol concentration is 2×10^{-4} M. The photodegradation reaction processes are nearly the same according to section 2.3.4.1. The difference is that high performance liquid chromatography (HPLC) was used for the determination of the phenol concentration .

Phenol photodegradation under visible light. In the case of visible illumination, another photocatalytic reaction system was used (see **Appendix III**). A 300 mL three-mouth flask was used for the container. 300 mg of photocatalyst was dispersed in 300 mL of phenol solution (2×10^{-4} M, 18.8 ppm). Then, the suspension was ultrasonicated for 30 seconds to disperse the powder into tiny particles. The suspension in the container was bubbled with oxygen at a flow rate of 20 cm^3 per min. A visible lamp (MASTER TL Mini Super 80 8W/840 from Philips, the emission spectrum is shown in **Appendix III**) with a power of 8 W was used as the light source. A peristaltic pump is used to drive the suspension cycle in this system. The speed of the pump was set at 200 rpm. A 4 mL aliquot was taken at certain time interval. Millipore filters were used to remove the suspended powders and to obtain clear supernatants.

The supernatants were analyzed using high performance liquid chromatography. Analyses were carried out by using a Varian Prostar 230 ternary gradient pump combined with a Prostar 330 photodiode array detector (D2 lamp), by a method developed in our laboratory (LCP). For elution, an isocratic mobile phase consisting in 75 % of H_2O and 25 % ACN, at a 1 mL min^{-1} flow rate, was used. Identification of degraded phenol or intermediates

was done by the means of UV absorbance at 270 nm. The column was Adsorbosphere C18 reverse phase (5μm, l: 150 mm, ID: 4.6 mm, Alltech) combined with All-Guard cartridge system TM (7.5 × 4.6 mm, Alltech). For data acquisition, Star software was used.

2.4.3 Photodegradation of Methyl Orange

The photocatalytic experiments were carried out in a XPA-7 photochemical reactor (Nanjing Xujiang Machine-electronic Plant, China). The detailed description of the apparatus can be found in **Appendix IV**.

For the photocatalytic reactions under UV illumination, a 300 W mercury lamp was used as the light source. Optical filters were employed to cut off the unwanted light. Only the illumination longer than 270 nm and shorter than 400 nm can pass through the filter. Typically, 20 mg of synthesized photocatalyst was dispersed in 20 mL of methyl organe (MO) with an initial concentration of 20 mg L^{-1}. The suspension was loaded in a silica tube, followed by ultrasonication for 30 seconds to disperse the powder. After that, the solution was kept stirring on a magnetic stirrer in the dark for 30 minutes in order to reach the equilibrium between adsorption and desorption of MO on the surface of photocatalysts. After that, the slurry was subjected to UV irradiation under magnetic stirring and oxygen bubbling (flow rate of 200 mL min^{-1}). A 2 mL syringe equipped with a long needle was used to take aliquots from the reactor at fixed time intervals. The suspensions were centrifuged at 4000 rpm for 20 minutes to obtain clear supernatants. Then, the supernatants were analyzed by spectrophotometry.

In the case of visible photocatalytic degradation, a 500 W Xenon lamp was used as the light source, equipped with another optical filters cutting wavelengths shorter than 450 nm.

References

[1] Remita, H.; Lampre, I.; Mostafavi, M.; Balanzat, E. and Bouffard, S., *Rad. Phys. Chem.* **2005**, *72*, 575.

[2] Doherty, R. P.; Krafft, J.-M.; Methivier, C.; Casale, S.; Remita, H.; Louis, C. and Thomas, C., *J. Catal.* **2012**, *287*, 102-113.

[3] Duff, D. G. and Baiker, A., *Langmuir* **1993**, *9*, 2301-2309.

[4] Duff, D. G.; Baiker, A. and Edwards, P. P., *J. Chem. Soc., Chem. Commun.* **1993**, 96-98.

[5] Duff, D. G. and Baiker, A., *Langmuir* **1993**, *9*, 2310-2317.

[6] Colbeau-Justin, C.; Kunst, M. and Huguenin, D., *J. Mater. Sci.* **2003**, *38*, 2429-2437.

CHAPTER III

MODIFICATION OF TITANIA WITH AU AND CU BIMETALLIC NANOPARTICLES AND THEIR APPLICATIONS IN WATER TREATMENT

Chapter 3 Modification of Titania with Au and Cu Bimetallic Nanoparticles and Their Applications in Water Treatment

In this chapter, surface modification of TiO_2 with Au and Cu monometallic and Au-Cu bimetallic nanoparticles were carried out through two main different deposition routes, colloid deposition and deposition precipitation, aiming to improve the photocatalytic activity of TiO_2 under UV and visible light.

Colloid deposition of Au and Au-Cu bimetallic NPs on commercial TiO_2 compounds (P25) by radiolysis method is presented in section 3.2 and 3.3. Au-Cu metal colloids were prepared by radiolytic reduction. The choice of the stablilizer is important to obtain metal nanoparticles homogeneous in size. The mean nanoparticle size decreased obviously when Au is associated with copper. In case of radiolytic synthesis, stabilization of NPs with PAA leads in general to homogeneous bimetallic nanoparticles. Nevertheless, surface deposition on TiO_2 with the help of PVA can result in a higher metal NPs surface loading. But the inevitable process for this method is that the stabilizers must be removed. Calcination was conducted to burn up the polymer stabilizer, followed by H_2 reduction. The Au-Cu NPs modified P25 were characterized using TEM, DRS, and TRMC. The characterization techniques showed that Au-Cu bimetallic NPs are alloys. The TRMC signals show that the Au-Cu alloyed NPs supported on P25 are efficient in scavenging electrons leading to an enhancement of photoactivity under UV illumination. The bimetallic NPs modified P25 show better photoactivity than monometallic Au NPs under UV light. However, the modification with Au-Cu NPs resulted in a decrease of the photocatalytic activity under visible illumination.

Furthermore, Au, Cu and Au-Cu bimetallic NPs prepared by chemical method with THPC were prepared on the surface of P25, as is described in section 3.4. THPC simultaneously acts as reductant and stablilizer. The alloyed structure of Au-Cu NPs was confirmed by HAADF-STEM, EDS, HRTEM and XPS techniques. The photocatalytic properties of the modified TiO_2 were studied for phenol and rhodamine B photodegradation in aqueous suspensions under UV-visible irradiation. The photocatalysts prepared by chemical

method exhibit enhanced photocatalytic activities under UV illumination. The photocatalytic activity increased with the Cu proportion in the bimetallic NPs. The highest photoactivity obtained is modified P25 with Au/Cu1:3 NPs. On the contrary, the photocatalytic activity decreased under visible light. Their electronic properties were studied by Time Resolved Microwave Conductivity (TRMC) to follow the charge-carrier dynamics. TRMC measurements show that the TiO_2 modification with Au, Cu and Au-Cu nanoparticles plays a role in charge-carrier separations, increasing the activity under UV-light. Indeed, the metal nanoparticles act as a sink for electrons, decreasing the charge carrier recombination. The TRMC measurements show also that the bimetallic Au-Cu nanoparticles are more efficient in electron scavenging than the monometallic Au and Cu ones.

Besides these results, Au, Cu and Au-Cu bimetallic NPs modified P25 were also achieved by deposition precipitation method with urea (DPU), followed by gamma irradiation to reduce *in-situ* the deposited metal ions (in section 3.5). A two-step deposition was found to be important for an efficient deposition: a suspension containing P25 in a Au^{III} and urea solution, is firstly heated in water bath, and then Cu ions are introduced. The alloyed structure of the supported Au-Cu bimetallic NPs was evidenced by HRTEM, DRS, HAADF-STEM, EDS and XPS techniques. The Au-Cu bimetallic modified photocatalysts exhibited a better enhancement in photoactivity compared to monometallic Au modified P25 under UV illumination. As expected, the modified P25 with Au/Cu 1:3 NPs exhibited the highest photoactivity under UV illumination. The mechanism that Au-Cu alloyed NPs act as an electron sink prompting electron-hole separation was confirmed by the photocatalytic degradation and TRMC signals.

3.1 Introduction

TiO_2 has been extensively studied for decades since it was used in photocatalytic splitting of water initiated by Fujishima. Afterwards, TiO_2 has attracted much attention because of its photocatalytic properties, its excellent resistance to photocorrosion, and in addition it is also non-toxic and environment friendly. These properties make it the most suitable material for photocatalysis. TiO_2 exists in Nature in three crystallographic phases: anatase, rutile and brookite. Among them, anatase and rutile are most commonly used in photocatalysis, their band-gap energy are 3.1 and 3.0 eV respectively. Electron-hole pairs can be generated in the core of TiO_2 irradiated with light with wavelength shorter than 387 nm.

The great shortcoming of TiO_2 in photocatalysis is the requirement of high energy UV light to excite the electrons from the valence band to the conduction band. Many endeavors have been attempted to resolve this challenge, such as doping with N, C, S, P or halogen elements,[1-7] surface modification with semiconductor and plasmonic metal nanoparticles, and TiO_2 composite with Graphene Oxide or CNTs.[8-17] All of the above approaches are intended to narrow the band-gap, or to introduce transition energy level between the valence band and conduction band.

For the UV light driven photocatalysis, it is important to restrain the recombination of excited electrons and holes. Therefore the photoactivity of TiO_2 systems (especially anatase) was typically enhanced by modification with noble metals such as Pt, Pd, Ir, Au and Ag on the surface.[18-30] Furthermore, anatase-oxide mixtures using ZrO_2, SnO, WO_3, Al_2O_3, Y_2O_3, or other systems aiming at influencing the electron-hole separation was successfully attempted.[31-38] Only a few studies report modification of titania with bimetallic nanoparticles. Recently, improved photoactivity under visible light irradiation has been reported for modified titania with bimetallic silver-gold NPs prepared by microemulsion method.[39]

In the past decades, metallic nanoparticles have been widely studied due to their excellent properties compared to those of the corresponding bulk ones. Because of the

confinement of the charge carriers in such a small nano-scale, there exists a shift of the plasmon resonance absorption, non-linear optical effects, non-metallic conductivity, and nano-catalytic effects. Therefore, metal nanoparticles have potential applications in the field of optics, catalysis, photocatalysis, chemical sensing, and biomedicine, etc. In addition, bimetallic and multi-metallic nanoparticles could often exhibit enhanced catalytic, electronic magnetic properties, which differ from their monometallic counterparts. Particularly, bimetallic nanoparticles show better catalytic performances in terms of activity, selectivity, and stability, compared to the separate components.

To the best of our knowledge, a lot of methods are employed for preparing metal nanoparticles, such as hydrothermal, solvothermal, chemical vapor deposition (CVD), lithography and so forth.[40-42] In addition to those common methods, radiolysis synthesis of metal nanoparticles is a characteristic approach. Fujita was the first scientist who introduced the radiolytic technique into aqueous synthesis of inorganic and metal nanoparticles. In 1962, he prepared Au sol from Chloroauric Acid ($HAuCl_4$) solution via γ-Irradiation.[43] By this method, a variety of metallic nanostructures with specific properties have been synthesized, including platinum nanowires, gold nanorods and porous Pt-Pd nanoballs.[44-46] The advantage of radiolysis synthesis is that it induces a homogeneous reduction and nucleation, therefore generates uniform nanoparticles. Radiolysis is also a powerful method to synthesize bimetallic nanoparticles of controlled structure (alloys or core-shell).

In particular, bimetallic nanoparticles based on gold have attracted increased attention because of their optical properties and their application in catalysis and electrocatalysis.[47-49] Only a few studies report on synthesis, structure and properties of Au-Cu nanoparticles.[50-53] Recently, it has been shown that Au-Cu bimetallic nanoparticles exhibit higher catalytic activities than monometallic gold catalysts, for both CO oxidation and PROX reactions.[54-55] Bimetallic Au–Cu NPs on TiO_2 were found more active and selective towards propene epoxidation by nitrous oxide than monometallic Au or Cu samples supported on TiO_2.[48] Carbon electrodes modified by bimetallic Au-Cu NPs were found promising for electrocatalytic oxidation of glucose in alkaline solution.[56] Brodie-Linder *et al.* reported Cu^{II} grafted silica based mesoporous materials (SBA-15) by the impregnation method. The

presence of the $[Cu(NH_3)_3(H_2O)_3]^{2+}$ complex in the reaction solution is the key to control the Cu^{II} loadings from 6-20%. The presence of Cu^{II} on the surface of SBA-15 materials reduces and inhibits the production of H_2 by electron irradiation.[57-58]

Many methods are developed to deposit metal nanoparticles on oxide surfaces such as colloid-deposition, precipitation-deposition, and photo-deposition. In our experiments, colloid deposition and deposition-precipitation were used to prepare modified photocatalysts. For the colloid deposition method, the primary step is to synthesize small NPs homogeneous in size and well dispersed in solution. Moreover, stabilizers have an influence on the deposition of metal NPs on the substrates. Hence, choosing appropriate stabilizing agents is important. In our experiments, Poly Acrylic Acid (PAA) was used for preparation of small and homogeneous metallic NPs. The subsequent addition of Polyvinyl Alcohol (PVA) facilitated the deposition of metallic NPs on the support.

Deposition-precipitation with urea has been developed on the basis of a deposition precipitation method with NaOH initiated by Haruta.[59] In the DP method, the metal precursors are mixed with the supports forming an aqueous suspension, subsequently precipitated as a hydroxide by increasing the pH value. The key point of the DP is the prevention of precipitation away from the surface of the supports.[60-61] Zanella and Hugon *et al.* synthesized Au, Pd or some other noble metal NPs supported on TiO_2 and Al_2O_3 with DPU method.[48, 62-63] However, these works just focused on the deposition of noble metals and monometallic systems. Furthermore, calcination and H_2 reduction are necessary to obtain metal particles on the support. In this thesis, we, for the first time, attempted to prepare noble Au and non-noble Cu bimetallic NPs supported on TiO_2 by a modified DPU method. Au and Cu were deposited at different stages followed by gamma reduction to obtain Au-Cu bimetallic NPs modified titania.

The prepared photocatalysts were studied for degradation of model pollutants, such as phenol, rhodamine B (RhB) and methyl orange (MO) under UV and visible illumination. TRMC measurements were carried out to reveal the correlation of electron-hole recombination with photocatalytic activity after UV excitation.

3.2 Colloid-deposition of Au-Cu metallic NPs on P25 by radiolysis in the presence of stabilizers

3.2.1Radiolytic synthesis of Au monometallic nanoparticles

Figure 3.1 (a) show the evolution with dose of the spectra of a solution containing $AuCl_4^-$ in the presence 2-propanol (as electron scavenger) and of PAA (as stabilizer).

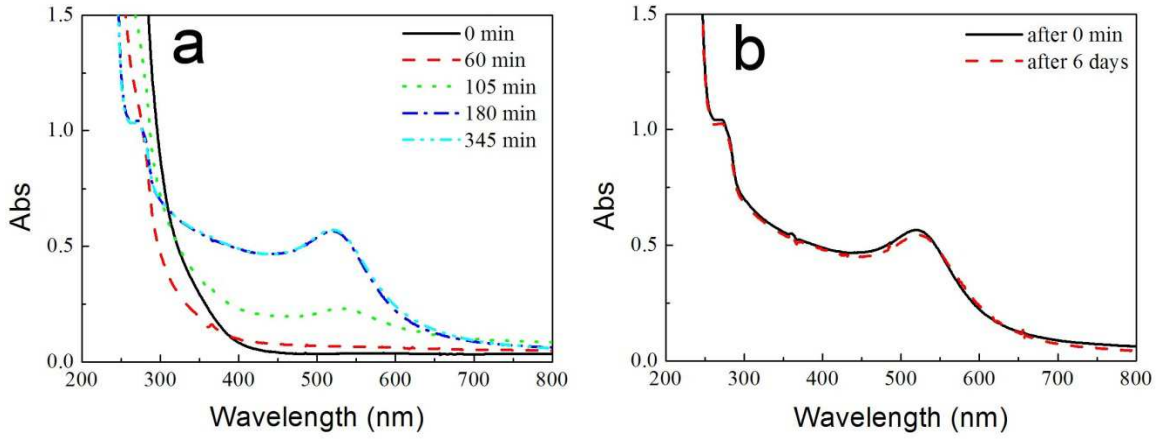

Figure 3.1 (a) Evolution of UV-Visible absorption spectrum with irradiation time of a $HAuCl_4$ solution containing PAA and 2-propanol, $[HAuCl_4] = 10^{-3}$ M, **(b)** evolution of spectrum with standing time in irradiated $HAuCl_4$ solution (180 min). [PAA] = 0.1 M, [2-propanol] = 0.1 M, optical path: 2 mm. The solutions were degassed with N_2 prior to irradiation, dose rate: 1.4×10^3 Gy/h.

From **Figure 3.1a** it can be seen that there is no absorption in the visible region before irradiation. The absorption peaks in the visible increase with irradiation time. At the beginning stage of the γ-irradiation (until 60 min), the absorption in the visible does not increase (**Figure 3.1a**, 60 min). This indicates there are nearly no Au atoms generated during the first 60 minutes. The reduction of Au^{III} into Au^0 is a multi-step process.[64-66] Pulse radiolysis studies have shown that Au^{II} does not directly disproportionate but dimerizes into a long-lived dimer, $(Au^{II})_2$, which then dissociates into Au^{III} and Au^{I}. It could be concluded from the studies of the dose-dependent yields in the steady state radiolysis that a comproportionation reaction of nascent gold atoms Au^0 with excess Au^{III} ions takes place to yield Au^{II} and Au^{I}. This reaction will take place until the reduction of all Au^{III} complexes into Au^{I} After, the coalescence of Au^0 atoms into gold clusters might occur. The reduction reactions of Au^{III} to

Au^0 are shown in the following equations:[64, 67]

$$Au^{III}Cl_4^- + e_{aq}^- \rightarrow Au^{II}Cl_4^{2-} \quad (3.1)$$

$$Au^{III}Cl_4^- + (CH_3)_2C^{\bullet}OH \text{ (or } H^{\bullet}) \rightarrow Au^{II}Cl_4^{2-} + (CH3)_2CO + H^+ \text{ (or } H^+) \quad (3.2)$$

$$Au^{II} + Au^{II} \rightarrow (Au^{II})_2 \rightarrow Au^{III} + Au^{I} \quad (3.3)$$

$$Au^{I} + e_{aq}^- \rightarrow Au^0 \quad (3.4)$$

$$Au^{I} + (CH_3)_2C^{\bullet}OH \text{ (or } H^{\bullet}) \rightarrow Au^0 + (CH_3)_2CO + H^+ \text{ (or } H^+) \quad (3.5)$$

$$Au^{III} + Au^0 \rightarrow Au^{II} + Au^{I} \quad (3.6)$$

With increasing dose, an absorption peak emerged at ~530 nm which corresponds to the plasmon band of gold. The intensity of the absorption peak increased with irradiation dose and reaches a plateau after 180 min irradiation (dose = 4.2 kGy). For doses higher than 4.2 kGy, the spectra are the same. The radiolytic reduction rate of Au^{III} is equal to 0.6 μmol J^{-1}. The polymer PAA plays a significant role in the stabilization of Au colloids, preventing the further coalescence of small Au nanoparticles. Moreover, absorption spectra of Au solution (**Figure 3.1b**) show that the Au colloids are stable for several days (more than 6 days).

Gamma radiolysis of $CuSO_4$ solutions containing polyacrylic acid and polyvinyl alcohol induces the formation of copper nanoclusters absorbing at 570 nm, and which dissolve readily when brought into contact with oxygen. Oligomers of lower nuclearity stabilized by the polyacrylate ions are shown to absorb at 292, 350 and 455 nm.[68]

3.2.2 Radiolytic synthesis of Au-Cu bimetallic nanoparticles

Bimetallic nanoparticles often display better catalytic and electrocatalytic properties than the corresponding monometallic counterparts.[69-72]. Here, we chose gold and copper as the two components of bimetallic nanoparticles. Au/Cu metallic colloids of different molar ratios were prepared by radiolysis of aqueous solutions containing Cu^{II} and Au^{III} in the presence of polyacrylic acid (PAA) and/or polyvinyl alcohol (PVA). 2-propanol was added in the solution to scavenge the OH• oxidative radicals produced by radiolysis. The concentrations of 2-propanol and of each polymer were kept at 0.1 M. The details of the synthesized Au-Cu

colloids are listed in **Table 3.1**.

Table 3.1 The Au-Cu Colloid samples with various Au/Cu ratios prepared by radiolysis in the presence of different stabilizers.

Samples label	Molar Ratio of Au/Cu	$[HAuCl_4]$ (mol/L)	$[CuCl_2]$ (mol/L)	Stabilizer
[a]AuCu13PAA	1:3	5×10^{-4}	1.5×10^{-3}	PAA (0.1 M)
AuCu11PAA	1:1	10^{-3}	10^{-3}	PAA (0.1 M)
AuCu31PAA	3:1	1.5×10^{-3}	5×10^{-4}	PAA (0.1 M)
AuCu13PVA	1:3	5×10^{-4}	1.5×10^{-3}	PVA (0.1 M)
AuCu13PP	1:3	5×10^{-4}	1.5×10^{-3}	PAA (0.1 M) and PVA (0.1 M)
[b]AuCu11PP	1:1	10^{-3}	10^{-3}	PAA (0.1 M) and PVA (0.1 M)
AuCu31PP	3:1	1.5×10^{-3}	5×10^{-4}	PAA (0.1 M) and PVA (0.1 M)

[a]AuCu13PAA: colloidal solution of Au-Cu bimetallic NPs with a molar ratio of 1:3 prepared by radiolysis in the presence of stabilizer PAA.

[b]AuCu11PP: PP indicates the mixture of polymer PAA and PVA.

The UV-Vis absorption spectra of the prepared Au-Cu colloids with different Au/Cu ratios are shown in **Figure 3.2**. The absorption peak at ~530 nm increases with gamma irradiation time. These absorption is due to the surface plasmon resonance (SPR) of gold and copper particles. Au and Cu are known to exhibit a plasmon band with maxima respectively at 520 and 570 in aqueous solution. It is known that surface plasmon resonance is due to the collective oscillation modes of the free conduction band electrons induced by the localized electromagnetic field. The intensity of plasmon band is proportional to the concentration of metal atoms.[73-74] As a result, the maximum intensities of absorption peaks with various Au-Cu ratios (in case of alloys) are relatively proportional to the overall concentration of Au and Cu. It should be pointed out the absorption peak is located at the same wavelength and does not shift with irradiation time (see **Figure 3.2a,c,e**). It can be assumed that the compositions of Au-Cu bimetallic nanoparticles were the same from the beginning to the end

of irradiation, namely the synthesized Au-Cu bimetallic nanoparticles have probably an alloyed structure. The as-prepared Au-Cu colloids are stable even after more than 6 days (**Figure 3.2b**,**d**).

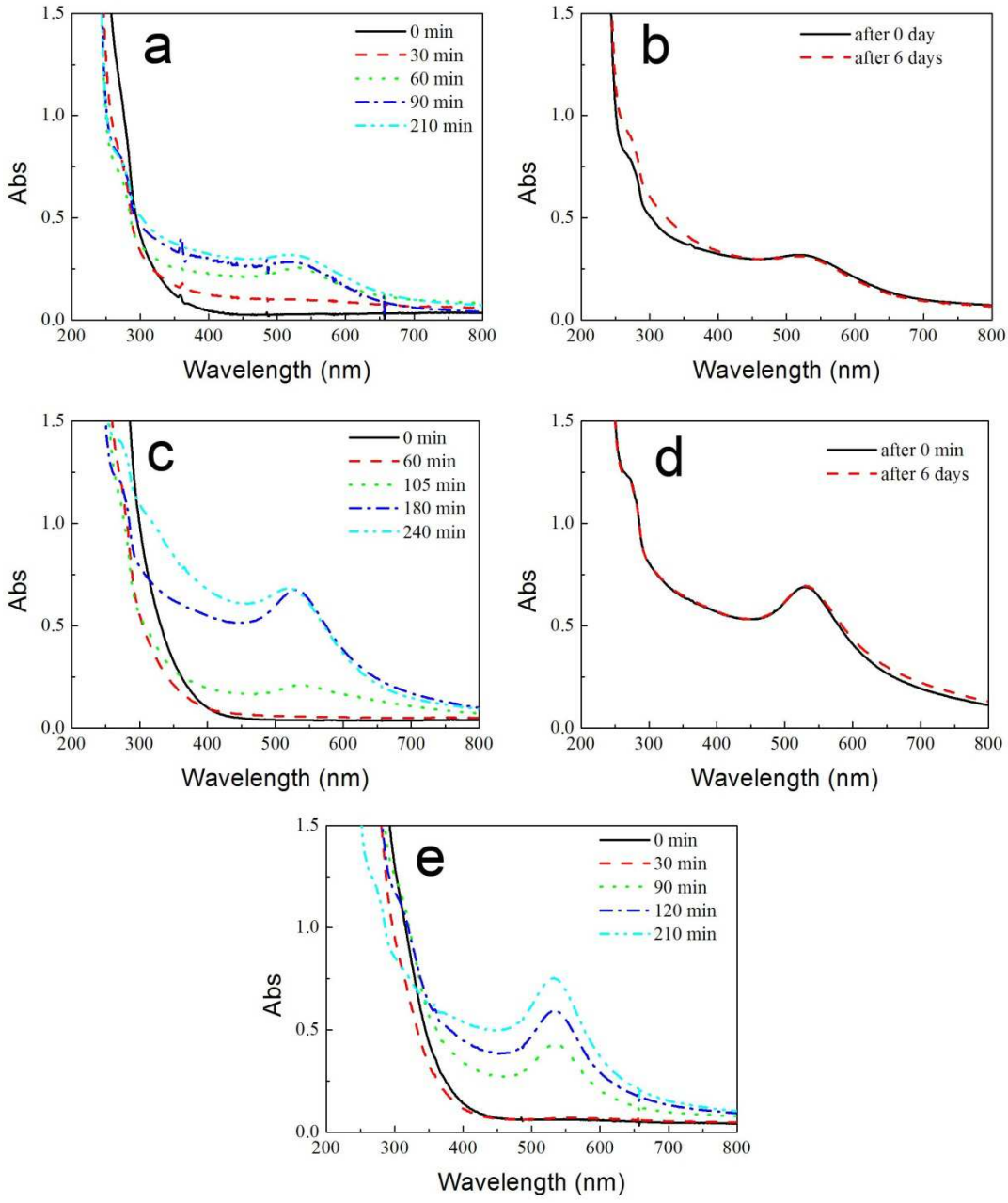

Figure 3.2 Evolution of UV-Visible absorption spectra with irradiation time of irradiated $HAuCl_4/CuCl_2$ solutions containing PAA (0.1 M) and 2-propanol (0.1 M) **(a)** AuCu13PAA, $[HAuCl_4] = 5\times10^{-4}$ M, $[CuCl_2] = 1.5\times10^{-3}$ M, **(c)** AuCu11PAA, $[HAuCl_4] = 10^{-3}$ M, $[CuCl_2] = 10^{-3}$ M, **(e)** AuCu31PAA, $[HAuCl_4] = 1.5\times10^{-3}$, $[CuCl_2] = 5\times10^{-4}$ M; and evolution of UV-visible spectra with standing time of corresponding solutions **(b)** AuCu13PAA (irradiated 210 min), **(d)** AuCu11PAA (irradiated 180 min). Optical path: 2 mm. The solutions were degassed with N_2 prior to irradiation, dose rate: 1.4×10^3 Gy/h.

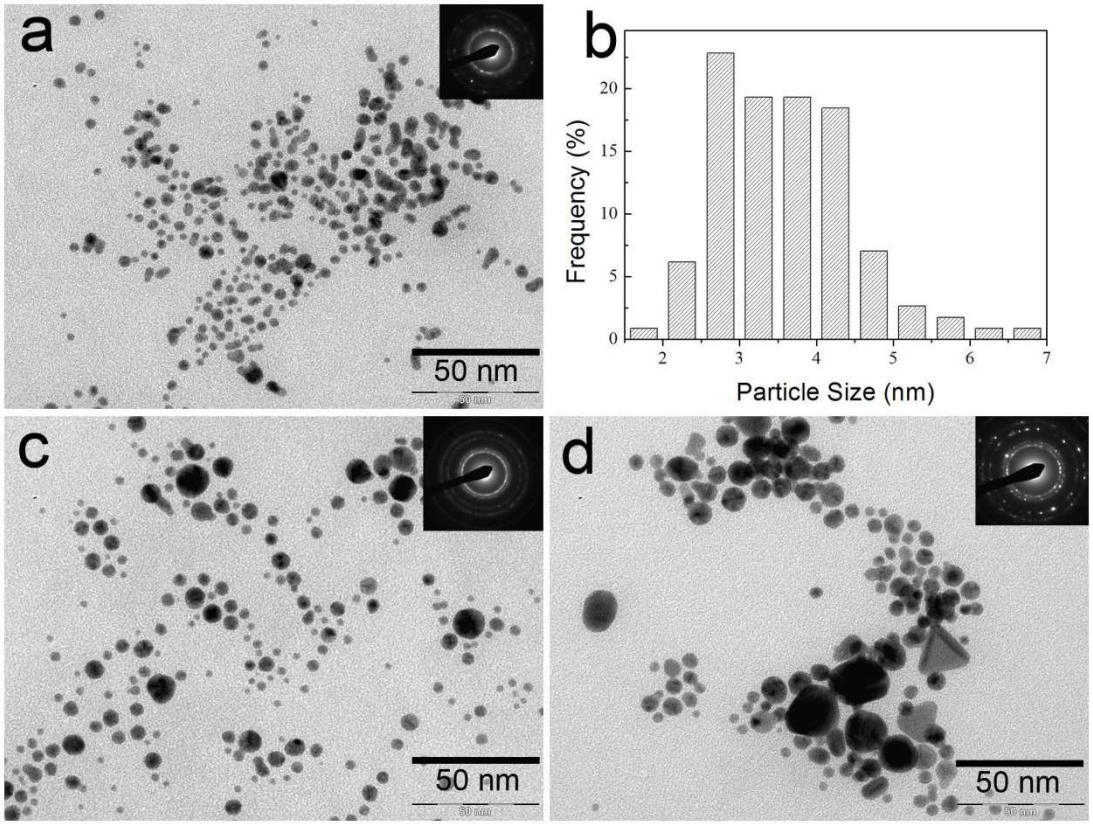

Figure 3.3 TEM images of Au-Cu nanoparticles with different compositions **(a)** AuCu13PAA, **(c)** AuCu11PAA, **(d)** AuCu31PAA, prepared by radiolysis in the presence of PAA. Inset: the corresponding SAED patterns. **(b)** Size distribution of the sample AuCu13PAA.

The morphologies of the synthesized Au-Cu bimetallic nanoparticles with PAA were characterized by TEM technique. The mean diameter of Au-Cu bimetallic AuCu13PAA nanoparticles is 3.6 nm. The size of AuCu13PAA varies from 1.9 nm to 6.6 nm (**Figure 3.3a,b**). The nanoparticle size of AuCu11PAA is relatively larger, varying from 3 nm to 13 nm. The size of the AuCu31PAA NPs is comparatively much larger than that of AuCu13PAA and AuCu11PAA NPs. A few large nanoparticles more than 20 nm can be seen in the TEM images (**Figure 3.3d**). Additionally, few triangular crystals can also be observed. Such a triangle structure is usually observed in the preparation of monometallic Au NPs in the presence of a polymer stabilizer. The triangular structure is one of the typical Au crystal morphologies and it is easily formed. Therefore, it can be obviously concluded that the Au-Cu bimetallic NPs are getting smaller and more homogeneous along with the increase of the Cu proportion in the bimetallic NPs. The probable mechanism we proposed is that the presence of Cu ions handicaps the deposition of Au ions on the surface of Au^0 clusters. Hence, the

comproportionation reaction between Au^0 and Au^{III} may be inhibited. Consequently, the nuclei number of Au increased. As a result, the growth of Au crystal was limited and the crystal size decreased.

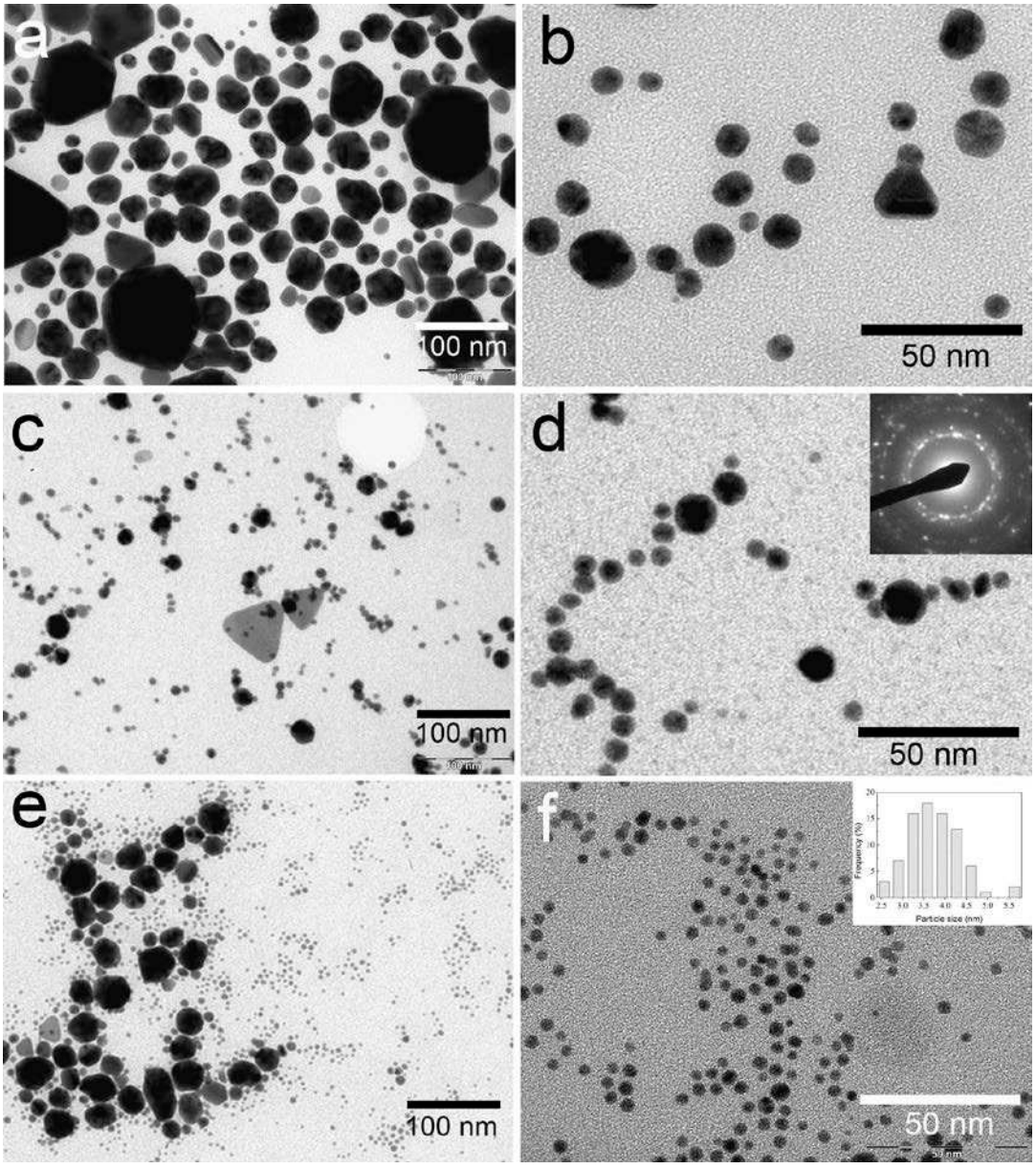

Figure 3.4 TEM images of the sample AuCu31PP **(a, b)**, AuCu11PP **(c, d)**, and AuCu13PP **(e, f)**, prepared by radiolysis in the presence of PAA and PVA.

The morphology of the radiolytic synthesized samples in the presence of PAA and PVA were observed by TEM technique. As seen in **Figure 3.4(a,b)**, the nanoparticle size of AuCu31PP has a large distribution, ranging from ~6 nm to ~110 nm. Very few large triangular crystals can also be seen. In the case of AuCu11PP, the Au-Cu NP size is smaller than that of

AuCu31PP, ranging from ~5 nm to ~30 nm. Besides that, the Au-Cu bimetallic triangular nanoplates with a side length of around 60 nm also formed. The SAED pattern in **Figure 3.4d** gives the spacing value (2.344 Å) of the inner diffraction ring, which is close to the spacing between (111) lattice planes of gold (2.355 Å, JCPDS-PDF 04-0784). For the AuCu13PP, the nanoparticle size exhibits two distinct distributions: Small NPs from 2.5 to 5.6 nm and larger ones (with a large distribution from ~15 nm up to 40 nm) are observed. In brief, the synthesized Au-Cu bimetallic NPs with co-stabilizer of PAA and PVA have a larger size distribution. The size is smaller and the distribution becomes narrow with the increase of copper proportion in the Au-Cu bimetallic NPs.

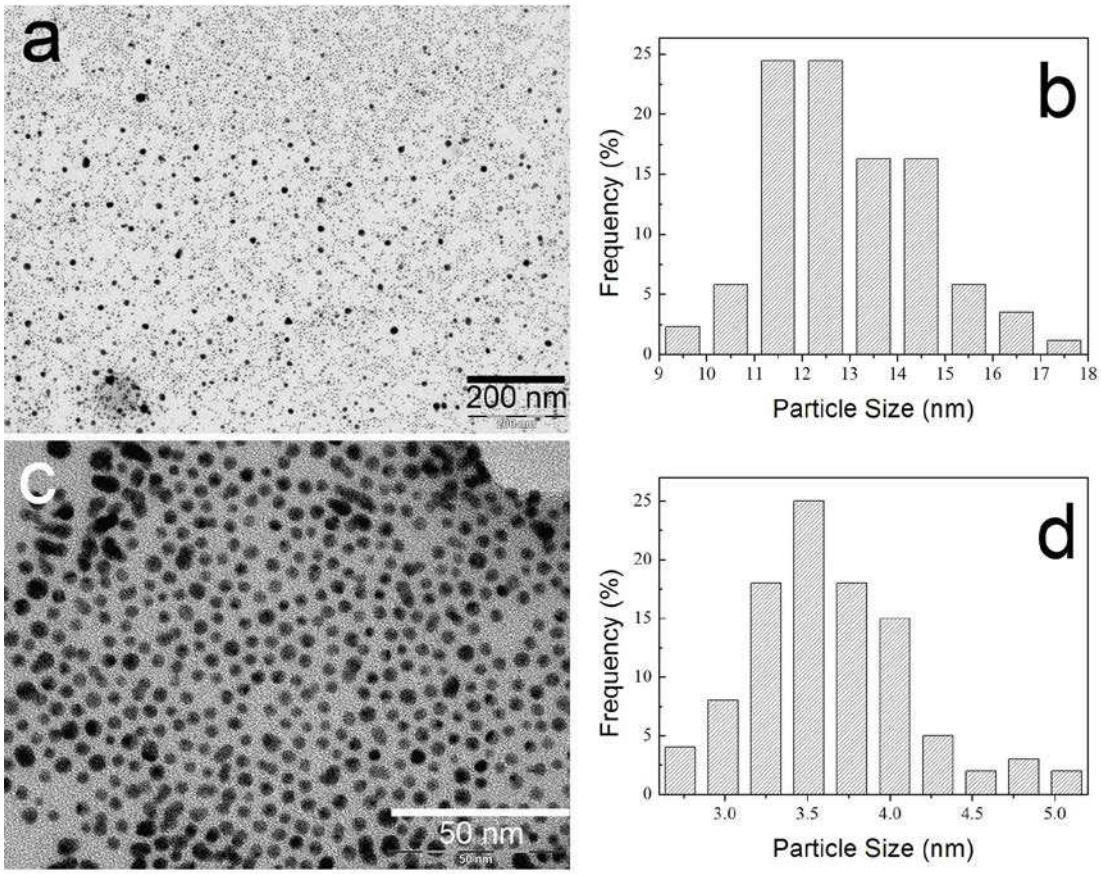

Figure 3.5 TEM images of the sample AuCu13PVA prepared by radiolysis in the presence of PVA, at a lower **(a)** and a higher **(c)** magnification; size distributions of the sample AuCu13PVA at **(b)** the larger size region and **(d)** smaller size region.

When PVA was used in the radiolytic synthesis of Au-Cu NPs, the nanoparticle sizes presented two distributions in size with a first maximum at around 3.6 nm (**Figure 3.5a**) and a second maximum located at around 13 nm: indeed NPs with sizes ranging from 9.7 to 17.5

nm were also observed (**Figure 3.5c**,**d**).

Considering the inhomogeneous dispersion on the Au-Cu NP size, the polymer PVA is not as fine a stabilizer as PAA for the preparation of Au-Cu NPs by radiolysis.

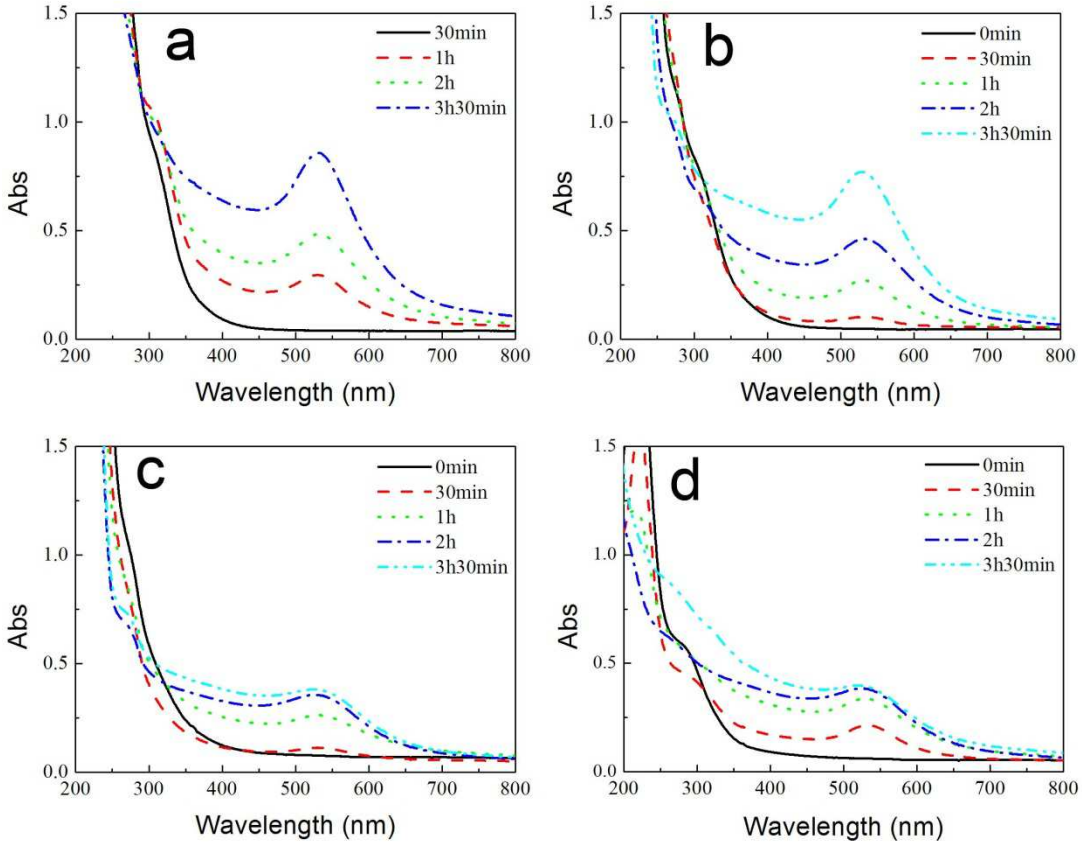

Figure 3.6 Evolution of UV-Vis absorption spectra of the sample **(a)** AuCu31PP, $[HAuCl_4]$ = 1.5×10^{-3} M, $[CuCl_2]$ = 5×10^{-4} M, **(b)** AuCu11PP, $[HAuCl_4]$ = 10^{-3} M, $[CuCl_2]$ = 10^{-3} M, **(c)** AuCu13PP, $[HAuCl_4]$ = 5×10^{-4} M, $[CuCl_2]$ = 1.5×10^{-3} M, and **(d)** AuCu13PVA, $[HAuCl_4]$ = 5×10^{-4} M, $[CuCl_2]$ = 1.5×10^{-3} M. [PAA] = 0.1 M and [PVA] = 0.1 M, [2-propanol] = 0.1 M. Dose rate = 1.4 kGy/h. Optical path: 2mm.

The UV-vis absorption spectra of the prepared Au-Cu colloids in the presence of PAA and PVA by radiolysis are shown in **Figure 3.6**. The absorption peaks at 540 nm are due to the surface plasmon resonance of Au and Cu metal NPs. It is worth noting that the absorbance maximum at 540 nm for the synthesis with polymer PVA is obvious even after 30 minutes of gamma irradiation, indicating that the Au-Cu bimetallic NPs substantially formed (**Figure 3.6d**). By contrast, the absorbance at 540 nm for the parallel synthesis with PAA is nearly negligible (**Figure 3.2a**,**c**,**e**). Moreover, when the two stabilizers, PVA and PAA, were employed simultaneously, the absorbance is located in between those obtained for the

individual ones. A probable mechanism is proposed: the nucleation is the dominant process in the presence of PAA while the crystal growth of Au is more predominant with the PVA stabilizer.

3.2.3 Deposition of Au-Cu NPs on the support P25

All of the modified photocatalysts are pink or pink-violet. Details of the prepared photocatalysts are summarized in **Table 3.2**.

Table 3.2 The List of the synthesized Au and Au-Cu NPs supported on P25.

Photocatalysts	Molar ratio of Au/Cu	Content of metal precursor (wt %)		Stabilizer
		Au	Cu	
AuPAA@P25(1)	-	1	-	Poly Acrylic Acid
[a]AuCu31PAA@P25(1)	3:1	1	0.11	Poly Acrylic Acid
AuCu11PAA@P25(1)	1:1	1	0.32	Poly Acrylic Acid
AuCu13PAA@P25(1)	1:3	1	0.97	Poly Acrylic Acid
AuPVA@P25(1)	-	1	-	Polyvinyl Alcohol
AuCu13PP@P25(1)	1:3	1	0.97	PAA and PVA
AuCu13PAA@P25(0.5)	1:3	0.5	0.48	Poly Acrylic Acid
AuCu11PAA@P25(0.5)	1:1	0.5	0.16	Poly Acrylic Acid
AuCu31PAA@P25(0.5)	3:1	0.5	0.05	Poly Acrylic Acid

[a]AuCu31PAA@P25(1): The modified P25 with AuCu31PAA bimetallic NPs, **(1)** indicates the mass percentage of Au to P25 is 1%.

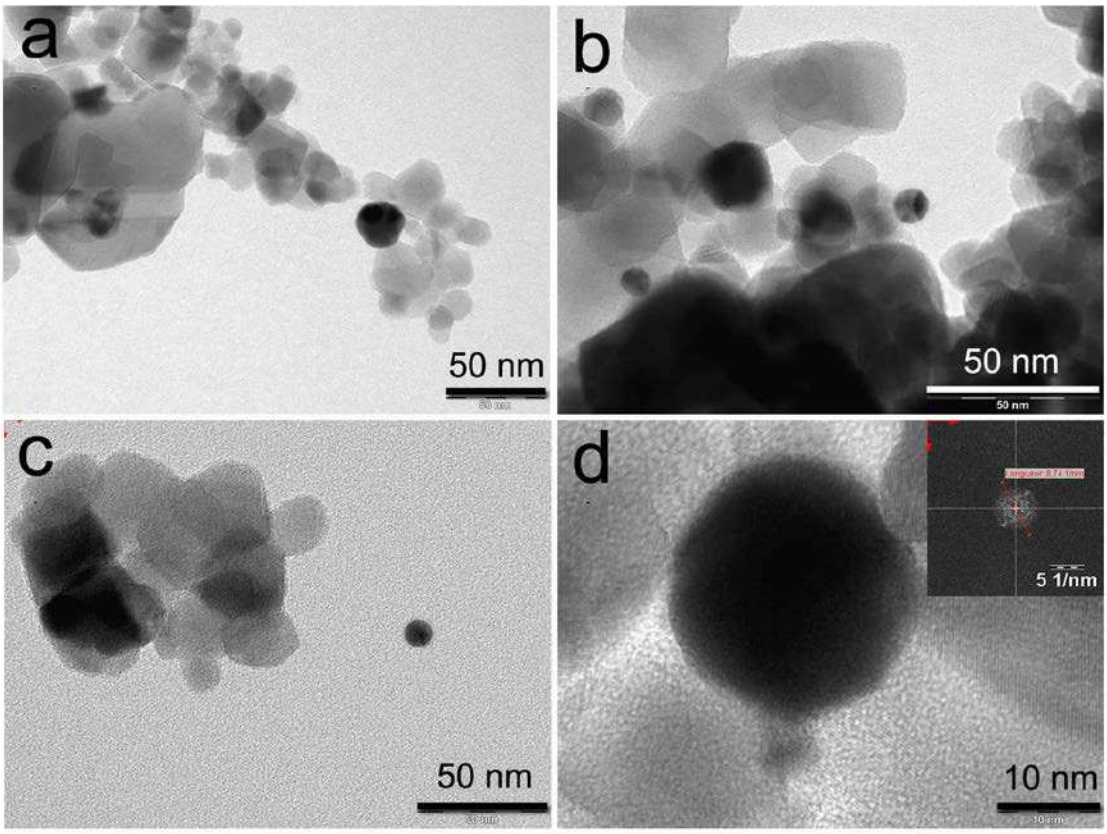

Figure 3.7 TEM images of the sample AuCu13@P25PAA(1) at a lower **(a-c)** and higher magnification **(d)**, inset: the fourrier transform of the image, the mass percentage of Au to P25 is 1%.

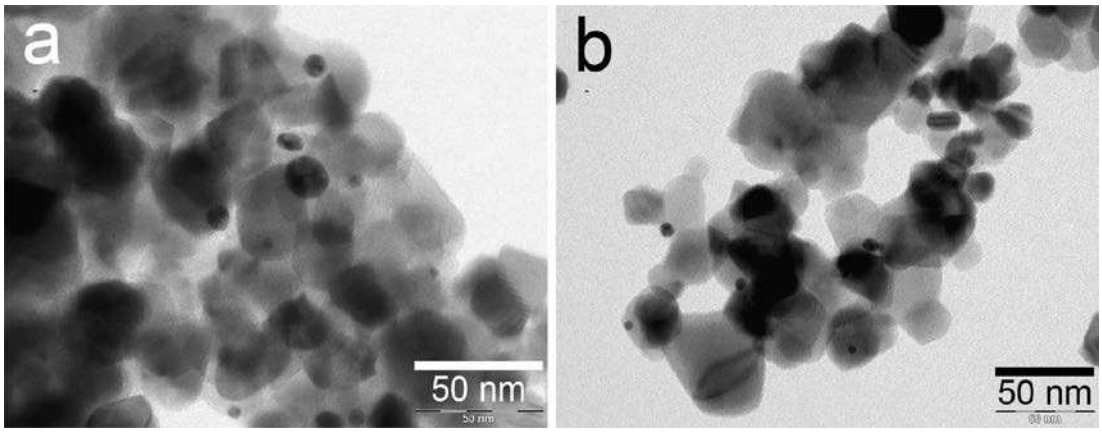

Figure 3.8 TEM images of AuCu13@P25PP(1).

TEM observations in **Figure 3.7** show gold NPs distributed on P25 for the sample AuCu13@P25PAA(1). The average size of the Au-Cu bimetallic NPs is about 10 nm. Only a small part of the Au-Cu NPs are deposited on TiO_2. Compared to the smaller size of nanoparticles of AuCu13PAA, a big change in nanoparticle size was induced after the

deposition on the substrate P25 (increase by more than 6 nm, the mean size increases from 3.6 nm to 10 nm). Two probable interpretations can be given for the size increase. The first one is that the NPs aggregate when they deposit on the surface of TiO_2. The other one, most probably, is that the Au-Cu NPs of smaller size rarely attach to surface of P25. Furthermore, it can be seen that a few Au-Cu bimetallic nanoparticles are not well deposited on TiO_2 (**Figure 3.7c**). This can be confirmed by the slight violet supernatant of the sample AuCu13@P25PAA(1), indicating the Au-Cu bimetallic NPs are still present in the supernatant. The inset in **Figure 3.7d** is the Fourier transform pattern of the selected Au-Cu NPs. The calculated value of the crystalline interplanar distance is 2.29 Å, which corresponds to the spacing value (2.355 Å, JCPDF 04-784) of Au (111) lattice planes. According to the Vegard's law, the slight decrease of the *d* value is ascribed to the introduction of Cu atoms in the Au crystalline structure. The results show that the deposition of Au-Cu NPs on TiO_2 in the presence of PAA is not efficient.

In the case of deposition of Au-Cu NPs on TiO_2 with the co-stabilizers PAA and PVA, an improved deposition performance was observed. **Figure 3.8** shows the TEM images of the sample AuCu13@P25PP(1). It can be seen that the deposited NPs have a size in range from ~4.2 to 16 nm. The number of deposited NPs is slightly larger than that with PAA only. Compared to the AuCu13PP before deposition, just a small change of the nanoparticle size was induced by the deposition process. This implies that the deposition of Au-Cu NPs in the presence of the co-stabilizers PAA and PVA is much more efficient than the deposition with only PAA.

The electronic properties of the as-prepared photocatalysts were characterized by DRS. The UV-Vis absorption spectra of pristine P25 and modified Au-Cu-P25 are shown in **Figure 3.9**.

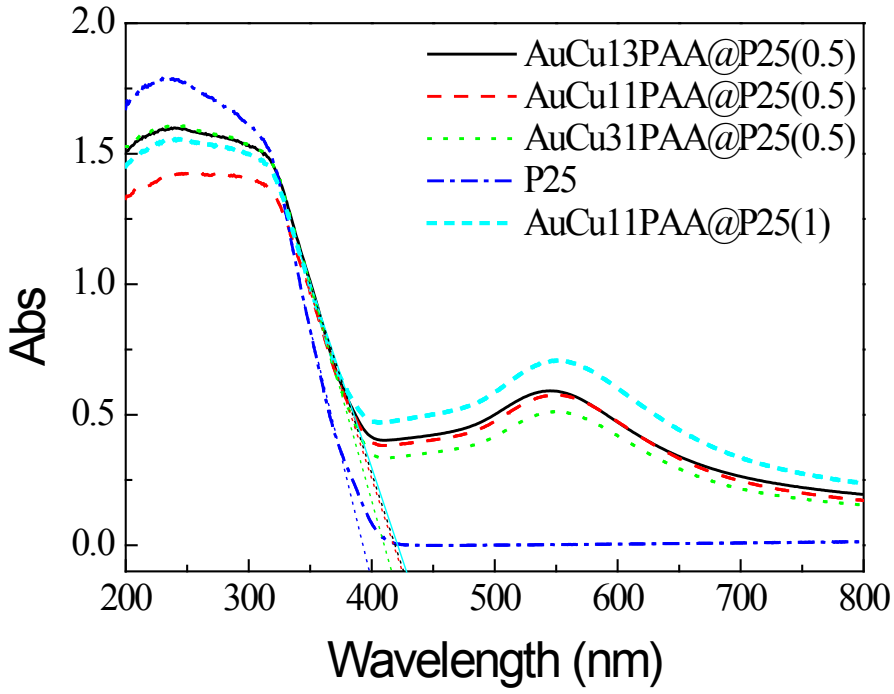

Figure 3.9 Diffuse reflectance UV-Vis spectra of the modified photocatalysts and pure P25.

The strong absorption bands at around 300 nm is attributed to the intrinsic absorption of TiO_2, resulting from excitation of O 2p electrons to the Ti 3d level.[75] The absorbance for the modified P25 in the visible region is always higher than that for the pristine P25. Note that wide absorption with a maximum at 550 nm is obtained with Au-Cu modified P25. This absorption results in the pink -violet color of the modified TiO_2 samples. The band-gap value E_g for pure P25 can be calculated from the extrapolated intercept on axis of wavelength. According to Einstein's equation $E = hv$ and the transform $E = 1240/\lambda$, the E_g obtained from experiment is 3.1 eV, which is consistent with the characteristic band-gap value of TiO_2. It is worth noting the DRS spectra for the modified P25 show a slight shift in the band-gap transition to longer wavelengths. Approximately, the shift toward lower energy (longer wavelength) increases with the copper nominal loading. For example, the band-gap of AuCu31PAA@P25(0.5) is estimated to be equal to 2.98 eV (absorption edge of 416 nm) and AuCu13PAA@P25(0.5) is 2.90 eV (427.5 nm). This effect was observed in the case of Ag- and Pt- modified TiO_2.[76-77] Such an effect can be attributed to a stronger stabilization of the conduction band of TiO_2 by the conduction band of the Au-Cu NPs compared to the stabilization of the valence band. Au and Cu nanoparticles are known to exhibit a plasmon

band with a maximum at around ~520 nm and ~570 nm in aqueous solution, respectively. This plasmon band is sensitive to the environment and can be shifted depending on the substrate or on the stabilizer. The plasmon bands in case of and Au-Cu/TiO_2 are red-shifted because of the coupling between the metal nanoparticles and TiO_2 substrate having a high reflective index (the absorption coefficient and refractive index for anatase phase at a wavelength of 380 nm are 90 cm^{-1} and 2.19, respectively). [78-79]

3.2.4 Photocatalytic activity under UV illumination

The photocatalytic activities of the modified P25 were evaluated by photodegrading RhB. RhB aqueous solution is considerably stable subjected to UV and visible illumination. As is shown in **Figure 3.10a**, it is a typical plot for RhB photodegradation. The RhB display two absorbance maxima at 554 nm and at 258 nm. The main absorption peak decreased remarkably with UV irradiation time.

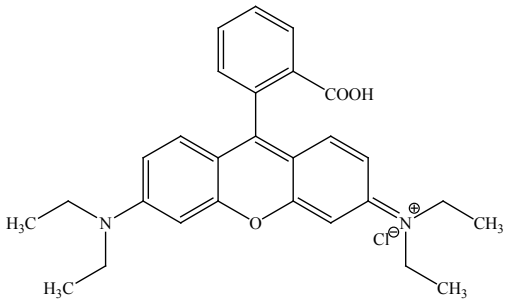

Scheme 3-1 Molecular formula of rhodamine B.

Commonly, Evonik P25 is used as the reference to evaluate the relative photocatalytic activity because of its high photoactivity in dye degradation under UV light. 10^{-4} M of RhB was photodegraded in the presence of Au-Cu1:3 bimetallic NPs modified P25 with different metal loadings of 1% and 0.5%; The results are illustrated in **Figure 3.10(a,b)**. Compared to pure P25, both of the modified photocatalysts are less efficient for the photocatalytic degradation of RhB compared with P25 (**Figure 3.10c**). The decrease of the photoactivity can be due to several reasons as follows. Firstly, the Au-Cu NPs cover the surface of P25 so that less photons are incident onto P25 surface, consequently inducing less electron-hole pairs. Another explanation could be also proposed that the metal NPs act in this case as

recombination center for the charge carriers.

It should also be pointed out that the modified P25 with a lower metal loading of 0.5% is slightly higher in photocatalytic activity, although both of them are worse than pristine P25.

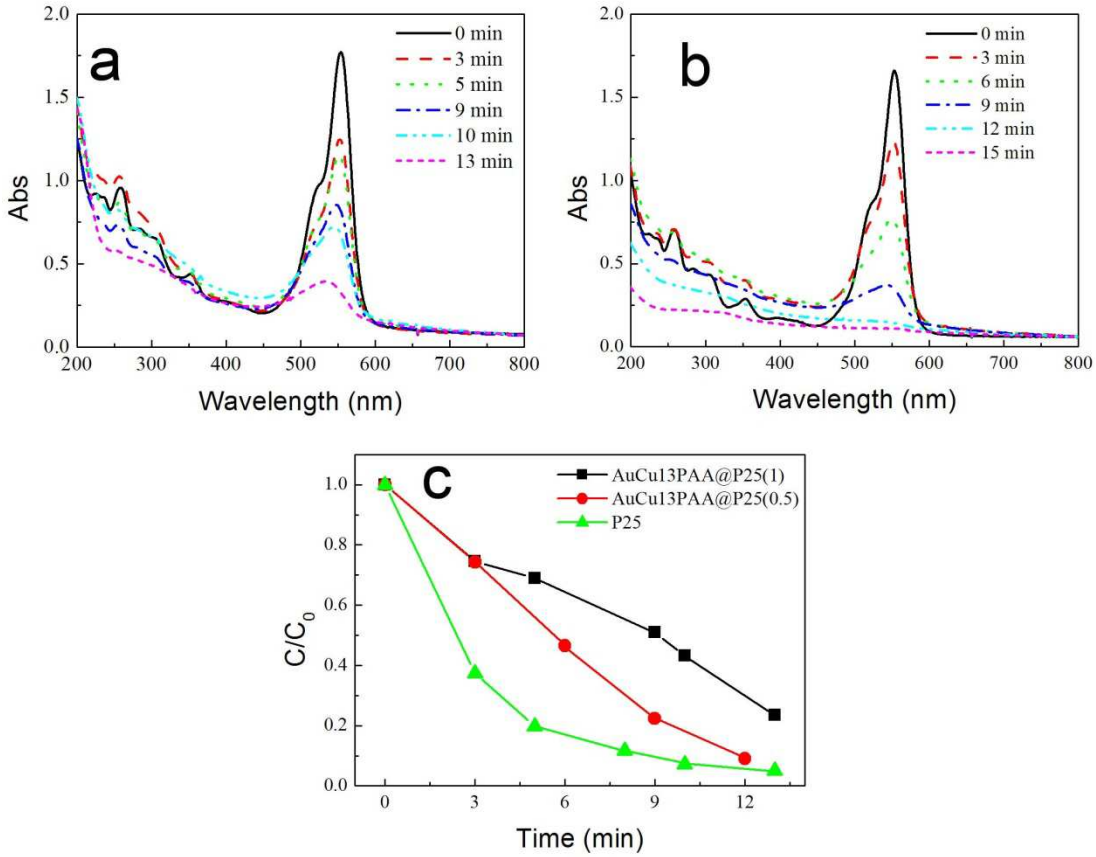

Figure 3.10 Evolution of UV-Vis absorption spectra of RhB in photocatalytic reaction with **(a)** AuCu13PAA@P25 (1), and **(b)** AuCu13PAA@P25(0.5) under UV illumination, optical path 2mm, **(c)** time runs of RhB relative concentration in photodegradation in the presence of pristine and modified P25 under UV illumination.

The photoactivity of the modified samples was also investigated for the degradation of phenol under UV illumination. As it can be seen in **Figure 3.11**, pure P25 is highly photoactive in phenol degradation under UV light. After 330 minutes of irradiation, 97% of phenol was degraded. The catalyst AuCu13PAA@P25(0.5) exhibits a slightly higher photocatalytic activity than AuCu11PAA@P25(0.5). It can be concluded that the photoactivity increases with the copper proportion in the bimetallic NPs.

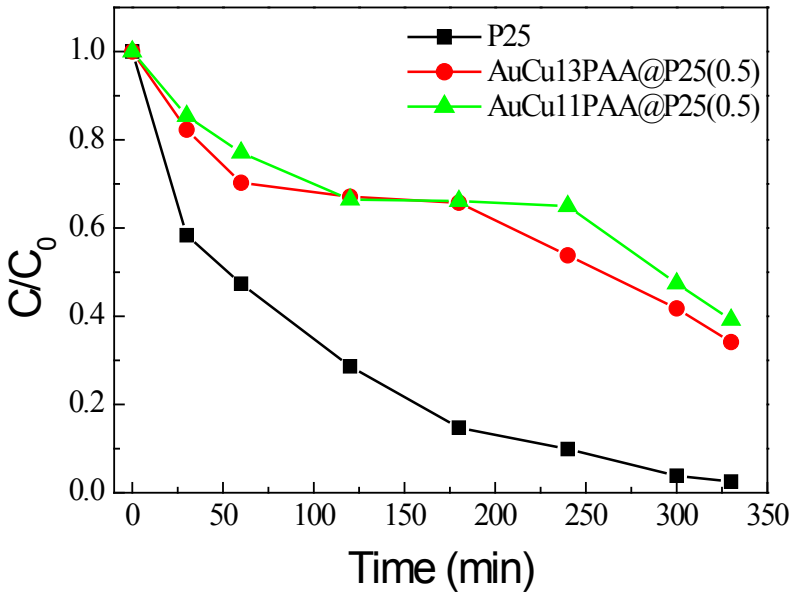

Figure 3.11 Time runs of phenol relative concentration in photodegradation in the presence of pristine P25, AuCu13PAA@P25(0.5), and AuCu11PAA@P25(0.5) under UV illumination.

3.2.5 Photocatalytic activity under visible illumination

The photodegradation of RhB with Au-Cu/P25 photocatalysts under visible illumination are shown in **Figure 3.12**. As it was studied widely, the photodegradation of RhB follows different processes: photo-bleaching and N-deethylation.[80-83] Considering the molecular structure of RhB is N,N,N′,N′-tetraethylrhodamine (**Scheme 3-1**), it can be deethylated into various intermediates by N-deethylation. As is shown in **Table 3.3**, the intermediates have different absorption peaks, decreasing to shorter wavelength with the N-deethylation processing. It can be obviously seen from **Figure 3.12** that the absorption peaks shift a lot and the shift is accompanied by a decrease of the absorbance. It is observed that: (1) the absorbance maxima decreased at the beginning of illumination and increased at longer illumination time; (2) the absorption peaks did not shift at longer irradiation time. Here, we give the probable interpretations. For the first question, the intermediates generated in the N-deethylation process have different extinction coefficient. Apparently, ε increases with the decrease of ethyl in the molecule (not including RhB). For instance, ε of TER (3 ethyl) is 5.5 L mol^{-1} cm^{-1} and rhodamine (0 ethyl) is 8.4 (see **Table 3.3**). Hence, from the Beer-Lambert law: $A = \varepsilon cl$, it can be concluded the absorbance decreased at the beginning and increased

afterwards. Certainly, this case occurred just when the photo-bleaching could be ignored compared to N-deethylation. For the second observation, the reason is that after the N-deethylation completed, the aromatic structures in rhodamine cannot be destroyed with the modified P25 by visible photocatalysis. Thus the main absorption peaks at 495 nm are due to a stable intermediate of rhodamine degradation generated by the effect of N-deethylation.

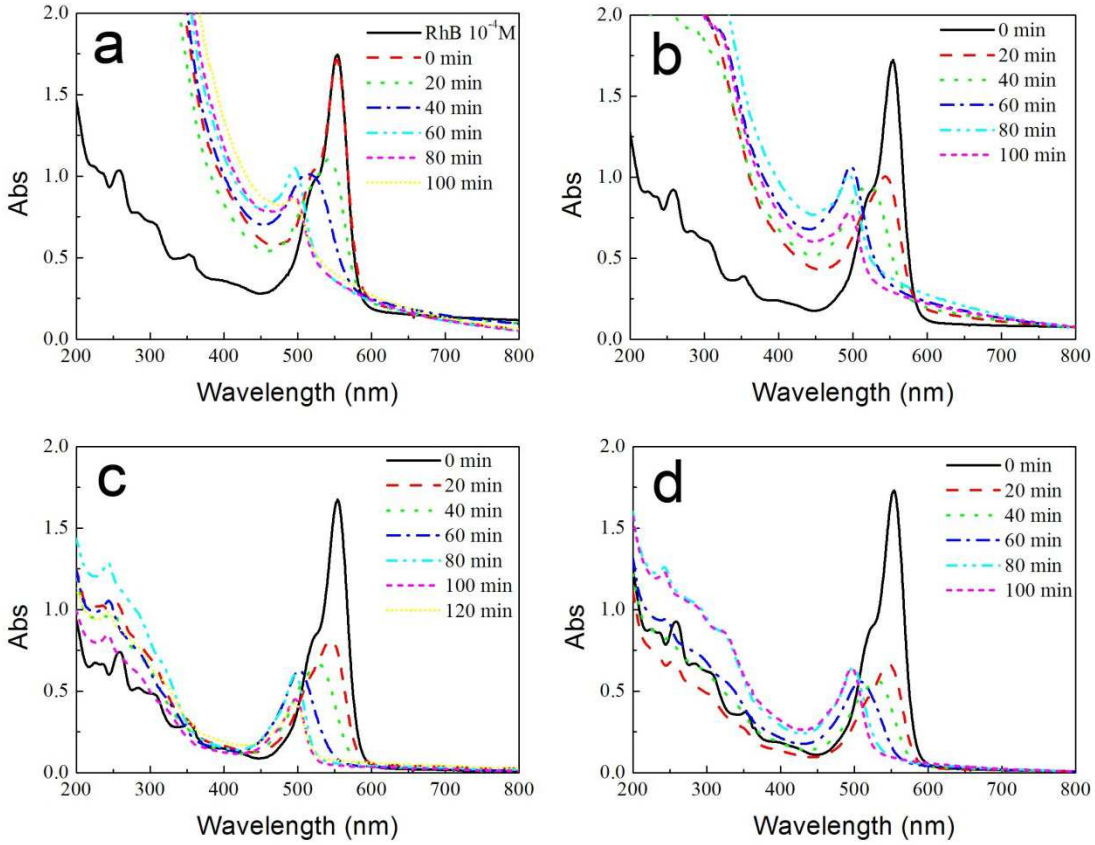

Figure 3.12 UV-vis absorption spectra of RhB degraded under visible light in the presence of **(a)** AuPAA@P25(1), **(b)** AuCu31PAA@P25(1), **(c)** AuCu11PAA@P25(1), **(d)** AuCu13PAA@P25(1). Optical path: 2 mm; illumination, λ > 450 nm; photocatalyst suspended 1 g/L.

It is complicated to evaluate the photodegradation kinetic processes due to the various intermediates existing in the reaction system. Nevertheless, we could just consider the absorbances at 554 nm to assess the N-deethylation capability of a series of modified P25 photocatalysts. **Figure 3.13** shows the time runs of RhB photodegradation under visible illumination. As it can be seen that RhB in solution is quite stable under visible light irradiation. All of the modified P25 photocatalysts showed better activities than the bare P25. The most efficient one is AuCu13PAA@P25(1). Generally, it can be concluded that the

Au-Cu-P25 photocatalysts with a higher Cu proportion leads to a higher photocatalytic activity in N-de-ethylation.

In order to evaluate the rate of RhB N-de-ethylation process with various photocatalyst, wavelength (at absorption peaks) change as a function of irradiation time was plotted in **Figure 3.14**. Without photocatalyst, there is no shift in the position of the absorption wavelength maximum of the RhB with irradiation time (**Figure 3.14B**). The modified Au-Cu/P25 results in larger wavelength changes compared to the pristine P25. The ultimate absorption peaks of photodegraded RhB with the modified photocatalysts were located at 498 nm, indicating the intermediates of rhodamine degradation accumulated. Among the as-prepared photocatalysts, more Au proportion leads to faster N-de-ethylation. Qu *et al.* reported that the pH values can affect the rate of the RhB N-de-ethylation process. The higher the pH, the slower the N-de-ethylation. In the solution of pH 10, no N-de-ethylation can be observed in the P25 suspension with RhB. [80] In our experiments, considering that the Au precursor chloroauric acid is acidic, a higher Au content means a low pH value of the solution, which decreases the amount of OH^- on the TiO_2 surface. In consequence, a higher Au content in the modified P25 is related to a lower pH value of P25 suspension with RhB. In brief, a higher Au proportion results in a higher rate of N-de-ethylation of RhB.

Table 3.3 Spectroscopic Data for the Dyes in the Photocatalytic Reaction of RhB.[81]

Dyes	Absorbance maximum, nm		$^{\alpha}\ \varepsilon_{max}, \times 10^{-4}$ $L \bullet mol^{-1} \bullet cm^{-1}$
	In water	In MeOH	
Rhodamine B	555	547	11.5
N,N,N′-triethylrhodamine (TER)	539	539	5.5
N,N′-Diethylrhodamine (DER)	522	525	7.2
N-Ethylrhodamine (MER)	510	516	6.1
Rhodamine	498	503	8.4

$^{\alpha}$ In dilute ($10^{-6} \sim 10^{-5}$ M) methanolic solution at 20 °C.

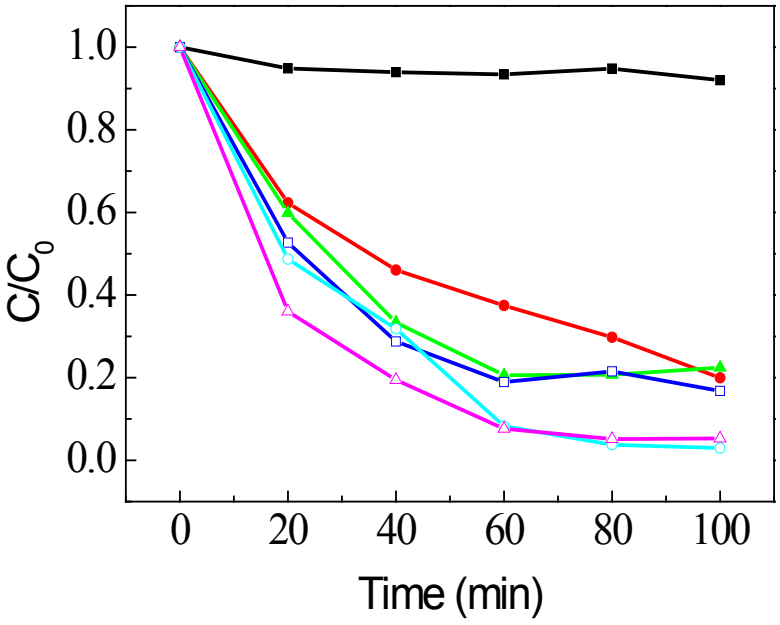

Figure 3.13 Time runs of RhB relative concentration in photodegradation with no photocatalyst (solid square ■), P25 (solid circle ●), AuPAA@P25(1) (solid triangle ▲), AuCu31PAA@P25(1) (empty square □), AuCu11PAA@P25(1) (empty circle ○), AuCu13PAA@P25(1) (empty triangle △). The initial concentration of RhB is 10^{-4} M; illumination λ > 450 nm; optical path: 2 mm.

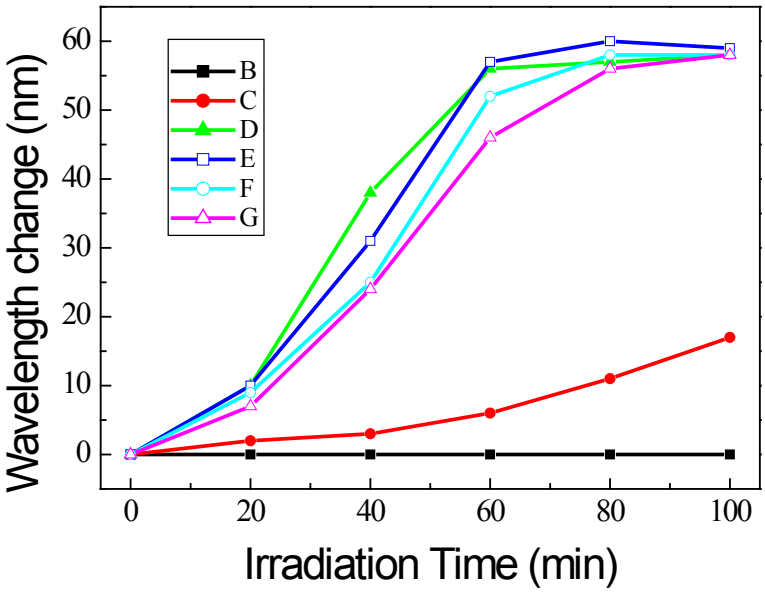

Figure 3.14 Wavelength shifts of the absorbance maxima in photocatalytic degradation of RhB with no photocatalyst (**B**, solid square ■), P25 (**C**, solid circle ●), AuP25PAA@P25(1) (**D**, solid triangle ▲), AuCu31PAA@P25(1) (**E**, empty square □), AuCu11PAA@P25(1) (**F**, empty circle ○), AuCu13PAA@P25(1) (**G**, empty triangle △); illumination, λ > 450 nm.

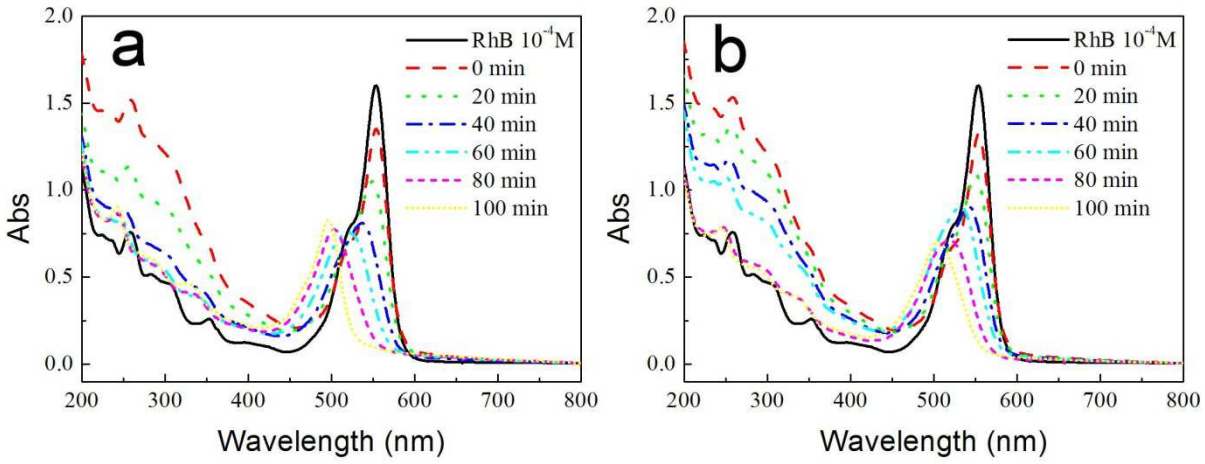

Figure 3.15 Evolution of UV-Vis spectra of RhB photodegraded in the presence of the sample **(a)** AuCu11PP@P25(1), and **(b)** AuCu13PP@P25(1) under visible light. Illumination > 450 nm, optical path: 2 mm.

We also studied the photocatalytic activity of the synthesized catalysts with polymers PAA and PVA. As shown in **Figure 3.15**, in the degradation of RhB under visible irradiation, the same trend as in the case of the presence of PAA only was observed: the absorbance maxima shifted to shorter wavelength. Furthermore, the wavelength change is larger for the sample AuCu11PP@P25(1) than for AuCu13PP@P25(1). This is consistent with the conclusion that a higher Au proportion results in a higher rate of N-de-ethylation of RhB.

3.2.6 Influence of wash-treatment on the photocatalytic activity

In order to remove the stabilizers PAA and PVA from the surface of supported metal nanoparticles on P25, wash-treatment with hot water, according to Lopez-Sanchez's method, with some modifications, was attempted.[84] Au-Cu/TiO_2 samples were treated with water under stirring at 80 °C for 150 minutes. The supernatant was slightly pink. The precipitate is dried in an oven at 60 °C and then finely ground. The color of the photocatalyst obtained after wash-treatment turned to a slightly lighter colour than before. The results of photocatalytic degradation of RhB under visible light in the presence of AuCu13PAA@P25(1) after treatment are illustrated in **Figure 3.16**. The absorbance maxima decreased and the wavelength of absorbance maxima shifted toward shorter wavelengths with illumination. Compared to AuCu13PAA@P25(1) without treatment, a decrease of the photocatalytic activity was observed as well as a shift in the absorbance maximum wavelength with

irradiation time(**Figure 3.16b**). It can be concluded that washing caused partial desorption of the Au-Cu bimetallic NPs leading to a decrease in the photocatalytic activity.

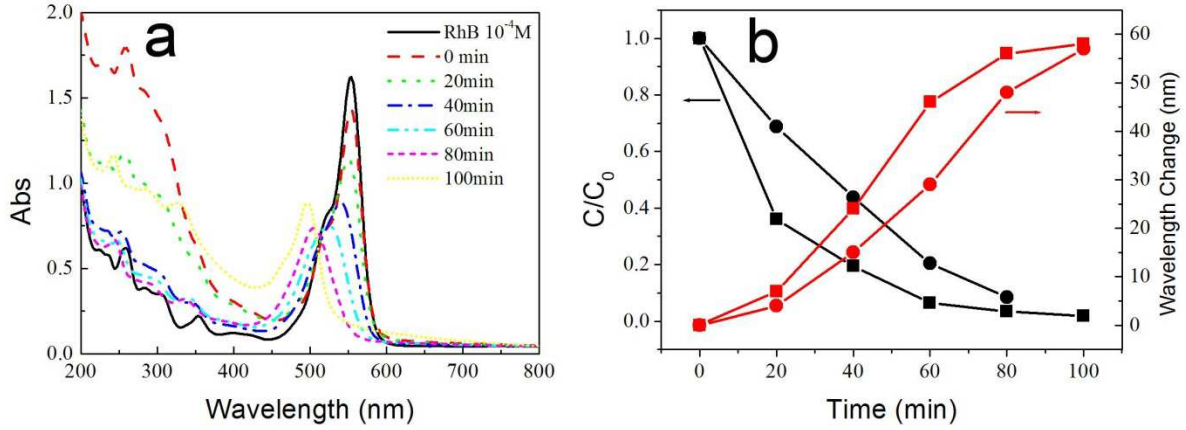

Figure 3.16 (a) Evolution of the UV-Vis spectra of RhB photodegraded in the presence of the sample AuCu13PAA@P25(1) after washing with water, **(b)** time courses of RhB relative concentration and wavelength changes of absorbance maxima in photocatalytic degradation of RhB in the presence of the sample AuCu13PAA@P25(1) (**square**), and after wash-treatment with water (**circle**).

3.2.7 Decomposition of the stabilizing polymers followed by TGA

The colors of the thermal-treated samples changed to grey- or dark-purple. The color changed more obviously with the increase of Cu proportion in the Au-Cu bimetallic NPs. For AuCu31PAA@P25(0.5), the color slightly changed to light purple, while the color turned to grey for the AuCu13PAA@P25(1).

DRS-TGA was used to investigate the polymer decomposition as a function of temperature in order to optimize the calcination temperature. The DSC-TGA curves of modified photocatalysts are illustrated in **Figure 3.17**. When the temperature was below 250 °C, the slow decrease of weight was attributed to the removal of the adsorbed surface water molecules, accounting for 2% (**Figure 3.17a**,**b**). The major weight loss of 3.5% and 7% in the temperature range from 220 °C to 350 °C was assigned to the decomposition of PAA in AuCu31PAA@P25(0.5) and AuCu11PAA@P25(1), respectively. In the case of AuCu13PAA@P25(1), another sharp weight loss at 200 °C appeared, probably attributed to the abundant residual chloride ions owing to higher $CuCl_2$ ratio.

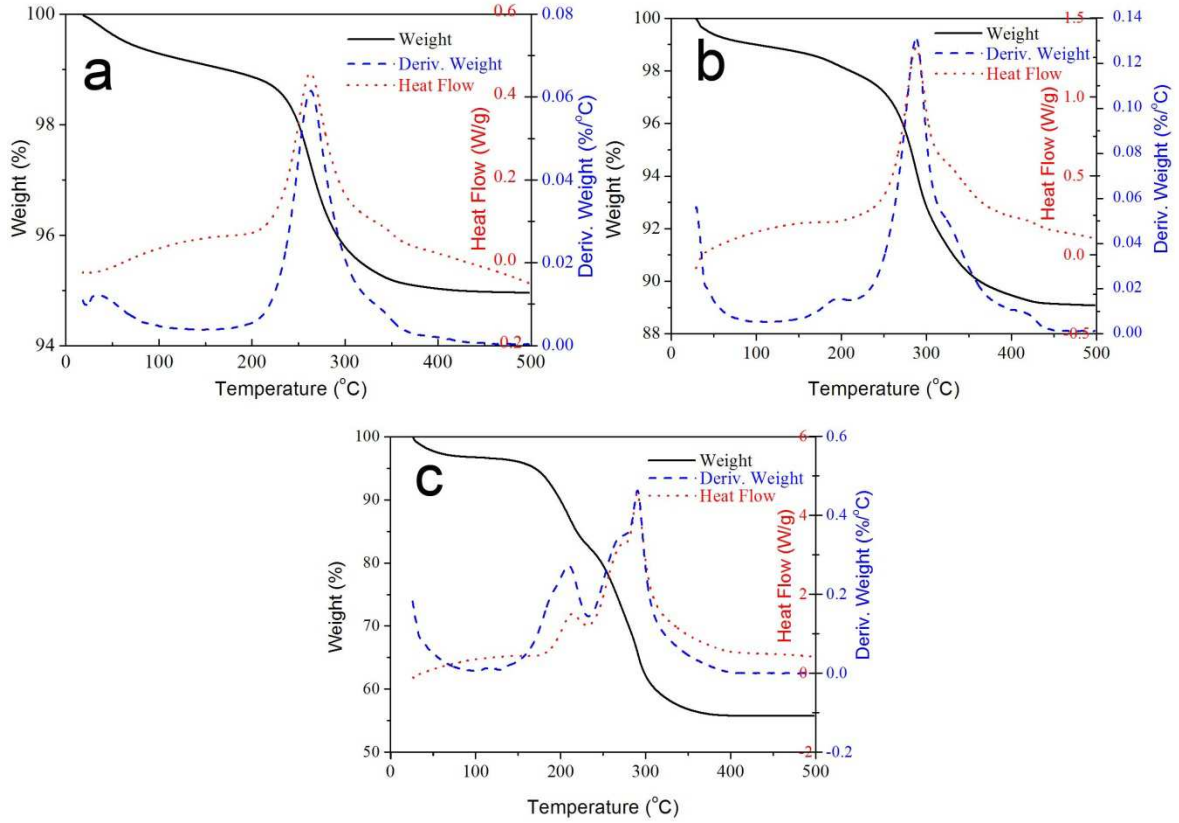

Figure 3.17 DRS-TGA of the sample **(a)** AuCu31PAA@P25(0.5), **(b)** AuCu11PAA@P25(1), and **(c)** AuCu13PAA@P25(1).

The photocatalytic activity of the thermal-treated samples was investigated for RhB degradation. Evolutions of UV-vis spectra of RhB in the photocatalytic reaction with the samples of AuCu31PAA@P25(0.5), AuCu11PAA@P25(1), and AuCu13PAA@P25(1) after thermal treatment are shown in **Figure 3.18**. It is worth noting that the absorbance maxima have no obvious shift in the presence of the three thermal treated samples. The sample AuCu31PAA@P25(0.5) has the highest activity. After 100 minutes of illumination under visible light, 55% of RhB was degraded. However, the degradation rate is still lower than that for the pristine P25 reference (75%). In the case of AuCu13PAA@P25(1), nearly no degradation of RhB was observed, indicating a negative effect on the photocatalytic activity of Au-Cu modified TiO_2 induced by the thermal treatment.

From the analysis above, we knew that calcination under air is harmful to the photoactivity of modified TiO_2. For this reason, reducing under Hydrogen at 500 °C was performed after the calcination in the later experiments.

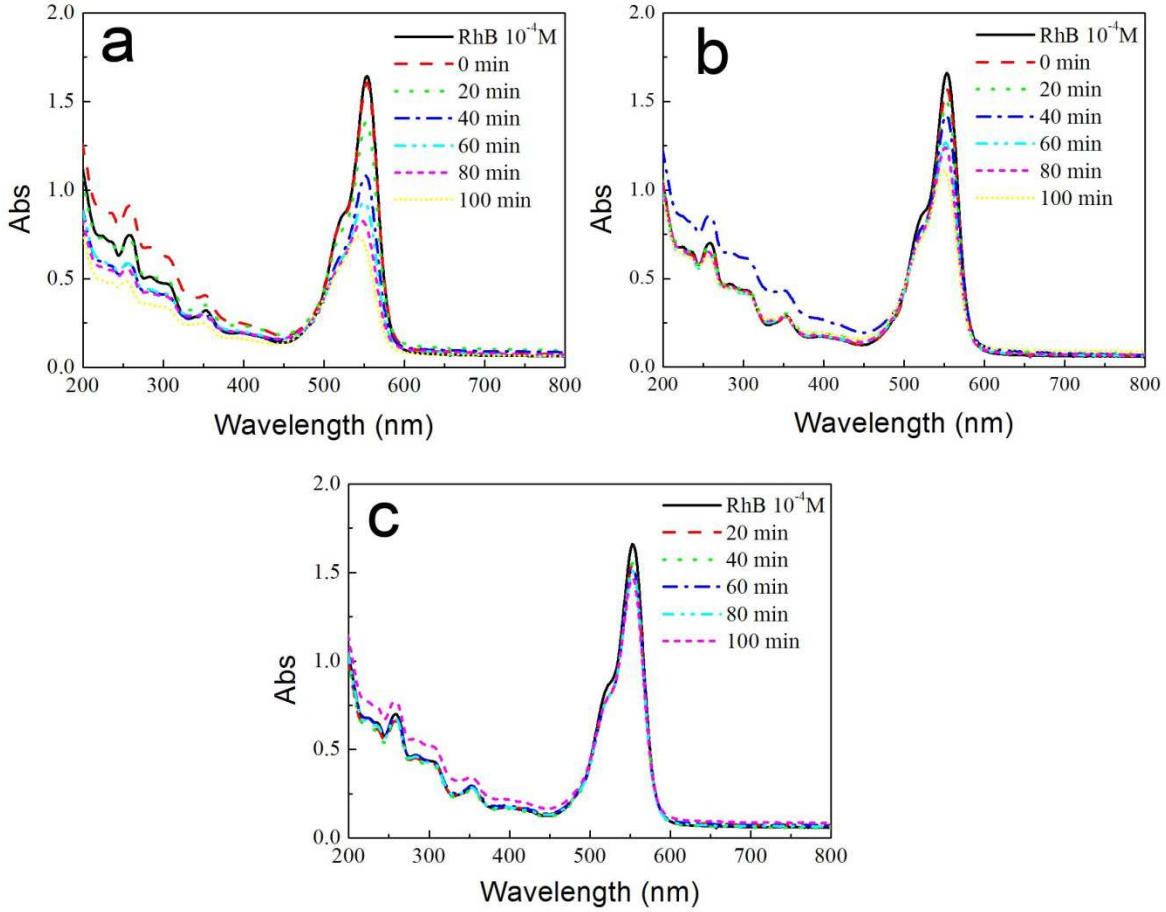

Figure 3.18 Evolution of UV-Vis spectra of RhB photodegraded in the presence of the sample **(a)** AuCu31P25PAA(0.5) after calcination, **(b)** AuCu11P25PAA(1) after calcination, and **(c)** AuCu13P25PAA(1) after calcination. Illumination > 450 nm. Optical path: 2 mm.

3.2.8 Conclusions of this section

Au-Cu bimetallic NPs were synthesized by radiolysis and deposited on the surface of P25 via a colloid-deposition route. The polymers PAA and PVA were used, separately or together, as stabilizers. The obtained Au-Cu NPs in the presence of polymer PAA are smaller and more homogeneous in size compared with the NPs stabilized by PVA. The mean nanoparticle size decreased obviously when Au is associated with copper (3.6 nm for AuCu13PAA NPs). The presence of PVA improved the deposition efficiency of Au-Cu bimetallic NPs on P25. The synthesized photocatalysts exhibit reduced photoactivities compared to the pristine P25 under UV illumination. Among the synthesized catalysts, the optimal one is that with a higher copper proportion (Au/Cu 1:3) or suitable metal loading of 0.5%. Under visible illumination, the modified photocatalysts in the presence of PAA have

great capability in N-de-ethylation of RhB. The increase of Cu ratio in Au-Cu bimetallic NPs led to a higher activity of RhB degradation. Besides, the higher Au proportion results in a higher rate of N-de-ethylation of RhB, due to the lower pH value of the suspension.

3.3 Modification of TiO_2 with Au-Cu bimetallic NPs by radiolytic colloid-deposition route

3.3.1 Characterization of the Photocatalysts

Details of the synthesized photocatalysts are summarized in **Table 3.4**. The resulting modified monometallic catalyst was 0.5 wt% Au on P25, referred as Au/P25. The bimetallic Au-Cu modified catalysts were 0.45 wt% Au and 0.05 wt% Cu on P25 (Au/Cu molar ratio = 3:1), referred as AuCu31/P25. In the same manner, the supported bimetallic photocatalysts of 0.38 wt% Au and 0.12 wt% Cu on P25, 0.25 wt% Au and 0.25 wt% Cu on P25 were named as AuCu11/P25 and AuCu13/P25, respectively.

Table 3.4 List of modified P25 prepared by radiolysis followed by deposition onto the P25 substrate.

Photocatalyst	Molar ratio of Au/Cu	Content of metal precursor/P25 (wt%)		[a]TEM size (nm)	[b]$\tau_{1/2}$ (ns)
		Au	Cu		
Au/P25	1:0	0.5	0	5.8	22.7
AuCu31/P25	3:1	0.45	0.05	-	-
AuCu11/P25	1:1	0.38	0.12	4.4	55.4
AuCu13/P25	1:3	0.25	0.25	3.8	36.3

[a] TEM size: this was measured manually with a program (Nano measurement);

[b] $\tau_{1/2}$: is the time to obtain intensity $I_{max}/2$ of the TRMC signal, for pure P25 $\tau_{1/2}$ is 88.9 ns.

3.3.1.1 TEM Characterization

The morphologies of the surface modified P25 were observed using TEM technique (**Figure 3.19**). The TEM observations show small nanoparticles distributed on P25. The mean size of Au/P25 was 5.8 nm. When Au was associated to Cu, the average size decreased. For the sample AuCu11/P25 and AuCu13/P25, the mean size decreased to 4.4 nm and 3.8 nm respectively. Besides the decrease of particle size, the distributions also became more

homogeneous when Cu was associated to Au. In the case of Au monometallic modified P25, nanoparticles up to 13 nm were found. However, there was no particles larger than 6 nm as it can be seen from the TEM images of the sample AuCu13/P25. This fact confirms the result that we found in the radiolytic preparation of Au-Cu colloids; the size decreases and distribution is more narrow with the increase of Cu proportion in bimetallic Au-Cu NPs.

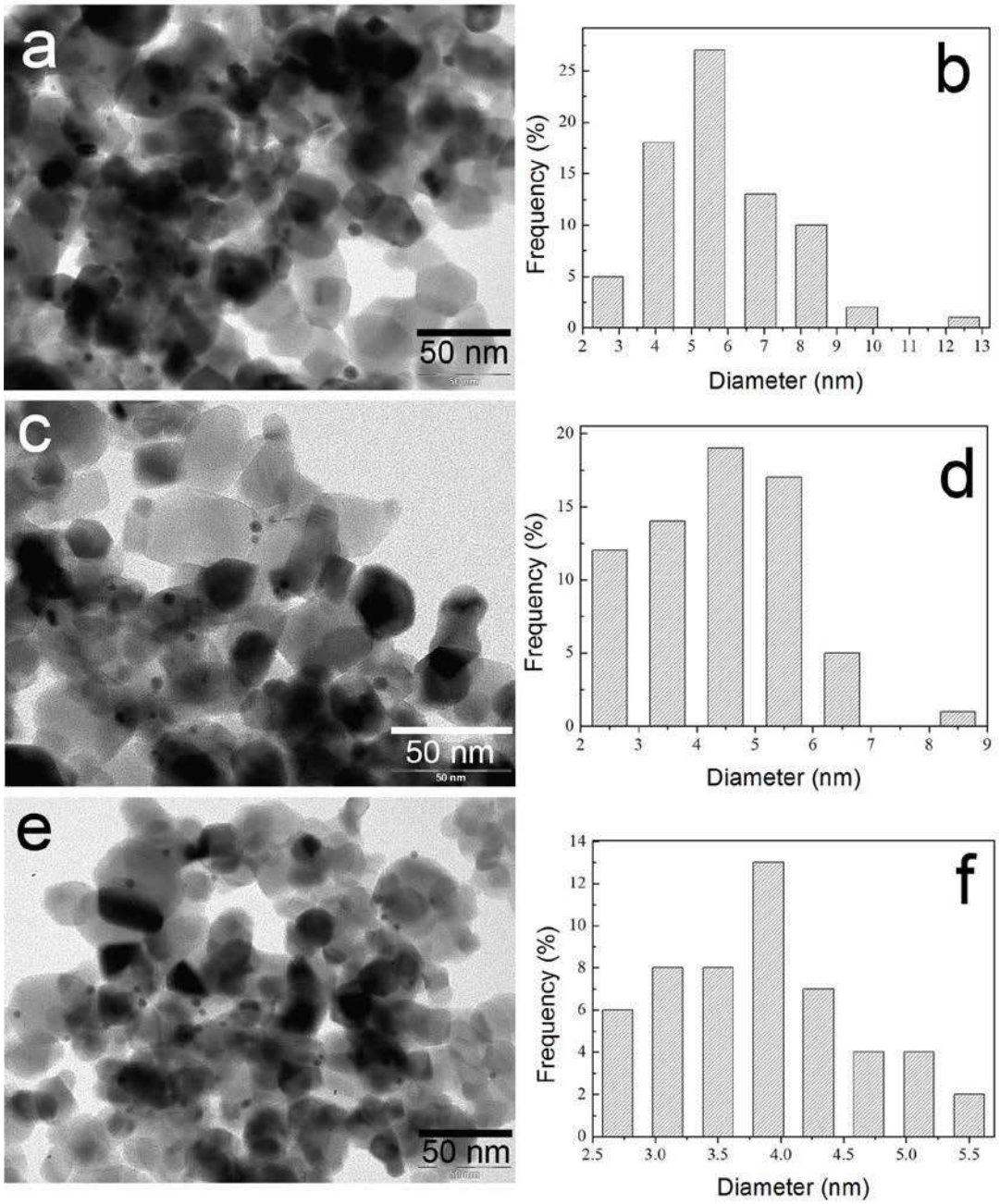

Figure 3.19 TEM images of metallic nanoparticle modified P25 and the corresponding size distributions of the supported metallic NPs **(a, b)** Au/P25, **(c, d)** AuCu11/P25, and **(e, f)** AuCu13/P25.

3.3.1.2 UV-vis Spectra of the Supernatants

The synthesized PAA stabilized Au- or Au-Cu colloids were characterized using UV-vis spectrophotometry. The results are shown in **Figure 3.20** (trace **a-c**). The absorption peaks at ~525 nm reveal the formation of Au- or Au-Cu nanoparticles. In addition, the broadening of the absorption bands for AuCu31PAA and AuCu13PAA toward longer wavelength region was observed, indicating the formation of bimetallic Au-Cu nanoparticles. The bimetallic nature of the nanoparticles cannot fully be determined by UV-vis spectra alone. Though it cannot be definitively ascertained whether the nanoparticles are alloys or core-shells, it strongly suggests that the Au-Cu nanoparticles are bimetallic in nature.

After deposition of the PAA/PVA stabilized Au-Cu colloids on P25, the supernatants were monitored by UV-vis spectra (**Figure 3.20** trace **d-f**). There was no absorption in visible region, demonstrating that all the NPs were deposited on the support. The absorbance in the UV region was attributed to the stabilizers, PAA or PVA which are absorbing strongly in the UV region (**Figure 3.20 g**, **h**).

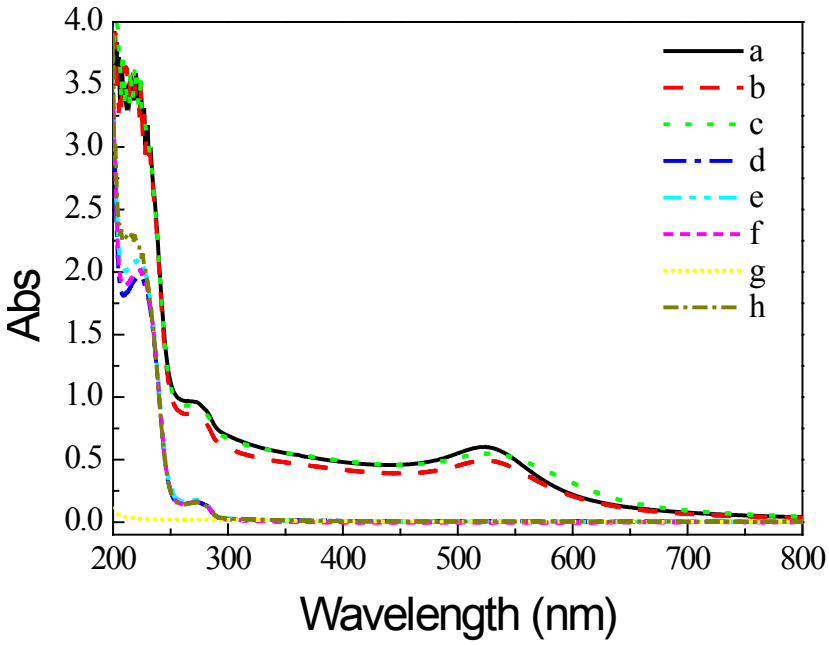

Figure 3.20 UV-vis spectra of the colloid **(a)** AuPAA, **(b)** AuCu13PAA, **(c)** AuCu31PAA, the supernatant of **(d)** Au/P25, **(e)** AuCu11/P25, **(f)** AuCu31/P25 and the solution of **(g)** PVA (0.1 M), and **(h)** PAA and PVA (0.1 M of each).

Fringes with uniform thickness at the edges of modified P25 particles without thermal treatment and hydrogen reduction can be seen in **Figure 3.21**. Although the Au-Cu modified P25 samples were washed several times with water to remove the stabilizing polymers, the metal nanoparticles or substrate P25 were still covered by the polymer molecules. The polymers on the surface are unfavourable to the photocatalytic activity because of the decrease of contact between photocatalyst surface and model dyes. It is necessary to remove these polymers. Hence calcination, following by H_2 reduction, was attempted later.

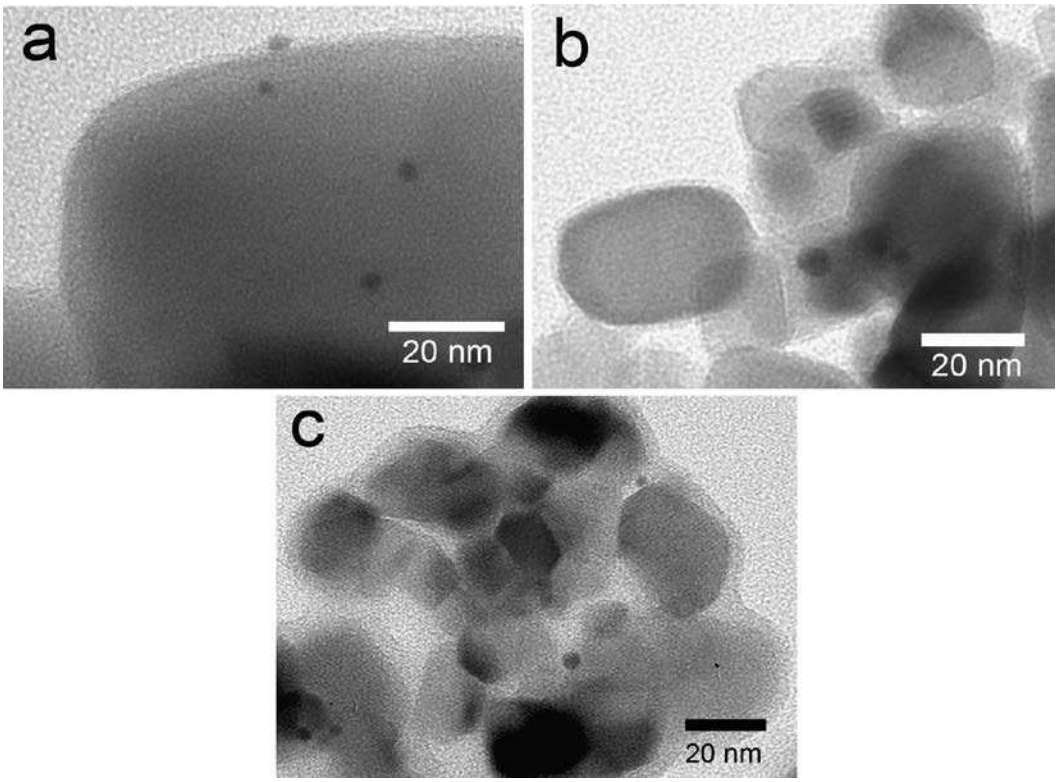

Figure 3.21 TEM images of **(a)** Au/P25, **(b)** AuCu11/P25, and **(c)** AuCu13/P25 at a high magnification, all the samples are without thermal treatment and H_2 reduction.

3.3.1.3 DRS Analysis

The optical properties were investigated using diffuse reflectance spectroscopy. **Figure 3.22** shows the spectra of pristine and modified P25. It is worth noting that the modified samples exhibit a light shift in the band-gap transition to larger wavelengths. For pristine P25, the absorption edge is 398 nm, and for the modified P25 it increases to 420 nm. This effect was previously observed in the case of Ag- and Pt- modified TiO_2. This effect can attributed to a stronger stabilization of the conduction band of TiO_2 by the conduction band of the Au-

or Au-Cu particles compared to the stabilization of the valence band. The absorbance in the visible region is always higher for the modified TiO_2 than pure P25. The absorbance maxima of the modified photocatalysts Au/P25, AuCu31/P25 and AuCu13/P25 are at 561 nm, 573nm and 580 nm, respectively. These maxima explain the pink-violet color of the modified TiO_2 samples. The sample Au/P25 shows a deep purple color while AuCu13/P25 is pink-violet. The absorption peak of Au/P25 shows a shift toward longer wavelength compared to that of the stabilized Au colloid (at 525 nm), indeed the plasmon band is sensitive to the environment and the substrate. The plasmon bands in case of Au/TiO_2 and $Au\text{-}Cu/TiO_2$ are blue-shifted because of the coupling between the metal nanoparticles and TiO_2 support having a high reflective index. It should also be pointed out that the absorption peak exhibits a shift towards longer wavelength with the increase of Cu proportion in the bimetallic nanoparticles. Au and Cu nanoparticles are known to exhibit a plasmon band with a maximum at 520 nm and 570 nm, respectively. Hence, it can be assumed that the shift toward longer wavelength is caused by the increase of Cu.

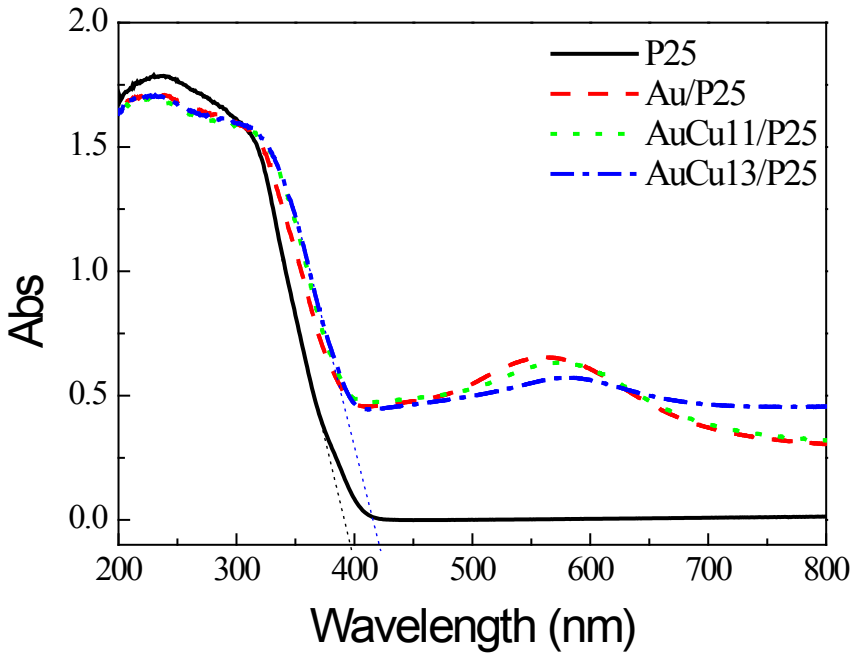

Figure 3.22 DRS spectra of pure P25 and the modified samples with thermal treatment.

The UV-vis spectra of Au- or Au-Cu modified P25 without calcination and H_2 reduction are also shown in **Figure 3.23**. The similar shifts in the band-gap transition toward longer

wavelengths were observed. However, a significant difference is that the absorption maxima for all the modified samples are at 535 nm. Note that the absorbance in the range from 550 nm to 800 nm for the sample AuCu31/P25 is higher than that for Au/P25, indicating the existence of Cu in a form of atoms or clusters. It can be ascertained that the Au-Cu nanoparticles are not alloys at this step, because the increase of the amount of Cu did not result in a shift of the plasmon band maximum of Au-Cu. The Au-Cu bimetallic structure might be in a form of Au-Cu core-shell. After the modified samples were calcinated at 500 °C, the Au-Cu bimetallic nanoparticles restructured and formed an alloyed structure. In the case of alloyed Au-Cu bimetallic structure, the proportion of Cu had a great influence on the wavelength of plasmon resonance maximum (**Figure 3.22**).

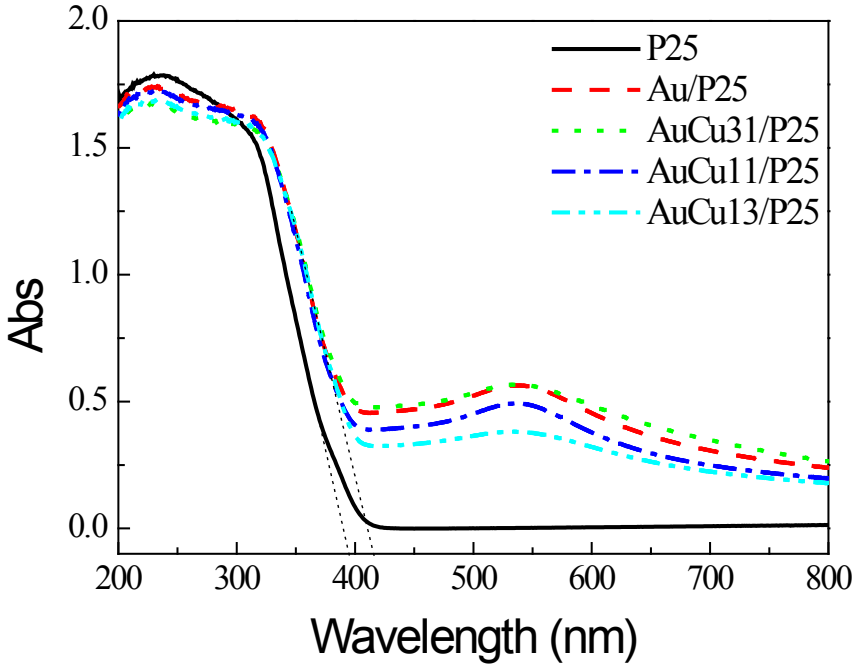

Figure 3.23 DRS spectra of pristine and modified P25 without thermal treatment.

3.3.1.4 BET Analysis

Nitrogen sorption isotherms were generated to investigate the porous structure and the Brunauer-Emmett-Teller (BET) surface areas of the modified photocatalysts. The data are shown in **Figure 3.24**. The sample AuCu13/P25 exhibits a typical-IV isotherm pattern and it shows steep hysteresis loop at high relative pressure (**Figure 3.24a**).[85-88] The hysteresis

loop as a result of capillary condensation of N_2 inside the pores is ascribed to the existence of mesopores.[87-88] The BET surface area was obtained as 41.5 m^2 g^{-1}. Compared to the pristine P25 (51.4 m^2 g^{-1}), a considerable decrease in the BET surface area was found, attributed to the calcination at 500 °C.[85, 88] The pore size distribution for the modified P25 was obtained by the Barrett-Joyner-Halenda (BJH) method [89] and is presented in **Figure 3.24b**. The sample AuCu13/P25 shows bimodal pore size distributions with a maximum pore diameter of 2.5 nm and 29 nm respectively, indicating the presence of intra-aggregated and inter-aggregated pores (represented by the hysteresis loop in the higher P/P_0 range). It was reported that Degussa P25 titania powders prepared by flame hydrolysis of $TiCl_4$ exhibited a monomodal pore-size distribution with a maximum pore diameter at 2.3 nm. The significant difference in pore-size distribution for the modified sample is probably due to the non-uniform drying stresses when the modified P25 slurry was drying.[85, 90] It is noteworthy that the pore volume of intra-aggregated pore (at 3.1 nm, **Figure 3.24b**) is remarkably smaller compared to that of photocatalysts prepared by THPC or DPU method (**Figure 3.57b** and **Figure 3.40b**). The possible cause is that the high-concentrated stabilizing polymer PAA and PVA induced a uniform particle packing on the account of electrostatic repulsion.[85]

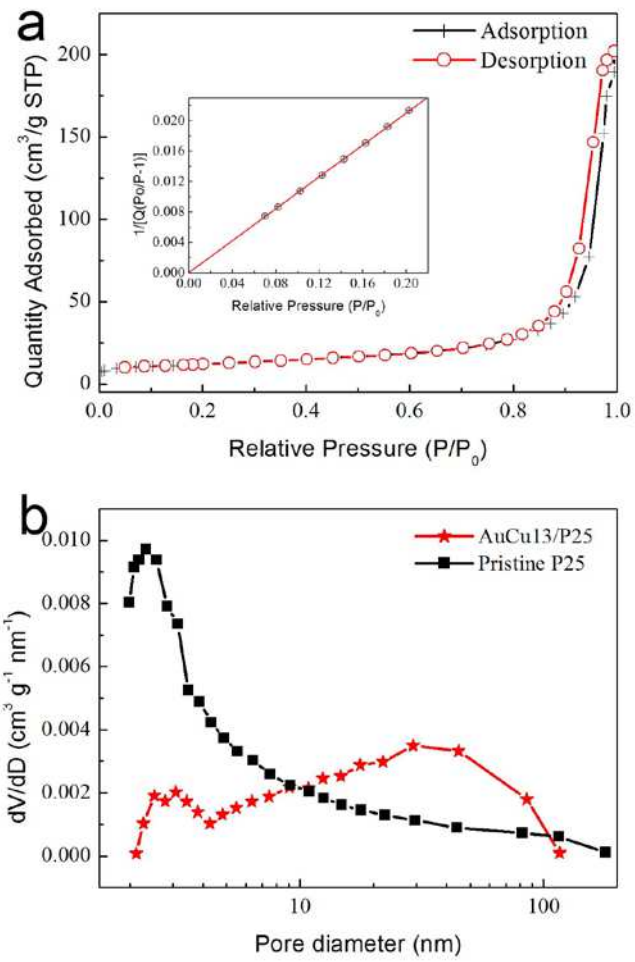

Figure 3.24 (a) N_2 adsorption-desorption isotherms for the sample AuCu13/P25. Inset: BET surface area plot, **(b)** the corresponding pore size distribution.

3.3.2 Photocatalytic Tests

The photocatalytic activities of the prepared samples were investigated for RhB and Phenol degradations under UV and visible light.

3.3.2.1 Photocatalytic Activity under UV Irradiation

For the RhB degradation under UV illumination, Evonik P25 is highly photoactive, which is used as the reference. After 10 minutes illumination in the presence of P25, 99% of RhB was degraded. The results of photocatalytic degradation with the modified P25 are shown in **Figure 3.25**. RhB concentration decreased slower for the sample Au/P25 than for pure P25. While for AuCu11/P25 and AuCu13/P25, RhB decomposition is slightly faster. These photocatalytic reactions can be approximately regarded as first-order kinetics. Rate

constant (k) was used to evaluate the photocatalytic activities. It can be calculated according to the following formula:

$$-\frac{dC_t}{dt} = kC_t \tag{3.7}$$

$$kt = -\ln(C_t/C_0) = -\ln(A_t/A_0) \tag{3.8}$$

where C_t and C_0 are the concentration at time t and the initial concentration of the model pollutant, respectively. C_t/C_0 can be directly deduced based on the relative absorbance A_t/A_0. Consequently, k can be obtained by linear fitting of $\mathrm{Ln}(A_t/A_0)$ as a function of irradiation time t. Rate constants in the photodegradation of RhB under UV illumination are 5.7×10^{-3}, 9.4×10^{-3}, and 9.2×10^{-3} s^{-1} for the modified Au/P25, AuCu11/P25, and AuCu13/P25 respectively (**Figure 3.26**). Compared to the rate constant of pure P25 (8.7×10^{-3} s^{-1}), deposition of Au NPs on P25 has a negative effect on the photodegradation of RhB under UV light. However, the photocatalytic activities were enhanced by over half with the association of Au to Cu.

The photocatalytic activities under UV of the modified P25 were also evaluated with phenol as the model pollutant. Similar results as those obtained for RhB were observed (**Figure 3.25**). Au NPs supported P25 ($k = 4.66 \times 10^{-3}$ s^{-1}) resulted in a decrease of the photocatalytic activity compared to pure P25 ($k = 6.72 \times 10^{-3}$ s^{-1}). AuCu13/P25 exhibited the highest activity among the modified P25 catalysts, even higher than pristine P25.

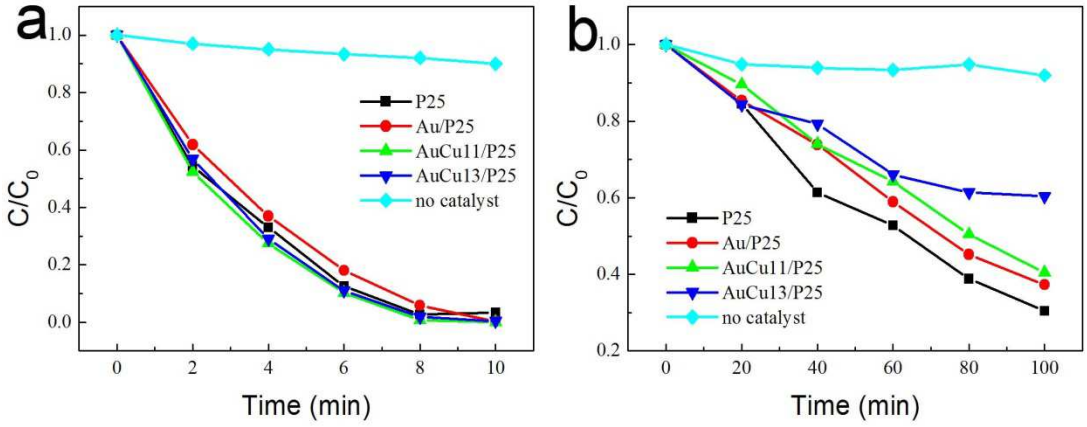

Figure 3.25 The time runs of relative RhB concentration in photodegradation in the presence of pristine and modified P25 under **(a)** UV, and **(b)** visible illumination.

3.3.2.1 Photocatalytic Activity under Visible Irradiation

In the case of photodegradation of RhB under visible illumination, 70% of RhB was degraded after 100 minutes illumination in the presence of pure P25. Pristine P25 barely exhibits any photocatalytic activity under visible light ($\lambda > 450$ nm) because the illumination energy is below the band-gap. Such an efficient degradation can be attributed to the photo-sensitivity of RhB, namely the injection of excited electrons from RhB molecules to the conduction band of TiO_2, consequently resulting in oxidation of RhB molecules. The results of visible light driven degradation of RhB are shown in **Figure 3.25**. All of the modified P25 resulted in slower degradation of RhB compared to bare P25. Furthermore, the rate for RhB photodegradation decreased with the rising copper proportion. AuCu13/P25 (v = 0.40 μmol L^{-3} min^{-1}) has the lowest photocatalytic activity, decreasing by nearly half compared with pure P25 (0.70 μmol L^{-3} min^{-1}).

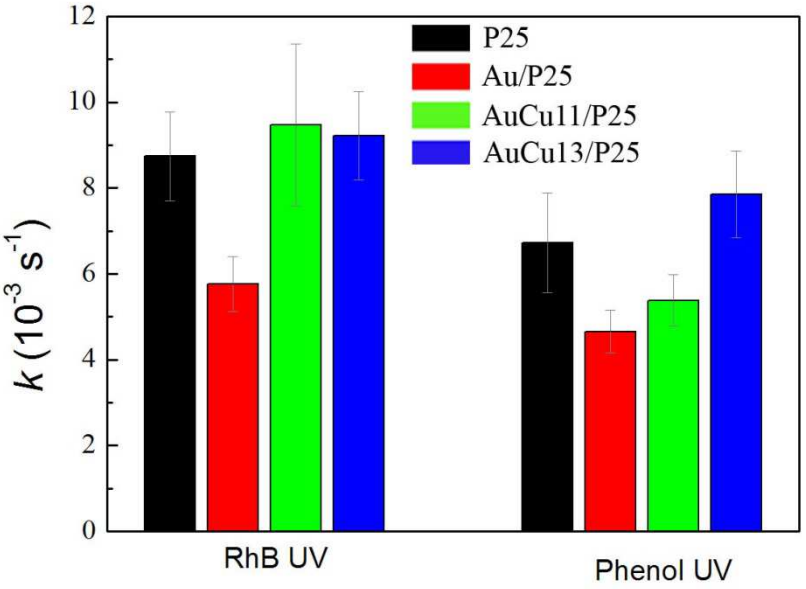

Figure 3.26 Histogram of rate constants of the first-order kinetic of RhB or phenol photodegradation in the presence of pristine and modified P25 under UV light.

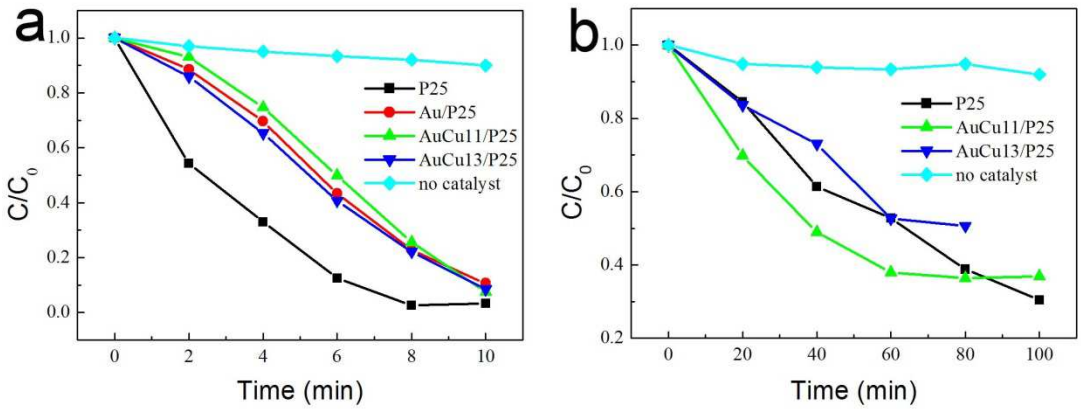

Figure 3.27 The time runs of relative RhB concentration in photodegradation in the presence of pristine and modified P25 under **(a)** UV, and **(b)** visible illumination without thermal treatment.

On the basis of analysis above, a mechanism is proposed: Au-Cu Alloyed NPs act as electron scavengers decreasing the recombination of excited electrons and holes in the case of UV illumination. Therefore more oxidative holes participate in the photocatalytic reactions, consequently improving the photocatalytic activity. Such Au-Cu NPs also scavenge electrons transferred from the excited photo-sensitive molecules to Ti_2O. The electrons, in this case, greatly contribute to the degradation of photo-sensitive dyes under visible light. The alloyed structure for Au-Cu bimetallic NPs is essential to efficiently scavenge electrons. By contrast, the Au-Cu modified P25 but without thermal treatment were tested for the photodegradation of RhB under UV and visible light. The results show that the non-thermal-treated photocatalysts exhibit very low activities under UV illumination and higher activities under visible light (**Figure 3.27**), compared to the corresponding results (**Figure 3.25**) for the thermal-treated samples. The photoactivities of polymer-covered Au-Cu/P25 are higher than those of the thermal-treated ones, even than those of pure P25 (**Figure 3.27b**), indicating the polymers are not the handicap. To briefly summarize, the Au-Cu alloyed NPs are efficient electron scavenger, resulting in a photoactive increase for the modified P25 under UV light, while a decrease of the photocatalytic activity is obtained under visible illumination.

3.3.3 TRMC Signals

Time resolved microwave conductivity (TRMC) experiments were conducted to study the electronic properties of the modified P25. The TRMC measurements realized under UV laser irradiation show TRMC signals presented in **Figure 3.29**. The TRMC signal has two principal parameters: the maximum value (I_{max}) and the decay $I(t)$. Halftime life $\tau_{1/2}$ is the time to obtain intensity $I_{max}/2$ of the signal. The surface modification with Au- or Au-Cu NPs show a strong influence on the charge-carrier decay of P25. The overall decays of the signal for all the modified P25 are accelerated (**Figure 3.28**). $\tau_{1/2}$ of pure P25, Au/P25, AuCu11/P25, and AuCu13/P25 are 88.9 ns, 22.7 ns, 55.4, and 36.3 ns, respectively (**Table 3.4**). This influence on the decay can be related to the activity in the case of RhB or Phenol degradation under UV light.

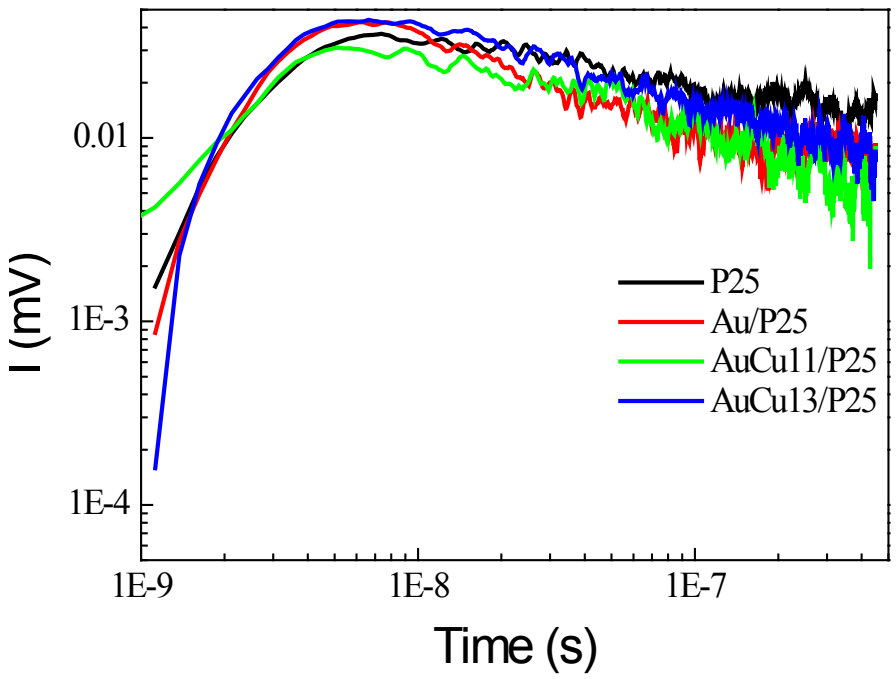

Figure 3.28 TRMC signals of pristine and the modified P25 Au/P25, AuCu11/P25 and AuCu13/P25 after thermal treatment.

In the case of TiO_2, the TRMC signal can be attributed to the electrons because their mobility is much larger than that of the positive holes.[40, 91] The decrease of the TRMC signal is then probably due to efficient electron scavenging by the nanoparticles deposited on TiO_2. It implies a decrease of the charge-carrier recombination that is beneficial to the photoactivity. Such acceleration has also been reported for the Ag modified TiO_2.[76]

However, it is different from our previous observations made with Pt- and Pd- modified TiO_2,[77, 92] where a slowdown of the overall decay was observed. Indeed, contrary to metals such as Pt and Pd which provide an ohmic contact, metals such as Ag, Au and Cu exhibit capacitive properties.[93] In the modified TiO_2, electrons migrate from the semiconductor to Cu metal owing to the higher work function that Cu displays.[94] Formation of Schottky barrier at the metal-semiconductor interface served as an efficient electron trap in preventing electron-hole recombination.[75]

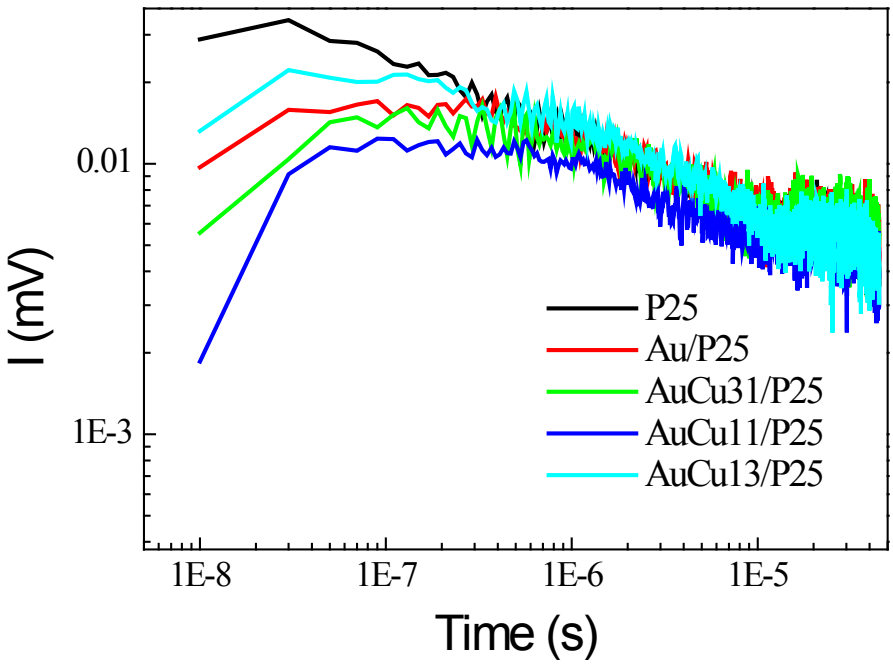

Figure 3.29 TRMC signals of pristine P25 and the modified P25 Au/P25, AuCu31/P25, AuCu11/P25 and AuCu13/P25, without thermal treatment.

Furthermore, the modification with Au-Cu NPs increases I_{max}. In general, a high value of I_{max} can be considered to be good crystalline structure of the semiconductor. The modified P25 samples have better crystallization because of their calcination at 500 °C. By contrast, in the case of the samples without thermal treatment, the TRMC signals are highly lower for the prepared photocatalysts than for the pure P25 (**Figure 3.29**). Besides that, a slowdown of the overall decay was observed, corresponding to the decrease of photoactivity with UV light (**Figure 3.27a**).

At 532 nm, there is no TRMC signal with all the samples. Under excitation in the visible

region there is no direct light absorption of pure TiO_2 but the metal NPs deposited on modified titania (Au and Au-Cu) are absorbing light through their plasmon resonance. Since no TRMC signal is observed at this excitation wavelength, one can conclude that no electron transfer from the NPs to the conduction band of TiO_2. This is consistent with the photocatalytic results under visible light. As it is discussed above, the photoactivity obviously decreased under visible illumination owing to no excess electrons excited from metal NPs to P25, furthermore, the excited electrons from photosensitive dyes were probably trapped by metal NPs.

3.3.4 Conclusion of this section

Au-Cu bimetallic NPs were synthesized by radiolysis in the presence of the stabilizing polymer PAA, and deposited on P25 in the presence PAA and PVA. The affixing of Cu to Au NPs resulted in a smaller nanoparticle size; especially the smallest NPs are formed at a ratio of Au/Cu 1:3 (mean size is 3.8 nm). The Au-Cu NPs modified P25 were characterized using TEM, DRS, and TRMC. The Au-Cu bimetallic NPs have an alloyed structure. The TRMC signal showed that the Au-Cu alloyed NPs supported on P25 are efficient in scavenging electrons, contributing to the enhancement of the photoactivity under UV illumination. The bimetallic NPs modified P25 exhibit better photoactivity than TiO_2 modified with monometallic Au NPs under UV light. The modification with Au-Cu NPs resulted in the decrease of the photocatalytic activity under visible illumination.

3.4 Modification of TiO_2 with Au-Cu bimetallic nanoparticles by radiolysis, deposition-precipitation route with Urea

The resulting modified monometallic catalyst was 0.5 wt% Au on P25, referred as Au/P25DPU, where DPU refers to deposition-precipitation method with urea. Correspondingly, AuCu11/P25DPU represents the sample P25 modified with Au-Cu NPs with a molar ratio of 1:1. The total nominal metal content was kept at 0.5 wt%. The compositions of the modified P25 by DPU are listed in details in **Table 3.5**.

Table 3.5 The List of the Prepared Au, Cu, and Au-Cu Modified P25 by Deposition Precipitation with Urea.

Photocatalyst	Molar Ratio of Au/Cu	Content of metal precursor/P25 (wt%)		Color	mean size (nm) (from TEM pictures)
		Au	Cu		
Au/P25DPU	1:0	0.5	0	Violet	8.4
AuCu1:1/P25DPU	1:1	0.38	0.12	Light-violet	8.2
AuCu1:3/P25DPU	1:3	0.25	0.25	Grey-violet	6.4
Cu/P25DPU	0:1	0	0.5	Light-green	[a]N/A

[a] N/A: Cu nanoparticles are unable to be observed from the TEM images

3.4.1 Deposition of Au-Cu ions on P25

In order to evaluate the deposition efficiency of the Au-Cu ions with the DPU method, the supernatants of the mixture were monitored using UV-vis absorption spectrophotometer. Typically, the spectrum of AuCu1:1/P25DPU supernatant before irradiation (**Figure 3.30a**) shows no absorption peaks in both of UV and visible region except for the peak at 200 nm, which is attributed to urea in the solution. This illustrates that the $[AuCl_4]^-$ and Cu^{2+} are not present in the supernatant, namely they completely deposited on the surface of TiO_2. The spectrum of AuCu1:1/P25DPU after irradiation was almost the same as that before irradiation except for the small absorption peak at 262 nm. We assumed that this small peak was due to the instrinsic absorption of TiO_2 in the UV region. This was confirmed by UV-Vis absorption

spectra of the supernatant along with filtration cycling. The absorption peak at 262 nm obvioulsy decreased after the first filtration by a millipore filter whose pore size is about 0.45 μm. For the second filtration, the same filter was repeatly used. The decrease of the absorption peak at 262 nm was considerably smaller than the first time. This is reasonable because after filtration the number of larger TiO_2 NPs decreases. Nevertheless, the smaller TiO_2 NPs could not be filtrated (by the filter we used). The peak at 262 nm deceases in intensity with the increase of filtration times until reaching a plateau (see **Figure 3.34b-f**).

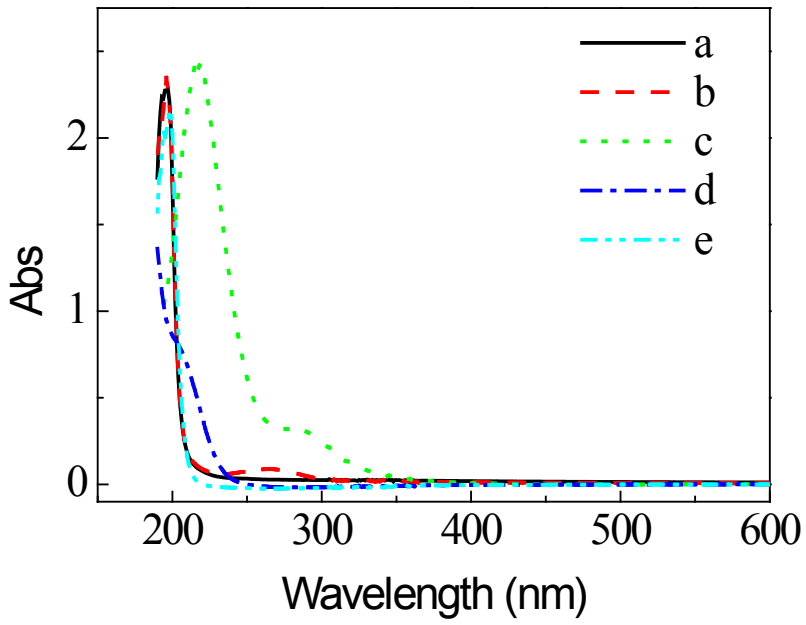

Figure 3.30 UV-Vis absorption spectra of **(a)** AuCu1:1/P25DPU supernatant before irradiation, **(b)** AuCu1:1/P25DPU supernatant after irradiation, **(c)** 1.25×10^{-4} M of Au solution, **(d)** 1.25×10^{-4} M of Cu solution, and **(e)** 2.5×10^{-2} M of urea solution after water bath at 90 °C for 2 hours. Optical path: 10 mm.

Considering TiO_2 is an amphoteric oxide (point of zero charge, PZC_{TiO2} ~ 6.3), a colloidal TiO_2 suspension just could be formed when the solution pH is less than 6. Before irradiation, the solution was nearly neutral. Gamma irradiation leads to pH decrease. In this case, TiO_2 particles can be easily separated by centrifugation. After gamma irradiation, when the pH value decreased below PZC_{TIO2}, it was impossible to remove the tinny particles by centrifugation. The supernatent spectrum indicates that all the Au and Cu ions were efficiently deposited on TiO_2. For the other prepared mono- and bimetallic modified photocatalysts,

similar results obtained are shown in **Figure 3.31**, **Figure 3.32** and **Figure 3.33**.

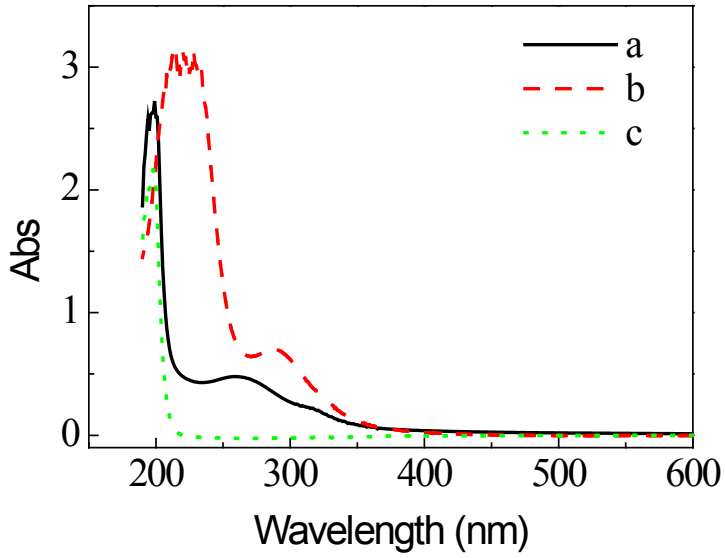

Figure 3.31 UV-Vis absorption spectra of **(a)** supernatant of Au/P25DPU after irradiation, **(b)** 2.5×10^{-4} M of Au solution, and **(c)** 2.5×10^{-2} M of urea solution after water bath at 90 °C for 2 hours. Optical path: 10 mm.

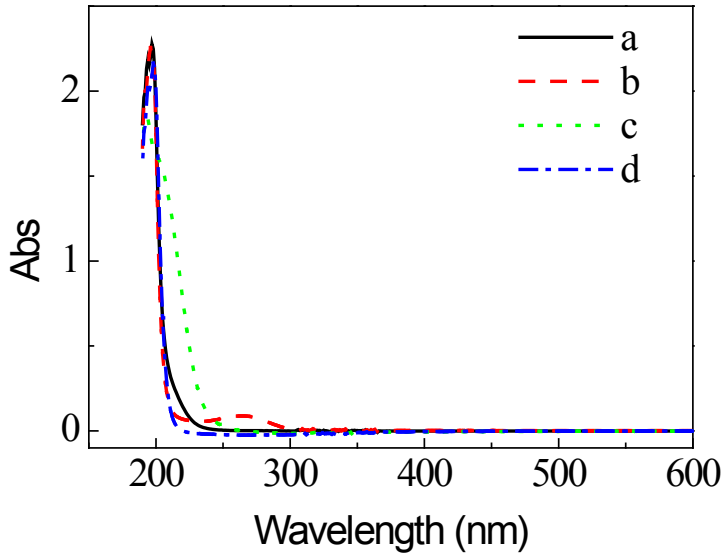

Figure 3.32 UV-Vis absorption spectra of **(a)** the supernatant of Cu/P25DPU before irradiation, **(b)** supernatant of Cu/P25DPU after irradiation, **(c)** 2.5×10^{-4} M Cu solution, and **(d)** 2.5×10^{-2} M of urea solution after water bath at 90 °C for 2 hours. Optical path: 10 mm.

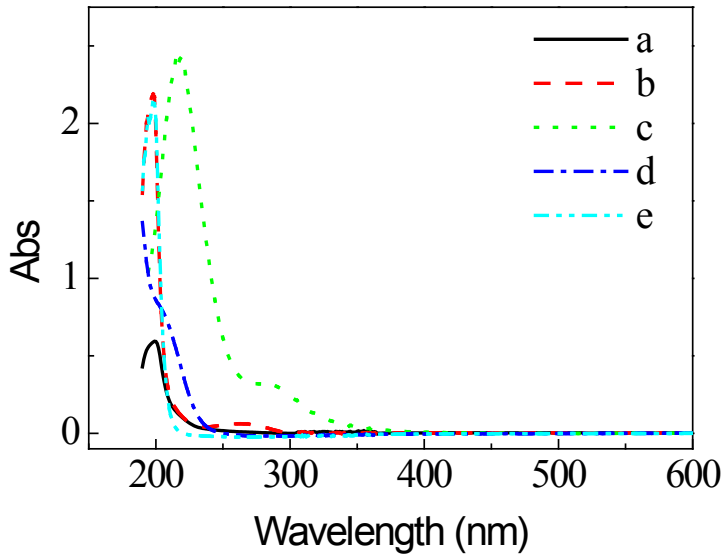

Figure 3.33 UV-Vis absorption spectra of **(a)** supernatant of AuCu13/P25DPU before irradiation, **(b)** supernatant of AuCu1:3/P25DPU after irradiation, **(c)** 1.25×10^{-4} M of Au solution, **(d)** 1.25×10^{-4} M of Cu solution, and **(e)** 2.5×10^{-2} M of urea solution after water bath at 90 °C for 2 hours. Optical path: 10 mm.

In order to confirm that the absorption peak at 262 nm is due to the intrinsic absorption of TiO_2, a filter with an average pore of 0.22 μm was used to remove the TiO_2 colloidal particles. The UV-Vis absorption spectra are shown in **Figure 3.34**. After the first filtration, the absorption peak at 262 nm decreased significantly. A series of filtration induced a decrease in the absorption at 262 nm. However, the peak remains with a low intensity, probably because the very small TiO_2 NPs cannot be removed by the filter (see **Figure 3.34c,d,e,f**).

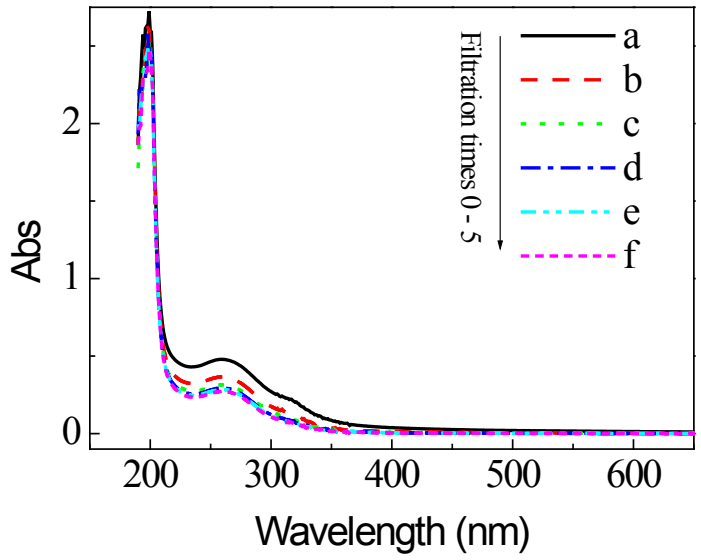

Figure 3.34 UV-Vis spectra of Au/P25DPU supernatants before and after several filtration cyclings. Optical path: 10 mm.

The first chemical step that occurrs during DPU preparation of Au on TiO_2 is the formation of a surface complex. The complex $AuCl_3(OH)^-$ sticks to the TiO_2 surface by the interaction with surface OH groups to form Ti-O-$AuCl_2$ (instead of an electrostatic interaction). In the case of preparation of Au modified P25 by irradiating a mixture of P25 and Au^{III}, the Au nanoparticleswere not well deposited on TiO_2. In the case of DPU, the adsorption of gold hydroxy chlorides on TiO_2 increased as the pH increased; increasing the pH value means more OH on the surface. The pH (~6.5) was slightly higher than PZC_{TiO2} after the end of the deposition. Thus, the surface of TiO_2 is negatively charged. Furthermore, the $AuCl(OH)_3^-$, $AuCl_2(OH)_2^-$ and $AuCl_3(OH)^-$ are also negative. At this moment, Cu^{2+} was introduced into the suspension, it can adsorb on the TiO_2 surface or can interact electrostatically with the Au complexes.

3.4.2 Characterization of the photocatalysts

3.4.2.1 TEM Characterization

The morphologies of the surface modified catalysts were characterized by TEM. As is shown in **Figure 3.35**(**a**,**c**,**e**), the darkest dots are the metal NPs (mono- Au or bi- Au-Cu NPs) distributed on the TiO_2 surfaces. One noteworthy thing is that the size of metal NPs decreased slightly with the increase of Cu proportion in the bimetallic NPs (for monometallic Au NPs on P25, the mean size is around 8.4 nm, for AuCu1:3/P25DPU, the mean size is around 6.4 nm). It has been reported that the size of Au-Cu alloyed NPs decreased with increasing the amount of Cu in the bimetallic NPs. In the case of monometallic Cu NPs on TiO_2, no particles could be observed on the TiO_2 support, probably because of the small contrast between copper and titianium (the images are not shown).

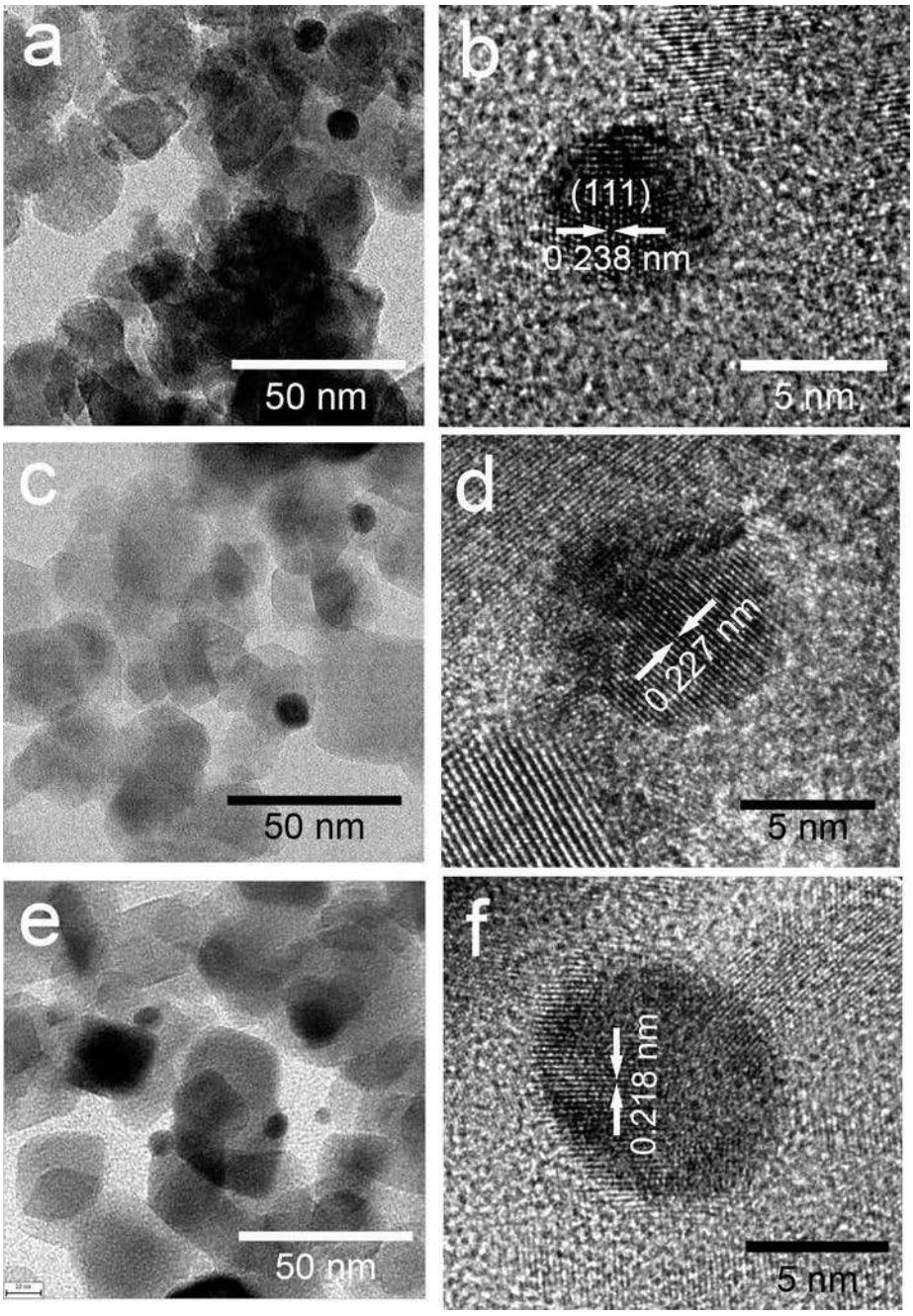

Figure 3.35 TEM and HR-TEM images of **(a,b)** Au/P25DPU, **(c,d)** AuCu1:1/P25DPU, **(e,f)** AuCu1:3/P25DPU. Dose rate: 170 Gy/min, dose in total: 20 kGy.

The supported monometallic Au and bimetallic Au-Cu NPs were observed using HRTEM. **Figure 3.35b** shows the HRTEM observation on the sample Au/P25DPU. The interplanar crystal spacing was measured as 0.238 nm from the lattice fringes. The value is coincident with the interplanar crystal spacing of Au(111) (standard of 0.235 nm from the JCPDS-PDF 04-0784). This result comfirms that the supported nanoparticles are Au. For the sample AuCu1:1/P25DPU (**Figure 3.35d**), the interplanar crystal spacing of the supported

nanoparticle decreased to 0.227 nm. According to the Vegard's law, we could get the theoretical value of 0.2215 nm for the (111) lattice planes of alloyed Au/Cu1:1 NPs. We can conclude that the Au-Cu bimetallic NPs have an alloyed structure with a rough ratio of 1:1. Furthermore, in the case of the sample AuCu1:3/P25DPU, the spacing value of the Au-Cu bimetallic nanoparticle on P25 is smaller (0.218 nm, **Figure 3.35f**), indicating a higher proportion of Cu in the bimetallic Au-Cu NPs. The HRTEM results probably evidenced the alloyed bimetallic nanostructure for the supported Au-Cu NPs on P25. However, it should also be pointed out that the Vegard's law is not necessarily followed by nanoalloys.

3.4.2.2 EDS Analysis

The composition of the prepared Au-Cu modified P25 was further characterized by STEM-Electron dispersive X-ray spectroscopy (EDS). EDS profile scans were carried out across the different Au-Cu NPs of the sample AuCu1:1/P25DPU. A representative nanoparticle is shown in **Figure 3.36**. The Au-Lα1 and Cu-Kα1 line scan signals show the intensity disperse apparently symmetrically along with the scanning regions of the NPs, implying that the Au and Cu atoms are approximately homogeneously dispersed. Both of the Au-Lα1 and Cu-Kα1 peaks in the center of the Au nanoparticle demonstrate that the Au and Cu atoms are apparently homogeneously dispersed. Therefore, the EDS profile scans evidenced the alloyed structure of bimetallic Au-Cu NPs. Considering the low diffraction capability of Cu, the Cu signal is much lower than that of Au. Indeed, the atomic ratio of Au to Cu was around 1:2 from the EDS spectrum, deviated from the nominal ratio of 1:1. Furthermore, EDS elemental mapping was also attempted to detect respective elements (**Figure 3.36**, bottom). AuLα1 and CuKα1 maps clearly identified the alloyed structure of Au-Cu bimetallic NPs.

HR-TEM images and EDS analyses show that the supported bimetallic Au-Cu NPs on P25 are nanoalloys.

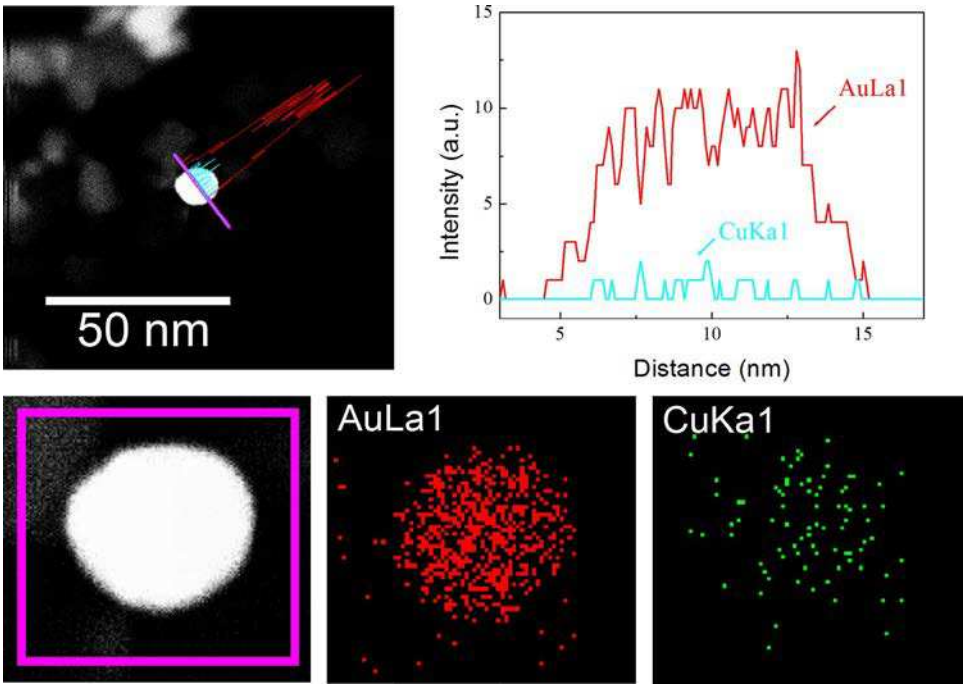

Figure 3.36 Top. HAADF-STEM image of AuCu1:1/P25DPU (left) and the corresponding Energy Dispersive X-ray Spectroscopy line scan across an Au/Cu1:1 nanoparticle (right. The The profile was taken along the purple line, the blue line corresponds to CuK and the red one to AuL signal). **Bottom**. Mapping EDS analysis performed at a metallic nanoparticle of AuCu1:1/P25DPU.

3.4.2.3 DRS Analysis

Diffuse reflectance spectroscopy (DRS) is a useful method to characterize the electronic status of optical materials. **Figure 3.37a** shows the UV-Vis spectra of pristine and modified P25. P25 has a significant absorbance of UV light (λ is shorter than 400 nm), which is attributed to the large band gap (3.1 eV) of P25. Apparently, all of the modified P25 have notable absorbance in the visible region with respect to pure P25. The absorption maxima of Au/P25DPU, AuCu1:1/P25DPU and AuCu1:3/P25DPU appeared at 552 nm, 565 nm and 563 nm, respectively. The absorption bands with maxima at various wavelengths result in the diverse violet color of the modified photocatalysts. For the sample Cu/P25DPU, the absorbance maximum was found at 750 nm. It is well known that Au and Cu nanoparticles exhibit respectively a plasmon band with a maximum at ~520 nm and ~570 nm in aqueous solution. The absorption shift of the modified P25 photocatalysts is because the plasmon band is sensitive to the environment and depended on the stabilizer or on the substrate. The plasmon bands in case of Au/TiO_2 and $Au\text{-}Cu/TiO_2$ are red-shifted because of the coupling

between the metal nanoparticles and TiO_2 support having a high reflective index,. However in case of Cu/TiO_2, the metal nanoclusters are very small and the wide absorption band in the visible and near infra-red region observed in this case could be due to inter-band transitions in the Cu clusters deposited on different phases and sites of TiO_2 and with strong interaction with the support. It should also be pointed out there is a slight shift in band-gap transition to longer wavelengths from the DRS spectra of the modified photocatalysts. A similar effect was also previously observed with Pt- and Ag- modified TiO_2. This effect can be ascribed to a stronger stabilization of the conduction band of TiO_2 by the conduction band of the Au-Cu NPs compared to the stabilization of the valence band. The band-gap of the as-prepared samples could be calculated by the equation:

$$(\alpha h\nu)^n = k(h\nu - E_g) \tag{3.9}$$

where α is the absorption coefficient, k is the parameter related to the effective mass associated with the valence and conduction bands, n equals to 1/2 for the indirect transition semiconductor, $h\nu$ is the discrete photon energy of incident light and E_g is the band-gap energy.[19, 95] Plot of $(\alpha h\nu)^{1/2}$ versus the energy of absorbed light $h\nu$ based on the DRS response is shown in **Figure 3.37b**, giving the E_g value according to the extrapolated intercept. The absorption band edges of the modified P25 reduced from 3.1 eV of the pristine P25 to around 2.95 eV. Approximately, modified P25 with a higher Cu proportion in the bimetallic NPs leads to a lower band edge (AuCu1:3/P25DPU is estimated to 2.93 eV, and Au/P25DPU is 2.96 eV). The extended absorption to visible light region means an enhanced light-harvesting efficiency and results in a possible capability in solar-driven photocatalysis.

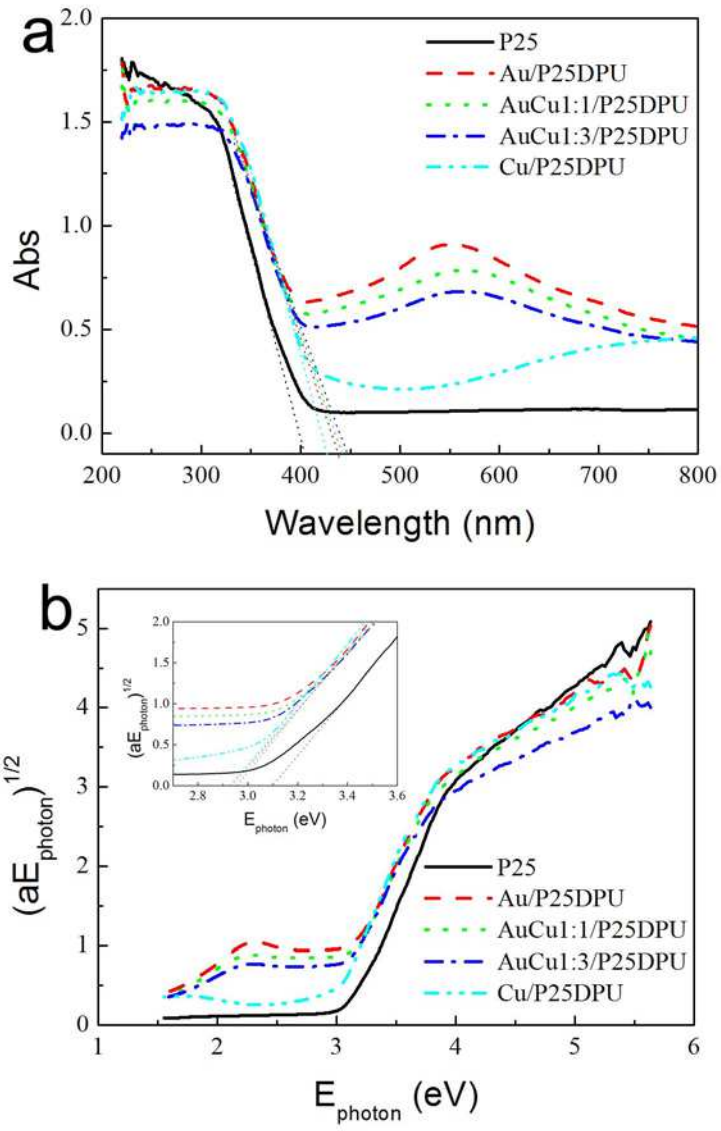

Figure 3.37 (a) Diffuse reflectance UV-Vis spectra of the modified photocatalysts and P25, and **(b)** the plot of transformed Kubelka-Munk function versus the energy of incident light, inset is the partial enlarged view.

3.4.2.4 XPS Analysis

In order to analyze the chemical composition of the prepared samples and to identify the chemical status of Cu element in the samples, X-ray photoelectron spectroscopy (XPS) measurements were attempted. The XPS survey spectrum of AuCu1:3/P25DPU is shown in **Figure 3.38a**. The peaks of Cu2p, Au4f, Ti2p, O1s, and C1s can be clearly detected. The weak peaks of C are contamination peaks arising mainly from CO_2 adsorbed on the surface of the sample .[96] The high resolution XPS spectrum of Cu in the region 2p for the sample

AuCu1:3/P25DPU is shown in **Figure 3.38b**. The binding energies of $Cu2p_{3/2}$ and $Cu2p_{1/2}$ peaks are located at 931.7 and 951.5 eV, respectively, which agree with those reported previously. Furthermore, the Auger CuLMM spectrum shows the peak position of kinetic energy is found at around 920 eV, illustrating that the main chemical state of Cu is in the zero valence.

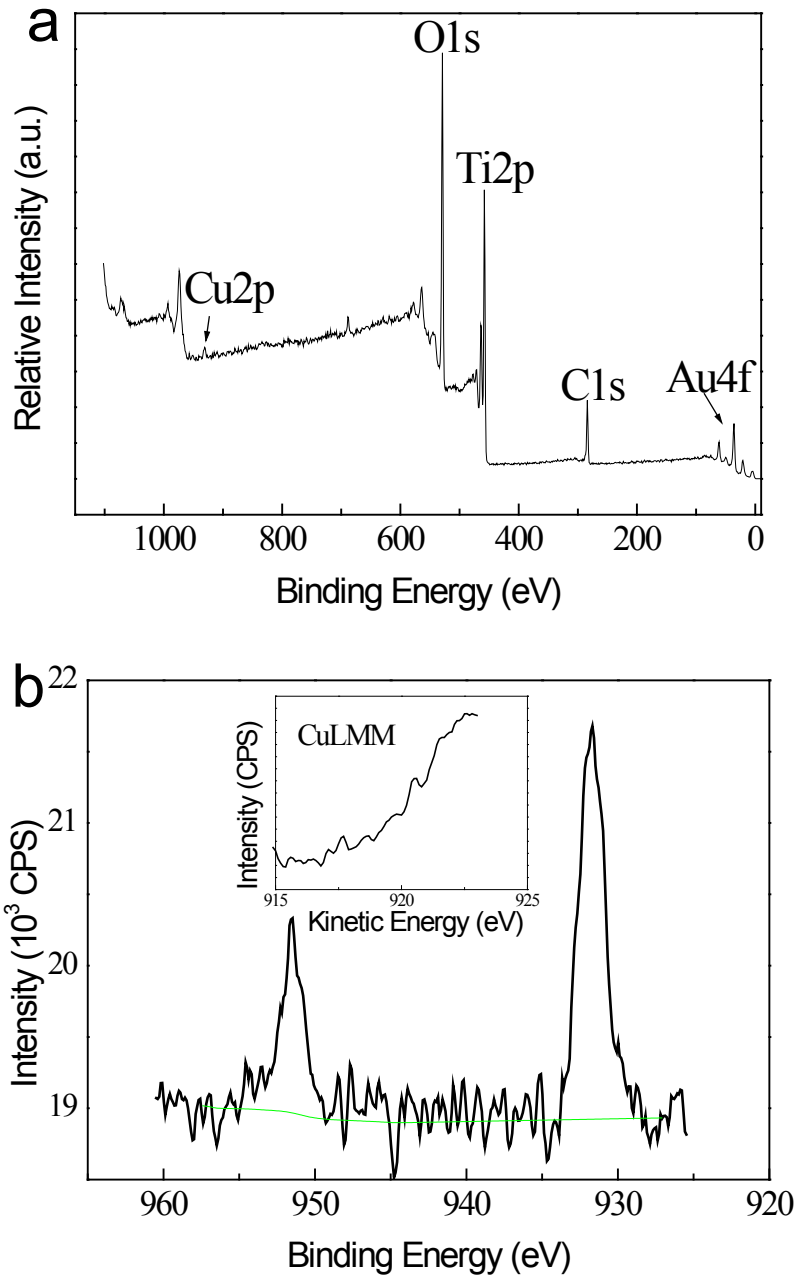

Figure 3.38 (a) XPS survey spectrum and **(b)** Cu2p region of the XPS spectra of sample AuCu1:3/P25DPU. The inset in b is Auger CuLMM spectrum of the sample.

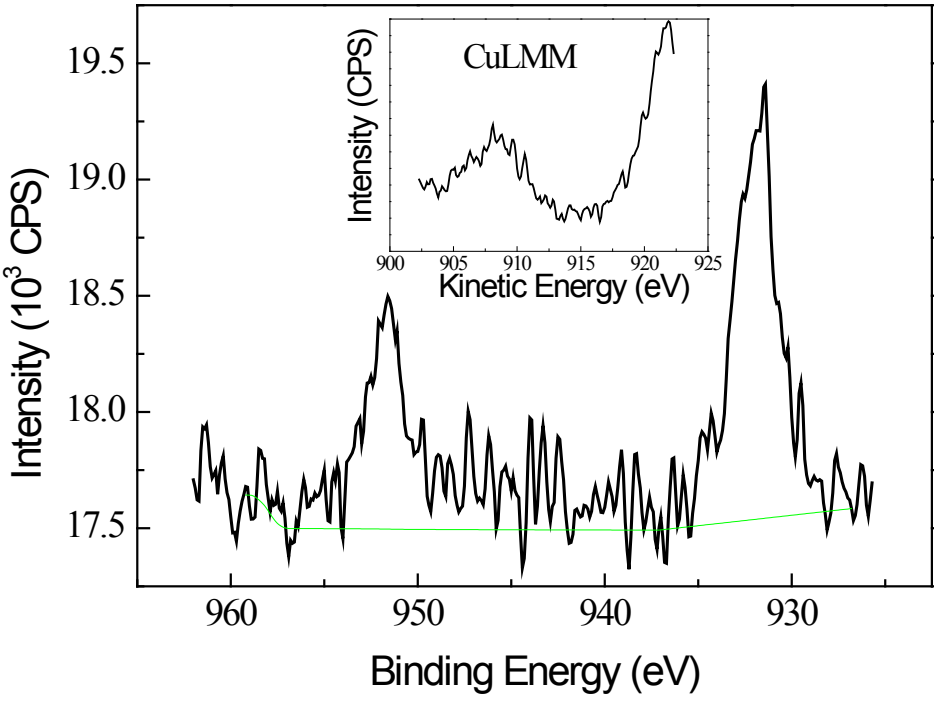

Figure 3.39 Cu2p region of the XPS spectra of sample AuCu1:3/P25DPU, after photocatalytic reaction under UV illumination. The inset is Auger CuLMM spectrum of the sample.

The sample AuCu1:3/P25DPU, after 15 minutes of photocatalytic reaction under UV light, was also characterized using XPS. The $Cu2p_{3/2}$ and $Cu2p_{1/2}$ peaks are found at 931.5 eV and 951.6 eV, and the Auger CuLMM peak is 921.9 eV (**Figure 3.39**), indicating the chemical status of Cu is still in zero valence. The unchanged violet color of the sample after reaction also confirmed the stabilization of the surface modified P25 with Au-Cu NPs in the photocatalytic reaction irradiated with UV light.

3.4.2.5 BET Analysis

Nitrogen sorption isotherms were generated to investigate the porous structure and the Brunauer-Emmett-Teller (BET) surface areas of the modified photocatalysts. The data are shown in **Figure 3.40**. The sample AuCu1:3/P25DPU exhibits a typical-IV isotherm pattern and it shows steep hysteresis loop at high relative pressure (**Figure 3.40**a).[85-88] The hysteresis loop as a result of capillary condensation of N_2 inside the pores is ascribed to the existence of mesopores.[87-88] The BET surface area was obtained as 47.02 $m^2\ g^{-1}$. Compared to the reference P25 (51.4 $m^2\ g^{-1}$), a slight decrease in the BET surface area was

found. The pore size distribution for the modified P25 was obtained by the Barrett-Joyner-Halenda (BJH) method [89] and is presented in **Figure 3.40b**. The sample AuCu1:3/P25DPU shows bimodal pore size distributions with a maximum pore diameter of 2.2 nm and 45.8 nm respectively, indicating the presence of intra-aggregated pores and inter-aggregated pores (represented by the hysteresis loop in the higher P/P_0 range). Degussa P25 titania powders prepared by flame hydrolysis of $TiCl_4$ exhibited a monomodal pore-size distribution with a maximum pore diameter at 2.33 nm. The significant difference in pore-size distribution for the modified sample is probably due to the non-uniform drying stresses when the modified P25 slurry was dried.[85, 90]

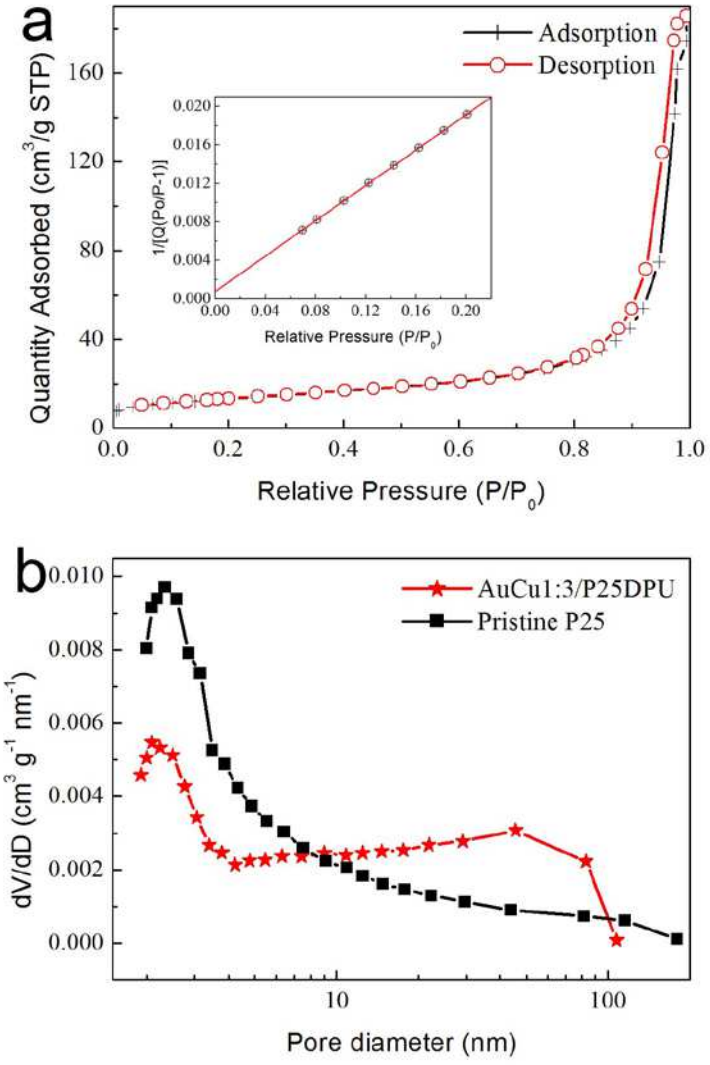

Figure 3.40 (a) N_2 adsorption-desorption isotherms for the sample AuCu1:3/P25DPU. Inset: BET surface area plot of, **(b)** the corresponding pore size distribution.

3.4.3 Photocatalytic Tests

The photocatalytic activity of the modified P25 was investigated for the degradation of methyl orange (MO).

A representative plot for the photodegradation of MO under UV-light with the sample AuCu1:3/P25DPU is shown in **Figure 3.41**. The absorption of the main peak at 465 nm is proportional to the concentration of MO. The slight absorbance decrease at 0 minute was due to the adsorption of MO on P25 surface. The modified P25 is highly photoactive in degradation of MO under UV light. 40% of MO was decomposed after 5 minutes, and nearly 98% of MO was degraded after 20 minutes (complete disappearance of absorption maxima at 465 nm and 272 nm).

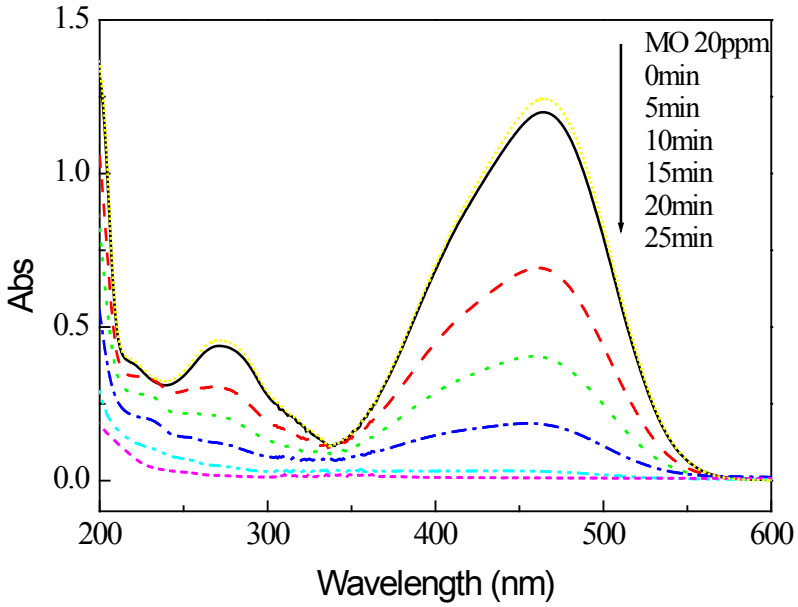

Figure 3.41 UV-vis absorption spectra of MO in photodegradation under UV illumination with the sample AuCu1:3/P25DPU.

The time runs of MO concentration are shown in **Figure 3.42a**. As seen, MO is very stable under UV illumination. The degradation is faster for the modified photocatalysts, except the monometallic Au modified P25, compared to the pristine P25. These photocatalytic reactions can be approximately regarded as first-order kinetics. The first order kinetics of MO photodegradation for the bare and modified P25 are shown in **Figure 3.42b**. Rate constants were obtained by the linear fittings of $Ln(C_t/C_0)$ versus time *t*.

Table 3.6 presents the detailed information of rate constants. Deposition of monometallic Au NPs on P25 caused a decrease in the photoactivity with respect to bare P25. In the case of modification with Au/Cu 1:1 NPs, the photocatalytic efficiency doubled compared to that of the sample Au/P25DPU. When the Cu/Au molar ratio increased to 3:1, the photoactivity of AuCu1:3/P25DPU on MO degradation increased up to three times in comparison with pure P25. As expected, modification with Cu leads to better enhancement in the photocatalytic activities compared to modification with Au.

The results confirm several conclusions induced in previous sections. Firstly, bimetallic Au-Cu NPs modified P25 have better photoactivity under UV light than monometallic Au modified ones. Secondly, modification of P25 with monometallic Cu NPs results in higher efficiency compared to the bare P25. Finally, modification with Au-Cu NPs with a Au/Cu ratio 1:3 always contributes to the highest activity.

For the photodegradation of MO under visible light, no degradation could be observed with the pristine or the Au, Cu, and Au-Cu modified P25. The phenomenon is not like that in RhB visible photodegradation. According to the oxidation potential of RhB and the conduction band edge of TiO_2,[38, 81] the excited RhB molecules can transfer electrons into the CB of TiO_2, and themselves become cationic radicals which undergo further transformation.[80] However, MO is a non-photosensitive dye. It cannot undergo a sensitized photoreaction. In our experiments, the modified P25 are not able to be excited by visible light. The surface modification with Au, Cu, and Au-Cu NPs by DPU method does not improve the photocatalytic activity under visible light.

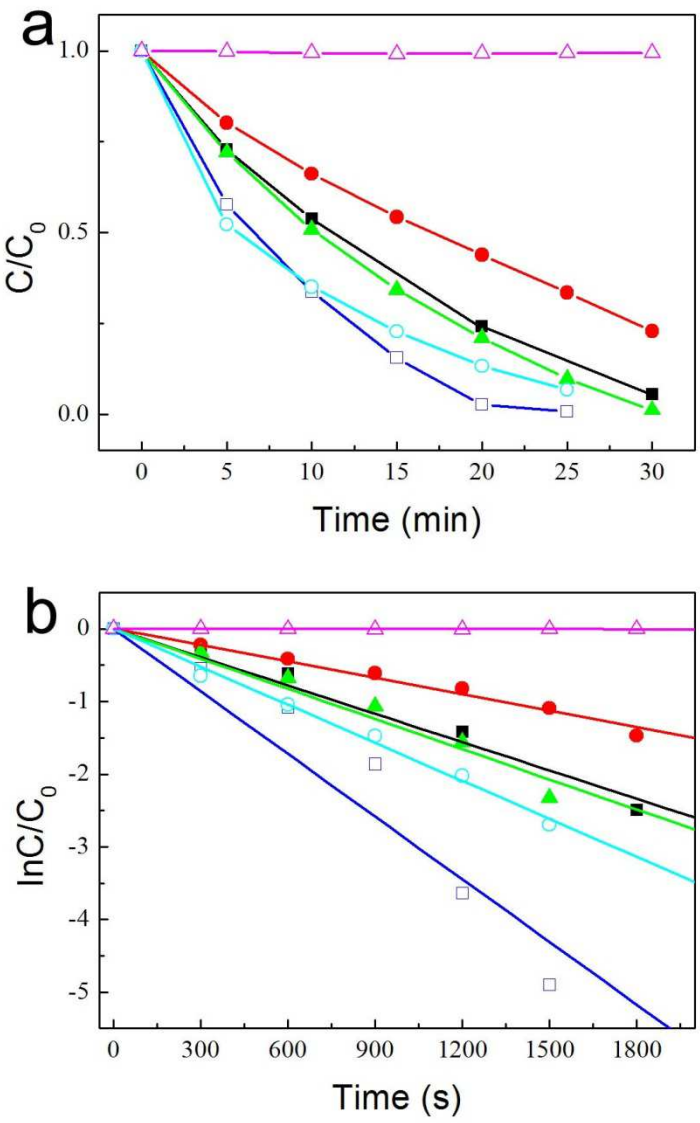

Figure 3.42 (a) The time runs of relative MO concentration, and **(b)** first-order kinetics in photodegradation under UV illumination in the presence of P25 (filled square), Au/P25DPU (filled circle), AuCu1:1/P25DPU (filled triangle), AuCu1:3/P25DPU (open square), Cu/P25DPU (open circle), and no photocatalyst (open triangle).

Table 3.6 Rate constants of the pseudo first-order fit of MO photodegradation under UV illumination.

Photocatalyst	*k* (rate constant) (10^{-3} s^{-1})	R (correlation coefficient)
P25	**1.2**±0.1	0.998
Au/P25DPU	**0.78**±0.04	0.992
AuCu1:1/P25DPU	**1.5**±0.1	0.986
AuCu1:3/P25DPU	**3.2**±0.4	0.972
Cu/P25DPU	**1.7**±0.1	0.996

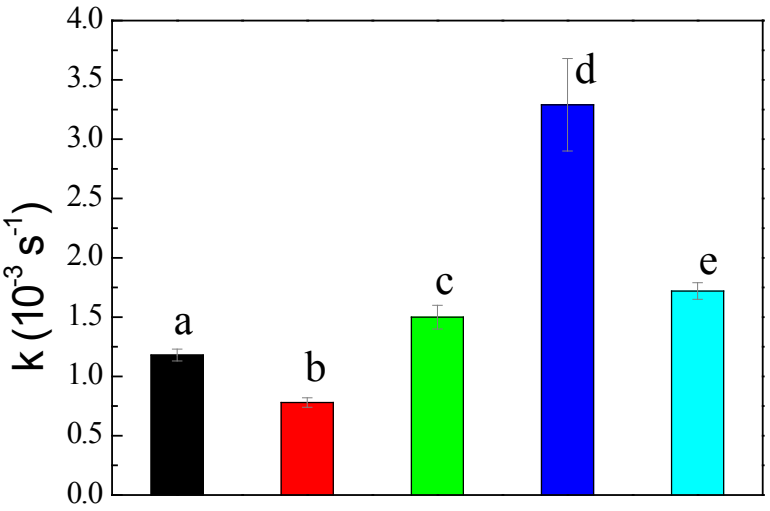

Figure 3.43 Rate constants of the first-order kinetic of MO photodegradation under UV illumination with, **(a)** P25, **(b)** Au/P25DPU, **(c)** AuCu1:1/P25DPU, **(d)** AuCu1:3/P25DPU, and **(e)** Cu/P25DPU.

Table 3.7 Summary of Au, Cu and Au-Cu modified P25 prepared by deposition precipitation and DPU-s methods.

Photocatalyst	Molar Ratio of Au/Cu	Content of metal precursor/P25 (wt%)		Color	TEM size (nm)
		Au	Cu		
Au/P25DUP-s	1:0	1	0	violet	14.0
[b]AuCu1:3/P25DPU-s	1:3	0.5	0.5	violet	22.9
Cu/P25DPU-s	0:1	0	1	Light-green	[a]N/A
Au/P25DP	1:0	1	0	Violet	16.7
[c]AuCu1:3/P25DP	1:3	0.5	0.5	violet	--
Cu/P25DP	0:1	0	1	Light-green	N/A

[a] N/A: Cu nanoparticles are unable to be observed from the TEM images

[b]AuCu1:3/P25DPU-s: DPU-s is deposition precipitation method with urea, but Au and Cu ions were added simultaneously before water bath.

[c]AuCu1:3/P25DP: DP means deposition precipitation method, without urea or other reagents.

3.4.4 The Effect of Urea on the Deposition and Photoactivity

We have also carried out experiments to evaluate the effect of urea in the deposition precipitation processes. These experiments were divided into two parts. In the first group, deposition precipitation was done with urea. However, Au and Cu ions were introduced to the solution simultaneously. After that, the suspension was heated with a water bath at 90 °C. Therefore, these samples are named ending with DPU-s. In another group, the deposition precipitation has been performed in the absence of urea. Photocatalysts prepared by this method were named ending with DP. Details of the prepared photocatalysts are summarized in **Table 3.7**.

The supernatant was measured using UV-vis spectrophotometer to check the probable residual metal ions. **Figure 3.44**a shows the absorption spectra of the supernatant of Au/P25DP. The absorbance maximum at 220 nm can be attributed to Au^{III}. 1.25×10^{-4} M of $HAuCl_4$ solution was used as the reference. The remained Au concentration was calculated as

around 7.35×10^{-5} M. Compared to the initial Au concentration (5×10^{-4} M) in the suspension, at least one seventh of Au ions was used in the deposition procedure.

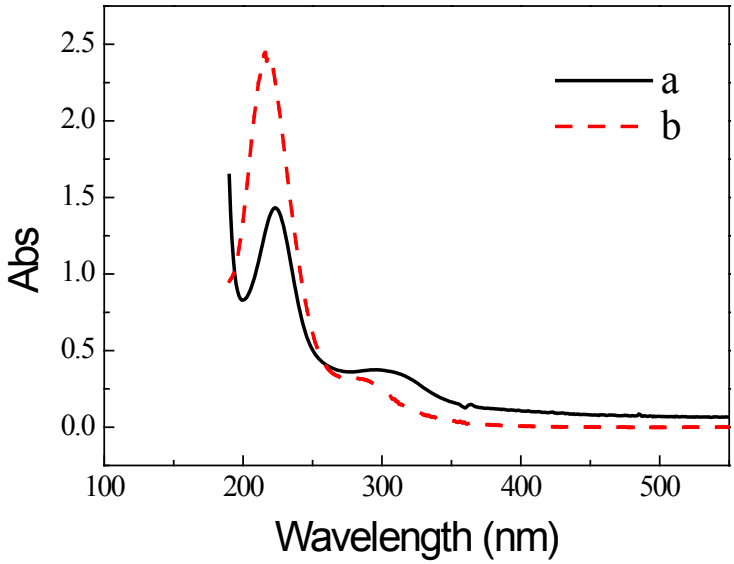

Figure 3.44 UV-vis absorption spectra of **(a)** the supernatant of Au/P25DP, and **(b)** 1.25×10^{-4} M $HAuCl_4$ solution. Optical path: 10 mm.

The morphologies of the samples were observed by TEM technique. In the absence of urea, larger Au NPs (mean size 16.7 nm in diameter, **Figure 3.45c**) were obtained by γ-irradiating the P25 suspension with $HAuCl_4$ at a dose rate of 20 Gy/min (total dose was 12 kGy). Even when the dose rate increased to 170 Gy/min, the size of Au NPs did not decrease significantly (**Figure 3.45d**).In general, smaller and more homogeanous NPs are obtained when increasing the dose rate. Nevertheless, in the presence of urea and at the same dose rate of 170 Gy/min, the size of Au NPs is about 10 nm (**Figure 3.35a**). In the presence of urea but at a lower dose rate of 20 Gy/min, the Au nanoparticle size increases to 15 nm (**Figure 3.45a**). In another case, when $HAuCl_4$ and $CuCl_2$ were introduced to P25 suspension simultaneously in the presence of urea at low dose rate, the size of Au-Cu bimetallic NPs increased, compared to the monometallic Au NPs, from 15 nm to 20 nm (**Figure 3.45b**). This is different from what we observed in the case of the DPU method and the bimetallic Au-Cu nanoparticle size (7 nm) is smaller than the monometallic Au NPs (10 nm, **Figure 3.35**). A brief summary is necessary to be made here, both of the DPU with two-steps and high dose rate are crucial to the formation of small metallic NPs and an efficient deposition.

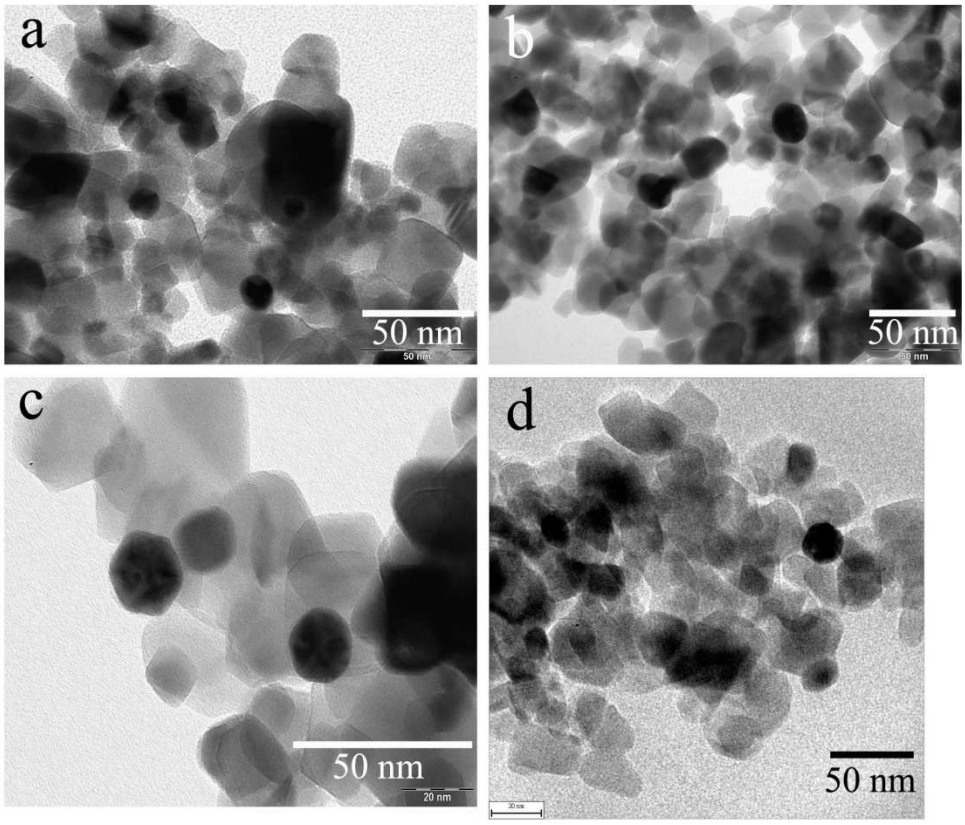

Figure 3.45 TEM images of the photocatalysts **(a)** Au/P25DPU-s, **(b)** AuCu1:3/P25DPU-s, **(c)** Au/P25DP at dose rate of 20 Gy/min; and **(d)** Au/P25DP at dose rate of 170 Gy/min.

The photocatalytic activities of the prepared catalysts were tested for RhB degradation under UV and visible light. For the samples prepared by DPU-s method, the photoactivities under UV illumination decreased overall compared to that of P25 (**Figure 3.46a**). Especially, the sample Cu/P25DPU-s exhibits an obvious decrease in the photocatalytic activity with respect to Au/P25DPU-s and AuCu1:3/P25DPU-s. In the case of visible illumination, all of the modified photocatalysts show great decrease in the photocatalytic activity (**Figure 3.46b**). The sample AuCu/P25DPU-s and AuCu13DPU-s even present no degradation of RhB. In this case, the modification with Cu incorporated Au NPs act probably as recombination centers for the charge carriers decreasing the photocatalytic activity.

In the case of deposition-precipitation without urea, the sample AuCu1:3/P25DP exhibits a slight higher photoactivity while Au/P25DP shows slower degradation under UV illumination (**Figure 3.47a**). For the degradation of RhB under visible light, AuCu1:3/P25DP exhibits nearly the same degradation kinetics as bare P25, and Au/P25DP shows a decreased activity for RhB photodegradation (**Figure 3.47b**).

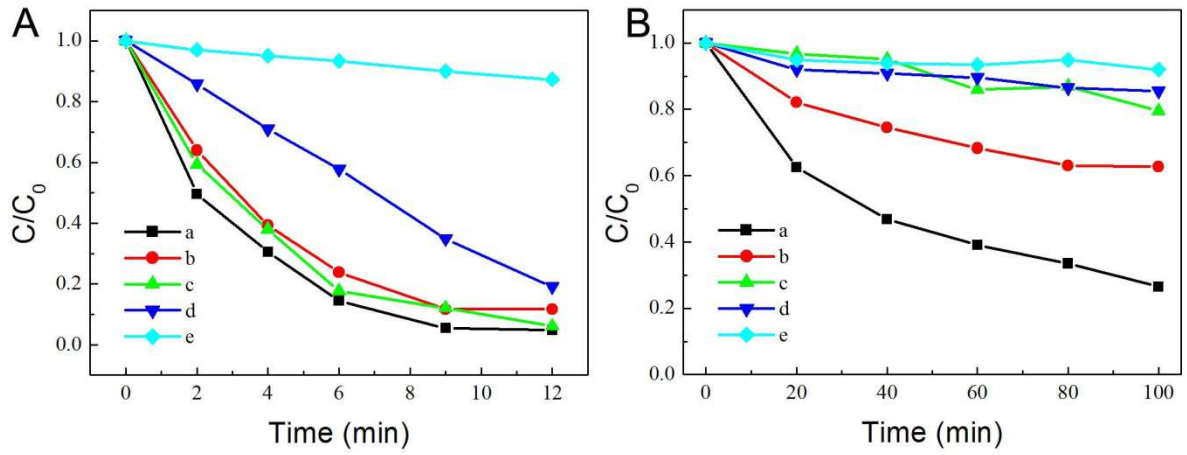

Figure 3.46 The time runs of RhB concentration in photodegradation under **(A)** UV, and **(B)** visible light with (a) P25, (b) Au/P25DPU-s, (c) AuCu1:3/P25DPU-s, (d) Cu/P25DPU-s, and (e) no photocatalyst.

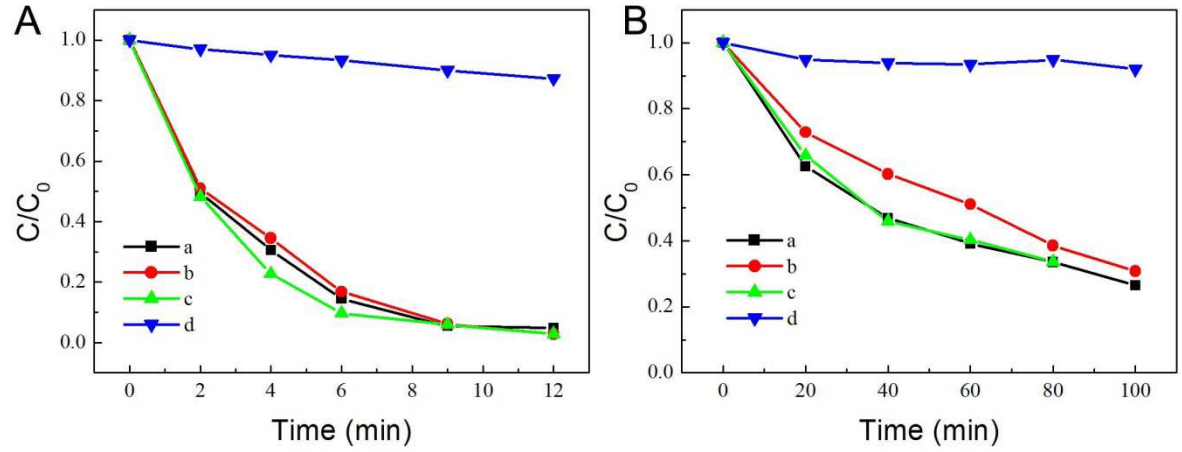

Figure 3.47 The time runs of RhB concentration in photodegradation under (A) UV, and (B) visible light with **(a)** P25, **(b)** Au/P25DP, **(c)** AuCu1:3/P25DP, and **(d)** no photocatalyst.

It can be concluded from the results discussed above that the modification with Au-Cu NPs by two-step deposition-precipitation in the presence of urea can result in small and homogeneous metallic NPs supported P25, and consequently leads to an enhancement in the photocatalytic activity.

3.4.5 Conclusion of this section

Small Au-Cu NPs (~7 nm) were synthesized by radiolysis *in-situ* on the P25 support after deposition precipitation in the presence of urea. Au and Cu ions were introduced at different stages during the deposition precipitation process to ensure an efficient deposition.

HR-TEM, HAADF-STEM, EDS, DRS, and XPS techniques have shown that the bimetallic Au-Cu NPs were alloys. The modification of P25 with Au-Cu bimetallic NPs induces an enhancement in the photocatalytic activity under UV-visible light. The highest UV photoactivity was obtained with modified P25 with Au/Cu 1:3 NPs, increasing by two times compared with pristine P25. The supported Au-Cu NPs are stable in the photocatalytic reaction as confirmed by TEM and XPS techniques. The modification of P25 with Cu nanoparticles also induces larger enhancement in the photocatalytic activity compared with its modification with Au NPs. This implies a more economical way for improving the photocatalytic activity of TiO_2. The two-step deposition precipitation with urea is efficient for depositing Au and Cu ions on P25, and it is applicable to deposition of other metals on TiO_2 or on other substrates.

3.5 Colloid-deposition of Au-Cu metallic NPs on P25 by chemical method with THPC

3.5.1 Characterization of Photocatalysts

The resulting modified monometallic catalyst was 0.5 wt% Au on P25, referred as Au/P25-T, where T refers to the agent THPC in this chemical method. Correspondingly, AuCu11/P25-T represents the sample P25 modified with Au-Cu NPs with a molar ratio of 1:1. The total nominal metal content was kept at 0.5 wt%. The compositions of the modified P25 are listed in details in **Table 3.8**.

The colours of the modified P25 are varied depending on the metal supported. The sample Au/P25-T is typically violet because of the plasmon band of Au NPs. The colour of AuCu13/P25-T altered to grey-violet. While Cu/P25-T exhibited light-green colour, owing to the Cu deposition on P25.

Table 3.8 Summary of the modified photocatalysts prepared by chemical method with THPC.

Photocatalyst	Molar Ratio of Au/Cu	Content of metal precursor/P25 (wt%)		Color	[a]TEM size (nm)	
		Au	Cu		[b]before	[c]after
Au/P25-T	1:0	0.5	0	violet	3.1	6.9
AuCu11/P25-T	1:1	0.38	0.12	Light-violet	3.9	5.2
[d]AuCu13/P25-T	1:3	0.25	0.25	grey-violet	2.9	4.8
Cu/P25-T	0:1	0	0.5	Light-green	N/A	N/A

[a] TEM size: this was measured manually with a program (Nano measurement);

[b] before: the prepared samples were before thermal treatment;

[c] after: the prepared samples were thermal treated.

[d]AuCu13/P25-T: modified P25 with Au-Cu NPs with a molar ratio 1:3, prepared by chemical method with THPC.

3.5.1.1 TEM Characterization

TEM observations show small nanoparticles homogenously dispersed on the surface of P25 (**Figure 3.48**). Calcination (used to remove the THPC residue) and hydrogen treatment (used for further reduction) induces an increase in NPs size. For the bimetallic Au-Cu NPs modified samples, the respective increases in average size are 2.3 nm and 1.9 nm for AuCu11/P25-T and AuCu13/P25-T. However, the monometallic Au modified P25 increased by 3.8 nm for the mean size (**Figure 3.49** and **Figure 3.50**). The mean particle size had slightly (after calcinations and H_2 treatment) decreased from 6.9 nm (for pure gold NPs) to 4.8 nm (for AuCu13 NPs) when gold is associated to Cu. In the latter case, smaller NPs and more homogeneous in size were obtained (see **Figure 3.48c**). As mentioned before, it has been already reported that the size of the bimetallic Au-Cu particles decreases as the amount of copper in the NPs increased.[39, 48] In case of Cu on TiO_2, we did not observe any particle on the support (**Figure 3.48d**), probably because of their small size and the small contrast between Cu and titania.

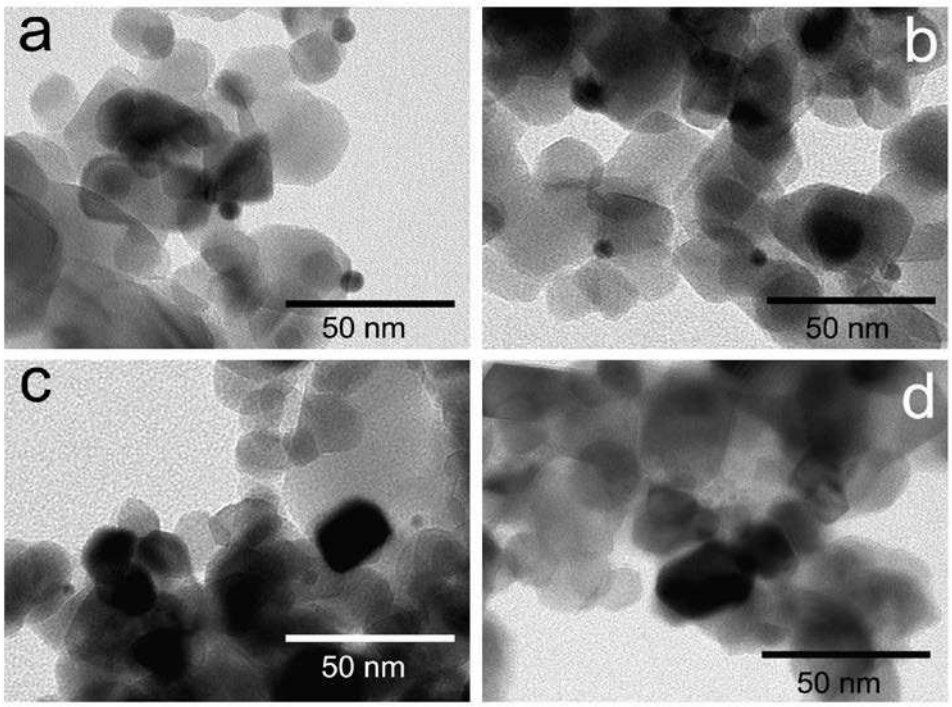

Figure 3.48 TEM images of the modified P25 with Au and Cu NPs. **(a)** Au/P25-T, **(b)** AuCu11/P25-T, **(c)** AuCu13/P25-T, and **(d)** Cu/P25-T.

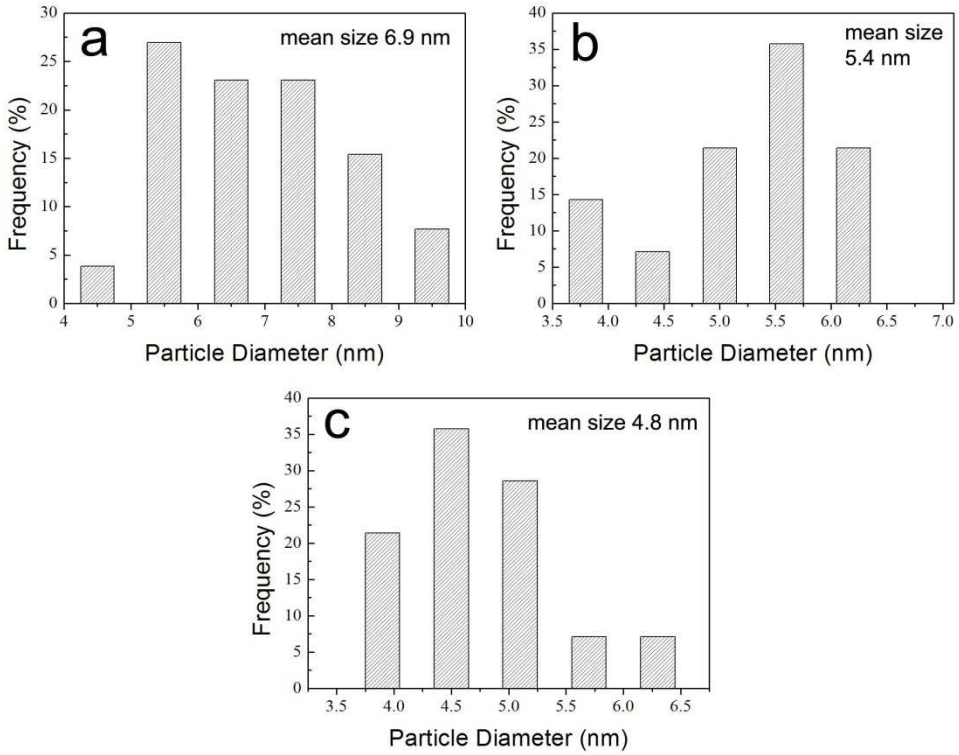

Figure 3.49 Size distributions of Au and Au-Cu NPs deposited on P25 prepared by chemical method with THPC, **(a)** Au/P25-T, **(b)** AuCu11/P25-T, and **(c)** AuCu13/P25-T.

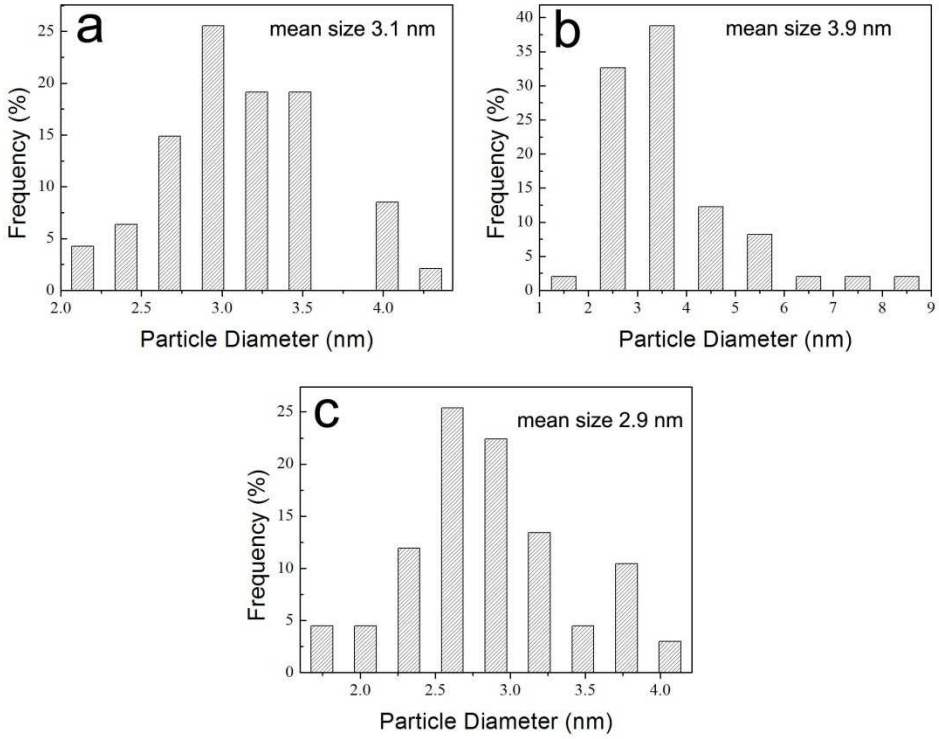

Figure 3.50 Size distributions of the modified P25 by chemical method with THPC, **(a)** Au/P25-T, **(b)** AuCu11/P25-T, and **(c)** AuCu13/P25-T. The samples were without thermal treatment.

3.5.1.2 STEM Characterization

HRTEM observations were also performed on bimetallic Au-Cu NPs on TiO_2. HAADF- and BF- STEM images of the monometallic Au nanoparticle of Au/P25-T are shown in **Figure 3.51a**,**b**. The interplanar crystal spacings were measured from the lattice fringes in different regions as 0.236 nm and 0.203 nm, which are coincident with the d spacing of lattice plane (111) and (200) of Au (standard 0.235 nm and 0.204 nm, JCPDS-PDF 04-0784). Besides, an interplane spacing of 0.359 nm can be attributed to the (101) lattice plane of Anatase (standard 0.352 nm, JCPDS-PDF 21-1272). HRTEM images acquired from HAADF- and BF- STEM of the AuCu11/P25-T NPs are shown in **Figure 3.51c**,**d**. The *d* spacings measured of different nanoparticles were found in the range of 0.223 - 0.229 nm, lying between the d spacings of monometallic Au (0.235 nm) and Cu (0.208 nm). According to the Vegard's law we could expect for a ratio Au/Cu 1:1, a value of 0.2215 nm for the (111) lattice planes. The measured *d* spacings might indicate the formation of Au/Cu 1:1 alloy nanoparticles, with a small fluctuating composition. Note however that the Vegard's law is not necessarily followed by nanoparticle alloys.

HAADF-STEM images of the NPs show that they are composed of an alloy of Au-Cu. **Figure 3.51c**,**d** shows the atomic composition in a Au-Cu nanoparticle. The contrast is roughly proportional to Z^2 where Z is the atomic number. Therefore due to the difference of the atomic number of Au and Cu the contrast is easy to see. Every spot in the image of **Figure 3.51c** corresponds to an atomic column. The bright spots correspond therefore to column richer in Au and the lighter spots to columns richer in Cu. We found that the nominal composition of the sample (Au/Cu = 1:1) is roughly followed in the image.

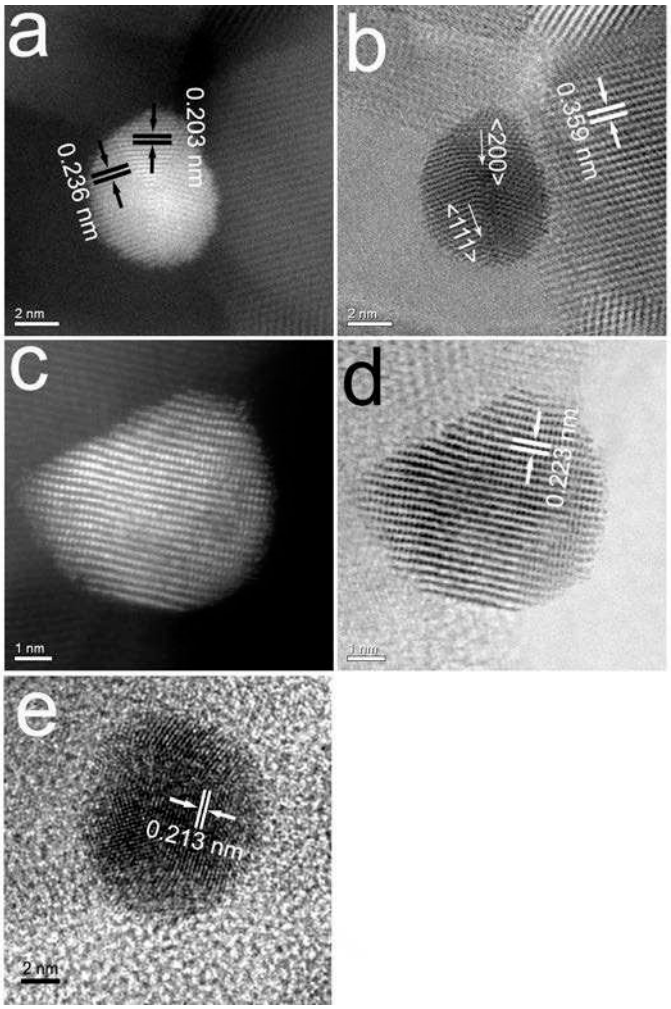

Figure 3.51 HAADF-STEM and BF-STEM images of **(a, b)** Au/P25-T, **(c, d)** AuCu11/P25-T, and **(e)** AuCu13/P25-T.

3.5.1.3 EDS Analysis

The composition of the supported Au-Cu nanoparticles was determined by STEM-Electron dispersive X-ray spectroscopy (EDS). Different metallic NPs were analyzed and the profile spectra across the different individual metallic NPs were taken. The HAADF-STEM images and the corresponding profile EDS of the modified photocatalysts Au/P25-T, AuCu11/P25-T, and AuCu13/P25-T are shown in **Figure 3.52**. We take AuCu11/P25-T for example, the Au and the Cu line scan signals (**Figure 3.52b2**), showed clearly the same intensity along the different regions of the NPs. The HAADF-STEM image of AuCu11/P25-T indicates the bimetallic nanoparticle deposited on the surface of TiO_2 **(Figure 3.52b1**): both of the Au-L and Cu-K peaks demonstrate that the Au and Cu atoms apparently homogeneously

dispersed. Therefore, the EDS line scans evidenced the bimetallic nanoparticles of AuCu11/P25-T have an alloyed structure. For the sample AuCu13/P25-T, similar results were observed (**Figure 3.52c1**,**c2**). In this case, the intensity of Cu-K was higher than that of Au-L owing to the higher Cu proportion. It should also be pointed out the high Cu-K background was due to the copper grid. For monometallic modified Au/P25-T, the EDS line scan indicated the deposited nanoparticles were gold.

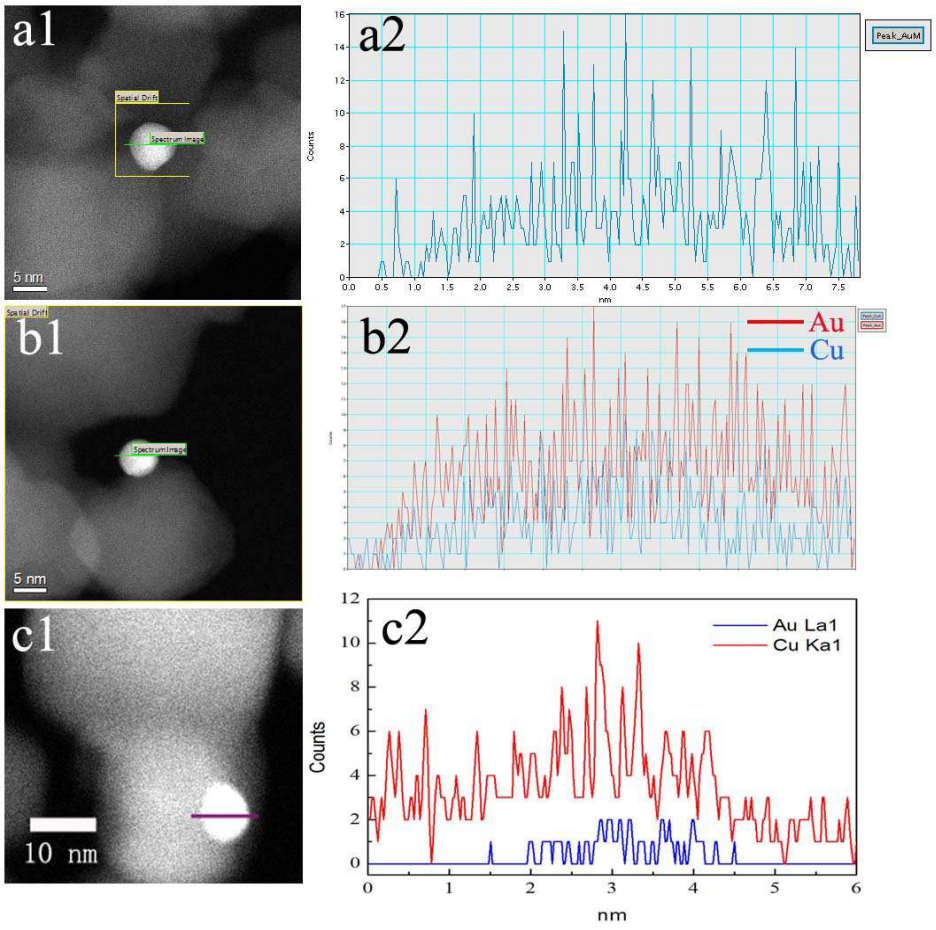

Figure 3.52 Energy dispersive X-ray spectroscopy line scans across external nanowires of nanoparticles (profiles were taken along the green or violet lines) and corresponding HAADF-STEM images for the samples of **(a1, a2)** Au/P25-T, **(b1, b2)** AuCu11/P25-T, and **(c1, c2)** AuCu13/P25-T.

We have also carried out EDAX elemental mapping for the respective elements, **Figure 3.53a** shows chemical maps for Au–Cu bimetallic NPs of the sample AuCu11/P25-T. Au (K, M) and Cu (K, L) maps clearly revealed the presence of the bimetallic Au-Cu alloys (Composite image of Au-Cu).

The information obtained from high resolution TEM images, HAADF-STEM and EDS profile analyses of the individual NPs confirm the formation of bimetallic alloy Au-Cu NPs.

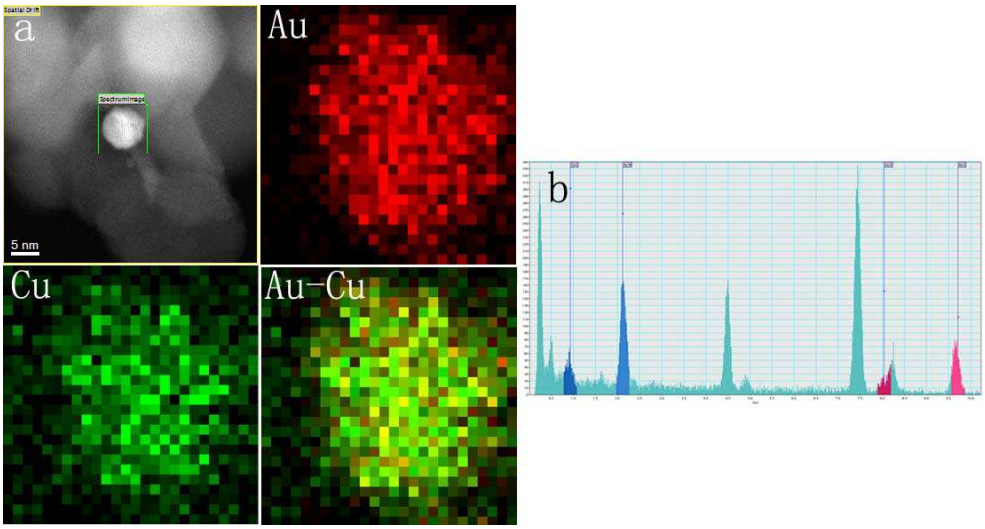

Figure 3.53 (a) HAADF-STEM image of AuCu11/P25-T and EDS elemental mapping analysis at the NPs; **(b)** EDS analysis of the selected area in **a**.

3.5.1.4 XPS Analysis

XPS analysis which is performed under 400 µm spot size probes a large number of particles layered onto the holder. It is a statistical measurement that provides the global response of a large number of nanoparticles. It is a complementary information of the other ones issued from local approaches. Obviously XPS demonstrates homogeneity of the preparations because signals for different layering of NPs on substrates are very reproducible in global chemical composition as in energy distribution whatever the core level investigated. Different preparations of Au/Cu-P25 TiO_2 NPs have been investigated. For each preparation XPS observed expected responses: Au, Ti, O core levels for Au/P25 NPs; Au, Cu, Ti, O core levels for Au/Cu/P25 NPs; Cu, Ti, O core levels for Cu/P25 NPs. Using atomic % determination for each element, we observed specific ratio ((% Au or % Au+ % Cu or % Cu) /(% Ti + %O)), which characterized the "metallic NPs /P25_TiO_2" networks and reflected the relative dispersion for both component after calcinations under air then reduction under H_2 at 500 °C. Again the different ratios are rather reproducible indicating the homogeneity of the dispersions.

Typical values are given in **Table 3.9**. An interesting feature concerns the Cu/P25_TiO_2 NPs for which we detected easily both Cu and TiO_2 signals demonstrating the presence of Cu NPs on TiO_2 particles, which was very difficult to observe by electron microscopy.

Table 3.9 Specific atomic ratio deduced from the XPS spectra for the samples Cu/P25, Au/P25, AuCu1:3/P25, AuCu1:1/P25

Sample	(%Au + %Cu)/(%Ti +%O)	%Au/% Cu
Au/P25	0.0014	[a]N/A
AuCu1:1/P25	0.003	0.7
AuCu1:3/P25	0.0062	0.14
Cu/P25	0.0093	N/A

[a]N/A: this value is not applicable.

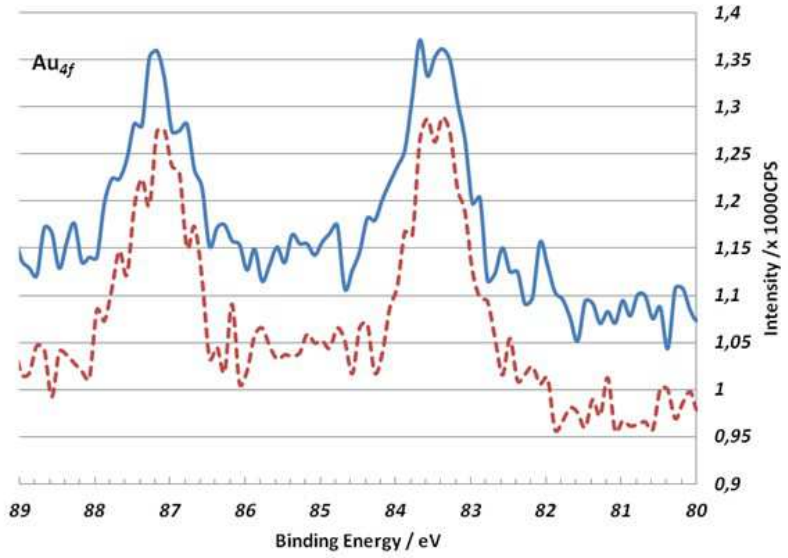

Figure 3.54 Au_{4f} region of the XPS spectra of the sample AuCu1:1/P25 (blue) and Au/P25 (red).

Another, important information deduced from XPS concerns the chemical state of the different metallic or bimetallic particles. It is clear that $Au4f_{7/2}$ core levels present their BE in the range 83.0-83.5 eV, so slightly negatively shifted compared to standard bare Au (84 eV) (see **Figure 3.54**). For Au signal, we can consider that the position range is in agreement with Au(0) chemical state but with a specific low BE position which has been already reported in

the literature.[91, 97] This shift can reflect the strong interaction of gold-based NPs with TiO_2 changing its electronic environment. Concerning $Cu2p_{3/2}$ core levels the BE positions are in the range of 932.5 - 933.0 eV (see **Figure 3.55**). The copper position range is in agreement with Cu(0) chemical state; This is comforted by the lack of satellite excluding any Cu(II) contribution. The XPS data on Cu confirms the stabilization of very small Cu(0) clusters by TiO_2. The interest of the comparison between metallic and bimetallic systems is that the energy repartition for each element can be considered as the same.

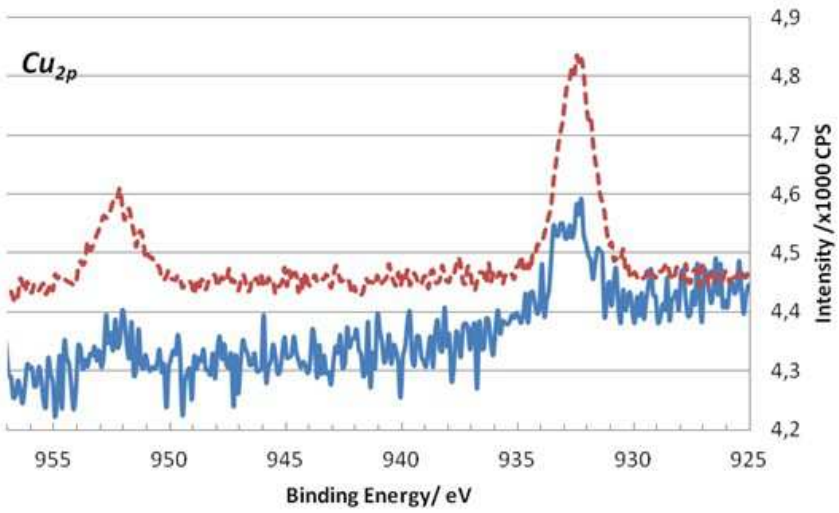

Figure 3.55 Cu_{2p} region of the XPS spectra of the sample AuCu1:1/P25 (blue) and Cu/P25 (red).

So the global characterization performed by XPS agrees with the local ones, that means that bimetallic NPs supported on P25 TiO_2 can be considered as homogeneously distributed.

3.5.1.5 DRS Analysis

The optical properties of the modified TiO_2 have been studied in details by Diffuse Reflectance Spectroscopy (DRS). **Figure 3.56a** shows the spectra of pure and modified TiO_2. It should also be pointed out that the DRS of the modified samples show a slight shift in the band-gap transition to longer wavelengths for all kinds of surface-modified photocatalysts. This effect was previously observed with Pt- and Ag- modified TiO_2. As mentioned before, this effect can be attributed to a stronger stabilization of the conduction band of TiO_2 by the

conduction band of the Au-Cu NPs compared with the stabilization of the valence band. The absorbance in the visible region is always higher for the modified than for pure P25. Note that wide absorptions with maxima at 550 and 750 nm are obtained respectively with Au and Cu-modified P25 (**Figure 3.56a**). Au-Cu-modified P25, absorb in the visible region with maxima respectively at 580 and 600 nm for AuCu11/P25-T and AuCu13P25-T. These absorptions result in violet or grey-violet colors of the modified TiO_2 samples. Au and Cu nanoparticles are known to exhibit a plasmon band with a maximum respectively at around 520 nm and 570 nm in water. This plasmon band is sensitive to the environment and can be shifted depending on the stabilizer or on the substrate. Because of the coupling between the metal nanoparticles and TiO_2 support, the plasmon bands in case of Au/TiO_2 and $Au\text{-}Cu/TiO_2$ are red-shifted. However in case of Cu/TiO_2, the metal nanoclusters are very small and the wide absorption band in the visible and near infra-red region observed in this case could be due to inter-band transitions in the Cu clusters deposited on different phases and sites of TiO_2 and with strong interaction with the support.

By contrast, we give the DRS results of the modified P25 before thermal treatment (**Figure 3.56b**). The similar shifts in the band-gap transition toward longer wavelengths were observed. However, a significant difference is the absorption maxima for all the modified samples at 548 nm. Note that the cross at 610 nm and the absorbance in the range from 610 nm to 800 nm for the sample AuCu13/P25-T is higher than that for Au/P25-T, indicating the existence of Cu probably in the form of small clusters. XPS results (not shown here) are very close to those obtained after thermal treatment for all the samples. They also attest in this case that Cu is in the zero valence.

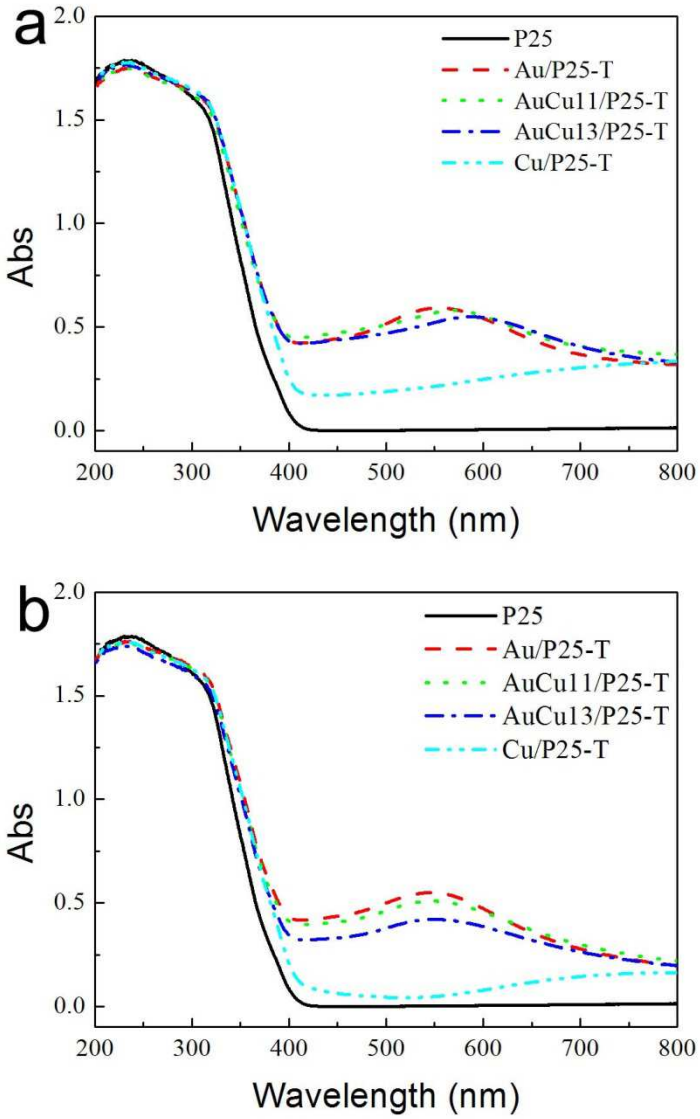

Figure 3.56 DRS spectra of pure and modified P25 with Au and Cu nanoparticles **(a)** thermal treated, **(b)** without thermal treatment, prepared by the chemical method with THPC.

3.5.1.6 BET Analysis

Nitrogen sorption isotherms were generated to investigate the porous structure and the Brunauer-Emmett-Teller (BET) surface areas of the modified photocatalysts. The data are shown in **Figure 3.57**. The sample AuCu13/P25-T exhibits a typical-IV isotherm pattern and it shows steep hysteresis loop at high relative pressure (**Figure 3.57a**).[85-88] The hysteresis loop as a result of capillary condensation of N_2 inside the pores is ascribed to the existence of mesopores.[87-88] The BET surface area was obtained as 50.09 m^2 g^{-1}. Compared to the reference P25 (51.4 m^2 g^{-1}), a very slight decrease in the BET surface area was found. The

pore size distribution for the modified P25 was obtained by the Barrett-Joyner-Halenda (BJH) method [89] and is presented in **Figure 3.57b**. The sample AuCu13/P25-T shows bimodal pore size distributions with a maximum pore diameter of 2.32 nm and 43.4 nm respectively, indicating the presence of intra-aggregated pore and inter-aggregated pore (represented by the hysteresis loop in the higher P/P_0 range). Degussa P25 titania powders prepared by flame hydrolysis of $TiCl_4$ exhibited a monomodal pore-size distribution with a maximum pore diameter at 2.3 nm. The significant difference in the pore-size distribution for the modified sample and the emergence of peak at 43.4 nm are probably due to the non-uniform drying stresses when the modified P25 slurry was dried.[85, 90] TiO_2 particles aggregate to generate larger pores.

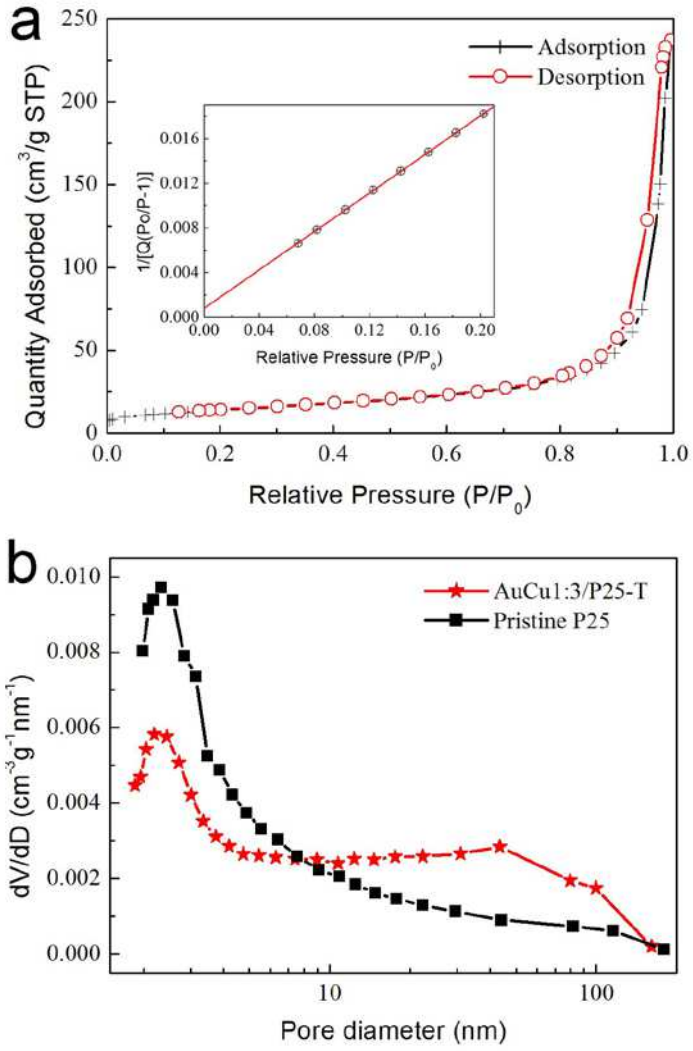

Figure 3.57 (a) N_2 adsorption-desorption isotherms for the sample AuCu13/P25-T. Inset: BET surface area plot, **(b)** the corresponding pore size distribution.

3.5.2 Photocatalytic Tests

The photocatalytic activities of the prepared samples were investigated for the degradation of RhB and Phenol under UV and visible light.

3.5.2.1 Photocatalytic activity under UV illumination

Evonik P25 is highly photoactive in phenol degradation under UV-Vis light. A representative plot on kinetics degradation of phenol in the presence of pristine P25 under UV and characterisation of degradation products by HPLC are shown in **Figure 3.58**. After 2 minutes of illumination, 50% of phenol was degraded. Meanwhile, intermediates, benzoquinone and hydroquinone were produced and accumulated. Their concentrations reached maxima at 3 minutes. After 6 minutes, phenol and the intermediates were completely degraded.

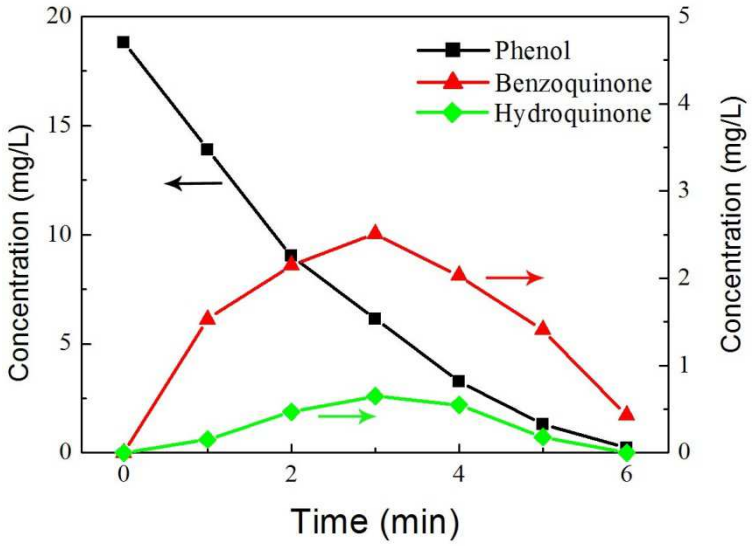

Figure 3.58 The time runs of phenol, benzoquinone, and hydroquinone concentrations in photodegradation with pristine P25 under UV illumination. The initial concentration of phenol is 2×10^{-4} M (equal to 18.82 ppm).

Figure 3.59a shows the time runs of relative phenol concentration photodegraded under UV light in the presence of pure and modified P25. Compared to pure P25, all of the modified catalysts exhibit faster decreases for phenol concentration. These photocatalytic reactions can be approximately regarded as first-order kinetics.[98-99] Rate constant (k) was used to evaluate

the photocatalytic activities. According to the equations 3.7 and 3.8, the rate constants of the first-order kinetic of phenol photodegradation for the bare- and modified TiO_2 are shown in **Table 3.10** and plotted in **Figure 3.59b**. Surprisingly, modification with Cu leads to better enhancement in the photocatalytic properties compared to modification with Au. Modification of P25 by Au-Cu NPs induces the highest enhancement in the photocatalytic properties. The best photocatalyst is the Au-Cu/P25 with Au/Cu 1:3. The photocatalytic efficiency for the sample AuCu13/P25-T increased by 40% than that for pure P25 based on the rate constants.

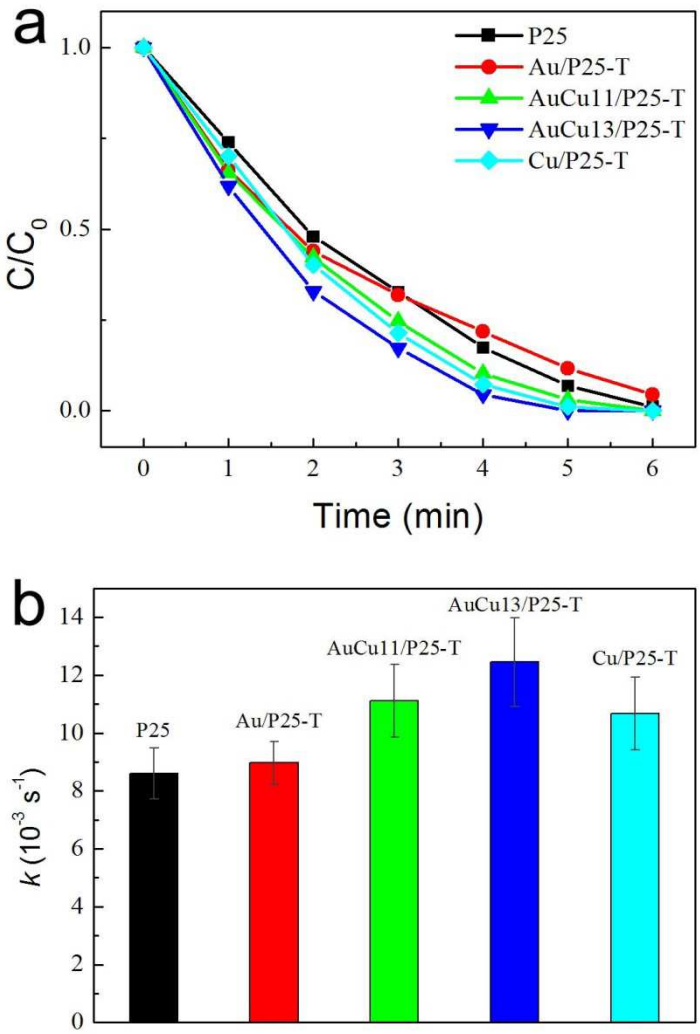

Figure 3.59 (a) The time runs of phenol relative concentration in photodegradation under UV illumination with pure P25, and modified P25, **(b)** the rate constants of the corresponding photodegradation.

Table 3.10 The rate constants of the pseudo first-order fitting in Phenol photodegradation

under UV illumination.

Photocatalysts	k (rate constant) (10^{-3} s^{-1})	R (correlation coefficient)
P25	8.6±0.9	0.979
Au/P25-T	8.9±0.7	0.980
AuCu11/P25-T	11.1±1.2	0.976
AuCu13/P25-T	12.5±1.5	0.978
Cu/P25-T	10.7±1.3	0.980

Photocatalytic tests on the Au and/or Cu modified P25 were also carried out for degradation of RhB under UV light. The time runs of RhB concentration and the histogram of rate constants are shown in **Figure 3.60**. The results are very consistent with those obtained in the phenol photodegradation. Modification of P25 with monometallic Cu NPs induces a better improvement in the photocatalytic activity compared to the modification with Au NPs. Bimetallic Au-Cu NPs modified photocatalyst with Au/Cu 1:3 showed the highest photoactivity.

We conclude that modification of P25 with Au-Cu alloyed NPs leads to higher photocatalytic activity under UV light. The mechanism will be studied by TRMC.

Table 3.11 The rate constants of the pseudo first-order fitting in RhB photodegradation under UV illumination.

Samples	k (rate constant) (10^{-3} s^{-1})	R (correlation coefficient)
P25	7.2±1.0	0.972
Au/P25-T	7.6±0.4	0.994
AuCu11/P25-T	7.9±0.4	0.996
AuCu13/P25-T	11.8±1.1	0.988
Cu/P25-T	9.6±0.6	0.996

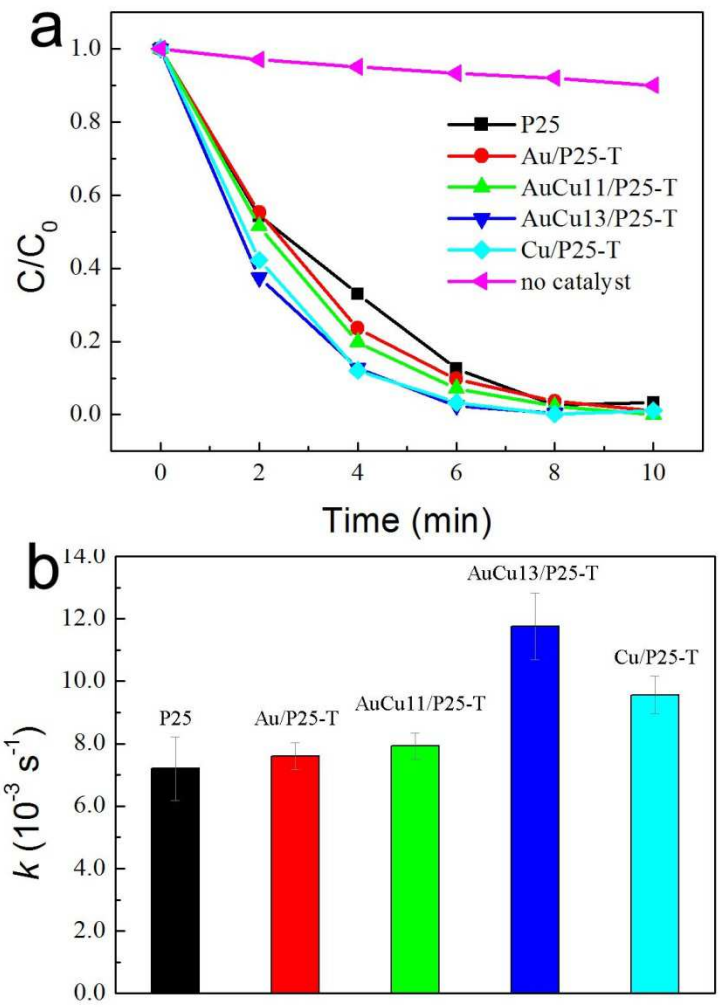

Figure 3.60 (a) The time runs of RhB relative concentration in photodegradation under UV illumination with no catalyst, pure P25, and modified P25, **(b)** the rate constants of the corresponding photodegradation.

3.5.2.2 Photocatalytic activity under visible illumination

Photocatalytic tests have been conducted under visible light. The results are shown in **Figure 3.61**. In that case, no improvement of the photocatalytic activity of modified titania was observed and the photocatalytic activity even decreased.

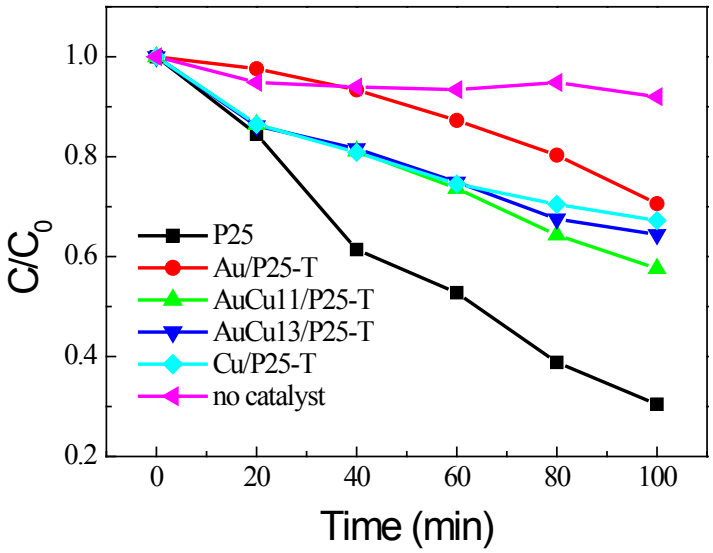

Figure 3.61 The time runs of phenol relative concentration in photodegradation under visible illumination with no catalyst, pure P25, and modified P25 without thermal treatment.

3.5.3 TRMC Signals

Time Resolved Microwave Conductivity (TRMC) experiments were conducted to study the charge carrier dynamics. TRMC signals obtained under UV illumination are shown in **Figure 3.62**. The surface modification with Au, Cu and Au-Cu NPs show a strong influence on the charge-carrier decay of P25**.** This influence on the decay can be related to the activity in the case of phenol degradation with UV-light.

The modification with Au, Cu and Au-Cu NPs accelerates the overall decay of the signal for all the modified TiO_2 compounds. As shown previously, the modification by these nanoparticles causes an increase in the photocatalytic activity of P25 (**Figure 3.59**). As already explained, the TRMC signal is mainly related to the electron mobility. The acceleration of the TRMC signal decay is then probably due to efficient electron scavenging by the nanoparticles deposited on TiO_2. It implies a decrease of the charge-carrier recombination that is beneficial to the photoactivity. It has to be noted that the acceleration of the decay is faster for P25 modified with bimetallic NPs **(Figure 3.62)**. This acceleration has also been observed for the modification of TiO_2 with Ag clusters.[76] The TRMC measurements show that bimetallic Au-Cu nanoparticles are very efficient in electron

scavenging. The electron scavenging scheme is shown in **Scheme 3-2**.

Furthermore, the modification with copper nanoparticles increases the maximum TRMC signal intensity in the case of Cu/P25-T **(Figure 3.62)**. This indicates that more electrons are produced under UV-illumination in the conduction band of Cu-modified P25. These excess electrons could be due to the electrons injected in the conduction band of TiO_2 after excitation of the copper nanoparticles which are easily oxidized.

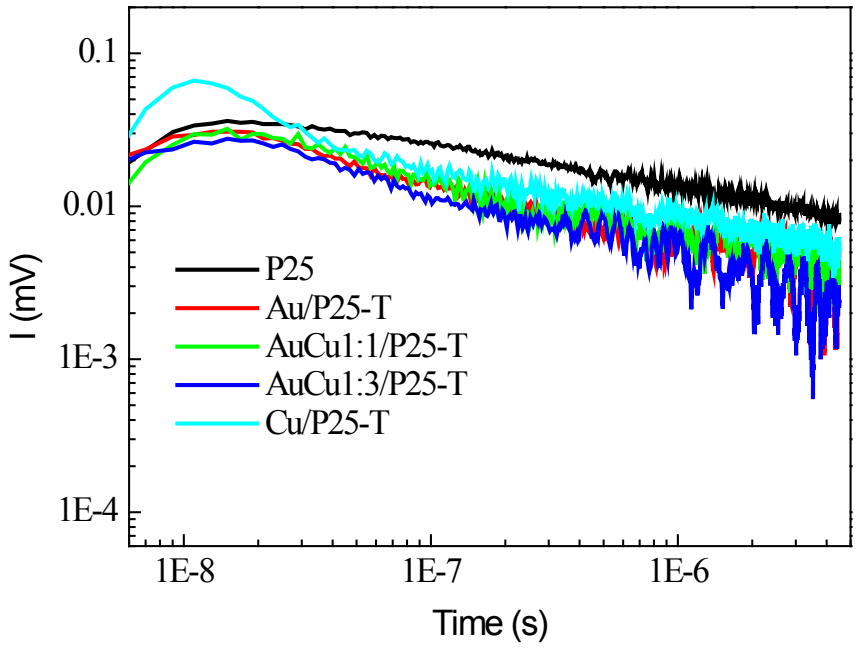

Figure 3.62 TRMC signals of pristine and modified P25 by the chemical method with THPC.

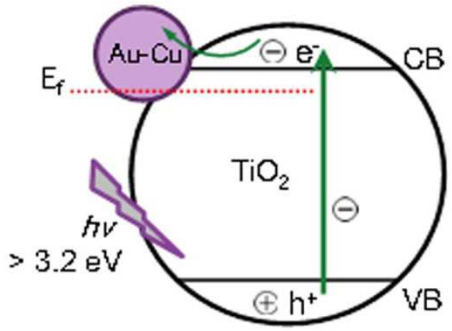

Scheme 3-2 Scheme of electron scavenging by P25 supported Au-Cu NPs after the absorption of UV photons.

At 532 nm (the second excitation wavelength of the laser), there are no TRMC signals

with all the samples including pure P25. Under excitation in the visible, there is no direct light absorption of pure TiO_2 but the metal NPs deposited on modified titania (Au and Au-Cu) are absorbing light through their plasmon, and in case of Cu/P25-T excited state of the Cu nanoclusters could be reached. Since no TRMC signal is observed at this excitation wavelength, one can conclude that no electron transfer from the metallic NPs or nanoclusters to the conduction band of TiO_2 occurs. This is consistent with the photocatalytic results under visible light.

3.5.4 Conclusion of this section

Small Au, Cu and bimetallic Au-Cu nanoparticles homogeneous in size were synthesized on P25 TiO_2 by the THPC method. HRTEM, HAADF-STEM, EDS and XPS have demonstrated the alloyed structure of the Au-Cu NPs. Titania surface modification with Au, Cu and bimetallic Au-Cu NPs enables the increase of the photocatalytic activity under UV-visible irradiation. We have found that very small amount of metal (0.5% wt.) can activate titania for photocatalytic applications, thus the costs of photocatalyst preparation are relatively low. TRMC measurements show that under UV irradiation Au, Cu and Au-Cu NPs act as electron scavengers hindering charge recombination in modified P25. The modification of titania by Cu nanoclusters induces a larger enhancement in the photocatalytic activity compared with its modification with Au NPs. The highest photocatalytic activity is obtained with P25 modified with Au-Cu 1:3. TRMC signals show that bimetallic nanoparticles are better electron scavenger than Cu and Au NPs. These bimetallic NPs can also have applications in catalysis and electrocatalysis. Modification of P25 with Au-, Cu- or Au-Cu NPs by this THPC method gave much better results for the nanoparticle size and distribution and photocatalytic activity than by the colloid-deposition method. Besides, this method is more facile than deposition precipitation method with urea.

3.6 Conclusions

Different methods were developed to modify the surface of TiO_2 with Au and/or Cu nanoparticles for photocatalytic applications. Some interesting results were obtained:

i) Au-Cu bimetallic NPs with small size (~4 nm) and homogeneous distribution were synthesized by radiolysis in the presence of stabilizing agent PAA. Polymer PVA can facilitate the deposition of metal NPs on the TiO_2 surface in the colloid deposition method.

ii) When synthesizing Au-Cu bimetallic NPs, the addition of Cu ions can lead to a smaller particle size and homogeneous size distribution compared to monometallic Au NPs. The trends exist for both colloidal deposition (by radiolysis and by THPC method) and deposition precipitation with urea.

iii) Deposition precipitation with urea followed by radiolytic reduction leads to modification of TiO_2 with Au-Cu bimetallic NPs with a high deposition yield and direct formation of Au-Cu alloyed NPs without thermal treatment.

iv) Modification of P25 with Au or/and Cu metal NPs by THPC method exhibited much better results than for the nanoparticle size and distribution and photocatalytic activity than by the radiolytic colloid-deposition method. The THPC method is an efficient and facile method to modify TiO_2 with gold, copper or other metals.

v) The monometallic NPs (Au and Cu) and alloyed Au-Cu bimetallic NPs are efficient for electron scavengers. Modification of TiO_2 with alloyed Au-Cu bimetallic NPs prompts electron-hole separation, consequently contributing to the enhancement of the photocatalytic activity under UV illumination.

References

[1] Asahi, R.; Morikawa, T.; Ohwaki, T.; Aoki, K. and Taga, Y., *Science* **2001**, *293*, 269-271.

[2] Khan, S. U. M.; Al-Shahry, M. and Ingler, W. B., *Science* **2002**, *297*, 2243-2245.

[3] Sun, H.; Wang, S.; Ang, H. M.; Tade, M. O. and Li, Q., *Chem. Eng. J.* **2010**, *162*, 437-447.

[4] Xiong, Z. and Xiusong, Z., *J. Am. Chem. Soc.* **2012**, *134*, 5754-5757.

[5] Ohno, T.; Akiyoshi, M. and Umebayashi, T., *Appl. Catal., A* **2004**, *265*, 115-121.

[6] Sakthivel, S.; Janczarek, M. and Kisch, H., *J. Phys. Chem. B* **2004**, *108*, 19384-19387.

[7] Jing, L. Q.; Zhou, J.; R., D. J.; Tang, J. W.; Liu, D. N. and Fu, H. G., *Energy Environ. Sci.* **2012**, *5*, 6552-6558.

[8] Wang, W. S.; Wang, D. H.; Qu, W. G.; Lu, L. Q. and Xu, A. W., *J. Phys. Chem. C* **2012**, *116*, 19893-19901.

[9] Eder, D. and Windle, A. H., *Adv. Mater.* **2008**, *20*, 1787.

[10] Woan, K.; Pyrgiotakis, G. and Sigmund, W., *Adv. Mater.* **2009**, *21*, 2233.

[11] Kongkanand, A.; Dominguez, R. M. and Kamat, P. V., *Nano Letter* **2007**, *7*, 676.

[12] Guldi, D. M.; Rahman, G. M. A.; Sgobba, V.; Kotov, N. A.; Bonifazi, D. and Prato, M., *J. Am. Chem. Soc.* **2006**, *128*, 2315.

[13] Farrow, B. and Kamat, P. V., *J. Am. Chem. Soc.* **2009**, *131*, 11124.

[14] Zhou, K.; Zhu, Y.; Yang, X.; Jiang, X. and Li, C., *New J. Chem.* **2011**, *25*, 353.

[15] Du, J.; Lai, X.; Yang, N.; Zhai, J.; Kisailus, D.; Su, F.; Wang, D. and Jiang, L., *ACS Nano* **2011**, *5*, 590.

[16] Zhang, H.; Lv, X. J.; Li, Y. M.; Wang, Y. and Li, J. H., *ACS Nano* **2010**, *4*, 380.

[17] Lee, J. S.; You, K. H. and Park, C. B., *Adv. Mater.* **2012**, *24*, 1084.

[18] Alaoui, O. T.; Herissan, A.; Quoc, C. L.; Zekri, M. M.; Sorgues, S.; Remita, H. and Colbeau-Justin, C., *J. Photochem. Photobiol. A* **2012**, *242*, 34-43.

[19] Wang, H.; Faria, J. L.; Dong, S. and Chang, Y., *Mater. Sci. Eng., B* **2012**, *177*, 913-919.

[20] Kumar, P. S. S.; Raj, M. R. and Anandan, S., *Sol. Energy Mater. Sol. Cells* **2010**, *94*, 1783-1789.

[21] Kochuveedu, S. T.; Kim, D.-P. and Kim, D. H., *J. Phys. Chem. C* **2012**, *116*, 2500-2506.

[22] Veres, A.; Rica, T.; Janovak, L.; Domok, M.; Buzas, N.; Zollmer, V.; Seemann, T.; Richardt, A. and Dekany, I., *Catal. Today* **2012**, *181*, 156-162.

[23] Takai, A. and Kamat, P. V., *ACS Nano* **2011**, *5*, 7369-7376.

[24] Tsukamoto, D.; Shiraishi, Y.; Sugano, Y.; Ichikawa, S.; Tanaka, S. and Hirai, T., *J. Am. Chem. Soc.* **2012**, *134*, 6309-6315.

[25] Kim, J.; Monllor-Satoca, D. and Choi, W., *Energy Environ. Sci.* **2012**, *5*, 7647-7656.

[26] Wongwisate, P.; Chavadej, S.; Gulari, E.; Sreethawong, T. and Rangsunvigit, P., *Desalination* **2011**, *272*, 154-163.

[27] Tiwari, V.; Jiang, J.; Sethi, V. and Biswas, P., *Appl. Catal., A* **2008**, *345*, 241-246.

[28] Wang, C.-M.; Heller, A. and Gerischer, H., *J. Am. Chem. Soc.* **1992**, *114*, 5230-5234.

[29] Choi, W.; Termin, A. and Hoffmann, M. R., *J. Phys. Chem.* **1994**, *98*, 13669-13679.

[30] Subramanian, V.; Wolf, E. E. and Kamat, P. V., *J. Am. Chem. Soc.* **2004**, *126*, 4943-4950.

[31] Zhang, Y.; Li, J. and Xu, H., *Appl. Catal. B* **2012**, *123-124*, 18-26.

[32] Libanori, R.; Giraldi, T. R.; Longo, E.; Leite, E. R. and Ribeiro, C., *J. Sol-Gel Sci. Technol.* **2009**, *49*, 95-100.

[33] Kamat, P. V., *J. Phys. Chem. C* **2007**, *111*, 2834.
[34] Kamat, P. V., *J. Phys. Chem. C* **2008**, *112*, 18737.
[35] Kiyonaga, T.; Akita, T. and Tada, H., *Chem. Commun* **2009**, 2011.
[36] Carp, O.; Huisman, C. L. and Reller, A., *Prog. Solid State Chem.* **2004**, *32*, 33.
[37] Kubacka, A.; Fernandez-Garcia, M. and Colon, G., *Chem. Rev.* **2012**, *112*, 1555-1614.
[38] Hoffmann, M. R.; Martin, S. T.; Choi, W. and Bahnemann, D. W., *Chem. Rew.* **1995**, *95*, 69-96.
[39] Zielinska-Jurek, A.; Kowalska, E.; Sobczak, J. W.; Lisowski, W.; Ohtani, B. and Zaleska, A., *Appl. Catal. B* **2011**, *101*, 504-514.
[40] Colbeau-Justin, C.; Kunst, M. and Huguenin, D., *J. Mater. Sci.* **2003**, *38*, 2429-2437.
[41] Schwerdtfeger, P., *Angew. Chem. Int. Ed.* **2003**, *42*, 1892-1895.
[42] Sun, Z. H.; Yang, Z.; Zhou, J. H.; Yeung, M. H.; Ni, W. H.; Wu, H. K. and Wang, J. F., *Angew. Chem. Int. Ed.* **2009**, *48*, 2881-2885.
[43] Fujita, H.; Izawa, M. and Yamazaki, H., *Nature* **1962**, *196*, 666.
[44] Ksar, F.; Surendran, G.; Ramos, L.; Keita, B.; Nadjo, L.; Prouzet, E.; Beaunier, P.; Hagege, A.; Audonnet, F. and Remita, H., *Chem. Mater.* **2009**, *21*, 1612-1617.
[45] Abidi, W.; Selvakannan, P. R.; Guillet, Y.; Lampre, I.; Beaunier, P.; Pansu, B.; Palpant, B. and Remita, H., *J. Phys. Chem. C* **2010**, *114*, 14794-14803.
[46] Lehoux, A.; Ramos, L.; Beaunier, P.; Uribe, D. B.; Dieudonne, P.; Audonnet, F.; Etcheberry, A.; Jose-Yacaman, M. and Remita, H., *Adv. Funct. Mater.* **2012**, *22*, 4900-4908.
[47] Doherty, R. P.; Krafft, J.-M.; Methivier, C.; Casale, S.; Remita, H.; Louis, C. and Thomas, C., *J. Catal.* **2012**, *287*, 102-113.
[48] Hugon, A.; Delannoy, L.; Krafft, J.-M. and Louis, C., *J. Phys. Chem. C* **2010**, *114*, 10823.
[49] Mirdamadi-Esfahani, M.; Mostafavi, M.; Keita, B.; Nadjo, L.; Kooyman, P. and Remita, H., *Gold Bull.* **2010**, *43*, 49-56.
[50] Rodriguez-Lopez, J. L.; Montejano-Carrizales, J. M. and Jose-Yacaman, M., *Appl. Surf. Sci.* **2003**, *219*, 56-63.
[51] Liu, X. Y.; Wang, A. Q.; Zhang, T.; Su, D. S. and Mou, C. Y., *Catal. Today* **2011**, *160*, 103.
[52] Liu, X. Y.; Wang, A. Q.; Li, L.; Zhang, T.; Mou, C. Y. and Lee, J. F., *J. Catal.* **2011**, *278*, 288.
[53] Chimentao, R. J.; Medina, F.; Fierro, J. L. G.; Llorca, J.; Sueiras, J. E.; Cesteros, Y. and Salagre, P., *J. Mol. Catal. A: Chem.* **2007**, *274*, 159-168.
[54] Kamat, P. V., *J. Phys. Chem. B* **2002**, *106*, 7729.
[55] Doherty, R. P.; Krafft, J.-M.; Methivier, C.; Casale, S.; Remita, H.; Louis, C. and Thomas, C., *J. Catal.* **2012**, *287*, 102-113.
[56] Tominaga, M.; Taema, Y. and Taniguchi, I., *J. Electronanal. Chem.* **2008**, *624*, 1-8.
[57] Brodie-Linder, N.; Lecaer, S.; Alam, M. S.; Renault, J. P. and Alba-Simionesco, C., *Phys. Chem. Chem. Phys.* **2010**, *12*, 14188-14195.
[58] Brodie-Linder, N.; Besse, R.; Audonnet, F.; Lecaer, S.; Deschamps, J.; Imperor-Clerc, M. and Alba-Simionesco, C., *Microporous Mesoporous Mater.* **2010**, *132*, 518-525.
[59] Haruta, M., *Catal. Surv. Jpn.* **1997**, *61*.
[60] Tsubota, S.; Cunningham, D. a. H.; Bando, Y. and Haruta, M., *Stud. Surf. Sci. Catal.* **1995**, *91*, 227.
[61] Tsubota, S.; Haruta, M.; Kobayashi, T.; Ueda, A. and Nakahara, Y., *Stud. Surf. Sci. Catal.* **1991**, *63*, 695.
[62] Zanella, R.; Delannoy, L. and Louis, C., *Appl. Catal., A* **2005**, *291*, 62-72.
[63] Zanella, R.; Giorgio, S.; Henry, C. R. and Louis, C., *J. Phys. Chem. B* **2002**, *106*, 7634-7642.

[64] Baxendale, J. and Koulkes-Pujo, A., *J. Chem. Phys.* **1970**, 1602-1607.
[65] Gachard, E.; Remita, H.; Khatouri, J.; Belloni, J.; Keita, B. and Nadjo, L., *New J. Chem.* **1998**, *22*, 1257-1265.
[66] Dey, G.; El Omar, A.; Jacob, J.; Mostafavi, M. and Belloni, J., *J. Phys. Chem. A* **2011**, *115*, 383-391.
[67] Abidi, W. and Remita, H., *Recent Pat. Eng.* **2010**, *4*, 170-188.
[68] Khatouri, J.; Mostafavi, M.; Amblard, J. and Belloni, J., *Chem. Phys. Lett.* **1992**, *191*, 351-356.
[69] Ksar, F.; Ramos, L.; Keita, B.; Nadjo, L.; Beaunier, P. and Remita, H., *Chem. Mater.* **2009**, *21*, 3677-3683.
[70] Redjala, T.; Remita, H.; Apostolescu, G.; Mostafavi, M.; Thomazeau, C. and Uzio, D., *Gas Oil Sci. Technol.* **2006**, *61*, 789.
[71] Wang, D.; Villa, A.; Porta, F.; Prati, L. and Su, D., *J. Phys. Chem. C* **2008**, *112*, 8617.
[72] Mirdamadi-Esfahani, M.; Mostafavi, M.; Keita, B.; Nadjo, L.; Kooyman, P. and Remita, H., *Gold Bull.* **2010**, *43*, 49-56.
[73] Chen, X.; Zhu, H.; Zhao, J.; Zheng, Z. and Gao, X., *Angew. Chem., Int. Ed.* **2008**, *47*, 5353-5356.
[74] Awazu, K.; Fujimaki, M.; Rockstuhl, C.; Tominaga, J.; Murakami, H.; Ohki, Y.; Yoshida, N. and Watanabe, T., *J. Am. Chem. Soc.* **2008**, *130*, 1676-1680.
[75] Xu, S.; Ng, J.; Zhang, X.; Bai, H. and Sun, D. D., *Int. J. Hydrogen Energy* **2010**, *35*, 5254-5261.
[76] Grabowska, E.; Zaleska, A.; Sorgues, S.; Kunst, M.; Etcheberry, A.; Colbeau-Justin, C. and Remita, H., *J. Phys. Chem. C* **2013**, *117*, 1955-1962.
[77] Kowalska, E.; Remita, H.; Colbeau-Justin, C.; Hupka, J. and Belloni, J., *J. Phys. Chem. C* **2008**, *112*, 1124-1131.
[78] Tang, H.; Prasad, K.; Sanjines, R.; Schmid, P. E. and Levy, F., *J. Appl. Phys.* **1994**, *75*, 2042-2047.
[79] Palik, E. in *Handbook of Optical Constants of Solids*, *Vol.* Academic Press, U. S., **1985**.
[80] Qu, P.; Zhao, J.; Shen, T. and Hidaka, H., *Journal of Molecular Catalysis, A: Chemical* **1998**, *129*, 257-268.
[81] Watanabe, T.; Takizawa, T. and Honda, K., *J. Phys. Chem.* **1977**, *81*, 1845-1851.
[82] Wu, T. X.; Liu, G. M.; Zhao, J. C.; Hidaka, H. and Serpone, N., *J. Phys. Chem. B* **1998**, *102*, 5845-5851.
[83] Hu, X. F.; Mohamood, T.; Ma, W. H.; Chen, C. C. and Zhao, J. C., *J. Phys. Chem. B* **2006**, *110*, 26012-26018.
[84] Lopez-Sanchez, J. A.; Dimitratos, N.; Hammond, C.; Brett, G. L.; Kesavan, L.; White, S.; Miedziak, P.; Tiruvalam, R.; Jenkins, R. L.; Carley, A. F.; Knight, D.; Kiely, C. J. and Hutchings, G. J., *Nature Chmistry* **2011**, *3*, 551-556.
[85] Kumar, K.-N. P.; Kumar, J. and Keizer, K., *J. Am. Ceram. Soc.* **1994**, *77*, 1396-1400.
[86] Shen, L. F.; Zhang, X. G.; Uchaker, E.; Yuan, C. Z. and Cao, G. Z., *Adv. Energy Mater.* **2012**, *2*, 691-698.
[87] Wang, Y. Y.; Zhou, G. W.; Li, T. D.; Qiao, W. T. and Li, Y. J., *Catal. Commun.* **2009**, *10*, 412-415.
[88] Yu, J. G.; Yu, J. C.; Leung, M. K.-P.; Ho, W. K.; Cheng, B.; Zhao, X. J. and Zhao, J. C., *J. Catal.* **2003**, *217*, 69-78.
[89] Kang, E.; Jung, Y. S.; Cavanagh, A. S.; Kim, G. H.; George, S. M.; Dillon, A. C.; Kim, J. K. and Lee, J., *Adv. Funct. Mater.* **2011**, *21*, 2430.
[90] Scherer, G. W., *J. Am. Ceram. Soc.* **1990**, *73*, 3-14.
[91] Fonash, S. J., *Solar cell device physics*, Academic Press, New York, London, **1981**, p.
[92] Tahiri Alaoui, O.; Herissan, A.; Le Quoc, C.; Zekri, M.; Sorgues, S.; Remita, H. and Colbeau-Justin,

C., *J. Photochem. Photobiol. A* **2012**, *242*, 34-43.
[93] Kamat, P. V., *J. Phys. Chem. Lett.* **2012**, *3*, 663-672.
[94] Linsebigler, A. L.; Lu, G. and John T. Yates, J., *Chem. Rew.* **1995**, *95*, 735-758.
[95] Zhang, J.; Shi, F.; Lin, J.; Chen, D.; Gao, J.; Huang, Z.; Ding, X. and Tang, C., *Chem. Mater.* **2008**, *20*, 2937-2941.
[96] Zhang, J.; Yu, J. G.; Zhang, Y. M.; Li, Q. and Gong, J. R., *Nano Lett.* **2011**, *11*, 4774-4779.
[97] Liu, X.; Wang, A.; Zhang, T.; Su, D.-S. and Mou, C.-Y., *Catal. Today* **2011**, *160*, 103-108.
[98] Wang, W.; Serp, P.; Kalck, P. and Faria, J. L., *J. Mol. Catal. A: Chem.* **2005**, *235*, 194-199.
[99] Laoufi, N. A.; Tassalit, D. and Bentahar, F., *Global NEST Journal* **2008**, *10*, 404-418.

CHAPTER IV

RADIOLYTIC SYNTHESIS OF Cu SULFIDES AND OXIDES NANOSTRUCTURES: APPLICATION IN PHOTOCATALYSIS UNDER VISIBLE ILLUMINATION

Chapter 4 Radiolytic synthesis of Cu sulfides and oxides nanostructures: application in photocatalysis under visible illumination

Although TiO_2 has been widely investigated because of its excellent photocatalytic activity, his wide band-gap restricts its application under visible illumination. As demonstrated in the former chapter, modification with noble metals or doping with non-metal atoms are costly and not easy methods. Therefore, non-titanium oxides or compounds are developed as potential photocatalysts. In this thesis, synthesis of copper oxides and copper sulfides with special morphologies and their photocatalytic activity were investigated. The study is divided into two sections.

In the first section, the controllable synthesis of copper oxides including CuO and Cu_2O was carried out, and their photocatalytic performance under visible light was investigated. Copper oxide (CuO) nanowires and cuprous oxide (Cu_2O) nanocrystals have been synthesized through γ-irradiation of aqueous solutions containing $CuCl_2$, NaOH, sodium dodecyl sulfate (SDS) and isopropyl alcohol under ambient conditions. The product composition can be changed by modulating the amount of the NaOH base. The morphology of the products can be accurately controlled by changing the concentrations of SDS and isopropyl alcohol. The effects of the surfactant and isopropyl alcohol on the product morphology were discussed. A possible formation mechanism was also proposed. The photocatalytic property of the synthesized copper oxides was evaluated for the degradation of a model pollutant (methyl orange, MO) under visible illumination. Cu_2O nanocrystals with specific morphology have an excellent photocatalytic activity for dye degradation under visible illumination. Especially, truncated octahedral Cu_2O exhibits the highest photoactivity.

In the second section, uniform CuS nanotubes (NTs) with a diameter of 200 nm were synthesized without template by gamma irradiation of aqueous solutions of $CuCl_2$ and

NaS_2O_3. The length of the CuS NTs are from hundreds nanometers up to ~2 micrometers. The external diameter and wall thickness are respectively ~220 nm and ~40 nm. The morphology of CuS NTs depends on the ratio of NaS_2O_3 to $CuCl_2$. The photocatalytic activity of the as-prepared CuS NTs was investigated for decomposition of rhodamine B (RhB) in aqueous solution. The synthesized CuS NTs exhibit a photocatalytic activity under visible light.

4.1 Synthesis of CuO and Cu_2O nanostructures of controlled morphology: application in photocatalysis under visible light

4.1.1 Introduction

Materials in nano-scale, because of their small-size and the quantum confinement effect, exhibit interesting physical and chemical properties, which differ from the corresponding bulk.[1-3] Different ways such as hydrothermal or solvothermal methods are used for the synthesis of nanomaterials.[4-5] γ-Irradiation is a distinctive approach which was first discovered for preparing nanomaterial by Fujita *et al.* in 1962.[6] In recent years, γ-Irradiation route has been well developed for the synthesis of semiconductors and inorganic nanomaterials.[7-19]

Nanosized semiconductors such as CuO and Cu_2O have been intensively investigated for their particular optical and electronic properties. As one of the most popular p-type semiconductor with a narrow band gap (1.2eV), CuO is employed as anodes for lithium ion batteries,[20-22] catalysts,[23-25] and gas sensor.[26-28] Cu_2O, which is an important p-type semiconductor with a direct band gap (2.17 eV), has been demonstrated to be used as a photocatalyst, and for solar energy conversion,[29-30] photochemical decomposition of water into H_2 and O_2 under visible light irradiation.[31-32] The different morphologies of Cu_2O nanocrystals can exhibit special properties. For example, octahedral Cu_2O nanocrystals with entirely {111} surfaces show a better performance in the photocatalytic degradation of dye molecules than those of other shapes. [33]

Previously, our group has reported radiolytic synthesis of cuprous oxides with various

morphologies such as eight-pod cubes, six-armed starlike, octahedral, and spindle like structures.[8, 34] In this work, we further designed an environmentally convenient way to prepare CuO nanowires, octahedral and cubic Cu_2O with smaller and more uniform distribution in size. Interestingly, through delicately modulating the ratio of copper ion and hydroxyl ion, we could control the synthesis of CuO nanowires and Cu_2O of octahedral or cubic structures. Moreover, it has been found that the amount of isopropanol has a significant impact on the morphology of Cu_2O crystals. The photocatalytic activity of the synthesized samples was investigated for degradation of methyl orange (MO) under visible illumination.

4.1.2 Results and discussion

4.1.2.1 Characterizations

Table 4.1 Synthesis Conditions and Morphology of the Obtained Products.

sample	[a]NaOH (mol/L)	[b]α	isopropyl alcohol (mL)	composition	morphology
1	9.3×10^{-2}	2.35	5	CuO	nanowires
2	7.5×10^{-2}	1.90	5	Cu_2O	octahedra
3	7.5×10^{-2}	1.90	12	Cu_2O	truncated octahedra
4	7.5×10^{-2}	1.90	20	Cu_2O	nanocubes
5	8.3×10^{-2}	2.10	5	CuO and Cu_2O	nanowires and octahedra

[a]NaOH: the concentrations are proportional to the total volumn of solution, 40 mL.

[b]α = molar ratio of OH^- to Cu^{2+}.

Figure 4.1a shows the XRD pattern of the synthesized CuO (sample 1). The XRD pattern shows the expected (110), ($\bar{1}11$), (111) and ($\bar{2}02$) reflection peaks. All of the peaks can be indexed to tenorite (monoclinic) CuO (JCPDS card no. 05-661) with cell parameters a = 4.684 Å, b = 3.425 Å, and c = 5.129 Å. The XRD pattern of the synthesized Cu_2O (sample 2) is shown in **Figure 4.1b**. All of the peaks can be indexed to cuprite (cubic) Cu_2O (JCPDS

card no. 05-667) with cell parameter a = 4.269 Å. No other characteristic peaks were observed, indicating the high purity of the as-synthesized products. As it can be seen, the high intensity of the (111) diffraction peak suggests that the obtained Cu_2O crystals (sample 2) are mainly dominated by the (111) facets.

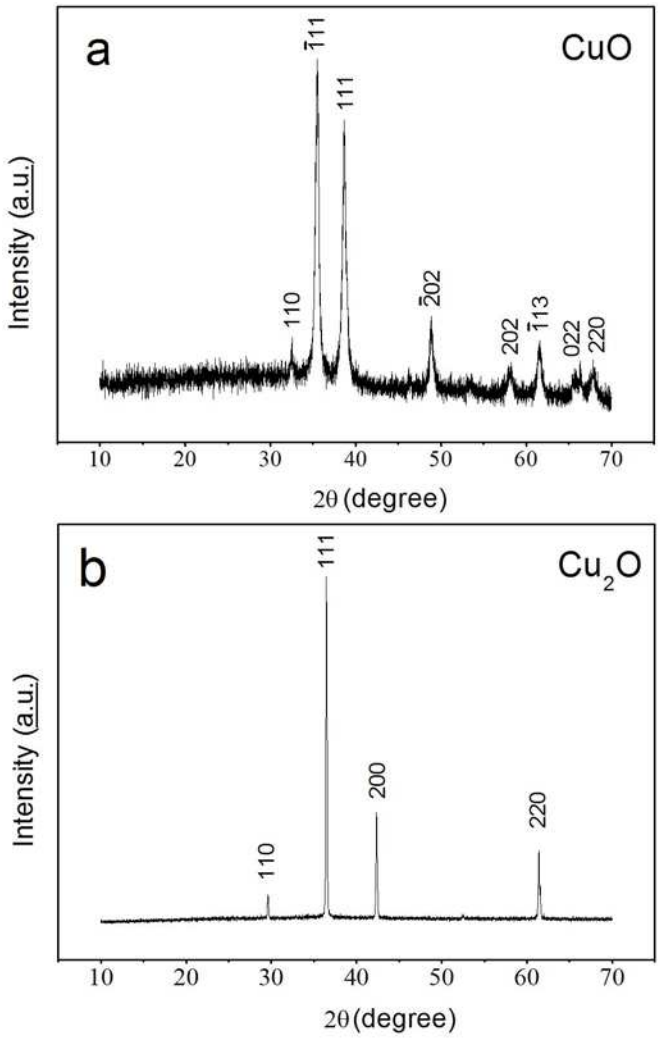

Figure 4.1 XRD patterns of **(a)** the synthesized sample 1, CuO nanowires; **(b)** the synthesized sample 2, Cu_2O octahedra.

The equations involved in the reaction processes are shown as follows:

$$H_2O \xrightarrow{\gamma-ray} e_{aq}^{-}, H^{\bullet}, HO^{\bullet}, H_3O^{+}, H_2, H_2O_2 \quad (4.1)$$

$$CH_3CH(OH)CH_3 + HO^{\bullet} \rightarrow CH_3C^{\bullet}(OH)CH_3 + H_2O \quad (4.2)$$

$$Cu^{2+} + e_{aq}^{-} \text{ or } (CH_3C^{\bullet}(OH)CH_3) \rightarrow Cu^{+} \quad (4.3)$$

$$Cu^{+} + OH^{-} \rightarrow CuOH \quad (4.4)$$

$$2CuOH \xrightarrow{\gamma-ray} H_2O + Cu_2O\downarrow \quad (4.5)$$

$$Cu^{2+} + 2OH^{-} \rightarrow Cu(OH)_2 \quad (4.6)$$

$$Cu(OH)_2 \xrightarrow{\gamma-ray} H_2O + CuO\downarrow \quad (4.7)$$

Radiolysis of aqueous solution induces many active intermediates, such as strong reductive hydrated electrons (standard redox potential equal to -2.87 V), H radicals and oxidative radicals $^{\bullet}OH$ (eq 4.1).[8, 34] Isopropyl alcohol is introduced to scavenge $^{\bullet}OH$,[35] leading to reducing $(CH3)_2C^{\bullet}OH$ radicals (-1.1 V). When a small quantity of NaOH is added in the solution, the dissolved Cu^{2+} can be mainly reduced into Cu^{+} by e_{aq}^{-} and $CH_3C_3(OH)CH_3$ radicals (eq 4.3), while OH^{-} quickly combines with Cu^{+} to form CuOH, which finally decomposes into Cu_2O (eqs 4.4 and 4.5) under γ-irradiation. Pure Cu_2O is obtained because of the stoichiometric ratio (the molar ratio of OH^{-} to Cu^{2+}; **Table 4-1**) close to 2 (equals 1.90). When the concentration of NaOH was increased to a certain extent (α ~ 2.35; Table 1), $Cu(OH)_2$ precipitate formed. Then, $Cu(OH)_2$ decomposes into CuO under γ-irradiation (eqs 4.6 and 4.7), forming nanowires. In order to study the role of γ-irradiation in the formation of CuO nanowires, blank experiments without γ-irradiation were carried out, while keeping other conditions the same as above. In this case, no CuO nanowires were found. So, γ-irradiation is important for the formation of CuO nanowires. **Scheme 4-1** shows the formation processes of CuO and Cu_2O.

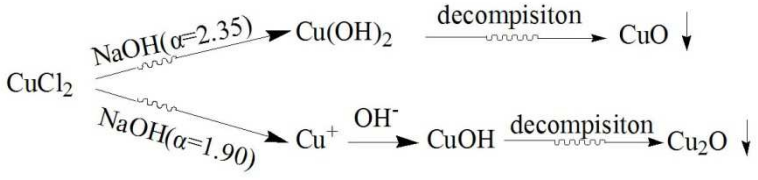

Scheme 4-1 Formation Processes of CuO and Cu_2O

To study the effect of NaOH on the product compositions, an experiment with an intermediate concentration (between sample 1 and sample 2) was conducted. For this sample, the molar ratio of OH^{-} to Cu^{2+} was 2.10 (**Table 4-1**, sample 5). **Figure 4.2** presents the XRD

pattern of the synthesized sample 5. It can be clearly seen that the product exhibits a two-phase composition: narrow peaks can be ascribed to Cu_2O, while broad peaks attributed to CuO.

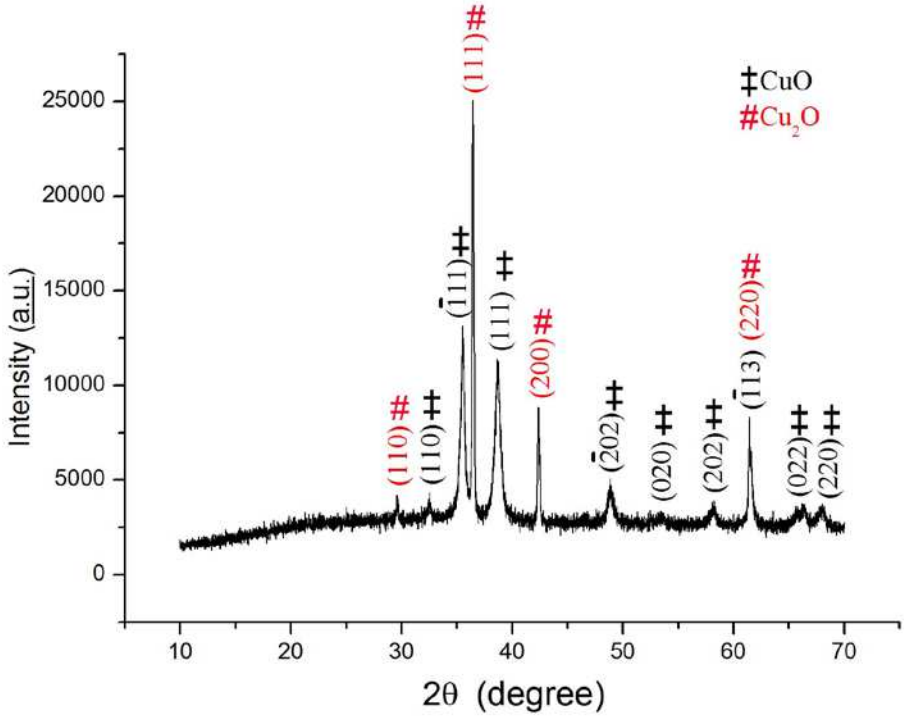

Figure 4.2 XRD pattern of sample 5.

TEM images in **Figure 4.3** show that the structures consisted of octahedrons and nanowires, corresponding to the Cu_2O and CuO respectively. This demonstrates that the excess OH^- has a significant effect on the radiolysis synthesis of copper oxides.

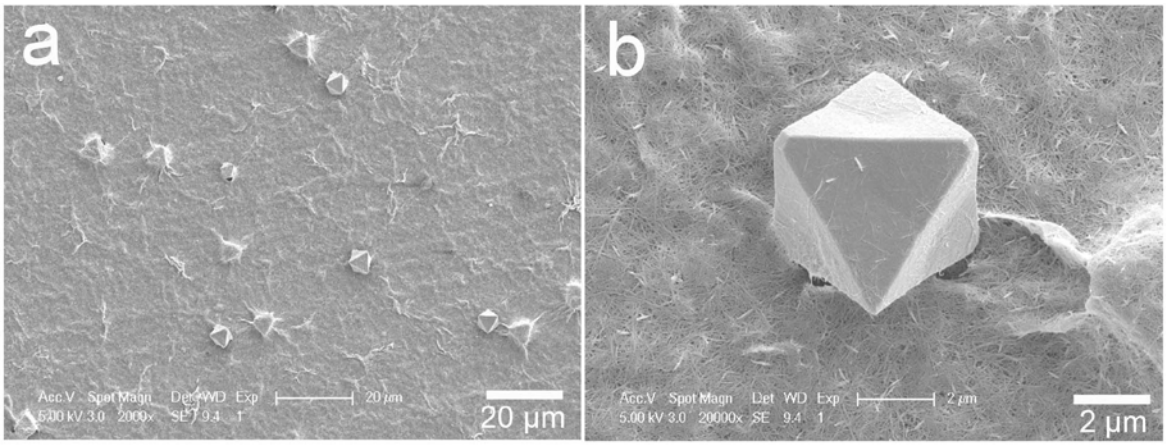

Figure 4.3 TEM images of the sample 5 at a lower magnification **(a)**, and a higher magnification **(b)**.

4.1.2.2 Effect of Isopropyl Alcohol

To evaluate the effect of isopropanol on the morphology of Cu_2O crystals, blank experiments with other amounts of isopropanol were carried out. Panel b, c and d of **Figure 4.4** show the SEM images of the Cu_2O products obtained with different quantity of isopropanol. In the presence of 5 mL isopropanol, the products are composed of uniform octahedral Cu_2O (**Figure 4.4b**), with sizes from 900 nm to 1100 nm. When the amount of isopropanol increased to 12 mL, the Cu_2O structures show the morphology of the truncated octahedra (**Figure 4.4c**). While this amount increased to 20 mL, nanocubes of Cu_2O are obtained with sizes in the same range as for sample 2 (**Figure 4.4d**). The results demonstrated above indicate that the amount of isopropanol has an important effect on the morphology of the obtained Cu_2Ostructures. The growth of Cu_2O crystals may be explained as this: at the early stage of irradiation, small Cu_2O seeds are formed. These small seeds then aggregate into larger particles. Isopropanol is employed as the $^{\bullet}OH$ oxidative radicals scavenger.[36] So more isopropanol is added, faster the small Cu_2O particles grow under γ-irradiation. Thereby, the amount of isopropanol might favor the growth rate along the [100] direction compared to that in the [111] direction. The ratio of growth rate of the [100] direction to that of [111] is defined as ***R***. Kuo and Wang reported that the morphology of Cu_2O was dependent on the value of ***R***.[33, 37-38] When ***R*** is ~ 0.58, perfect cubic Cu_2O crystals are formed. When ***R*** is ~1.73, octahedral crystals are synthesized. When ***R*** is ~1.15, the morphology of Cu_2O is truncated octahedra, a morphology between cubes and octahedra. In Kuo's study, the amount of the reducing agent $NH_2OH{\bullet}HCl$ in a $CuCl_2$-$NH_2OH{\bullet}HCl$-SDS-NaOH system influenced the value of ***R***.[33] In these radiolytic syntheses, it is believed that the formation processes are in agreement with the reported case. The amount of 2-propanol has an influence on the reducing radicals, consequently affects the value of ***R***, resulting in the morphology evolution from cubic to octahedral for Cu_2O cystals.

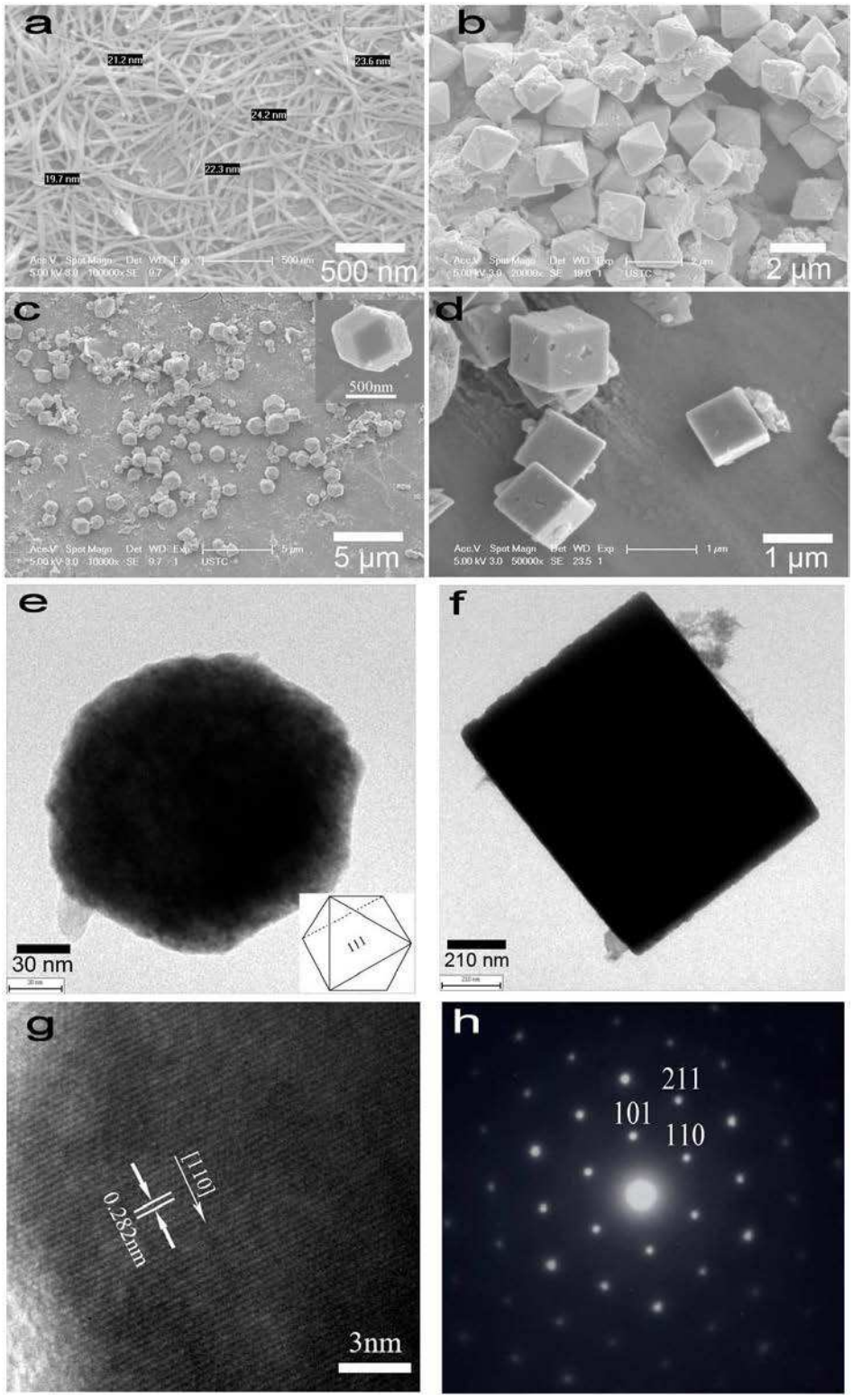

Figure 4.4 SEM images of sample 1-4 **(a, b, c** and **d)**; TEM images of sample 2 **(e)**, and sample 4 **(f)**; HRTEM image of sample 2 **(g)** and its corresponding SAED pattern **(h)**.

In Kuo's study, the syntheses of Cu_2O nanocrystals with systematic shape evolution from cubic to octahedral structures were achieved by simply varying the amount of the reductant $NH_2OH \cdot HCl$ added to the reaction mixture.[37] In the report, 0.25 mL of $NH_2OH \cdot HCl$ (0.2 M) added to $CuCl_2$-NaOH-SDS solution resulted in a truncated cubic nanostructure of Cu_2O. When the amount of $NH_2OH \cdot HCl$ was increased to 0.85 mL, octahedral Cu_2O nanostructures were obtained. Cuboctahedral and truncated octahedral Cu_2O nanostructures were also obtained with the increase of $NH_2OH \cdot HCl$. The reducing isopropyl alcohol radical plays a significant role in the radiolytic synthesis of these nanostructures.

4.1.2.3 Effect of SDS on the morphology of copper oxides

The morphology of the synthesized products was observed using SEM technique. The SEM image in **Figure 4.4a** shows that sample 1 is composed of wires with a diameter of ~20 nm. These CuO nanowires interlace together, as it can be seen from the image. The length of the nanowires, which could not be precisely measured, is larger than 5 μm.

The SDS plays a role in the formation of CuO nanowires. To understand this effect, parallel experiments without SDS were carried out. In this case only uniform nanoleaves are formed (**Figure 4.5a**). This proves that SDS affects the growth of CuO crystals, probably by poisoning specific facets.

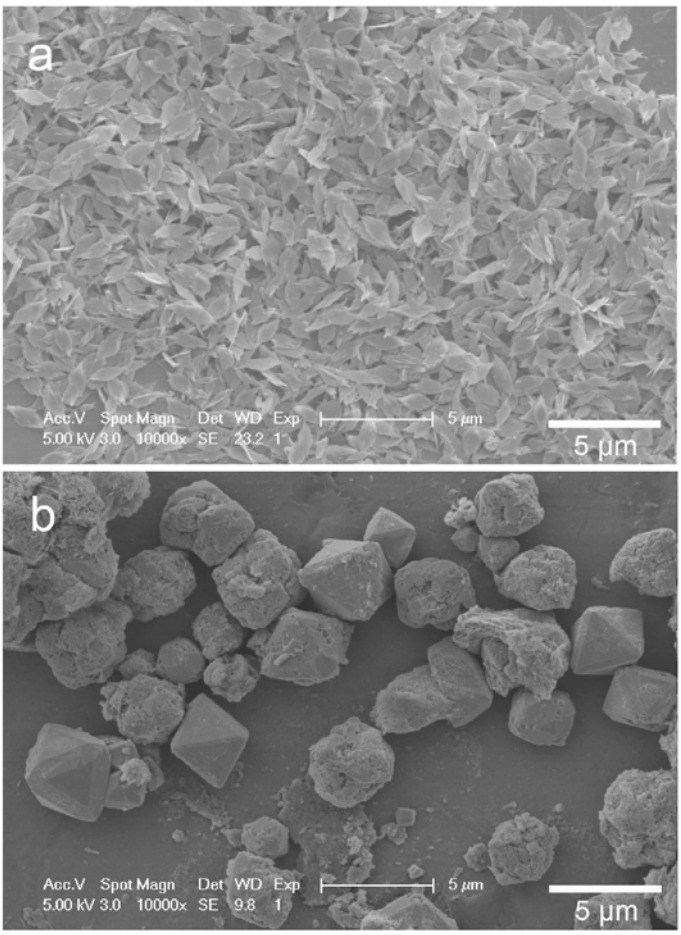

Figure 4.5 TEM images of CuO **(a)** and Cu_2O **(b)** prepared without SDS, the experimental conditions are corresponding to sample 1 and sample 2, respectively.

In the case of formation of Cu_2O particles, SDS has no obvious influence on the final Cu_2O structure. As shown in **Figure 4.5b**, Cu_2O octahedra were synthesized in the absence of SDS. However, the size of the octahedral Cu_2O nanostructures without SDS increased to ~ 3μm, as compared with 2 μm of Cu_2O octahedra in the presence of SDS.

The TEM images of sample 2 and sample 4 are shown in **Figure 4.4**, **e and f** respectively. **Figure 4.4g** gives the high-resolution TEM (HRTEM) image of the obtained Cu_2O crystals. The image clearly shows the lattice fringes with interplanar spacing of 0.282 nm, which is close to the distance between the (110) lattice planes of the cubic crystal structure of Cu_2O (0.302nm, standard in JCPDS card 05-667). The corresponding selected-area electron diffraction (SAED) pattern (**Figure 4.4h**) also verifies that the as-prepared products are signal of cubic Cu_2O crystals, in agreement with the XRD pattern

results.

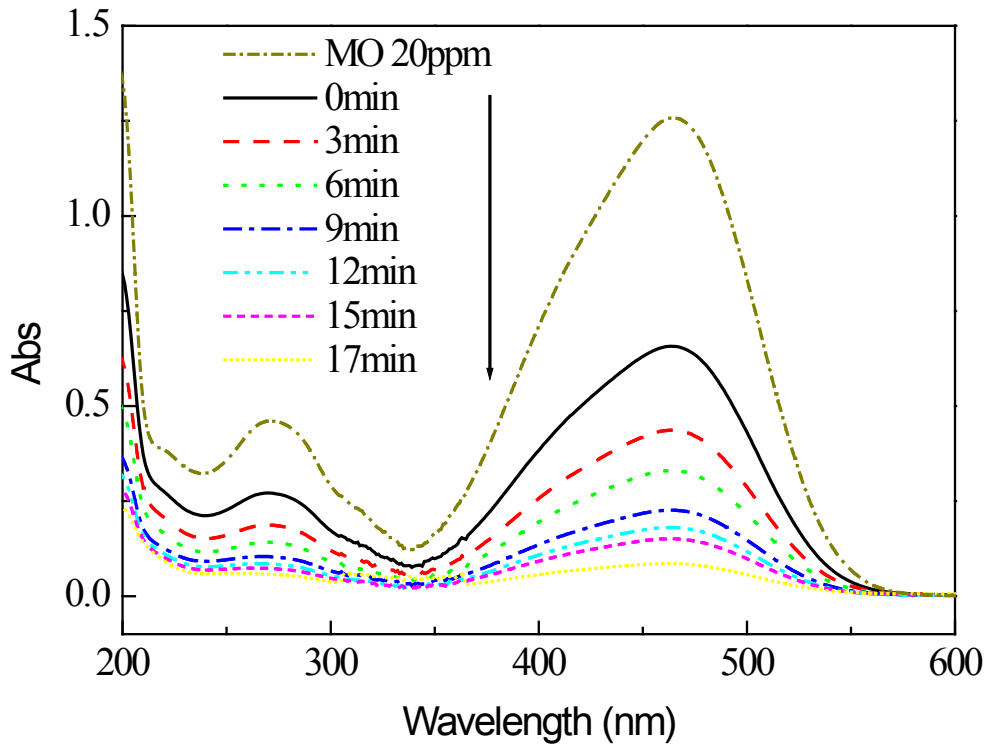

Figure 4.6 UV-vis absorption spectra showing the photodegradation of RhB in with truncated octahedral Cu_2O under visible illumination. Optical path: 2 mm.

4.1.2.4 Photocatalytic Tests

The photocatalytic activity of the synthesized copper oxides was studied for degradation of methyl orange under visible illumination. The truncated octahedral Cu_2O nanostructures exhibit an excellent photoactivity. As it can be seen in **Figure 4.6**, after 17 minutes of visible irradiation, nearly 94 % of MO was degraded. It also should be figured out that the sharp decrease of MO concentration at 0 minute with respect to the initial MO concentration is due to the adsorption of MO on the Cu_2O surface. The great adsorption of the dye MO on Cu_2O was also reported before.[33] This fast adsorption process is attributed to the electrostatic attraction between the positively charged surface of Cu_2O and the negatively charged MO molecules.[39-40]

Figure 4.7 presents the photodegradation of MO under visible light in the presence of CuO nanowires, octahedral and truncated octahedral Cu_2O structures. In the blank experiment

(**Figure 4.7a**, trace i), nearly no concentration decrease of MO is observed, indicating MO molecules are very stable subjected to visible illumination. CuO nanowires do not exhibit any activity in the MO photodegradation under visible light. In this study, truncated octahedral Cu_2O structures exhibit much higher photoactivity than the octahedral ones. In contrast, Xu *et al.* and Kuo *et al.* reported Cu_2O octahedra with entirely exposed {111} crystal surfaces exhibit higher photoactivity than cubic ones.[41] However, if one examines in detail their studies, it can be found that the octahedral Cu_2O structures have higher capability for adsorption than Cu_2O cubes. Namely, the MO degradation by Cu_2O octahedral is mainly due to the effective adsorption on Cu_2O {111} surfaces. It is hypothesized that the high photocatalytic efficiency of Cu_2O truncated octahedra is owing to its conjunct edges of {111} and {100} crystal surfaces. Further experiments are necessary to be conducted to evidence this hypothesis. MO concentration significantly decreases at the beginning of the photocatalytic reaction (**Figure 4.7a**, trace iii), which can be attributed to the great adsorption capability of octahedral Cu_2O structures for MO.

The first order kinetics fittings of MO photodegradation with the synthesized samples are shown in **Figure 4.7b**. MO photodegradation with truncated-octahedral Cu_2O structures presents a fine linear correlation for the first order kinetics fitting, indicating that the photocatalytic degradation is a steady reaction and the photocatalyst Cu_2O is stable.

It is worth noting the synthesized Cu_2O is hydrophobic. Cu_2O powder merely floats on the solution and cannot form a homogeneous suspension. The photocatalytic activity of the synthesized Cu_2O is weakened due to the insufficient contact between Cu_2O and dissolved MO molecules. On the other hand, the photocatalytic results may present a large error because the photocatalyst Cu_2O partially adheres to the side walls of the quartz reactors. In the case of hydrophilic P25, the suspension is homogeneous, which facilitates the photodegradation and ensures the steady reaction.

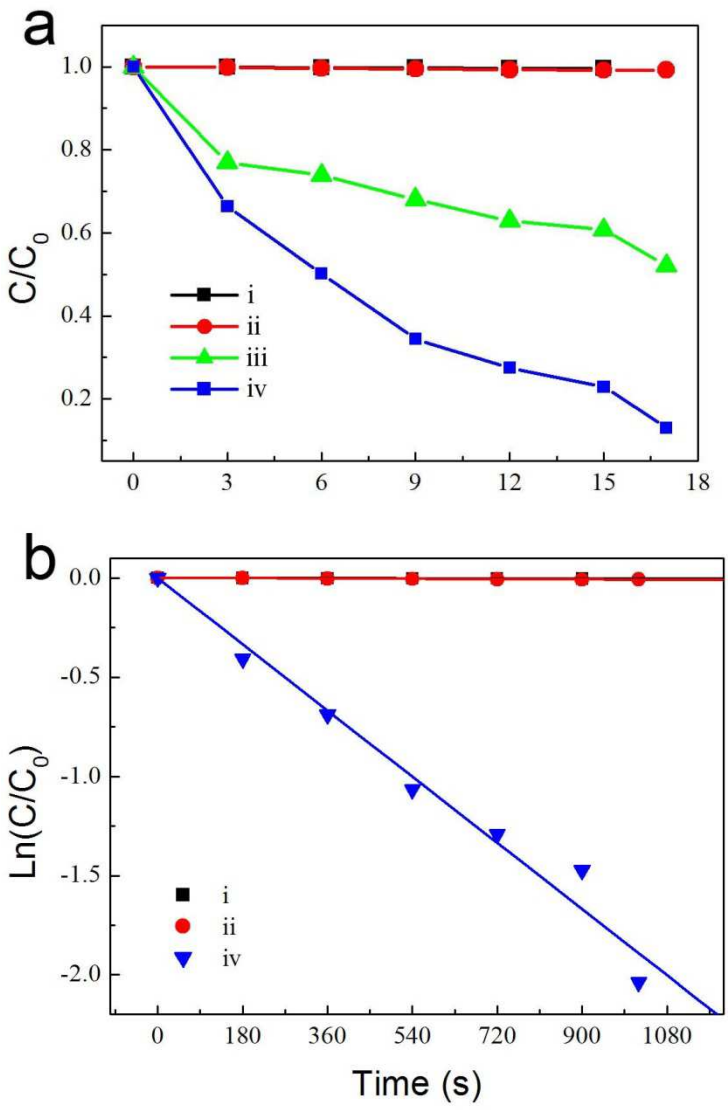

Figure 4.7 (a) The time runs of MO concentration and **(b)** pseudo first-order kinetic fittings for MO photodegradation in the presence of (i) no catalyst, (ii) CuO nanowires, (iii) Cu_2O octahedra and (iv) Cu_2O truncated-octahedra under visible illumination.

After the first photoreaction cycling under visible light for 18 minutes, the precipitate was collected, washed and dried. The powder is still brick-red, exhibiting no obvious change of color. The morphology of the Cu_2O after the first photocatalytic reaction cycling was observed using SEM technique. As presented in **Figure 4.8**, truncated octahedra can be clearly seen from the images before and after photoreaction. Furthermore, the size of the Cu_2O nanostructures do not change much after the photocatalytic reaction.

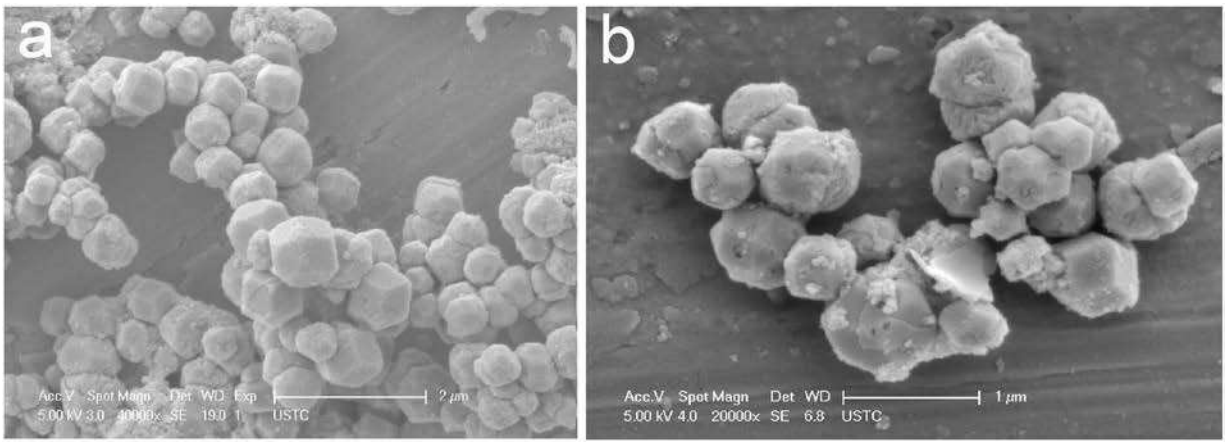

Figure 4.8 SEM images of **(a)** sample 3, and **(b)** sample 3 after the photocatalytic reaction under visible light for 18 minutes.

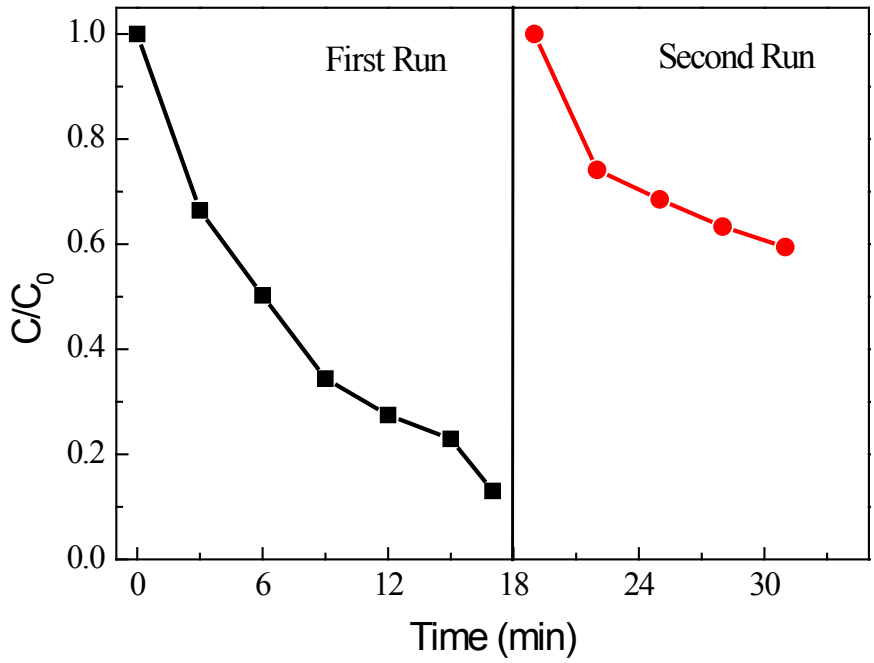

Figure 4.9 The plots for MO cycling photodegradation under visible light with the sample 3.

Cycling photodegradation of MO by truncated-octahedral Cu_2O (sample 3) was carried out to investigate the stability. As shown in **Figure 4.9**, the second run of photoreaction exhibits a slower degradation rate compared to the first run. Nevertheless, MO concentration decreases by 40 percent after 12 minutes, which is still fast for visible photodegradation. In the first run, 10 mg of Cu_2O was dispersed in 20 mL of MO solution with a concentration of 20 ppm. But, only 7 mg of Cu_2O was recycled after the reaction due to the inevitable quantity

loss. Note that Cu_2O powder is still hydrophobic after the first photoreaction run. Such a small amount of Cu_2O cannot form a well dispersed suspension, which severely decreases the efficiency of the photoreaction. As observed in the experiment, the MO solution turned to almost clear after 5 minutes because the few Cu_2O powder adhered to the side walls of the quartz reactor.

4.1.3 Conclusion of this section

In summary, CuO nanowires and Cu_2O nanocrystals with shape evolution from cubic to octahedral structures have been successfully prepared via a simple γ-irradiation route at room temperature and under ambient pressure. As far as we know, this is the first report of radiolytic synthesis of CuO nanowires and Cu_2O nanocubes. It has been found that the products composition could be changed by modulating the molar ratio of OH^- and Cu^{2+}. For Cu_2O crystals, the morphology can be accurately controlled by choosing the amount of isopropanol. A formation mechanism is proposed. Related studies surely enriched the applications of radiolysis in synthesis of nanomaterials.

Truncated octahedra Cu_2O exhibit a better performance in the photocatalytic degradation of MO molecules. Further studies are necessary to investigate the relation between the Cu_2O morphology and its photoactivity, and to understand the related mechanisms. This Cu_2O nanostructures with specific morphologies may find applications in photocatalysis and other solar conversion technologies.

4.2 Radiolytic synthesis of CuS nanotubes with photocatalytic activity under visible light

4.2.1 Introduction

One dimension nanostructures such as nanotubes, nanorods and nanowires have currently drawn much attention owing to their unique electric, photonic and thermal properties and their unique applications in fabrication of nanoscale devices.[33, 38, 42] Commonly, templates are used to restrict the growth of certain crystal orientation to form 1-D nanostructures. In other cases, linking agents are employed to prepare such nanostructures. Therefore, a facile and efficient route for synthesis of 1-D nanostructures is still a challenge.

Copper sulfide is a typical p-type semiconductor, which can form a variety of stoichiometric compounds including covellite (CuS), anilite (Cu_7S_4), digenite (Cu_9S_5), djurleite ($Cu_{1.95}$) and chalcocite (Cu_2S).[43] They were widely applied in the field of optical recording, bio-medical, photothermal conversion, superionic materials, optical filters and solar cell devices.[44-45] In addition, CuS was also found to be a potential photocatalyst with activity under visible illumination.[46-49] The structure and size of CuS have a great influence on its photocatalytic activity.[50-51] Huang *et al.* synthesized uniform CuS nanotubes by a sacrificial templating method, which exhibit photocatalytic activity under UV illumination.[52-54] Ding *et al.* prepared CuS nanoflowers by a polyol route and they showed their photocatalytic activity under visible illumination.[55]

On the other hand, radiolysis is a powerful method to synthesize metal and semiconductors nanoparticles of controlled size and shape.[56] Here, we synthesized, for the first time, the homogeneous CuS nanotubes via γ-irradiation route under ambient temperature and pressure. No template was employed in the preparation of CuS nanotubes. The photocatalytic activity was examined for decomposition of RhB, a model pollutant, under visible illumination.

4.2.2 Results and Discussion

4.2.2.1 Characterizations

The obtained XRD pattern of the synthesized structure is shown in **Figure 4.10**. The peaks correspond to the ones of the hexagonal covellite CuS (standard JCPDF no. 06-464; a=3.792Å, b=3.792Å, c=16.344Å; α=90°, β=90°, γ=120°). No other characteristic peaks were observed, implying that the product is a pure–phase covellite CuS. In addition, it can be seen from the XRD pattern that the width of peaks are broadened, giving the information that the grain sizes of the synthesized CuS products are very small.

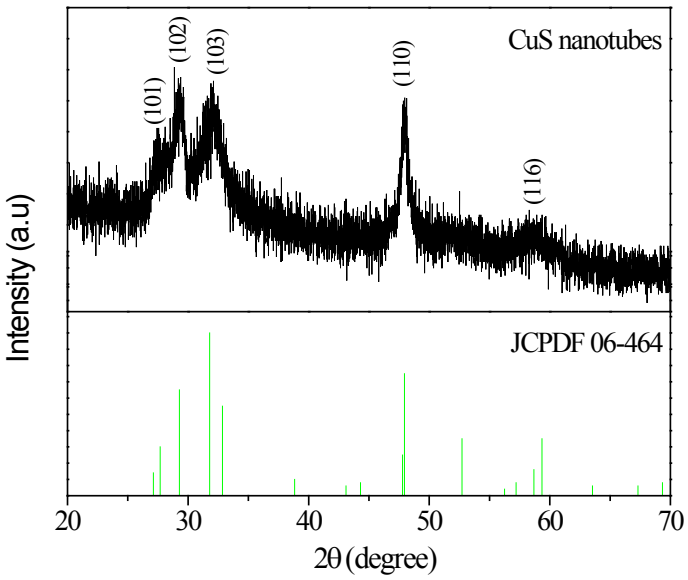

Figure 4.10 XRD pattern of the as-prepared CuS NTs, the bottom is the JCPDF card no. 06-464.

The possible reaction processes for the formation of CuS nanotubes could be described as follows:[11-12, 57]

$$Cu^{2+} + 2[S_2O_3]^{2-} \rightarrow [Cu(S_2O_3)_2]^{2-} \quad (4.8)$$

$$H_2O \xrightarrow{\gamma-ray} e_{aq}^-, H^\bullet, HO^\bullet, H_3O^+, H_2, H_2O_2 \quad (4.9)$$

$$2e_{aq}^- + [Cu(S_2O_3)_2]^{2-} \rightarrow Cu^{2+} + 2S^{2-} + 2SO_3^{2-} \quad (4.10)$$

$$Cu^{2+} + S^{2-} \rightarrow CuS\downarrow \rightarrow (CuS)n \quad (4.11)$$

When mixed Cu^{2+} and NaS_2O_3 are mixed, a green-blue complex $[Cu(S_2O_3)_2]^{2-}$ (Eq. 4.8)

forms. The reducing species (aqueous electrons and $H^{\cdot}$ radicals) are generated by water radiolysis (Eq. 4.9). Cu^{2+} and S^{2-} were released from the reduction of $[Cu(S_2O_3)_2]^{2-}$ by e_{aq}^{-} (Eq. 4.10). They combined *in-situ* with each other to form CuS molecules. Consequently, the CuS complexes aggregated to form nano-clusters and finally CuS nanotubes (Eq. 4.11).

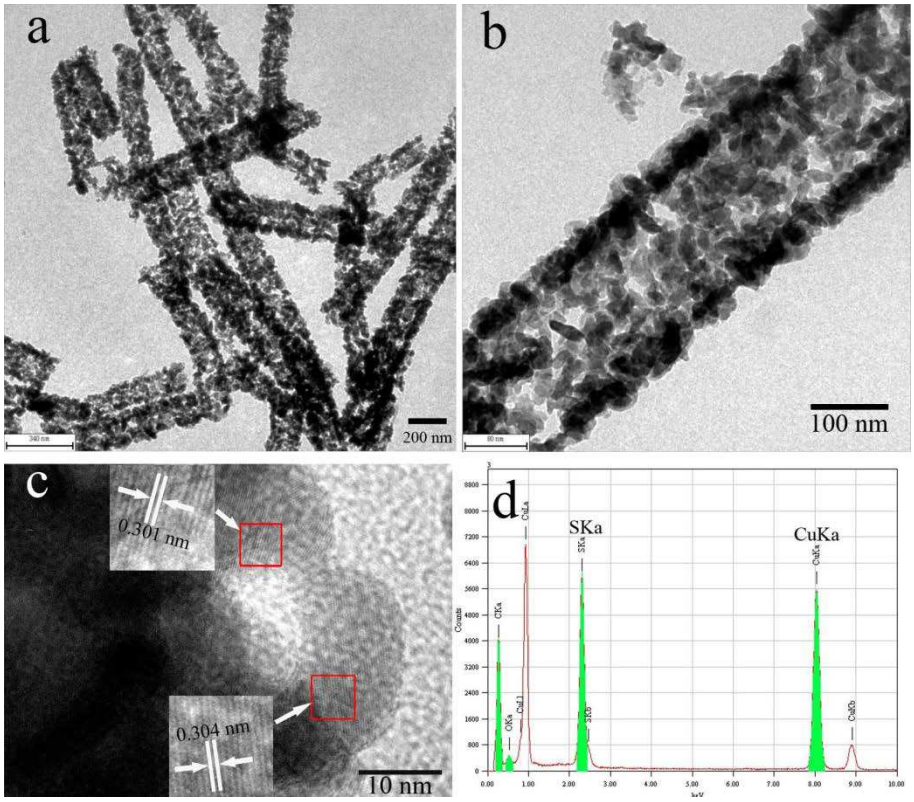

Figure 4.11 TEM images of as-prepared CuS nanotubes at low magnification **(a)**, high magnification **(b)**; HRTEM of CuS nanoparticles **(c)**; EDS of as-prepared CuS NTs **(d)**.

The morphology of the as-prepared CuS products was observed by transmission electronic microscopy (TEM) and High-Resolution TEM (HRTEM). **Figure 4.11a** shows that the CuS products have a one-dimensional structure, with external diameters of around 220 nm, and lengths are from several hundred nanometers up to about 2 micrometers. In addition, the difference in brightness between the edges and central parts gives the evidence that the one-dimension nanostructures of CuS exhibit a hollow structure. The internal diameter is about 140 nm. In **Figure 4.11b**, the structure of tubes is clearer. Moreover, the CuS nanotubes are composed of 1D-assembled small crystalline grains.

The X-ray energy dispersive spectrum (EDS) revealed that the products are composed of

Cu and S (**Figure 4.11d**). Besides the peaks of Cu and S, a weak signal corresponding to oxygen (probably due to the surface adsorption of air or to the oxidation by air), and the peak of carbon (due to the TEM grid) are obtained. The atomic ratio of Cu to S (determined from the area under the peaks of S Kα and Cu Kα) was found to be 48: 52, which is in well accordance with the stoichiometry of CuS.

Figure 4.11c shows an HR-TEM image of the nanotubes. The measured distances between fringes were 3.01 Å and 3.04 Å, and correspond to (102) planes of covellite CuS (JCPDF no. 06-464). HR-TEM images show also that the synthesized CuS nanotubes are polycrystalline in nature.

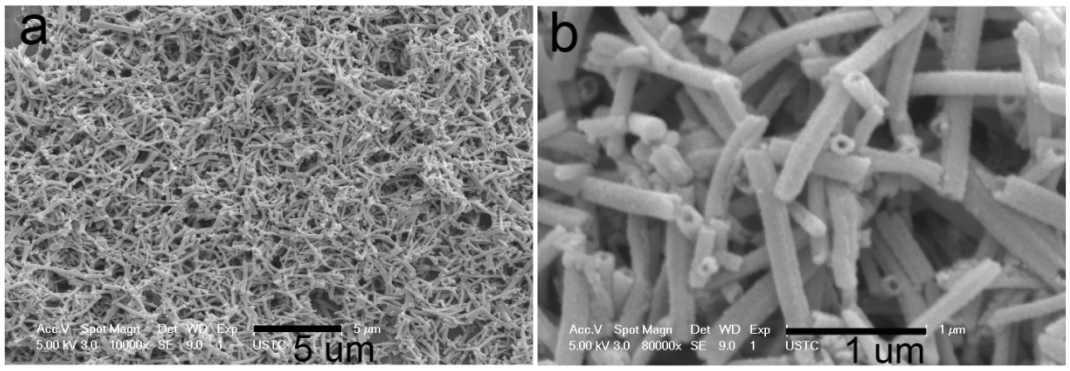

Figure 4.12 FE-SEM images of as-prepared CuS nanotubes at a low magnification **(a)**, and high magnification **(b)**.

Figure 4.12 shows the SEM images of the synthesized CuS nanotubes which are quite monodisperse in size with uniform diameter of ~220 nm and a length of a few micrometers.

The ratio of $Na_2S_2O_3$ to $CuCl_2$ had a significant influence on the CuS structure.[58-59] Indeed, when the molar ratio of $Na_2S_2O_3$ to $CuCl_2$ increased to 3:1, CuS porous microspheres instead of CuS porous nanotubes were obtained (to see **Figure 4.13**). The final structure of CuS is sensitive to the initial molar ratio of $Na_2S_2O_3$ to $CuCl_2$.

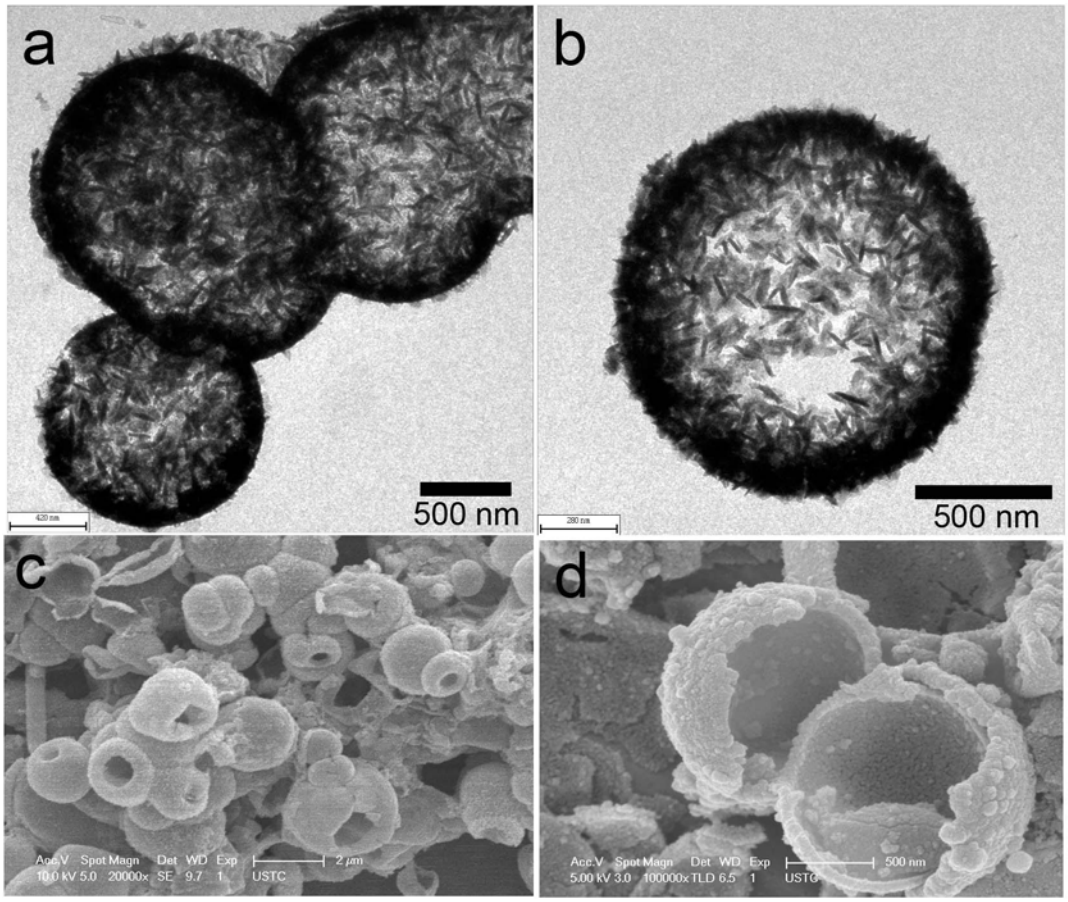

Figure 4.13 (a, b) TEM images and **(c. d)** SEM images of the synthesized CuS hollow spheres; the molar ratio of $Na_2S_2O_3$ to $CuCl_2$ is 3:1.

4.2.2.2 Photocatalytic Tests

The photocatalytic activity of these nanotubes under visible light was studied for RhB degradation. First, we studied the adsorption properties of these nanostructures. When RhB is put in dark in contact with the CuS nanostructures, the absorbance at its characteristic absorption peak at 554 nm decreased with time until a factor of 0.55 and reached a plateau after 20 min (**Figure 4.15**). This is due to the adsorption of RhB on the surface of CuS. This important adsorption can be ascribed to the nanotubes structure displaying a tremendous surface area, allowing sufficient contact between RhB and CuS. Photocatalytic tests were conducted after reaching this adsorption equilibrium. The results of the photocatalytic degradation of RhB under visible light are shown in **Figure 4.14**. The concentration of RhB decreased gradually with irradiation time. The absorption peak at 255 nm decreased and finally disappeared, indicating the cleavage of aromatic structures in the RhB molecules.[53]

RhB is quite stable under visible illumination (**Figure 4.14b**). However in the presence of the CuS photocatalyst, the degradation of RhB reached up to 70% after 100 minutes illumination. This result indicates that these porous CuS nanotubes are very photoactive under visible light. Further investigations will be attempted to study the stability of the photocatalyst under illumination and to optimize the photocatalytic properties of the synthesized CuS NTs.

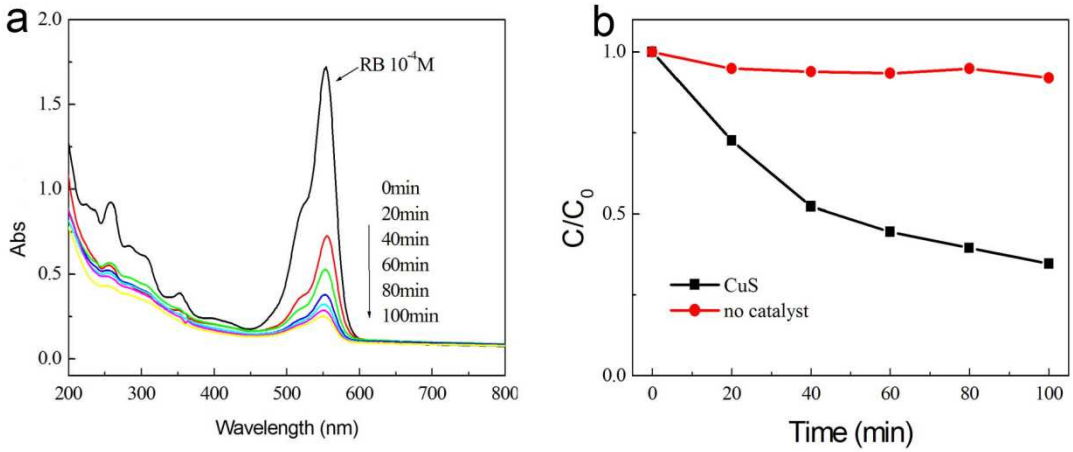

Figure 4.14 (a) UV-vis absorption spectra of RhB photodegration by CuS nanotubes under visible illumination, **(b)** time runs of relative RhB concentration in photodegradation with CuS (balck squares) and witout catalyst (red circles). Optical path: 2 mm.

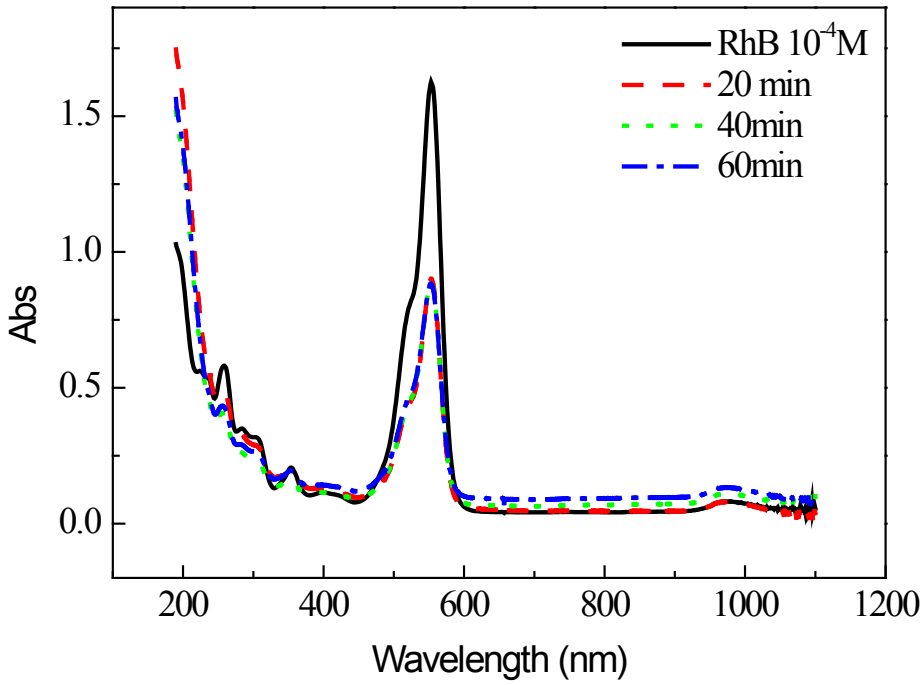

Figure 4.15 UV-Vis absorption spectra of RhB in the adsorption experiment with prepared CuS NTs in the dark.

4.2.3 Conclusion of this section

In summary, we have synthesized CuS nanotubes through a non-template route by γ-irradiation of an aqueous solution containing $CuCl_2$ and $Na_2S_2O_3$. The lengths of the CuS nanotubes are from several hundreds of nanometers to 2 micrometers. The external diameter and wall thickness of the synthesized CuS nanotubes are respectively ~220 nm and ~40 nm. The initial molar ratio of the precursors $Na_2S_2O_3$ to $CuCl_2$ has a significant influence on the final structure of CuS. The synthesized CuS nanotubes have a great ability in adsorbing RhB and they exhibit a high photocatalytic activity under visible light. Therefore, these nanostructures are promising for water treatment.

References

[1] Zeng, J.; Huang, J. L.; Lu, W.; Wang, X. P.; Wang, B.; Zhang, S. Y. and Kou, J. G., *Adv. Mater.* **2007**, *19*, 2172-2176.

[2] Chen, J. S.; Zhu, T.; Li, C. M. and Lou, X. W., *Angew. Chem.* **2011**, *123*, 676-679.

[3] Xia, Y. N.; Gates, B.; Yin, Y. D. and Lu, Y., *Adv. Mater.* **2000**, *12*, 693-713.

[4] Cushing, B. L.; Kolesnichenko, V. L. and O'connor, C. J., *Chem. Rev.* **2004**, *104*, 3893.

[5] Li, Y. D.; Liao, H. W.; Ding, Y.; Fan, Y.; Zhang, Y. and Qian, Y. T., *Inorg. Chem.* **1999**, *38*, 1382.

[6] Fujita, H.; Izawa, M. and Yamazaki, H., *Nature* **1962**, *196*, 666.

[7] Hu, Y.; Chen, J. F.; Chen, W. M. and Li, X. L., *Adv. Funct. Mater.* **2004**, *14*, 383.

[8] Liu, H. R.; Miao, W. F.; Yang, S. and Zhang, Z. M., *Cryst. Growth Des.* **2009**, *9*, 1733-1740.

[9] Yin, Y. D.; Xu, X. L.; Ge, X. W.; Xia, C. J. and Zhang, Z. C., *Chem. Commun.* **1998**, 1641.

[10] Hu, Y.; Chen, J. F.; Xue, X.; Li, T. W. and Xie, Y., *Inorg. Chem.* **2005**, *44*, 7280.

[11] Souici, A. H.; Keghouche, N.; Delaire, J. A.; Remita, H.; Etcheberry, A. and Mostafavi, M., *J. Phys. Chem. C* **2009**, *113*, 8050-8057.

[12] Souici, A. H.; Keghouche, N.; Delaire, J. A.; Remita, H. and Mostafavi, M., *Chem. Phys. Lett.* **2006**, *422*, 25-29.

[13] Mostafavi, M.; Liu, Y. P.; Pernot, P. and Belloni, J., *Radiat. Phys. Chem.* **2000**, *59*, 49-59.

[14] Grabowska, E.; Zaleska, A.; Sorgues, S.; Kunst, M.; Etcheberry, A.; Colbeau-Justin, C. and Remita, H., *J. Phys. Chem. C* **2013**, *117*, 1955-1962.

[15] Lehoux, A.; Ramos, L.; Beaunier, P.; Uribe, D. B.; Dieudonne, P.; Audonnet, F.; Etcheberry, A.; Jose-Yacaman, M. and Remita, H., *Adv. Funct. Mater.* **2012**, *22*, 4900-4908.

[16] Mirdamadi-Esfahani, M.; Mostafavi, M.; Keita, B.; Nadjo, L.; Kooyman, P. and Remita, H., *Gold Bull.* **2010**, *43*, 49-56.

[17] Redjala, T.; Apostolescu, G.; Beaunier, P.; Mostafavi, M.; Etcheberry, A.; Uzio, D.; Thomazeau, C. and Remita, H., *New J. Chem.* **2008**, *32*, 1403-1408.

[18] Dehouche, F.; Archirel, P.; Remita, H.; Brodie-Linder, N. and Traverse, A., *RSC Advances* **2012**, *2*, 6686-6694.

[19] Siril, P. F.; Lehoux, A.; Ramos, L.; Beaunier, P. and Remita, H., *New J. Chem.* **2012**, *36*, 2135-2139.

[20] Xiang, J. Y.; Tu, J. P.; Zhang, L.; Zhou, Y.; Wang, X. L. and Shi, S. J., *J. Power Sources* **2010**, *195*, 313.

[21] Wang, S. Q.; Zhang, J. Y. and Chen, C. H., *Scr. Mater.* **2007**, *57*, 337.

[22] Gao, X. P.; Bao, J. L.; Pan, G. L.; Zhu, H. Y.; Huang, P. X.; Wu, F. and Song, D. Y., *J. Phys. Chem. B* **2004**, *108*, 5547.

[23] Ramirez-Ortiz, J.; Ogura, T.; Medina-Valtierra, J.; Acosta-Oritz, S. E.; Bosch, P.; De Los Reyes, J. A. and Lara, V. H., *Appl. Surf. Sci.* **2001**, *174*, 177.

[24] Wang, W.; Zhan, Y.; Wang, X.; Liu, Y.; Zheng, C. and Wang, G., *Mater. Res. Bull.* **2002**, *37*, 1093.

[25] Switzer, J. A.; Kothari, H. M.; Poizot, P.; Nakanishi, S. and Bohannan, E. W., *Nature* **2003**, *425*, 490.

[26] Zhang, J.; Liu, J.; Peng, Q.; Wang, X. and Li, Y., *Chem. Mater.* **2006**, *18*, 867.

[27] Liao, L.; Zhang, Z.; Yan, B.; Zheng, Z.; Bao, Q. L.; Wu, T.; Li, C. M.; Shen, Z. X.; Zhang, J. X.; Gong, H.; Li, J. C. and Yu, T., *Nanotechnology* **2009**, *20*, 085203.

[28] Zhang, H.; Zhu, Q.; Zhang, Y.; Wang, Y.; Zhao, L. and Yu, B., *Adv. Funct. Mater.* **2007**, *17*, 2766.
[29] Ahmed, A.; Gajbhiye, N. S. and Joshi, A. G., *J. Solid State Chem.* **2011**, *184*, 2209-2214.
[30] Snoke, D., *Science* **2002**, *298*, 1368.
[31] Hara, M.; Kondo, T.; Komoda, M.; Ikeda, S.; Shinohara, K.; Tanaka, A.; Kondo, J. N. and Domen, K., *Chem. Commun.* **1998**, 357.
[32] Barreca, D.; Fornasiero, P.; Gasparotto, A.; Gombac, V.; Maccato, C.; Montini, T. and Tondello, E., *ChemSusChem* **2009**, *2*, 230-233.
[33] Kuo, C.-H. and Huang, M. H., *J. Phys. Chem. C* **2008**, *112*, 18355-18360.
[34] Miao, W. F.; Liu, H. R.; Zhang, Z. M. and Chen, J. F., *Solid State Sci.* **2008**, *10*, 1322-1326.
[35] Spinks, J. W. and Wood, R. J., *An Introduction to Radiation Chemistry*, Joh Wiley and Sons Inc., New York, **1976**, p.
[36] Marignier, J. L.; Belloni, J.; Delcourt, M. O. and Chevalier, J. P., *Nature* **1985**, *317*, 344.
[37] Wang, Z. L., *J. Phys. Chem. B* **2000**, *104*, 1153-1175.
[38] Kuo, C.-H.; Chen, C.-H. and Huang, M. H., *Adv.Funct. Mater.* **2007**, *17*, 3773-3780.
[39] Shoeib, M. A.; Abdelsalam, O. E.; Khafagi, M. G. and Hammam, R. E., *Adv. Powder Technol.* **2012**, *23*, 298-304.
[40] Liu, J. L.; Gao, Z. Y.; Han, H. J.; Wu, D. P.; Xu, F.; Wang, H. X. and Jiang, K., *Chem. Eng. J.* **2012**, *185-186*, 151-159.
[41] Kou, T. Y.; Wang, Y. Z.; Zhang, C.; Sun, J. Z. and Zhang, Z. H., *Chem. Eng. J.* **2013**, *223*, 76-83.
[42] Xu, H. L.; Wang, W. Z. and Zhu, W., *J. Phys. Chem. B* **2006**, *110*, 13829-13834.
[43] Xia, Y. N.; Yang, P. D.; Sun, Y. G.; Wu, Y. Y.; Mayers, B.; Gates, B.; Yin, Y. D.; Kim, F. and Yan, H., *Adv. Mater.* **2003**, *15*, 353-389.
[44] Lou, Y.; Chen, X.; Samia, A. C. and Burda, C., *J. Phys. Chem. B* **2003**, *107*, 12431-12437.
[45] Ancutiene, I.; Janickis, V. and Ivanauskas, R., *Appl. Surf. Sci.* **2006**, *252*, 4218-4225.
[46] Li, Y. B.; Lu, W.; Huang, Q.; Huang, M.; Li, C. and Chen, W., *Nanomedicine* **2010**, *5*, 1161-1171.
[47] Chen, J.; Deng, S. Z.; Xu, N. S.; Wang, S.; Wen, X.; Yang, S.; Yang, C.; Wang, J. and Weikun, G., *Appl. Phys. Lett.* **2002**, *80*, 3620-2622.
[48] Zhang, X. J.; Wang, G. F.; Gu, A. X.; Wei, Y. and Fang, B., *Chem. Commun.* **2008**, 5945-5947.
[49] Lu, Q. Y.; Gao, F. and Zhao, D. Y., *Nano Lett.* **2002**, *2*, 725-728.
[50] Luo, M.; Liu, Y.; Hu, J. C.; Li, J. L.; Liu, J. and Richards, R. M., *Appl. Catal. B* **2012**, *125*, 180-188.
[51] Wang, X. Y.; Fang, Z. and Lin, X., *J. Nanopart. Res.* **2009**, *11*, 731-736.
[52] Tan, Z. G.; Zhu, Q.; Guo, X. Z.; Zhang, J. F.; Wu, W. Y. and Liu, A. P., *Acta Chimica Sinica* **2011**, *69*, 2812-2820.
[53] Cheng, Z. G.; Wang, S. Z.; Wang, Q. and Geng, B. Y., *CrystEngComm* **2009**, *12*, 144-149.
[54] Li, F.; Wu, J. F.; Qin, Q. H.; Li, Z. and Huang, X. T., *Powder Technol.* **2010**, *198*, 267-274.
[55] Huang, J.; Wang, Y.; Gu, C. and Zhai, M., *Mater. Lett.* **2013**, *99*, 31-34.
[56] Ding, T. Y.; Wang, M. S.; Guo, S. P.; Guo, G. C. and Huang, J. S., *Mater. Lett.* **2008**, *62*, 4529-4531.
[57] Hai, Z. B.; Zhu, C. H.; Huang, J. L.; Liu, H. R. and Chen, J. F., *Inorg. Chem.* **2010**, *49*, 7217-7219.
[58] Hu, Y.; Chen, J. F.; Xue, X.; Li, T. W. and Xie, Y., *Inorg. Chem.* **2005**, *44*, 7280-7282.
[59] Xue, X.; Chen, J. F. and Hu, Y., *Mater. Lett.* **2007**, *61*, 115-118.

GENERAL CONCLUSIONS AND PERSPECTIVES

Conclusions and Perspectives

Conclusions

In this thesis work, two main aspects of photocatalysts were studied, i.e. the enhancement of photocatalytic activity of TiO_2 by modification with Au-Cu bimetallic NPs and the preparation of non-TiO_2 visible light photocatalysts.

Colloid deposition and deposition precipitation methods were used to prepare Au-Cu modified TiO_2 photocatalysts.

For the colloid deposition method by radiolysis, colloidal solutions of Au-Cu bimetallic NPs with small sizes (around 4 nm in diameter) were prepared in the presence of the stabilizing agent PAA. Addition of PVA facilitates the deposition of Au-Cu NPs on TiO_2 surface.

For the colloid deposition method by chemical method, very small Au-Cu bimetallic NPs homogeneous in size (around 3 nm in diameter) were synthesized and deposited on P25. We have found that very small amount of metal (0.5 % wt.) can activate TiO_2 for photocatalytic applications. We employed Cu, which is an abundant and a cheap metal to modify TiO_2, and the modification of the photocatalyst (with Cu or with Au-Cu NPs) resulted in an enhancement of the photocatalytic activity under UV light, thus, the cost of photocatalyst preparation is relatively low. TRMC results showed that the NPs act as efficient electron scavengers increasing the quantum yield of light conversion.

For the deposition precipitation method with urea followed by radiolytic reduction, Au-Cu bimetallic NPs with a size of about 7 nm were synthesized *in-situ* on the P25 substrate. This method ensures an efficient deposition performance. The modified Au-Cu bimetallic NPs are alloys without thermal treatment. This is convenient with respect to the colloid deposition method. P25 modified with Au/Cu1:3 bimetallic NPs shows a quite higher photocatalytic activity in MO degradation than the pristine P25, and the photocatalytic efficiency under UV light increased by more than 2 times.

The nanoparticle size decreases for the Au-Cu bimetallic NPs compared with those of the monometallic Au ones in the same preparation conditions. This trend exists in both cases of the colloid deposition method (by THPC or radiolysis) and the deposition precipitation method. Besides, the size distribution becomes more homogeneous when Cu is associated to Au NPs.

Modification of P25 with Au-Cu bimetallic NPs leads to a higher UV photocatalytic activity than that with monometallic Au or Cu ones all through the different deposition methods.

For all the deposition methods we used, modification of P25 with Au/Cu1:3 bimetallic NPs resulted in an enhancement of the photocatalytic activity under UV light. TRMC measurements show that alloyed Au-Cu bimetallic NPs are very efficient in electron trapping. They are even more efficient than monometallic Au and Cu in electron scavenging. These results explain the better photocatalytic activity obtained with Au-Cu modified TiO_2 compared to Au/TiO_2 and Cu/TiO_2.

CuO nanowires and Cu_2O crystals with shape evolution from cubic to octahedral were prepared by γ-irradiation method. The product composition for CuO or Cu_2O can be easily changed by modulating the molar ratio of the reactants NaOH to $CuCl_2$. The morphology of Cu_2O crystals can be accurately controlled by choosing the amount of isopropanol. Cu_2O truncated octahedral structures show excellent photocatalytic activity in MO degradation under visible light.

Uniform CuS nanotubes were synthesized by radiolysis through a non-template route. The external diameter and wall thickness of the synthesized CuS nanotubes are ~220 nm and ~40 nm, respectively. The initial molar ratio of the precursors $Na_2S_2O_3$ to $CuCl_2$ has a significant influence on the final structure of CuS. The synthesized CuS nanotubes show a high capability to adsorb RhB and exhibit a very good photocatalytic activity under visible illumination.

Perspectives

It is necessary to optimize the ratio of Au to Cu in the deposited Au-Cu NPs to obtain the highest photocatalytic activity. The cost should also be taken into account to balance the photocatalytic efficiency and economy.

Deposition precipitation method with urea is a promising method for depositing various metals such as Cu, Ag, Pt, Au on TiO_2. It also has potential applications in the preparation of Al_2O_3, SiO_2 supported composite materials. The catalytic applications of Au-Cu/TiO_2 will be investigated for different catalytic reactions in collaboration with the Laboratoire de Réactivité des Surfaces (UPMC, Université Paris 6).

It is also important to understand why different preparation methods or deposition procedures induce modified P25 with different photoactivities under UV irradiation. The size of deposited metallic NPs seems to be partly responsible for the differences. Apparently, the nanoparticle size should be around 5 nm (3 ~ 7 nm) for an enhancement of photoactivity under UV light. Further experiments should be carried out to find the relation between the photoactivity and the size of Au-Cu NPs caused by different preparation methods. Besides, the location and the interaction manner of Au-Cu metallic NPs with the support can also be a possible reason for the different photoactivity of modified P25 by various preparation methods both under UV and visible light. Experimental or theoretical studies need to be conducted to understand the effect of the size of the metal NPs and their interaction with TiO_2 on the photocatalytic activity of the system.

In this thesis work, we modified P25, which is a mixture of anatase and rutile. P25 is the best TiO_2 photocatalyst under UV light. However, it is known that it is very difficult to improve its activity under UV light. Here, we succeeded in this task by modifying its surface with Cu and Au-Cu nanoparticles. To better understand the effect of the metal nanoparticles on TiO_2 photocatalytic activity, the same study will be conducted on pure anatase TiO_2, in this case the system will be less complex to study.

It is also important to try to enhance the photoactivity of TiO_2 under visible light. For

example, we can synthesize larger (25 or 50 nm) Au-Cu bimetallic NPs well deposited on the TiO_2 support to study the size effect on the photoactivity. In case of P25, we can also attempt to deposit the Au-Cu NPs on the joint sites between anatase and rutile, promoting the electron transfer from the photoactivated metallic NPs to rutile and consequently to anatase. In this case, P25 can be photoactivated by excited electrons from metallic NPs under visible irradiation.

Further investigation should be carried out to reveal the mechanism on the excellent visible photocatalytic efficiency of truncated octahedral Cu_2O. The durability of these nanostructure will be studied. In addition, it is desirable to improve the hydrophilicity of Cu_2O microcrystals. On one hand, it can lead to higher photoactivity; on the other hand, it promises practical applications in industrial or commercial areas.

Further studies are also necessary to be conducted to investigate the radiolytic synthesis of copper sulfides and the photocatalytic properties of CuS with different morphologies, such as nanospheres, hollow spheres and nanotubes.

APPENDICES

Appendix I Gamma Ray Sources

In the preparations of copper oxides and copper sulfides and the doposition precipitation method with urea, the γ-irradiation source was a panoramic cobalt (^{60}Co) gamma facility, located in the Radiation Chemistry Laboratory of University of Science and Technology of China, Hefei. The initial activity of this source in March 2012 was 60000 Curies during reinstallation. The maximum dose rate in November 2012 was about 10 kGy•h^{-1}.

The walls of the radiation chamber are built with cement and extremely thick. A radioprotective sliding door is made of lead.

When the gamma ray source is working, the cobalt bars lift from a deep well (vertically placed in the column, see **Figure A.1**). The samples are put on the plateform, the dose rate depends on the distance of the sample to the column. When the irradiation is completed, the cobalt bars sank to the deep well filled with deionized water.

Figure A.1 Picture of the gamma ray source in Radiation Chemistry Laboratory of USTC.

Another gamma ray source used for the modification of TiO_2 with Au, Cu, and Au-Cu metal NPs by colloid deposition method is located in Laboratoire de Chimie Physique (LCP)

at Université Paris-Sud, Orsay.

The source of ionizing gamma radiation used in the laboratory (**Figure A.2**) was a panoramic ^{60}Co source in the form of a cylindrical bar stored in a lead container which retractions by remote control is remotely controlled from the control room.

The samples are placed by the operator in the panoramic room, where the irradiation takes place. The radiation chamber is enclosed by thick walls and a radioprotective sliding lead door. Samples of different volumes from a few microliters to several liters can be irradiated.

The initial activity of the source in 1995 was 7,000 Curies during the installation. The maximum dose rate at the beginning of this thesis, in September 2009, was 1850 $Gy.h^{-1}$.

Figure A.2 Picture of the gamma ray source in LCP at Université Paris-Sud, Orsay.

Appendix II Photocatalytic Reaction System A

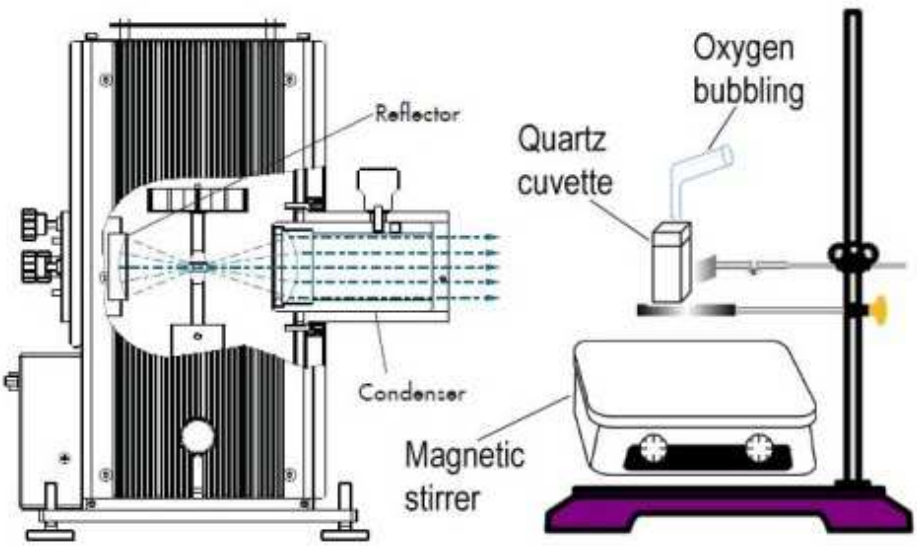

Figure A.3 Schematic illustration of the photocatalytic reaction system A.

Figure A.4 The LOT-Orien Xenon 300W lamp.

As shown in **Figure A.3**, the parallel light beam irradiates on the side wall of a quartz cuvette. A water filter (a large cell) was placed between the lamp and the reactor to screen the infrared light and avoid heating of the samples. The cell containing water is in quartz. Optical filters were used to obtain visible irradiance (wavelength larger than 450 nm).

A Xenon lamp of 300 Watts produced by LOT-Orien was used in our experiments (**Figure A.4**). The lamp can output a collimated beam of a continuous spectrum, ranging from the UV to near-infrared range (250 to 2000 nm). The radiation spectrum is presented in

Figure A.5. Xenon arc lamps have a color temperature of approx. 6000 K which is close to the sun spectrum. The main output is below 900 nm. It is an ideal light source for the visible photocatalysis.

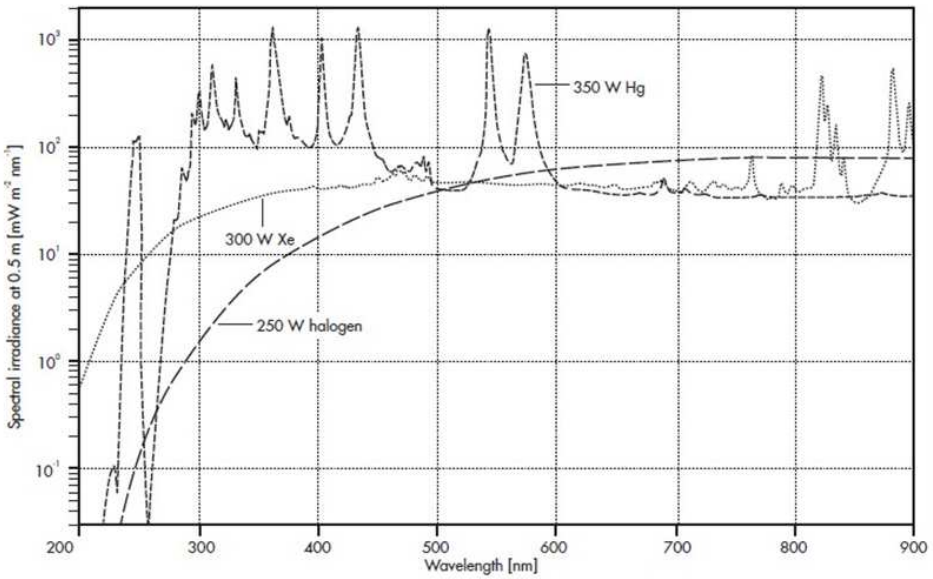

Figure A.5 Spectral irradiance of LOT-Orien Xenon lamps.

Appendix III Photocatalytic Reaction System B

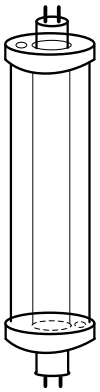

Figure A.6 Schematic illustration of the cylinder reactor.

Figure A.6 shows the reaction system B. The cylinder reactor is composed of two open tubes with a hollow space for the rodlike lamp. The inner wall of the cylinder reactor is made of silicon which is assumed to have nearly no absorption of ultraviolet and visible light. The cylinder reactor is connected to a suspension container with two pipes, one is for suspension inflow, and another one is for outflow. A peristaltic pump is used to drive the suspension in a

cyclic closed system. The suspension in the container was bubbled with oxygen at a flow rate of 20 cm^3 per min. A lamp of MASTER TL Mini Super 80 was used as the visible light source. The lamp and its emission spectrum are shown in **Figure A.7**. The main radiation spectrum lies in the region from 400 nm to 740 nm.

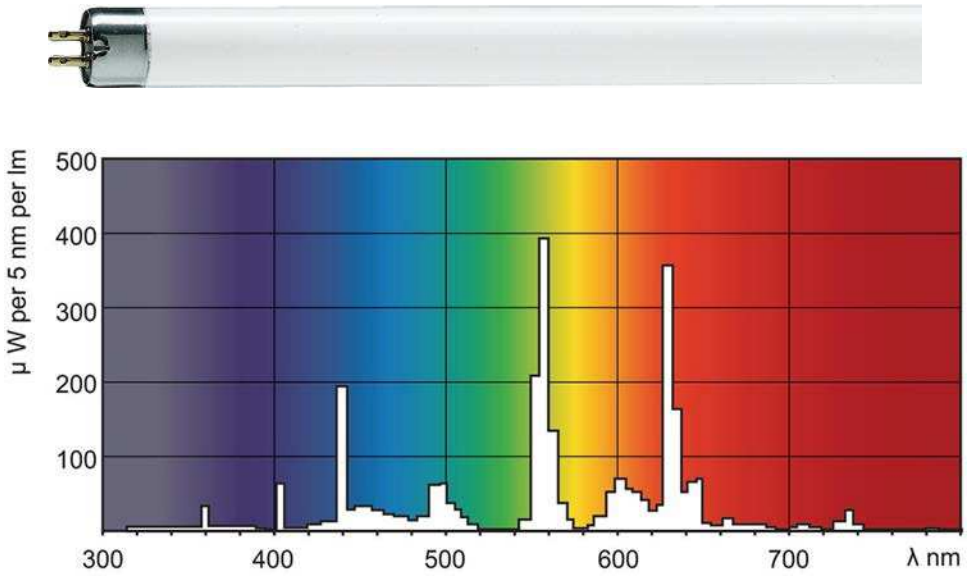

Figure A.7 The Philips TL-8W-840 lamp and its emission spectrum.

Appendix IV XPA-7 Photochemical Reactor

XPA-7 photochemical reactor (purchased from Nanjing Xujiang Machine-Electronic Plant, China) was also used in part of the photocatalytic degradation tests. As is shown in **Figure A.8**, a tube lamp is placed vertically in the center of a platform, surrounded by a quartz cooling pipe, which can romove the heat caused by the lamp and meanwhile permit thorough transmission of light ranging from ultraviolet to visible range. The optical filters vertically lie between the reactors and lamp. The reactors are placed outside of the platform, parallel to the tube lamp. The distance between the lamp and reactors is about 10 cm. The tube reactors are also made of quartz. Multiple magnetic agitators are installed just under the tube reactors.

To carry out the photocatalytic experiments under complete UV or visible illumination, two kinds of optical filters were employed. One is a visible optical filter, which can cut off the visible light with wavelengths higher than 400 nm (see **Figure A.10a**). And the UV optical

filter can cut the light with wavelengths shorter than 450 nm (see **Figure A.10b**).

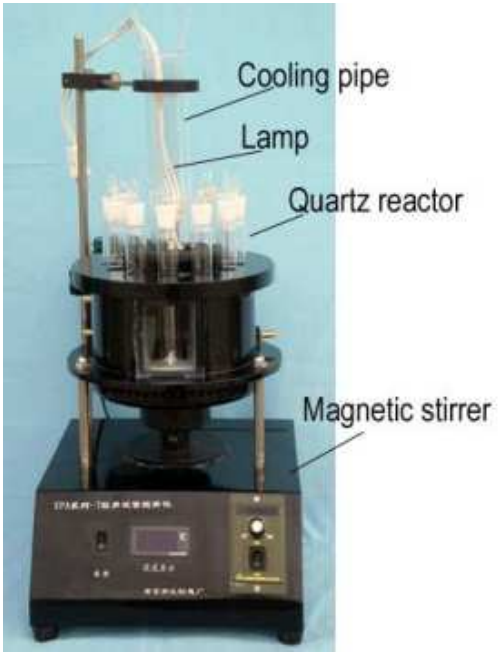

Figure A.8 Picture of XPA-7 photochemical reactor.

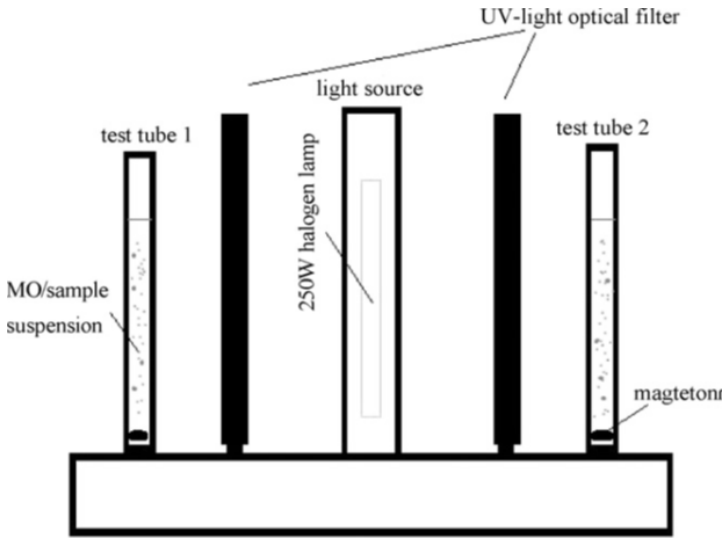

Figure A.9 Schematic illustration of Model XPA-7 photochemical reactor.[1]

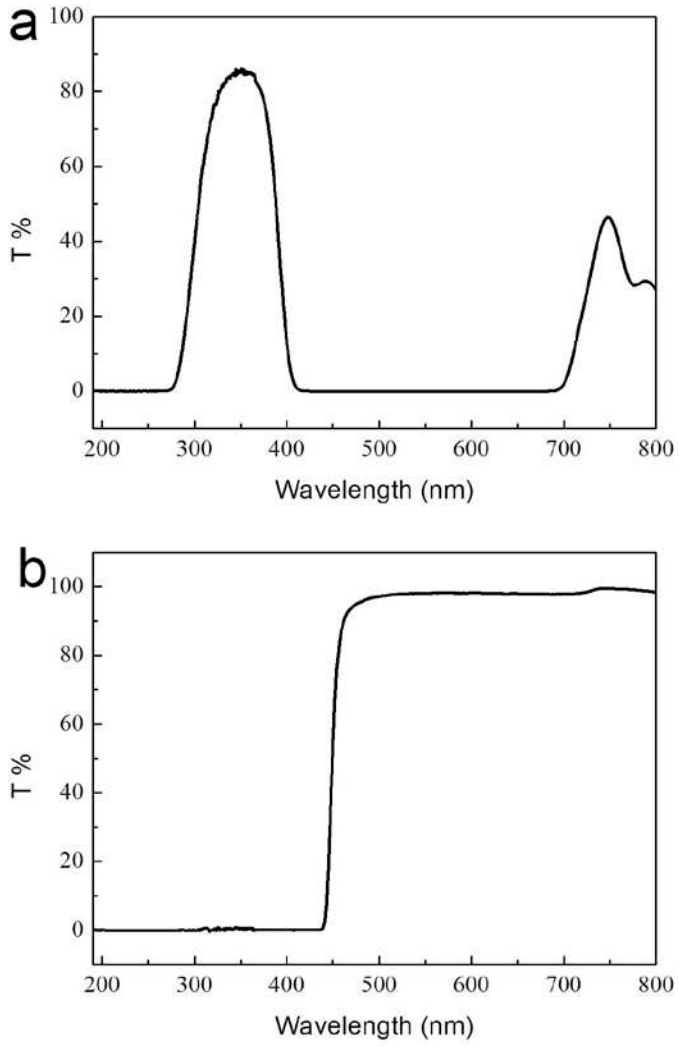

Figure A.10 UV-visible transmission spectra of (a) visible optical filter, (b) UV optical filter.

Appendix V Time Resolved Microwave Conductivity

Time Resolved Microwave Conductivity (TRMC) was employed to investigate the electronic properties of the photocatalysts. This setup is located in Laboratoire de Chimie Physique at Université Paris-Sud, Orsay. As is displayed in the scheme (**Figure A.11**), we can see that the powder sample was put inside a wave-guide, to proceed to its illumination by a UV pulse laser. After, the temporal evolution of microwave power reflected by the sample was recorded by a detector.

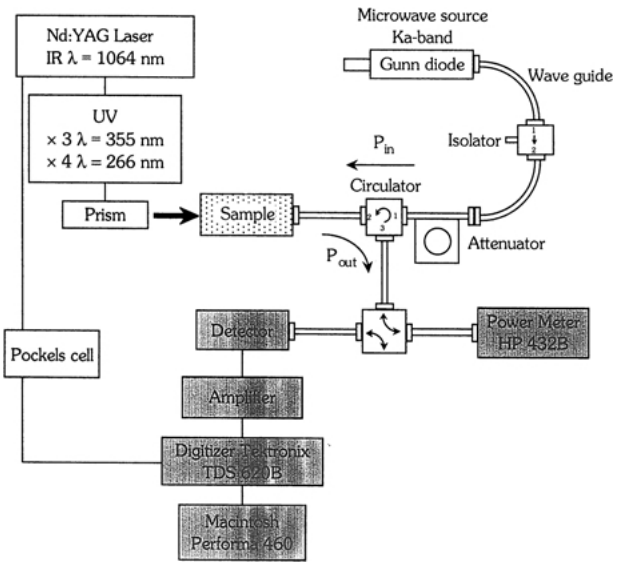

Figure A.11 Scheme of TRMC experimental set-up.[2]

Pulsed light source is an Nd:YAG laser giving an IR radiation at λ=1064 nm with a 10 Hz frequency. Full width at half-maximum of one pulse is 10 ns. UV light is obtained by tripling (355 nm) or quadrupling (266 nm) the IR radiation. The maximum light energy density received by the sample is 1.3 mJ•cm^{-2} for both wavelengths.

The incident microwaves are generated by a Gunn diode in the Ka band (28–38 GHz). The experiments were carried out at 31.4 GHz, this frequency corresponds to the highest microwave power. The reflected microwaves are detected by a Schottky diode. The signal is amplified and displayed on the digitizer.

The samples are put on a plane polymeric holder that has been specifically designed for powder measurements. It allows the samples to be illuminated inside the wave-guide in the form of powder, which results in the best microwave response.

This method is based on the measurement of the change of the microwave power reflected by a sample induced by laser pulsed illumination. The relative change, $\Delta P(t)/P$ can be correlated, for small perturbations of conductivity, to the difference of conductivity $\Delta\sigma(t)$ considering the following equation:

$$\frac{\Delta P(t)}{P} = A\Delta\sigma(t) = Ae\sum_i \Delta n_i(t)\mu_i \qquad (A.1)$$

where $\Delta n_i(t)$ is the number of excess charge-carriers i at time t and μ_i their mobility. The sensitivity factor A is independent of time but depends on different factors such as the microwave frequency or the dielectric constant.

Considering that the trapped species have a small mobility that can be neglected, Δn_i is reduced to mobile electrons in the conduction band and holes in the valence band. In the specific case of TiO_2, the TRMC signal can be attributed to electrons because their mobility is much larger than that of the holes.[3]

The TRMC signal can be characterized by two parameters: the maximum value (*Imax*) and the decay $I(t)$. Imax is determined by the electron mobility and by fast decay processes with an appreciable activity during the excitation (i.e. the first 10 ns). These two contributions cannot be separated easily for a system as TiO_2 powder. In general, a high value of I_{max} can be regarded as reflecting good electronic properties due to good crystalline structure of the sample. Because the signal decay is not entirely exponential, the general decay shape is characterized by several halftime lives, $\tau_{1/2}$ is the time to obtain intensity $I_{max}/2$ of the signal, $2\tau_{1/2}$ to obtain $I_{max}/4$.

Appendix VI Principle of Characterization Techniques

(High Resolution) Transmission Electron Microscopy

TEM is a technique in which a stream of accelerated electrons interacting with a sample deposited on a grid to form an image. The scheme of a TEM apparatus is shown in **Figure A.12**.

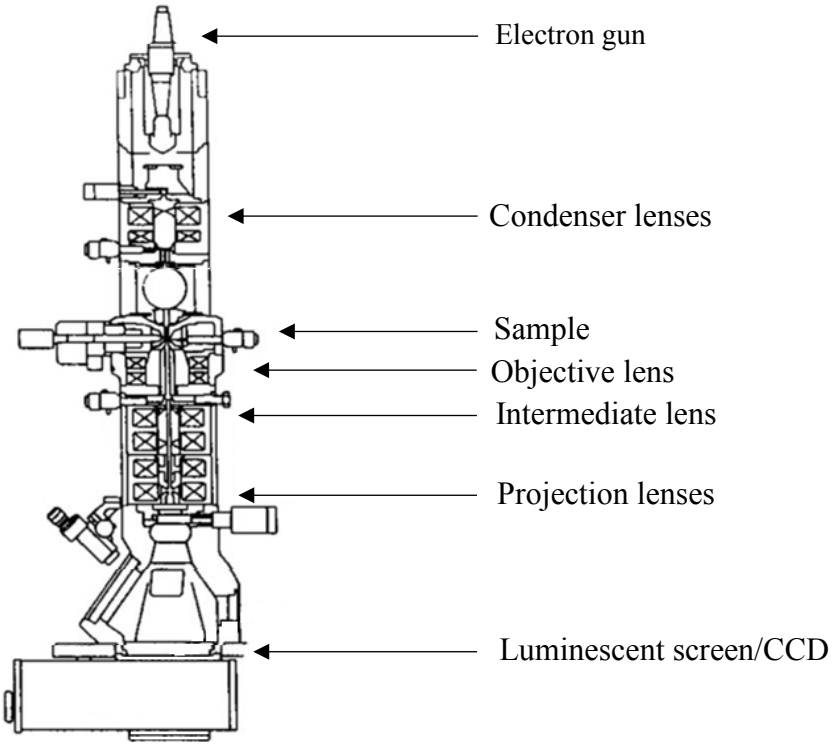

Figure A.12 Diagram of components of a transmission electron microscope.[4]

In the bright field mode, the incident electron beam can be deflected by collisions across the sample. The probability of a collision increases with the atomic number Z of the constituents of the sample and the sample thickness. The deflected electrons are not observed which caused by the most elastic collisions, so the areas are darker while areas with lower Z atoms and/or reduced thickness appear bright. This method is widely used to observe the metal structures for the metal atoms with a high atomic number, and provide excellent contrast against the bright background.

In the diffraction mode, the focal length of the intermediate lens, which allows passing a distance diffraction picture mode, is placed in the image focal plane. This mode allows us to observe the electron diffraction as a diffraction pattern. The shape of the diffraction pattern can initially determine whether the observed area is amorphous, polycrystalline or crystalline. A crystal structure defines spots while a polycrystalline structure present diffraction rings. The analysis of the diffraction patterns to determine these crystal structures through the interatomic distances observed. In the case of a bimetallic alloy, the distance between two diametrically opposed spots is intermediate between the distances of each metal characteristics in proportion to the ratio between the two metals. This technique can provide

information on the organization of atoms but also on the composition, provided that the atoms have interatomic distances sufficiently distinct. In the diffraction mode, it is also possible to make a SAED ("Selected Area Electron Diffraction"). A diaphragm area of selection is then introduced into the assembly at the image plane of the objective lens, for defining the area participating in the diffraction.

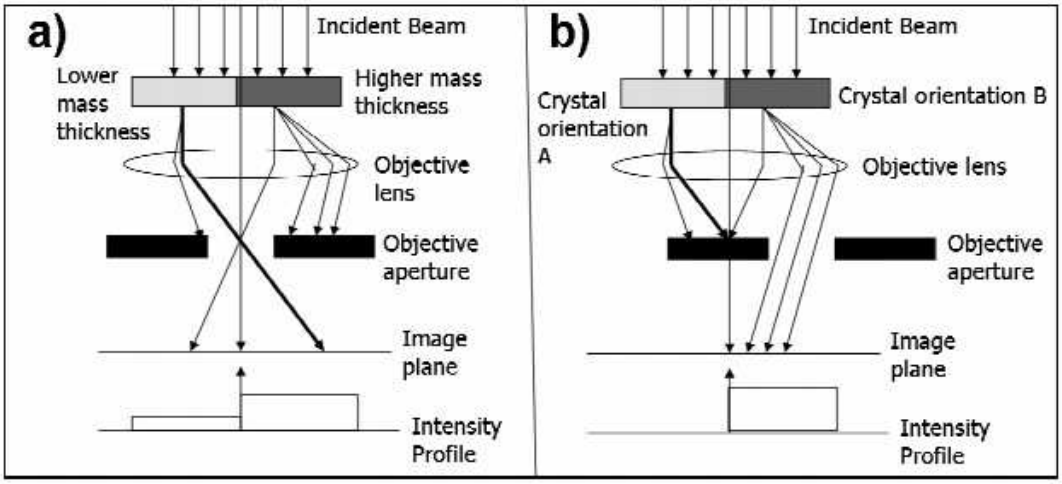

Figure A.13 (a) TEM mass contrast imaging mechanism. **(b)** TEM diffraction contrast imaging mechanism.[5]

There are several mechanisms of image formation in a TEM. The basic one is related to a projected mass thickness contrast (**Figure A.13a**). In this technique the bright regions of the observed images correspond to regions of the specimen that allow the electron beam to pass in the forward direction. The image is a map of the projected mass thickness of the specimen. This contrast mechanism can be better understood if we recall a simple expression for absorption of radiation (Beer's Law):

$$I = I_0 e^{-(\frac{\mu}{\rho})\rho t} \tag{A.2}$$

I_0 is the original intensity, ρ is the specimen density, t is the thickness of the specimen and μ/ρ is the mass absorption coefficient. This type of contrast mechanism is dominant in amorphous specimens and it is of primary importance in biological samples.

Other basic mechanism of image formation is the diffraction contrast, which is mainly relevant in crystalline specimens. Depending on the orientation of the sample with respect to

the electron beam, a crystalline specimen may cause the direction of propagation of the electron beam to be diffracted away from the optical axis of the microscope. Contrast can be generated between those regions that deflect the beam and those regions that do not (**Figure A.13b**). A diffraction contrast image is a map of those regions in the sample that are participating in diffraction processes. The most basic description of the condition for diffraction is Bragg's Law:

$$\lambda = 2 \cdot d_{hkl} \cdot \sin\theta \qquad \text{(A. 3)}$$

In this expression, λ is the wavelength, d_{hkl} is the distance between crystal planes (*hkl*) and θ is the Bragg angle. If this relationship between the wavelength, the interplanar spacing and the orientation of the electron beam with respect to the crystal planes happens to be satisfied, strong Bragg diffraction is expected. Diffraction contrast forms the basis for at least two different imaging modes: bright and dark field. Bright Field, where the TEM image is formed with those regions of the sample that are not being diffracted away from the optical axis; and Dark Field, where the TEM image is a map of the those regions of the specimen that are diffracting the electron beam away from the optic axis of the microscope such that they pass through an aperture inserted in the back focal plane of the objective lens, called the objective aperture.[5]

Two TEM setups were used in this thesis work. The first one is a JEOL 100 CXII operating at 100 kV in Laboratoire de Réactivité de Surface de l'Université Paris VI in collaboration with Patricia Beaunier. It was used in bright field and diffraction mode.

The second TEM setup is a JEOL-2010 operating at 200 kV located in Hefei National Laboratory for Physical Sciences at the Microscale at Univerisity of Science and Technology of China, Hefei.

Scaning Transmission Electronic Microscopy (STEM)

As illustrated in **Figure A.14**, in the Scanning Transmission Electron Microscope (STEM) the objective lens focuses the electron beam onto an atomic scale probe. All scattered

electrons can then be collected by a variety of detectors placed behind the specimen and their information exploited to the fullest extent. An image is generated simply by "scanning" the focused beam step by step over the specimen; in this matter STEM is very similar to Scanning Electron Microscopy (SEM). Hence a STEM image may be considered as a collection of individual scattering experiments. Different types of signals discriminated in scattering angle and/or energy loss yield different structural and chemical information and may be detected simultaneously in different channels.

The elastically scattered electron signal is used to form images that can be acquired by a variety of different detectors (HAADF, ADF). While the inelastically scattered electrons and related signals can be acquired by several different detectors (EELS, EDS) in order to obtain chemical, electronic and structural information from the sample. This simultaneous and controlled acquisition of information lends itself to quantitative analyses that are difficult to realize with other instruments. This ability of the STEM to provide a reference image makes it a very powerful instrument for microanalysis at high-spatial resolution.[5]

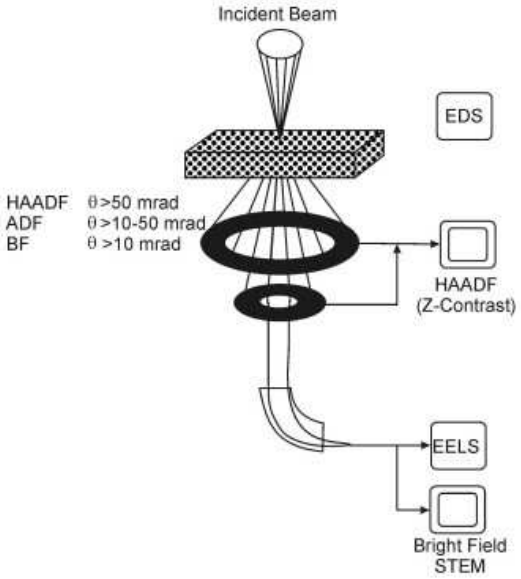

Figure A.14 Schematic of the STEM.[5]

High Angle Annular Dark Field images, also known as Z-contrast, are formed by collecting high-angle (< 50 mrad), incoherent and elastic scattering electron events on an annular detector (**Figure A.14**), also known as Howie detector. At increasing angles, the

coherent scattering is progressively replaced by thermal diffuse scattering. It is also more chemically sensitive since the scattering factors approach those for nuclear scattering (Rutherford-like scattering). In this sense, a good approximation to calculate the scattering cross-section for the atomic nucleus can be obtained from the relativistic Rutherford differential cross-section, shown below.

Two STEM setups were used in this thesis work. The first one is a JOEL JEM-ARM200F operating 200 kV, in collaboration with Miguel José Yacaman (University of Texas at Austin, USA). The second TEM setup is the same model, but located in Hefei National Laboratory for Physical Sciences at the Microscale at USTC, Hefei.X-ray Diffraction

A crystal is composed of a periodic subunit called a unit cell. A unit cell is a box with dimensions a, b, and c that contains the specific locations of the atoms. From this unit cell, families of parallel planes with identical spacing between the planes can be drawn that interest all the atoms in the unit cell and thus the crystal.

These families of planes are identified by an index known as the Miller index, which is depicted by three numbers in parenthesis (*hkl*). These numbers are reciprocal multiples of where the planes intersect the characteristic dimensions of the unit cell.

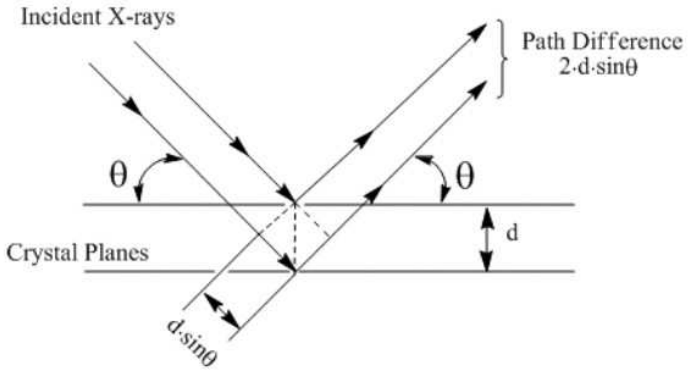

Figure A.15 A graphic representation of Bragg's Lawfrom a crystal surface.[6]

The diffraction condition from these crystal planes is given by Bragg's law (equation **A.3**) The property from which this law is derived is illustrated in **Figure A.15**. Here the path difference between the two incident X-rays must be equal to integer multiples of the radiation

wavelength (nλ) in order for constructive interference to occur. To arrive at equation **A.3** the n is absorbed into *d* forming d_{hkl} and the reflections are said to arise from the (n*h*, n*k*, n*l*) planes.

In a modern X-ray diffraction instrument X-rays of fixed wavelength (usually CuKα=1.54 Å) are directed onto a crystal and the reflections are measured as a function of the incident angle. In powder X-ray diffraction there is no single crystal since the powder is composed of many small crystals with random orientations and thus the orientation is not an issue. These crystals "reflect" the incident X-ray beam at the same angle of incidence thus making the angle between the incident and diffracted beams equal to 2θ.[6]

In this thesis work, XRD measurements were carried out on a Rigaku TTR-III X-ray diffractometer with Cu Kα radiation (λ=1.541 78 Å) in Hefei National Laboratory for Physical Sciences at the Microscale at USTC, Hefei.

X-ray Photon electron Spectroscopy

Deposits for the XPS analyses are performed on a sheet of indium, previously prepared by a succession of baths of sulfuric acid, hydrochloric acid and washed several times with deionized water to remove the oxide layer formed on its surface. The sample is first suspended in a solution and then dried under a stream of N_2. The photoelectrons are detected perpendicular to the support.

The XPS is a technique based on the photoelectric effect. The absorption of a photon by an atom, a molecule or surface, has the effect of ejecting an electron, if the incident photon energy is higher than the binding energy of the electron. The principle of the photoelectron emission is shown in **Figure A.16**.

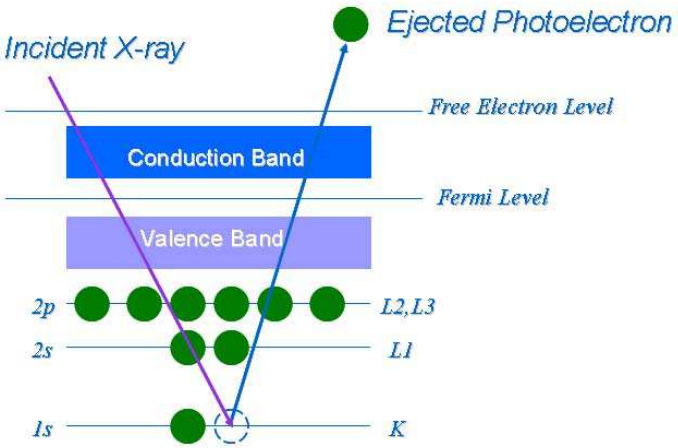

Figure A.16 The principle of photoelectron emission.

In our experiments, the X-ray photons generated from the K line of aluminum (1486.6 eV). The electrons ejected by these photons come regardless of the valence shell or layer of heart and are recorded as a function of their energy by the detector. The results are presented as a spectrum consisting of peaks according to their energy. The integration of the peaks can be traced back to the composition, the area under the peak is proportional to the amount of the element in question to the surface of the sample (up to 5 nm, sometimes more due to the porosity of the material). As the peak shape and binding energies are sensitive to oxidation phenomena and chemical state of the transmitter atom, XPS also provides information on the chemical bonding of the peak deconvolution.[4]

These experiments were performed in collaboration with Arnaud Etcheberry (ILV, Université Versailles Saint Quentin en Yvelines). The X-ray photoelectron spectroscopy (XPS) analysis was performed on a Thermo Electron ESCALAB 220i-XL. The XPS analyzer was a Thermo Electron ESCALAB 220i-XL. Either a non-monochromatic or a monochromatic X-ray Al Kα line was used for excitation.

Besides, in the section of deposition precipitation method with urea, XPS analysis was performed in USTC at a Perkin-Elmer RBD upgraded PHI-5000C ESCA system.

Isotherm Absorption

Adsorption is the measure of deposition of absorbates on absorbents at a set temperature

over a range of pressures to form a graph called an adsorption isotherm. N_2 adsorption is by far the most practiced method due to its ability to accurately determine the properties of a wide range of adsorbents.[6]

The relationship between the amount of a substance adsorbed by an absorbent material and the pressure in equilibrium at a constant temperature is called adsorption isotherm. In contrast, a desorption isotherm is for the release of adsorbed gas on the surface of solids when the relative pressure decreases.

The pace of adsorption isotherm reflects the texture of the material studied. This is an experimental data from which quantitative data, such as specific surface area (or specific surface area) and the average pore size can be extracted.

Several types of isotherms were differentiated. The easiest is the Langmuir isotherm and it is used to describe the formation of a molecular monolayer on the surface of the solid progressive occupation of all possible sites.

The generalization of this theory to multilayer Langmuir is the BET theory. The classification of isotherms into five classes was performed by Brunauer, Deming and Teller then supplemented by a sixth isothermal steps.

All absorbents are generally classified into three basic types, microporous, mesoporous, and nonporous according to their pore width/diameter. These adsorbents have five very distinct isotherms (see **Figure A.17**, I~V), which are used to determine their properties.

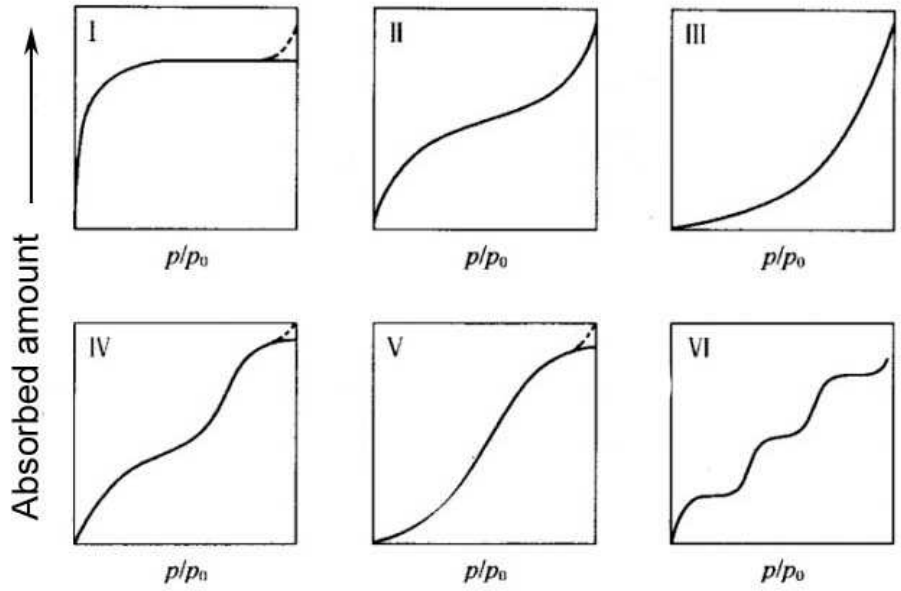

Figure A.17 The classification of the adsorption isotherm.

-- Isothermal Type I: The main feature is the presence of a horizontal reflecting the saturation of the adsorbent. The adsorbent for this type of isotherm is an adsorbent with micropores that fill quickly.

-- Isotherm type II: the amount of adsorbed gas is gradual and continuous function of the relative pressure. This type of isotherm is characteristic of the adsorption of several molecular layers and appears in non-porous or macroporous adsorbents.

-- Type IV isotherm: This isotherm has the same shape at low pressures the isotherm type II. For higher pressures, it is characterized by the appearance of a level of saturation (sometimes just a small inflection point) corresponding to a mesoporous material. Inside the mesopores there is a capillary condensation. Desorbing the nitrogen condensed in the capillary is not reversible and generates a hysteresis of desorption with respect to the adsorption.

-- Isothermal type III and V: They differ respectively from isothermal II and IV by the shape of the curve adsorption isotherm at low pressures, because the interactions between adsorbent and adsorbable are low, as in the case of the water vapor adsorption on a hydrophobic surface.

--The isotherm type VI: This isotherm, also called multi-step isothermal is relatively rare and is observed for homogeneously energetic materials on which adsorbed layers are formed one after the other.[4]

Isotherm adsorption measurements were carried out using a Tristar II 3020M surface area analyser by a multipoint BET method in the relative pressure (P/P_0) range of 0.07-0.2. This setup is also in Hefei National Laboratory for Physical Sciences at the Microscale at USTC, Hefei.

References

[1] Zhou, S.; Lv, J.; Guo, L. K.; Xu, G. Q.; Wang, D. M.; Zheng, Z. X. and Wu, Y. C., *Appl. Surf. Sci.* **2012**, *258*, 6136-6141.

[2] Colbeau-Justin, C.; Kunst, M. and Huguenin, D., *J. Mater. Sci.* **2003**, *38*, 2429-2437.

[3] Fonash, S. J., *Solar cell device physics*, Academic Press, New York, London, **1981**, p.

[4] Lehoux, A. **Synthèse et caractérisation de nanostructures induites par radiolyse en mésophases hexagonales**, Université Paris-Sud, 2012.

[5] Gutiérrez, D. I. G. **Transmission Electron Microscopy Characterization of Composite Nanostructures**, University of Texas at Austin, 2006.

[6] Nash, M. **An Investigation Into the Photocatalytic Properties of Microporous Titansilicate Materials**, University of Delaware, Chemical Engineering, 2008.

PUBLICATIONS

Peer Review Articles

1. Hai, Z. B.; Zhu, C. H.; Huang, J. L.; Liu, H. R. and Chen, J. F. Controllable synthesis of CuO nanowires and Cu_2O crystals with shape evolution via γ-Irradiation, *Inorg. Chem.* **2010,** 49, 7217-7219.

2. Hai, Z. B.; Chen, J. F. and Liu, H. R. Preparation and characterization of CuS submicrometer hollow structure by γ-Irradiation, *J. Radiat. Res. Radiat. Process.* **2010,** 28, 20-23.

3. Hai, Z. B.; Huang, J. L.; Remita, H. and Chen, J. F. Radiolytic synthesis of CuS nanotubes with photocatalytic activity under visible light, *Mater. Lett*. (Accepted)

4. Hai, Z. B.; Kolli, N.; Beaunier, P.; Etcheberry, A.; Sorgues, S.; Colbeau-Justin, C.; Chen, J. F.and Remita, H. Modification of TiO_2 by Bimetallic Au-Cu Nanoparticles for Wastewater Treatment, *J. Mater. Chem. A.* (In revision)

5. Zhu, C. H.; Hai, Z. B.; Cui, C. H.; Li, H. H.; Chen, J. F. and Yu, S. H. In situ controlled synthesis of thermosensitive Poly(N-isopropylacrylamide)/Au nanocomposite hydrogels by Gamma radiation for catalytic application. *Small*. **2012,** 8, 930-936.

6. Albiter, E.; Hai, Z.; Alfaro, S.; Remita, H.; Valenzuela, M. A. and Colbeau-Justin, C. A comparative study of Photo-assisted Deposition of Silver Nanoparticles on TiO_2, *J. NanoSci. NanoTech.*, **2013**, 13, 4943-4948.

7. Hai, Z. B.; EL Kolli, N.; Lü, J.; Chen, J. F. and Remita, H. Radiolytic synthesis of Au-Cu Bimetallic Nanoparticles Supported on TiO_2 and their Application in Water Treatment. *J. Phys. Chem. C*. (Prepared to be submitted)

Communications in Conferences

1. Hai, Z. B.; Remita, H.; EL KOLLI, N. et al. Modification of TiO_2 with bimetallic Au-Cu nanoparticles application in water treatment" *Journées des doctorants*, LCP Unversite Paris-Sud 11, July 4th, 2012, Orsay, France. (**Oral Conference**)

2. Hai, Z. B.; EL Kolli, N.; Sorgues, S.; Colbeau-justin, C.; Beaunier, P. and Remita, H. Modification of Au/Cu bimetallic nanoparticles on TiO_2: Application in water treatment. *International Conference on Nanoscience + Technology (ICN+T2012)*, July 23rd-27th, 2012, Paris, France. (**Poster**)

3. Hai, Z. B.; Remita, H.; Chen, J. F.; EL Kolli, N.; Beaunier, P.; Sorgues, S. and Colbeau-justin, C. Modification of titania with Au/Cu bimetallic nanoparticles: application for water treatment. *4th Asia Pacific symposium Radiation Chemistry (APSRC-2012)*, Oct. 30th - Nov. 3rd, **2012**, Huangshan, China. (**Oral Conference**)

4. Hai, Z. B.; El Kolli, N.; Sorgues, S.; Colbeau-Justin, C.; Chen J. and Remita, H. Modification of TiO_2 by Bimetallic Au-Cu Nanoparticles for Wastewater Treatment, "*The 2nd International Conference on Photocatalytic and Advanced Oxidation Technologies for Treatment of water, Air, Soil and Surfaces (PAOT-2)*", Sep. 9th-12nd, **2013**, Gdansk University, Poland. (**Invited Conference**)

GENERAL ABSTRACT

Photocatalysis is recently extensively studied because it implies a variety of potential industrial applications ranging from the hydrogen generation of water splitting to the treatment of waste water. Among all the semiconductors, TiO_2 has attracted the most attention. But the rate of the electron-hole recombinations is very important and TiO_2 is active only under UV light. Various methods are developed to enhance the photoactivity of TiO_2. Other semiconductors like copper oxides and copper sulfides also attracted attention due to their lower band-gaps which allow applications in solar photocatalysis.

In this work, different kinds of photocatalysts were developed and studied: surface modified TiO_2 with metal nanoparticles and copper sulfides and oxides. The nanostructures were characterized by different techniques: HRTEM, SEM, XRD, XPS, HAADF-SEM, and TRMC. Their photocatalytic activity was studied for degradation of model pollutants: phenol, rhodamine B and methyl orange.

Different chemical and radiolytic methods have been investigated to modify the surface of TiO_2 by mono- and bimetallic (Au, Cu and Au-Cu) nanoparticles in the aim to improve its photocatalytic activity. The best results in term of photocatalytic activity have been obtained with reduction of THPC (tetrakis (hydroxymethyl) phosphonium chloride) and with radiolytic reduction after deposition with urea. Titania surface modification with Au, Cu and bimetallic Au-Cu NPs enables the increase of the photocatalytic activity under UV light. We have found that very small amounts of metal (0.5% wt.) can activate titania for photocatalytic applications, thus the costs of photocatalyst preparation are relatively low.

Radiolytic syntheses of non-TiO_2 photocatalysts including Cu_2O and CuS nanostructures with different morphologies have been developed. The photocatalytic activity of the synthesized photocatalysts has been studied. Truncated octahedral Cu_2O exhibit an excellent photocatalytic activity under visible illumination. CuS nanotubes (NTs) exhibit both a high ability to adsorb dyes and a photocatalytic activity under visible light.